

Pressure and Electrokinetically Driven Flows of Viscoelastic Fluids through a Model Porous System



DOCTOR OF PHILOSOPHY

by

Mohd Bilal Khan

(2018CHZ0001)

DEPARTMENT OF CHEMICAL ENGINEERING
INDIAN INSTITUTE OF TECHNOLOGY ROPAR

September, 2023

Pressure and Electrokinetically Driven Flows of Viscoelastic Fluids through a Model Porous System

A Thesis Submitted

In Partial Fulfillment of the Requirements
for the Degree of

DOCTORATE OF PHILOSOPHY

by

Mohd Bilal Khan

(2018CHZ0001)



DEPARTMENT OF CHEMICAL ENGINEERING

INDIAN INSTITUTE OF TECHNOLOGY ROPAR

Punjab, India-140001

September, 2023

Mohd Bilal Khan: *Pressure and Electrokinetically Driven Flows of Viscoelastic Fluids through a Model Porous System*

Copyright ©2023, Indian Institute of Technology Ropar

All Rights Reserved

*This thesis is dedicated to my loving parents, sister, and brother
for their endless support and encouragement.*

Declaration

I hereby declare that the work which is being presented in the thesis entitled "Pressure and Electrokinetically Driven Flows of Viscoelastic Fluids through a Model Porous System" has been solely authored by me. It presents the result of my own independent research conducted during the time period from 31 July 2018 to May 2023 under the supervision of Dr. Chandi Sasmal, Assistant Professor, Department of Chemical Engineering, IIT Ropar. To the best of my knowledge, it is an original work, both in terms of research content and narrative, and has not been submitted or accepted elsewhere, in part or in full, for the award of any degree, diploma, fellowship, associateship, or similar title of any university or institution. Further, due credit has been attributed to the relevant state-of-the-art and collaborations (if any) with appropriate citations and acknowledgments, in line with established ethical norms and practices. I also declare that any idea/data/fact/source stated in my thesis has not been fabricated/ falsified/ misrepresented. All the principles of academic honesty and integrity have been followed. I fully understand that if the thesis is found to be unoriginal, fabricated, or plagiarized, the Institute reserves the right to withdraw the thesis from its archive and revoke the associated Degree conferred. Additionally, the Institute also reserves the right to appraise all concerned sections of society of the matter for their information and necessary action (if any). If accepted, I hereby consent for my thesis to be available online in the Institute's Open Access repository, inter-library loan, and for the title abstract to be made available to outside organizations.



Signature

Name: Mohd Bilal Khan

Entry no.: 2018CHZ0001

Program: PhD

Department of Chemical Engineering

Indian Institute of Technology Ropar

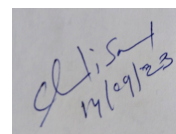
Rupnagar, Punjab 140001

Date:

Certificate

This is to certify that the thesis entitled “Pressure and Electrokinetically Driven Flows of Viscoelastic Fluids through a Model Porous System”, submitted by Mohd Bilal Khan (2018CHZ0001), for the award of the degree of Doctor of Philosophy of Indian Institute of Technology Ropar, is a record of bonafide research work carried out under my guidance and supervision. To the best of my knowledge and belief, the work presented in this report is original and has not been submitted, either in part or full, for the award of any other degree, diploma, fellowship, associateship, or similar title of any university or institution.

In my opinion, the Project Report has reached the standard of fulfilling the requirements of the regulations relating to the Degree.

A rectangular box containing a handwritten signature in blue ink. The signature appears to be 'Chandi Sasmal' with the date '14/09/23' written below it.

Signature

Dr. Chandi Sasmal

Department of Chemical Engineering

Indian Institute of Technology Ropar

Rupnagar, Punjab 14000

Date: 14/09/2023

Acknowledgements

All praise is due to Allah, by whose honor and majesty, deeds of virtue are accomplished. Good research involves hard work, unconditional support, and guidance. I want to express my sincere gratitude to my Ph.D. guide Dr. Chandi Sasmal for his valuable support and guidance during this work. His determination, persistence, sincerity, and motivation have inspired me in the research. During my Ph.D., he taught me the procedure to conduct research and to present the outcome as good as possible. It was my honor to study and work under his guidance. I also like to thank Prof. Raj P. Chhabra, who gave all his support and guided us to make our research work accurate and presentable. I am incredibly thankful to all my doctoral committee members for their valuable suggestions and for sharing their expertise during my Ph.D.

I want to express my deep and sincere thanks to all the faculties of the chemical engineering department; under them, I benefited enormously from their excellence as a teacher and a person. I am extending my thanks to the office staff of the chemical engineering department for their support, especially Ms. Sanpreet Kaur, who helped me to learn the purchase procedure and bill processing.

I am also grateful to my friends and colleagues, who are always present whenever I need them. I consider myself lucky to have friends like Faizan, Chandra Shekhar, Ashish, Jyoti, and Sahil; seniors like Piyush, Tarani, and Sadanand; juniors like Akanksha, Akash Bajpai, Akash Tyagi, Pratibha, Richa, Vishal, Nilanjan, and lab mates Shivam, Anant, Faheem, Ankit, and Mayank. Their presence always makes me happy and supports me in completing my work successfully.

Finally, I am grateful to my parents for their love, support, and sacrifices in providing me with everything I need for my education. The help and valuable suggestions I am getting from my brother Dr. Faisal, and sister Dr. Ayesha are also appreciable for completing my Ph.D. successfully. They all have a special place in my heart; without them, it was impossible.

Abstract

The flow of viscoelastic fluids through a porous media such as polymer or wormlike micellar solutions is encountered in many pragmatic applications ranging from enhanced oil recovery (EOR) process to soil remediation. This particular flow system deserves special attention in the complex fluids research community due to the occurrence of the viscoelastic instability phenomenon resulting from the interaction between the non-linear elastic stresses and a high streamline curvature present in this flow system. The present thesis aims to investigate the complex flow dynamics of these viscoelastic fluids through various model porous systems, such as a straight microchannel with step expansion and contraction or a microchannel with in-built obstacles, under both pressure and electrokinetically driven flow conditions. Extensive finite volume method (FVM) based computational fluid dynamics (CFD) simulations and limited microfluidic experiments comprising soft lithography and micro-particle image velocimetry (μ -PIV) techniques have been conducted to achieve the objectives of the present thesis. Additionally, the present dissertation performs a detailed rheological study of viscoelastic fluids and uses the data-driven reduced-order modeling technique to explain and understand the results in more detail. The chapter-wise abstract of the present thesis is written below.

Chapter 4 discusses the rheological investigation of rhamnolipid, a well-known bacterial biosurfactant produced by the *Pseudomonas aeruginosa* bacteria. This chapter presents a thorough and complete investigation of this biosurfactant's shear and extensional rheological behaviours. While steady shear and small amplitude oscillatory shear (SAOS) measurements are conducted to investigate the shear rheological behaviour, the dripping-onto-substrate (DoS) extensional rheometry technique is used to understand its extensional rheological behaviour. A chemically derived surfactant (cetyltrimethyl ammonium bromide (CTAB)) is also used in the analysis to show and discuss the qualitative and quantitative differences in their rheological behaviours. Along with the detailed rheological study, some studies on the physicochemical properties, such as surface tension, contact angle, particle size analysis, thermal stability, etc., are also conducted to compare the two surfactants. Both surfactants show strong shear-thinning and extensional

hardening behaviors in shear and extensional rheological flows, respectively. However, the zero-shear rate viscosity and extensional viscosity are higher for rhamnolipid surfactant solutions than for CTAB. The corresponding shear and extensional relaxation times also follow the same trend. Furthermore, the surface tension is found to be less, and the contact angle is found to be more for rhamnolipid biosurfactant than for CTAB. Rhamnolipid shows more excellent thermal stability, particularly at high temperatures, than CTAB. Therefore, the results and discussion presented in this chapter will help to choose the present rhamnolipid biosurfactant for any particular application, particularly where the knowledge of the rheological responses of a surfactant solution is essential.

The flow of wormlike micellar solutions past a microfluidic cylinder confined in a channel is considered in chapter 5. Earlier experiments showed the existence of an elastic instability for the flow of a wormlike micellar solution in this model porous system after a critical value of the Weissenberg number in the creeping flow regime. This chapter presents a detailed numerical investigation of this elastic instability in this model porous system using the two-species VCM (Vasquez-Cook-McKinley) constitutive model for the wormlike micellar solution. In line with the experimental trends, we also observe a similar elastic instability in this flow system once the Weissenberg number exceeds a critical value. We also find that the breakage and reformation dynamics of the wormlike micelles greatly influence the elastic instability in this model geometry. In particular, the onset of such an elastic instability is delayed or even maybe suppressed entirely as the micelles become progressively easier to break. Furthermore, this elastic instability is associated with the elastic wave phenomena, which have been recently observed experimentally for polymer solutions. The present study reveals that the speed of such an elastic wave increases non-linearly with the Weissenberg number similar to that seen in polymer solutions.

Chapter 6 presents an extensive numerical investigation of the flow characteristics of wormlike micellar solutions past a single and two vertically aligned microcylinders placed in a microchannel in the creeping flow regime. For the case of a single microcylinder, as the blockage ratio (ratio of the cylinder diameter to that of the channel height) is gradually varied, we find the existence of a flow bifurcation in the system and also a gradual transition for a range of flow states, for instance, steady and symmetric or Newtonian like, steady and asymmetric, unsteady periodic and asymmetric, unsteady quasi-periodic and asymmetric, and finally, unsteady quasi-periodic and symmetric. For the case of two

microcylinders, we observe the presence of three distinct flow states in the system, namely, diverging (D), asymmetric-diverging (AD), and converging (C) states as the intercylinder spacing between the two cylinders is varied. Recent experiments dealing with wormlike micellar solutions also observe similar flow states. However, we show that either this transition from one flow state to another in the case of a single microcylinder or the occurrence of any flow state in the case of two microcylinders is strongly dependent upon the values of the Weissenberg number and the non-linear VCM model parameter ξ , which indicates how easy or hard it is to break a micelle. Based on the results and discussion presented herein for the single and two microcylinders, we hope this study will facilitate the understanding behind the formation of preferential paths or lanes during the flow of viscoelastic fluids through a porous media, which was seen in many prior experiments in the creeping flow regime.

Chapter 7 presents a detailed numerical investigation of the electrokinetic transport of both Newtonian and viscoelastic fluids in a model porous system consisting of a long micropore with step expansion and contraction. Over the whole range of conditions encompassed in this study, a steady and symmetric flow field is observed for a Newtonian fluid. However, for a viscoelastic fluid, we observe a transition in the flow field from steady and symmetric to unsteady and asymmetric once the Weissenberg number (ratio of the elastic to that of the viscous forces) exceeds a critical value. We show that this transition is caused due to the onset of an electro-elastic instability in the system. The critical value of this Weissenberg number (at which this transition occurs) depends on various factors. In particular, this value increases with the polymer viscosity ratio and expansion and contraction lengths of the micropore. At fixed values of the electric field strength, polymer viscosity ratio, contraction, and expansion lengths of the micropore, we observe the existence of different vortex dynamics within this model porous system as the Weissenberg number gradually increases, such as the emergence of the entrant and re-entrant lip vortices, oscillating lip vortices, multi vortices, etc. Therefore, the electrokinetic flow dynamics of viscoelastic fluids in a porous system are much more complex than that of simple Newtonian fluids. We hope this study for a model porous system will facilitate a better understanding of the electrokinetic transport phenomena of viscoelastic fluids in an actual porous media. Furthermore, we show how this model system of a long micropore with step expansion and contraction could also be successfully

utilized for other practical applications, such as mixing two viscoelastic fluids.

Chapter 8 investigates the electroosmotic flows of viscoelastic fluids through a microfluidic setup consisting of a straight microchannel with an in-built cylindrical obstacle present in it with the help of both numerical simulations and experiments. It has been found that the flow dynamics of viscoelastic fluids inside this microfluidic setup become unsteady and fluctuating as the applied electric field strength is gradually increased, even though the Reynolds number remains much lower than one. This is because of the origin of the electro-elastic instability (EEI) phenomenon, resulting from the interaction between the non-linear elastic stresses in viscoelastic fluids and streamline curvature present in the flow system. This instability ultimately leads to a flow-switching phenomenon inside the microfluidic setup, observed both in numerical simulations and experiments. The results and discussion of this chapter could facilitate a better understanding of the electrokinetic flows of complex fluids through a porous media, which is encountered in many practical applications such as electro-chromatography, micro-pumping, chemical radiation of contaminated soil, etc. Furthermore, this chapter shows that this flow-switching phenomenon could successfully mix viscoelastic fluids in this simple, easy-to-fabricate microfluidic setup. Additionally, the data-driven dynamic mode decomposition (DMD) analysis has been employed in this study to understand better the dynamical behaviour of various coherent flow structures that originated due to this flow-switching phenomenon and their subsequent influence on the mixing phenomenon.

List of Publications

1. Effect of chain scission on flow characteristics of wormlike micellar solutions past a confined microfluidic cylinder: A numerical analysis, M. B. Khan, C. Sasmal, Soft Matter 16 (22), 5261-5272, 2020.
2. Flow and heat transfer characteristics of a rotating cylinder in a FENE-P type viscoelastic fluid, M. B. Khan, C. Sasmal, R. P. Chhabra, Journal of Non-Newtonian Fluid Mechanics 282, 104333, 2020.
3. Combined influence of fluid viscoelasticity and inertia on forced convection heat transfer from a circular cylinder, C. Sasmal, M. B. Khan, R. P. Chhabra, Journal of Heat Transfer 142 (4), 041801, 2020.
4. Elastic instabilities and bifurcations in flows of wormlike micellar solutions past single and two vertically aligned microcylinders: Effect of blockage and gap ratios, M. B. Khan, C. Sasmal, Physics of Fluids 33 (3), 033109, 2021. **Invited Article**
5. Bifurcation in flows of wormlike micellar solutions past three vertically aligned microcylinders in a channel, M. B. Khan, C. Sasmal, Physics of Fluids 34 (5), 054107, 2022.
6. Effect of micelle breakage rate on flows of wormlike micellar solutions through pore throats, M. B. Khan, C. Sasmal, Journal of Non-Newtonian Fluid Mechanics 307, 104853, 2022.
7. A detailed and systematic study on rheological and physicochemical properties of rhamnolipid biosurfactant solutions, M. B. Khan, C. Sasmal, Journal of Colloid and Interface Science Open, 100067, 2022.
8. Electro-elastic instability in electroosmotic flows of viscoelastic fluids through a model porous system, M. B. Khan, C. Sasmal, European Journal of Mechanics-B/Fluids 97, 173-186, 2023.
9. Flow-switching and mixing phenomena in electroosmotic flows of viscoelastic fluids, MB Khan, F. Hamid, N. Ali, V. Mehandia, C. Sasmal, Physics of Fluids 35 (8), 083101, 2023. **Featured Article**

Contents

Declaration	i
Certificate	i
Acknowledgements	iii
Abstract	iv
List of Figures	xii
List of Tables	xxi
Nomenclature	xxii
1 Introduction	1
2 Literature survey	9
2.1 Rheological and physicochemical studies of biosurfactant and chemically derived micellar solutions	9
2.2 Pressure driven flows of wormlike micellar solutions past a single micro- cylinder confined in a channel	13
2.3 Pressure driven flows of wormlike micellar solutions past two vertically aligned microcylinders confined in a channel	17
2.4 Electrokinetically driven flows of viscoelastic fluids through a microchannel with step expansion and contraction	20
2.5 Electrokinetically driven flows of viscoelastic fluids past a microcylinder confined in a channel	23
2.5.1 Major objectives of the present thesis	26
3 Methodology	27
3.1 Numerical Methodology	27
3.1.1 Governing equations for pressure driven creeping flows of viscoelas- tic wormlike micellar solutions	27

3.1.2	Governing equations for electrokinetically driven creeping flows of viscoelastic polymer solutions	29
3.1.3	Numerical solution technique	31
3.2	Experimental Methodology	35
3.2.1	Rheological and physicochemical characterization of micellar solutions	35
4	Rheological and physicochemical studies of biosurfactant and chemically derived micellar solutions	40
4.1	Results and Discussion	40
4.1.1	Surface tension and contact angle	40
4.1.2	Particle size measurement	43
4.1.3	Thermal gravimetric analysis	45
4.1.4	Steady shear rheological measurements	45
4.1.5	Small amplitude oscillatory shear (SAOS) measurements	48
4.1.6	Capillary thinning and pinch-off dynamics by DoS rheometry	51
5	Pressure driven flows of wormlike micellar solutions past a single microcylinder confined in a channel	59
5.1	Problem formulation	59
5.2	Numerical solution procedure and its validation	60
5.3	Results and discussion	62
5.3.1	Hydrodynamics	63
5.3.2	Variation of micellar concentration and principal stress difference	72
5.3.3	Variation of pressure drop	75
6	Pressure driven flows of wormlike micellar solutions past two vertically aligned microcylinders confined in a channel	77
6.1	Problem formulation	77
6.2	Numerical details	78
6.3	Results and discussion	80
6.3.1	Single microcylinder case: Effect of blockage ratio	80
6.3.2	Two vertically aligned microcylinders case: Effect of gap ratio	92

7	Electrokinetically driven flows of viscoelastic fluids through a microchannel with step expansion and contraction	100
7.1	Problem illustration	100
7.2	Numerical details	101
7.3	Results and discussion	103
7.3.1	Effect of Weissenberg number	103
7.3.2	Effect of expansion and contraction lengths	109
7.3.3	Effect of polymer viscosity ratio	113
7.3.4	Further applications	115
8	Electrokinetically driven flows of viscoelastic fluids past a microcylinder confined in a channel	119
8.1	Microfluidic setup	119
8.2	Methodology	120
8.2.1	Numerical details	120
8.2.2	Dynamic mode decomposition (DMD) analysis	121
8.3	Microfluidic experiments	122
8.4	Results and discussion	124
9	Conclusions and future scope	135
	Bibliography	139

List of Figures

1.1	Representation of the hitchhiker’s guide to the universe of complex viscoelastic fluids by Professor Gareth McKinley [6].	2
1.2	Schematic representation of various model porous systems used in the present study.	2
1.3	Schematics of different geometries where a purely elastic flow instability was observed as presented by Poole [19] and then modified by Datta et al. [20]. Here the numbers on the geometry name designate the corresponding reference number of the article by Datta et al. [20].	5
1.4	Schematic of the formation of different-shaped micelles in a solution. . . .	6
3.1	An illustration of the transformation of a physical model into discrete forms in numerical simulation methodology [177].	31
3.2	Subdivision of domain into finite volume elements or cells, (a), typical interconnected polyhedral cells (b) having a common face. Each face inside the domain is shared by two cells; one is the owner, and the other is the neighboring cell [177].	32
3.3	A simple case file structure in OpenFOAM [183]. After initiating the terminal, the command is typed to carry out the simulation and the post-processing.	34
3.4	Flowchart of the steps followed to solve the present problem using OpenFOAM.	34
3.5	Representation of molecular structure of (a) rhamnolipid and (b) CTAB. (c) FTIR results of di-rhamnolipid surfactant, which reveal the presence of mono-rhamnolipid as 10% impurity in it. This observation is in line with that seen by Rahman et al. [185]. The first marked circle from the left side represents -OH stretch due to the hydrogen bonding (3310 cm^{-1}), and the second marked circle represents an aliphatic bond stretching ($2960 - 2859\text{ cm}^{-1}$). Rhamnose rings and hydrocarbon chains are found in these two regions. The third marked circle confirms the presence of di-rhamnolipid.	36

3.6	Schematic representation of the dripping-onto-substrate (DoS) rheometry setup. It consists of a light source for backlighting the liquid filament, and a high-speed camera connected to a computer system to record the filament thinning and pinch-off dynamics of the liquid bridge formed between the dispensing system and the glass substrate. The dispensing system consists of a syringe pump that releases a known amount of test sample through a nozzle of diameter D_o placed at a height H from the glass substrate. . . .	39
4.1	Representation of surface tension as a function of surfactant concentration for both rhamnolipid and CTAB surfactant solutions at 25 °C.	41
4.2	(a) Representation of wetting force as a function of immersion depth (b) advancing and receding contact angles (in degree) as a function of wetting cycle number for both CTAB and rhamnolipid surfactant solutions on pre-equilibrated Wilhelmy platinum plate at 1.0 wt.% concentration. The immersion depth and speed were kept at 3 mm and 5 mm/min, respectively.	42
4.3	Particle size distribution for 1.0 wt.% of (a) CTAB and (b) rhamnolipid surfactant solution at 25 °C.	44
4.4	Representation of TGA curves in terms of weight loss in % for both surfactants under nitrogen atmosphere conditions and ramp rate 30 °C/min.	44
4.5	Variation of the steady shear viscosity with shear the rates both for CTAB and rhamnolipid solutions at 25 °C.	46
4.6	Variation of zero-shear viscosity with concentration both for CTAB and rhamnolipid solutions at 25 °C.	46
4.7	Representation of storage (G') and loss (G'') moduli as a function of angular frequency (ω) both for CTAB and rhamnolipid surfactant solutions at 25 °C and shear strain 0.1 %. Slopes 1 and 2 represent the divergence for rhamnolipid biosurfactant.	48
4.8	Representation of storage (G') and loss (G'') moduli as a function of strain (%) both for CTAB and rhamnolipid surfactant solutions at 25 °C. . . .	49
4.9	Representation of shear relaxation time (λ_s) as a function of surfactant concentration both for CTAB and rhamnolipid surfactant solutions at 25 °C.	49

4.10	Representation of different filament shapes and pinch-off obtained using the dripping-onto-substrate (DoS) method at different times for (a) CTAB and (b) rhamnolipid surfactants at 1 wt.% concentration.	52
4.11	Evaluation of radius as a function of time for CTAB and Rhamnolipid surfactant at different concentrations. The plot displayed how the pinch-off time shifted as the surfactant concentration increased.	53
4.12	Filament radius evaluation plot as a function of time at different concentrations of CTAB and Rhamnolipid. Here the time axis is shifted with time t_c . This figure shows the presence of two regimes: one is the inertia-capillary regime (IC) before t_c and elasto-capillary regime (EC) after t_c	54
4.13	(a) Variation of the extensional relaxation time (λ_E) with the surfactant concentration. (b) Variation of the ratio of the extensional and shear relaxation times (λ_S) with the surfactant concentration.	55
4.14	Extensional viscosity (η_S) as a function of Hencky strain (ϵ) for both surfactant at different concentrations.	57
5.1	(a) Schematic of the present problem (b) A typical mesh used in the present study with a zoomed view near the cylinder surface.	59
5.2	(a) Variation of the non-dimensional shear viscosity versus the shear rate in homogeneous shear flow (b) Variation of the non-dimensional extensional viscosity versus the extensional rate in homogeneous planar extensional flow.	60
5.3	Comparison between the present results (lines) and the results of Cromer et al. [239] (symbols) for the flow of a wormlike micellar solution through a straight microchannel at a non-dimensional pressure gradient of $P = 1$. Non-dimensional streamwise velocity at (a) $= 10^{-3}$ and (b) $= 10^{-1}$. The magnitude of the non-dimensional conformational tensor component of the long chain A at two different non-dimensional values of the diffusivity parameter, namely, (c) $D = 10^{-3}$ and (d) $D = 10^{-1}$. Other non-dimensional VCM parameters are: $\beta = 7 \times 10^{-5}$, $\mu = 1.9$, $c_{Aeq} = 0.9$, $c_{Beq} = 1.4$, $\epsilon = 6.27 \times 10^{-4}$, $\xi = 0.3$	61
5.4	Representative of streamline profiles (a) Newtonian fluid (b) WLM solution, $\xi = 0$, $Wi = 0.445$, (c) $\xi = 0.01$, $Wi = 0.001$	63

5.5	(a) Variation of the non-dimensionalized stream-wise velocity both for Newtonian and VCM fluids upstream and downstream mid-plane of the cylinder (b) Temporal variation of the stream-wise velocity at a point downstream of the cylinder for VCM fluids at two different values of the Weissenberg number.	63
5.6	Representative streamline patterns at various values of the Weissenberg number and for two values of the non-linear VCM model parameter ξ , namely, 0.01 and 0.1.	64
5.7	(a) Temporal variation of X-component velocity at a position near to the front stagnation point (b) Power spectral density plot of the temporal variation of X-component velocity at $Wi = 2.5$ and $\xi = 0.01$	65
5.8	Temporal variation of the normal stress component $\tau_{w,YY}$	67
5.9	(a) Variation of extension rate ($\dot{\epsilon}_{XX}$) along the mid-plane downstream of the cylinder at $Wi = 2.0$ at two different times (b) Temporal variation of the maximum extension rate ($\dot{\epsilon}_M$) downstream of the cylinder at $Wi = 2.0$ (c) Variation of the local extensional Weissenberg number (Wi_{Ext}^L) with the Weissenberg number	67
5.10	Velocity magnitude plot (a) $Wi = 1.5, \xi = 0.01, t = 49$ (b) $Wi = 2.5, \xi = 0.01, t = 49.1$ (c) $Wi = 2.5, \xi = 0.01, t = 50$ (d) $Wi = 1.5, \xi = 0.1, t = 49$ (e) $Wi = 2.5, \xi = 0.1, t = 49.1$ (f) $Wi = 2.5, \xi = 0.1, t = 50$	68
5.11	Velocity magnitude plots (a) Newtonian fluid (b) WLM solution, $\xi = 0.01$, $Wi = 0.001$	69
5.12	Cross-correlation function plot for the X-component velocity at two locations, one at the upper gap region and another at the lower gap region of the channel.	70
5.13	Variation of the elastic wave speed with the Weissenberg number. Here the results are presented for the non-linear VCM model parameter $\xi = 0.01$	71
5.14	Variation of dye concentration at (a) $t = 0$ (b) $t = 35.0$ and (c) $t = 35.7$	71
5.15	Distribution of the long chain number density (a-d) and principal stress difference (e-h). (a,e) $Wi = 1.5, \xi = 0.1$ (b,f) $Wi = 1.5, \xi = 0.01$ (c,g) $Wi = 2.5, \xi = 0.1$ (d,h) $Wi = 2.5, \xi = 0.01$. (i) Flow-induced birefringence image taken in the experiments of Sun and Huang [245] at $Wi = 1.48$	73

5.16	Distribution of the long chain number density (a-d) and principal stress difference (e-h). (a,e) $Wi = 0.001, \xi = 0.1$ (b,f) $Wi = 0.001, \xi = 0.01$ (c,g) $Wi = 0.5, \xi = 0.1$ (d,h) $Wi = 0.5, \xi = 0.01$	74
5.17	Variation of the pressure drop with the Weissenberg number and non-linear VCM model parameter ξ	75
6.1	Schematic of the present problem for (a) single microcylinder and (c) side-by-side vertically aligned two microcylinders. A typical mesh density was used in the present study for single (b) and two (d) microcylinders. Here the flow direction is shown by arrows in the schematic.	78
6.2	Variations of the non-dimensional shear stress (a) and shear viscosity (b) with the non-dimensional shear rate (or the shear Weissenberg number) and first normal stress difference (c) and extensional viscosity (d) with the non-dimensional extension rate (or the extensional Weissenberg number) in homogeneous shear and uniaxial extensional flows, respectively. Here, the symbols (both filled and open) are used to discuss some results presented in section 6.3.	79
6.3	Representative streamline and velocity magnitude plots for Newtonian fluid with blockage ratio of $BR = 0.34$	81
6.4	Representative streamline and velocity magnitude plots of a WLM solution at $Wi = 1.0$ and $\xi = 0.01$ for different blockage ratios, (a) $BR = 0.67$, (b) $BR = 0.34$, (c) $BR = 0.25$, (d) $BR = 0.167$	82
6.5	Surface plot of principle stress difference of a WLM solution at $Wi = 1.0$ and $\xi = 0.01$ for different blockage ratios, (a) $BR = 0.67$, (b) $BR = 0.34$, (c) $BR = 0.25$, (d) $BR = 0.167$	83
6.6	Representative streamline and velocity magnitude plots of a WLM solution at $Wi = 2.5$ and $\xi = 0.01$ for different blockage ratios, (a) $BR = 0.67$, $t = 30$ (b) $BR = 0.67$, $t = 30.2$, (c) $BR = 0.34$, (d) $BR = 0.25$, (e) $BR = 0.167$	85
6.7	(a) Temporal variation of the stream-wise velocity component at a probe location placed in the middle in between the cylinder surface and upper channel wall and (b-d) power spectral density plot of the velocity fluctuations at different blockage ratios at $Wi = 2.5$ and $\xi = 0.01$	86

6.8	Surface plot of principle stress difference of a WLM solution at $Wi = 2.5$ and $\xi = 0.01$ for different blockage ratios, (a) $BR = 0.67$, (b) $BR = 0.34$, (c) $BR = 0.25$, (d) $BR = 0.167$	88
6.9	Variation of the flow asymmetry parameter (I_s) with the Weissenberg number and blockage ratio at $\xi = 0.01$	89
6.10	Variation of the flow asymmetry parameter (I_s) with the blockage ratio at $Wi = 2.5$ and $\xi = 0.01$. In this figure (I) steady and symmetric (II) steady and asymmetric (III) unsteady, periodic, and asymmetric (IV) unsteady, quasi-periodic and asymmetric, and (V) unsteady, quasi-periodic, and symmetric.	90
6.11	Representative streamline and velocity magnitude plots at $BR = 0.34$ and $Wi = 2.5$. (a) and (b) $\xi = 0.00001$, (c) $\xi = 0.1$	92
6.12	Representative streamline and velocity magnitude plots for vertically side-by-side two microcylinders case at $\xi = 0.01$, (a) $G = 0.28$, Newtonian (b) $G = 0.28$, $Wi = 0.3$ (c) $G = 0.28$, $Wi = 1.0$ (d) $G = 0.28$, $Wi = 2.5$ (e) $G = 0.5$, Newtonian (f) $G = 0.5$, $Wi = 0.3$ (g) $G = 0.5$, $Wi = 1.0$ (h) $G = 0.5$, $Wi = 2.5$	93
6.13	Temporal variation of the stream-wise velocity component at a probe location $X = 0$ and $Y = 0$ for two gap ratios, namely, 0.28 (a) and 0.5 (b). The corresponding power spectral density plot of the velocity fluctuations at $G = 0.28$ (b) and at $G = 0.5$. Here all the results are presented for non-linear VCM model parameter $\xi = 0.01$	95
6.14	Variation of the flow asymmetry parameter for the two microcylinders case at $G = 0.28$ (a-c) and at $G = 0.5$ (d-f). In subfigure (c), (I) Newtonian-like state (II) Diverging or 'D' state and (III) Asymmetric-diverging or 'AD' state, whereas in subfigure (f), (I) Newtonian-like state and (II) converging or 'C' state.	96
6.15	Variation of the principle stress difference for the two microcylinders case (a) $G = 0.28$, $Wi = 1.0$ (b) $G = 0.28$, $Wi = 5.0$ (c) $G = 0.5$, $Wi = 1.0$ (d) $G = 0.5$, $Wi = 5.0$	97
7.1	(a) Schematic of the present problem (b) Computational domain	101

7.2	Comparison of the stream-wise velocity in a microfluidic channel between the present numerical and analytical results of Afsono et al. [252] at a constant wall zeta potential of $\xi_0 = -110$ mV. Note that the results are presented here for the half non-dimensional height of the microchannel. .	102
7.3	Streamlines and velocity magnitude plots for (a) Newtonian and viscoelastic fluids with different Weissenberg numbers, namely, (b) $Wi = 0.5$, (c) $Wi = 2$, (d) $Wi = 7$, (e) and (f) $Wi = 15$ at two different times.	103
7.4	(a) Temporal variation of the non-dimensional stream-wise (U_x) velocity component at the origin of the micropore at different Weissenberg numbers. (b) and (c) Power spectral density plots of velocity fluctuations.	104
7.5	Variation of the non-dimensional stream-wise (U_x) and span-wise (U_y) velocity components along horizontal (a and b) and vertical (c and d) mid-planes passing through the origin of the micropore.	106
7.6	Variation of the Pakdel-McKinley M parameter at different Weissenberg numbers, namely, (a) $Wi = 0.5$, (b) $Wi = 6$, and (c) $Wi = 15$	107
7.7	Streamlines and velocity magnitude plots inside the micropore at two different values of EL , namely, 2 (a) and 8 (b) at $Wi = 3$. Note that here the x-axis label values in the zoomed-in figures are non-dimensional. . . .	109
7.8	Temporal variation of the stream-wise velocity at a probe location placed at the origin of the micropore at $Wi = 3$ (a) and 15 (c) at two different values of the expansion length, namely, 2 and 8. The corresponding power spectrum plot of the velocity fluctuations is presented in (b) and (d), respectively.	110
7.9	Streamlines and velocity magnitude plots inside the micropore with $CL = 3$ (a) and 5 (b). The temporal variation of the stream-wise velocity and power spectrum of velocity fluctuations are shown in sub-Figures (c) and (d). Here all the results are presented at $Wi = 3$. Note that the x-axis label values in the zoomed-in figures are non-dimensional.	111

7.10	Streamlines and velocity magnitude plots at different values of the polymer viscosity ratio, (a) $\beta = 0.2$, (b) $\beta = 0.4$, and (c) $\beta = 0.6$. (d) Temporal variation of the stream-wise velocity at a probe location placed at the origin of the micropore at two different values of the polymer viscosity ratio. (e) The corresponding power spectrum plot of velocity fluctuations at $\beta = 0.2$. Here all the results are presented at $Wi = 3$	113
7.11	Phase diagram showing the existence of different flow states in $\beta - Wi$ space.	114
7.12	Instantaneous dye concentration profile inside the micropore. (a) $Wi = 0.1$ (b) $Wi = 6$ and (c) $Wi = 15$. Here the profile at different values of the Weissenberg number is shown at the same non-dimensional time of $t = 100$. Other simulation parameters are kept constant as $E_x = 5000$ and $\beta = 0.4$.	115
7.13	Variation of the mixing efficiency parameter η with the Weissenberg number.	116
8.1	(a) Schematic of the present problem and (b) grid structure (grid G3) used in the present numerical simulation. (c) SEM image of PDMS microfluidic setup, and (d) experimental setup with the platinum electrode and connected DC power supply. Here, the blue dot in the schematic of the problem setup is the probe location where the velocity is measured and analyzed.	120
8.2	(a) Variation of the shear viscosity with the shear rate. (b) Variation of the storage (G') and loss (G'') modulus with the angular frequency for viscoelastic Boger fluids at 30 °C both in the presence of salt and without salt.	123
8.3	Velocity vector and magnitude plots both for Newtonian ((a) and (b)) and viscoelastic fluids ((c) and (d)) at an applied electric field strength of $E_x = 1428.57 \text{ V/m}$ and $Wi = 3.53 \times 10^{-4}$. (e) Temporal variation of the non-dimensional stream-wise (U_x) velocity at a probe location placed at the upper cylinder gap region for both fluids at the same conditions. . . .	124

8.4	Velocity vector and magnitude plots for viscoelastic fluids at $E_x = 2857.14$ V/m and $Wi = 7.06 \times 10^{-4}$ for two different times both in simulations ((a) $t = 0.077$, (b) $t = 0.08$) and experiments ((f) $t = 0.087$ (g) $t = 0.092$). The same at $E_x = 4285.71$ V/m and $Wi = 1.05 \times 10^{-3}$ for three different times both in simulations ((c) $t = 0.09$, (d) $t = 0.093$, (e) $t = 0.098$) and experiments ((h) $t = 0.095$, (i) $t = 0.1$, (j) $t = 0.103$)	125
8.5	Temporal variation of the non-dimensional stream-wise (U_x) velocity component (a) and power spectral density plot of velocity fluctuations for viscoelastic fluids (b) at two values of the electric field strength, namely, 2857.14 V/m ($Wi = 7.06 \times 10^{-4}$) and 4285.71 V/m ($Wi = 1.05 \times 10^{-3}$). .	126
8.6	Surface plot of the non-dimensional elastic stress component τ_{xx} for $E_x = 1428.57$ V/m ($Wi = 3.53 \times 10^{-4}$) at $t = 0.071$ and $E_x = 2857.14$ V/m ($Wi = 7.06 \times 10^{-4}$) at two different times, namely, (b) $t = 0.077$ and (c) $t = 0.08$. .	129
8.7	Instantaneous dye concentration profiles (at a time $t = 5$ s) inside the microchannel at (a) 71.42 , V/m , (b) 1428.57 V/m , (c) 2857.14 V/m , and (d) 4285.71 V/m . The corresponding time-averaged mean dye concentration profiles ((e)-(h)) at the same applied electric field strengths.	129
8.8	Variation of the mixing efficiency parameter Φ with the applied electric field strength E_x . Here the calculation is performed for a time of 5 s. . .	130
8.9	Time coefficient norm ($ Co_j $) and growth rate (σ_j) against the frequency (St_j) at $E_a = 357.14V/m$ ((a) and (b), Low voltage case) and $E_a = 4285.71V/m$ ((c) and (d), High voltage case). The color bar in σ_j vs St_j represents the mode norm ($ \phi_j $). Also, in the same plot, the encircled modes are the modes sorted based on the time coefficient norm $ Co_j $, where unlabeled modes are complex conjugates of the labeled ones.	131
8.10	Instantaneous concentration field (a) and representative DMD modes (b)-(e) at $E_a = 357.14V/m$ (Low voltage case) and $E_a = 4285.71V/m$ (High voltage case), respectively. Here, (b) is the mean mode, and (c), (d), and (e) correspond to mode 1, mode 2, and mode 3, along with associated frequencies for each electric field strength.	133

List of Tables

4.1	Values of the advancing and receding contact angles for both CTAB and rhamnolipid surfactants as a function of concentration.	43
5.1	Boundary conditions for the present computation domain	60
8.1	Details of the grid independence study carried out at $E_x = 4285.71 \text{ V/m}$ and $Wi = 1.05 \times 10^{-3}$. Here $u_{x,avg}$ is the time-averaged stream-wise velocity evaluated at a probe location placed at the upper cylinder gap region (blue dot in sub-Fig.1(a)).	121

Nomenclature

ω	Angular Frequency, rad/s
A	Long Chain Micelles Tensor
B	Short Chain Micelles Tensor
$c_{i,0}$	Bulk Ion Concentration
c_i	Ion Concentration, $c_{i,0}exp(\frac{ze\Psi}{kT})$
C_p	Critical Packing Parameter, $\frac{v}{a_0l}$
Co	Courant number, $\frac{u\Delta t}{\Delta x}$
e	Electron Charge, $coulomb$
E_s	Modulus of Elasticity, Pa
El	Elasticity Number, $\frac{Wi}{Re}$
F	Faraday's Constant
f	Peterlin Function
F_z	Thrust Force, N
G'	Storage Modulus, Pa
G''	Loss Modulus, Pa
K_B	Boltzmann Constant, J/k
L^2	Polymer Extensibility Parameter
L_c	Flow Length, m
l_p	Persistence Length of Micelles, nm
N_1	Normal Stress Difference, N/m_2
n_A	Long Chain Micelles Density
n_B	Short Chain Micelles Density
p	Pressure, Pa
S_f	Face Area Vector
T	Temperature, K

t	Time, s
U	Helmholtz-Smoluchowski Velocity, m/s
U_∞	Free stream velocity, m/s
U_c	Flow Velocity, m/s
Wi	Weissenberg number, $\frac{\rho U_{in} d}{\eta}$
z	Ion Valency

Greek symbols

β	Polymer viscosity ratio, $\frac{\eta_s}{\eta_s + \eta_p}$
ΔS	Minimum cell area, m^2
Δt	Time step, $\frac{td}{U_{in}}$
Δx	Cell size, m
ϵ	dielectric constant, F/m
η_0	Zero Shear Rate Viscosity of Polymer Solution, $Pa.s$
η_p	Polymer viscosity, $Pa.s$
η_s	Solvent viscosity, $Pa.s$
λ	Polymer Relaxation Time, s
λ_A	Relaxation Time for Long Chain Worm A, s
λ_B	Relaxation Time for Short Chain Worm B, s
λ_d	Debye Length, nm
λ_{eff}	Effective Relaxation Time, s
μ	Fluid viscosity, $Pa.s$
$\dot{\gamma}$	Rate of deformation, s^{-1}
Ψ	Normal Stress Coefficient
ψ	Electric Potential, J/C
ρ	Density, $\frac{Kg}{m^3}$
ρ_e	Total Charge Density, $\sum z_i e c_i$
τ	Overall Deviatoric Stress Tensor, $\frac{N}{m^2}$
τ_p	Polymer Deviatoric Stress Tensor, $\frac{N}{m^2}$

τ_s	Viscous Deviatoric Stress Tensor, $\frac{N}{m^2}$
τ_w	Wormlike Micellar Deviatoric Stress Tensor, $\frac{N}{m^2}$
ξ	Chain Scission Parameter
ζ	Wall Zeta Potential, mV
\dot{c}'_{Aeq}	Equilibrium Breakage Rate for Long Chain Worm A
c_B	Reformation Rate for Short Chain Worm B, $c_B = c_{Beq}$
I	Identity Tensor

Acronyms/Abbreviations

BCG	Germann-Cook-Beris
CA	Contact Angle
CaBER	Capillary Breakup Extensional Rheometer
CCF	Cross Correlation Function
CFD	Computational Fluid Dynamics
CMC	Critical Micelles Concentration
CTAB	Cetyltrimethylammonium Bromide
CUBISTA	Convergent and Universally Bounded Interpolation Scheme for Treatment of Advection
DIC	Diagonal-based Incomplete Cholesky
DILU	Diagonal-based Incomplete LU
DLS	Dynamic Light Scattering Technique
DNS	Direct Numerical Simulation
DoS	Dripping-onto-substrate Rheometry
EC	Elasto Capillary Regime
EDL	Electrical Double Layer
EEI	Electro-elastic Instability
EIC	Extension Induced Structure
FENE–MCR	Modified Chilcott–Rallison Finitely Extensible Nonlinear Elastic Model
FFT	Fast Fourier Transform

FIB Flow-induced Birefringence
 FVM Finite Volume Method
 HPAM Hydrolyzed Polyacrylamide
 HWNP High Weissenberg Number Problem
 I-PTT Linear Phan-Thien-Tanner
 iBSD Improved Both Side Diffusion
 IC Inertia Capillary Regime
 MPI Message Passing Interface
 NaSal Sodium Salicylate
 NNLS Non-negative Least Squares Fit
 PB Poisson-Boltzmann
 PBiCG Preconditioned Bi-conjugate Gradient Solver
 PCG Preconditioned Conjugate Solver
 PEG Polyethylene Glycol
 PEO Polyethylene Oxide
 PSD Power Spectral Density
 PSD Principal Stress Difference
 SANS Small-angle Neutron Scattering
 SAOS Small Amplitude Oscillatory Shear
 SIMPLE Semi-Implicit Method for Pressure-Linked Equations
 UCM Upper Convective Maxwell Model
 VCM Vasquez–Cook–McKinley Model
 VCM-R Vasquez–Cook–McKinley Revised
 WLM Wormlike Micellar Solution

Chapter 1

Introduction

Viscoelastic fluids are a sub-class of complex fluids ubiquitous in daily life and many technological applications [1]. These fluids exhibit both viscous and elastic properties with varying extents under deformation depending upon the microstructure of the fluids and the flow condition in any particular application. This suggests that these fluids can deform and flow like a viscous fluid and store or dissipate elastic energy like an elastic solid [2]. The most common examples of these fluids are polymer solutions, suspensions, emulsions, melts, etc., routinely used in polymer and food processing applications. Furthermore, many biofluids, such as blood, saliva, sputum, synovial, cerebrospinal, etc., also exhibit a great extent of viscoelastic behaviour under deformation [3, 4]. Another example of viscoelastic fluids is a surfactant solution with long, flexible micellar chains. Above a critical surfactant concentration, the surfactant molecules are self-assembled and form large aggregates called micelles. Further increasing the surfactant concentration in the solution leads to the entanglement of these micellar chains, originating wormlike micelles in the solution [5]. The Hitchhiker's Guide to the Universe of complex fluids, presented by Professor Gareth McKinley, is the classic illustration of the complex viscoelastic fluids existing in nature and various technological applications, shown in Fig. 1.1.

The flow behaviour of these viscoelastic fluids through geometries of practical interest with an inhomogeneous flow field is found to be complex and rich in physics compared to that seen for simple Newtonian fluids under the same flow conditions. This is because a non-linear relationship is present between the stress and the applied deformation in the case of a viscoelastic fluid compared to that of a linear relationship present for Newtonian fluids. In particular, this thesis deals with the flow of such viscoelastic fluids through a porous geometry. This particular flow plays an essential role in many industrial and engineering operations, such as petroleum exploration (particularly in the enhanced oil recovery (EOR) process), groundwater remediation, oil filters, ceramic and textile engineering, biomedical membranes, etc. [7, 8, 9]. This flow is a matter of intense investigation from the past several decades and is still subject to many unsolved fundamental questions. Therefore, the investigation presented in this thesis aims to facilitate a profound

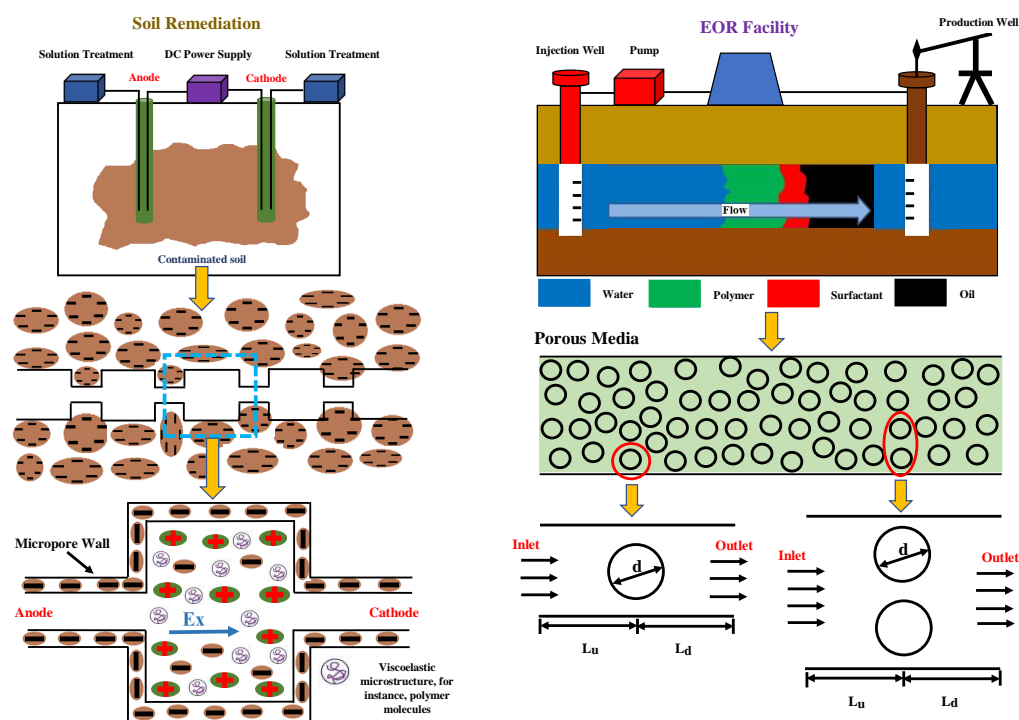
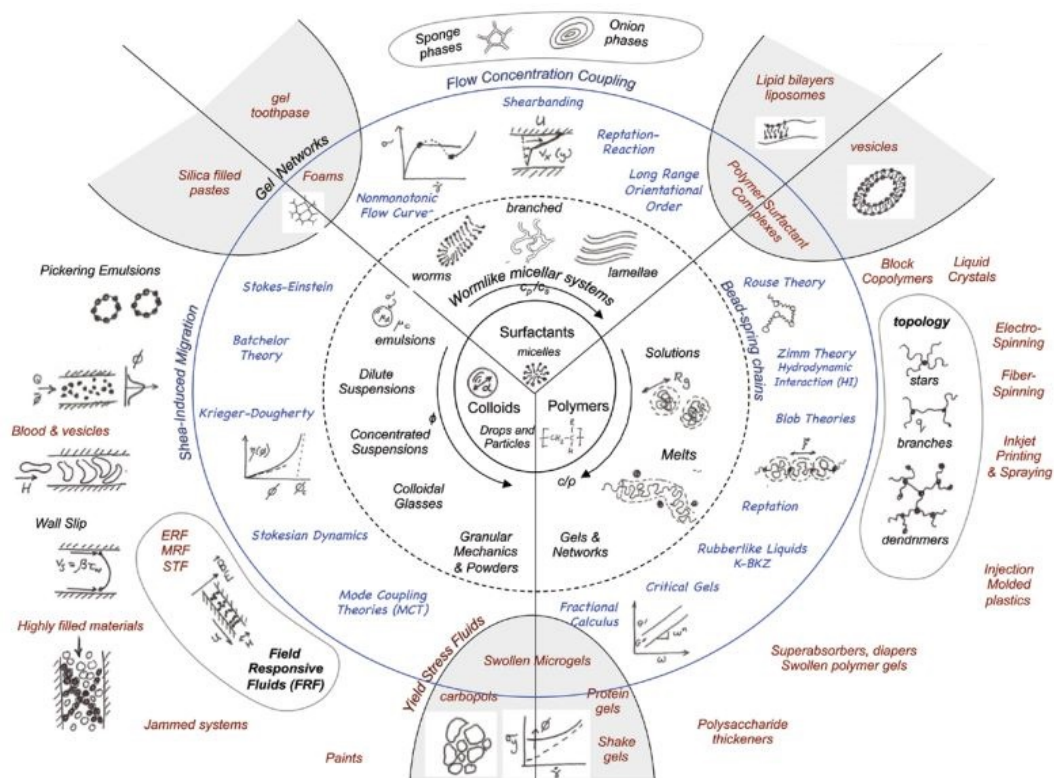


Figure 1.2: Schematic representation of various model porous systems used in the present study.

understanding of the complex flow behaviour of viscoelastic fluids in porous media.

However, it is readily acknowledged that an actual porous media consists of millions of interconnected pores of micron size through which the fluid flow happens. It is tremendously challenging to analyze the flow behaviour in such complicated flow paths of a porous media with the help of either state-of-the-art experiments or advanced numerical simulation techniques. Therefore, a model porous media is often used to understand the flow dynamics of complex fluids through a real porous system. A typical model porous system consists of a microchannel with many in-built micropillars, as presented in Fig. 1.2. This geometry is extensively used in the complex fluids research community to understand the flow behaviour of various complex fluids [10]. A simpler version of this model porous geometry is a straight microchannel with an obstacle or constriction present in it, as schematically shown in the same figure. All these model porous geometries are easy to fabricate experimentally or simulate numerically. Although these geometries are simple in structure, they can generate a highly inhomogeneous flow field inside the geometry, likewise in a real porous system, and facilitate a deeper understanding of the flow behaviour of complex viscoelastic fluids. Therefore, the fundamental understanding of the flow behaviour of viscoelastic fluids in these simple model porous geometries would provide better guidance on their handling and flow in a practical application.

Due to the presence of non-linear elastic stresses in a viscoelastic fluid, various complex flow behaviours are seen in this fluid. For instance, the rod climbing or extrude swell effect is a well-known example of this complex flow behaviour in a viscoelastic fluid [2]. Furthermore, these non-linear elastic stresses also generate instabilities in the viscoelastic fluid flow, even in the absence of inertial forces or at very low values of the Reynolds number (ratio of inertial to that of viscous forces) when the non-dimensional Deborah (De) or Weissenberg (Wi) number exceeds a critical value. Although a difference is present in their definitions; however, both these numbers signify a dimensional relaxation time compared to that of a characteristic time scale for the flow [11]. A viscoelastic fluid will become more elastic (or have more elastic stresses) as the value of either this Deborah or Weissenberg number increases. The time scale for flow in the case of the Deborah number is taken as the direct measurement of the time over which the flow happens, whereas it is the inverse of the imposed shear rate in the case of the Weissenberg number. These instabilities driven by purely elastic forces are known as viscoelastic flow or elastic

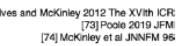
instabilities. These instabilities transit to a more chaotic and fluctuating flow state as this Deborah or Weissenberg number progressively increases, known as the elastic turbulence state. Although the topic of elastic turbulence has gained much more attention in the 21st century; however, the phenomenon and the term were known even in 1926 when Ostwald and Auerbach observed anomalously high-pressure drops during the pumping of some complex fluids through a tube at a flow condition where a laminar flow condition was expected to exist [12]. Almost 40 years later, Giesekus [13] extensively investigated this phenomenon in the flows of polyacrylamide solutions through converging nozzles and slits. Subsequently, many investigators found the existence of an unstable flow field due to these elastic instabilities and elastic turbulence in many polymer processing operations such as injection molding, and some excellent review articles are present on this [14, 15].

A more quantitative analysis of elastic instability was carried out by Muller, Larson, and Shaqfeh [16] in 1989. They conducted experiments and linear stability analyses on these viscoelastic flow instabilities in a Taylor-Couette flow geometry. They found a good qualitative agreement between the experiments and theory. In the subsequent years, many other studies for several canonical shearing flows were also carried out based on the linear stability theory, which Shaqfeh nicely documented in a review article in 1996 [17]. Later, McKinley and co-researchers suggested a scaling law to evaluate the critical conditions at which this elastic instability will emerge in a flow system [18]. They particularly devised a dimensionless Pakdel-McKinley parameter M , whose critical value M_{crit} signifies the onset of this pure elastic instability. It is defined as

$$\frac{\lambda \mathbf{U}}{\Re} \frac{N_1}{|\tau|} \geq M_{crit}^2 \quad (1.1)$$

where λ is the fluid relaxation time, \mathbf{U} is the characteristic streamwise fluid velocity, \Re is the characteristic streamline curvature, N_1 is the first normal stress difference in the fluid, and τ is the shear stress in the fluid. They demonstrated that elastic instability emerges in a flow field due to the interaction between streamline curvature in a flow field and normal elastic stresses along the streamlines. Poole [19] has presented a bucket of different small-scale geometries with curved streamlines where such a purely elastic flow instability was primarily observed experimentally. Figure 1.3 demonstrates the same as presented by Poole, which was then modified a bit by Datta et al. [20].

Experiments and simulations have also been conducted on more complex geome-



5

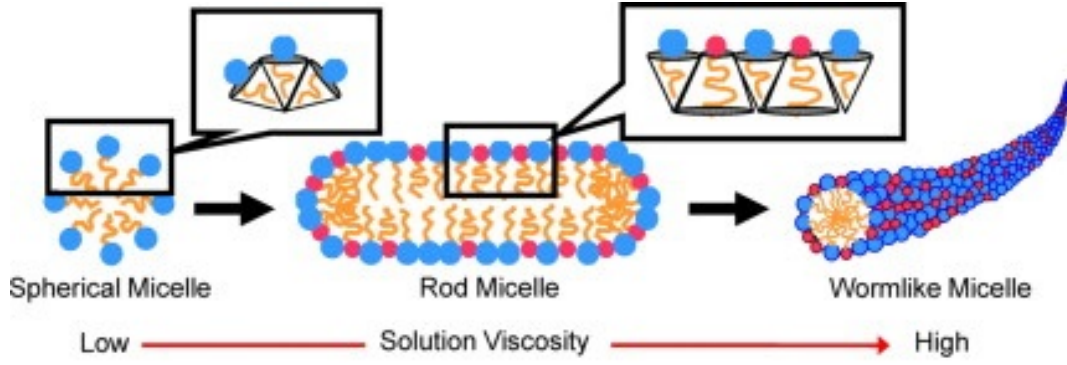


Figure 1.4: Schematic of the formation of different-shaped micelles in a solution.

tries to delineate this viscoelastic instability and its subsequent influence on the various complex flow phenomena. For instance, De and co-researchers found the presence of time-dependent preferential paths or lanes in the flows of viscoelastic fluids through a model porous geometry consisting of a microchannel with many micropillars placed in it [21, 22, 23]. Recently, Walkama et al. [24] experimentally demonstrated that the chaotic fluctuation arising from the elastic instability in this model porous geometry is suppressed as the geometric disorder increases. Subsequently, Haward et al. [25] proposed that the number of stagnation points near the micropillars controls the flow fluctuation in this model porous geometry. However, Chauhan et al. [26] very recently showed by numerical simulations that the chaotic fluctuation in this model porous system strongly depends on the rheological properties, such as shear-thinning and strain-hardening, of the viscoelastic fluid, which are a strong function of the polymer concentration and polymer size.

The present thesis further aims to demonstrate these elastic instabilities in various model porous geometries (as schematically shown in Fig. 1.2) when either a viscoelastic wormlike micellar or polymer solution flows through them. This thesis mainly focuses on the flow dynamics of the former solutions, which are formed when surfactant molecules are added to a solvent like water. These are also called "living polymers" because of the spontaneous breakage and reformation of the micelles under deformation. Due to this unique characteristic, wormlike micellar solutions are often preferred over polymer solutions in many applications, such as in enhanced oil recovery process [27]. In this particular application, polymer molecules may permanently degrade in a high-shearing zone of the porous oil reservoir, leading to a decrease in the overall volumetric sweeping

efficiency. This particular problem will be less for a micellar solution due to the micelles' spontaneous breakage and reformation dynamics. Figure 1.4 represents the mechanism behind the formation of wormlike micelles in a solution. Surfactant molecules are amphiphilic in nature, constituting both hydrophobic tail and hydrophilic head groups in their structure [28]. Adding surfactant into an aqueous solution at a concentration above their critical micellar concentration (CMC) leads to the self-assembly of the micellar structure [29]. The hydrophobic tail isolates itself from the water, while the hydrophilic head loves to be in contact with water, forming micelles in the solution. Conceptually, the shape of the micelles depends upon the critical packing parameter of the surfactant as $C_p = \frac{v}{a_0 l}$, where v is the volume and l is the length of the hydrophobic tail, and a_0 is the effective surface area of the surfactant head group [30]. When the critical packing parameter C_p is less than 0.33, the micelles are in a cone shape; however, at CMC, they are spontaneously assembled into a spherical shape. The micelles are supposed to form a cylindrical rod-like structure for $0.33 < C_p < 0.5$. When the values of the critical packing parameter are $0.5 < C_p < 1$ and $C_p = 1$, the vesicles and bilayers are expected to be present in the solution, respectively [31]. The critical packing parameter also depends on the surfactant concentration and the co-surfactant in the solution, resulting in the transformation of the structure of the micelles in the solution. In a dilute surfactant solution, the rod-like micelles have almost a cylindrical shape with two hemispherical end caps, and the curvature of the cylindrical body is smaller than the curvature of the end caps. However, further increasing the concentration of the surfactant in the solution results in a significant change in the shape of the micelles. The added surfactant relocates itself on the micelles' cylindrical body to reduce the solution's free energy, resulting in the uniaxial growth of micellar structures [32]. The change in the length of rod-like micelles leads to the formation of the long cylindrical structure known as the wormlike micelles.

In summary, the present thesis will aim to answer some unresolved questions in the field of flows of either micellar or polymer solutions through a model porous system; for instance, how will the breakage and reformation dynamics of micelles and the flow strength influence the elastic instability in flows through various model porous systems? Why do these complex fluids make preferential paths or lanes during their flows through porous systems? The present study employs both experiments and numerical simulations to answer these questions. The experiments include using the soft-lithography

technique to prepare the model microfluidic porous chips and the micro-particle image velocimetry technique (μ -PIV) to visualize the velocity fields. Numerical simulations involve computational rheology based on the computational fluid dynamics (CFD) technique. A detailed rheological study, in terms of both shear and extensional rheology, is also conducted in this study. This is because the rheological behavior of either micellar or polymer solutions is essential for understanding viscoelastic flow instabilities in flows through complex geometries. The rheological characteristics, such as shear-thinning and strain-hardening, can significantly control the onset and development of these viscoelastic flow instabilities. In particular, the present thesis focuses on the rheological study of a biosurfactant-derived micellar solution named rhamnolipid and shows a detailed comparison with a chemically-derived micellar solution. Furthermore, the present dissertation considers both pressure-driven and electrokinetically driven flows through these model porous geometries. Most of the studies conducted so far analyzed viscoelastic flow instabilities originating in pressure-driven flows. In contrast, few studies have analyzed elastic instabilities, particularly electro-elastic instabilities (EEI), developing in electrokinetically driven flows through these different model porous systems. Therefore, another major objective of the present thesis will be to fill this knowledge gap in the literature.

Literature survey

This chapter presents an extensive literature survey on the current status of the investigations that have been carried out so far on the rheological and physicochemical studies of micellar or polymer solutions and on the phenomenon of viscoelastic flow instabilities (both pressure and electrokinetically driven) that occur during their flows through various micro-scale model porous systems such as flow past confined microcylinders or flow through a channel with step expansion and contraction. This chapter also aims to find out the knowledge gap and set the present thesis's objectives.

2.1 Rheological and physicochemical studies of bio-surfactant and chemically derived micellar solutions

Surfactants are generally organic compounds containing both hydrophilic head and hydrophobic tail groups. In an aqueous solution, surfactants are generally self-assembled and form aggregates of various shapes, such as spherical, cylindrical, worm-like micelles, lipid bilayers, etc. This aggregation behaviour of surfactant molecules can be significantly affected by various external forces such as flow, temperature, pressure, etc. [33]. Most ionic and non-ionic surfactants are usually considered Newtonian fluids at low values of the deformation rate. However, as the deformation rate becomes significant, these surfactant solutions often exhibit complex rheological properties [34, 35]. For instance, surfactant solutions with worm-like micellar structures show a significant extent of viscoelastic behaviour [36, 37, 38]. It originates due to the formation of a transient network structure in the solution once the surfactant concentration exceeds a critical value, known as the critical micelle concentration (CMC) [39, 40, 41]. This network structure can undergo spontaneous scission and reformation mechanisms under an applied deformation field, which is why they are sometimes called living polymers [42, 43, 44].

Surfactants are classified into two categories based on their origin: chemically derived surfactant and biologically derived surfactant [45]. Chemically derived surfactants are

produced synthetically with the help of chemical reactions by combining a hydrophobic chain with a hydrophilic group. Some of the well-known synthetic surfactants are, for example, cetyltrimethylammonium bromide (CTAB), cetylpyridinium chloride (CPC), sodium dodecyl sulfate (SDS), etc. On the other hand, biosurfactants are a class of compounds with structurally different groups of surface-active bio-molecules produced by plants, animals, and microorganisms. Due to their unique structure and eco-friendly properties, biosurfactants are extensively used in many industrial applications like food, pharmaceuticals, cosmetics, agriculture, chemical and petrochemical industries, etc. [46]. Biosurfactants are less toxic and biodegradable compared to chemically derived surfactants. They also have good surface activity and perform excellently under harsh environmental conditions [47].

Among various biosurfactants, glycolipids are the most common and widely used biosurfactants. In this group of biosurfactants, rhamnolipid is a well-known bacterial biosurfactant produced by the *Pseudomonas aeruginosa* bacteria [48, 49, 50]. It consists of a glycosyl head group of rhamnose moiety and a tail group of 3-(hydroxyalkanoxyloxy) alcanoic acid (HAA) such as 3-hydroxydecanoic acid [49, 51]. Based on the attached number of rhamnose units, rhamnolipids are classified as mono and di-rhamnolipids. It has been found that mono-rhamnolipids have a higher capacity of micellar solubilization than di-rhamnolipids [52, 53]. Also, some studies show that rhamnolipids are weak acids due to the existence of a carboxylic group, which is supposed to undergo aggregation in the solution [54]. This biosurfactant is being widely used in the cosmetic industry as moisturizers and shampoo [55], in bioremediation of polluted sites and enhanced oil recovery [56], degradation of waste hydrocarbons [57], pharmaceuticals and therapeutics [58], in detergent and cleaner products industry [59], etc. Due to its widespread applications and excellent potential for further future applications, a voluminous number of studies are present on this [60, 61, 62, 63, 64]. Some of those studies are mentioned here for the sake of brevity. For instance, Mendes et al. [65] presented experimental results on the physicochemical properties of rhamnolipid biosurfactants and compared them with conventionally used synthetic surfactants. Their results showed that the rhamnolipid biosurfactant reduces the surface tension more than that of synthetic sodium dodecyl sulfate (SDS) surfactant. They found that rhamnolipid requires only 26 mg to reach the critical micellar concentration, whereas SDS requires 2.6 gm. Rhamnolipid also showed better

thermal resistance characteristics while heated from 4 to 80°C and then cooled back to 4°C. Ilori et al. [66] observed that after an exposure of 2 hours to heat (at 100°C), rhamnolipid biosurfactant had retained its original activity up to 77 %. Lovagilo et al. [67] used rhamnolipid as an emulsifier and evaluated the effect of pH on its stability. Due to the presence of the carboxylic group in the rhamnolipid molecular structure, both the stability and emulsifying activity increase with OH^- ion concentration. Therefore, rhamnolipid could be used in industrial processes that involve emulsifying activity at $\text{pH} \geq 5$. Camara et al. [68] investigated the ability of rhamnolipid biosurfactant in microbial-enhanced oil recovery. They found that rhamnolipid effectively reduces the surface tension from 72 to 35.26 mN/m at its CMC of 127 mg/L and increases the emulsification rate (E 24) by up to 69 % for crude oil. They also observed that rhamnolipid biosurfactant could recover the crude oil after two months of production. This shows the excellent biodegradability nature of rhamnolipid.

Although extensive investigations have been conducted on the physicochemical and thermophysical properties of rhamnolipid biosurfactants, almost no systematic study is available on the corresponding rheological properties of this biosurfactant. This characterization of surfactants is essential to investigate for their better and more efficient use in various applications, particularly in cosmetics and food [69, 70]. For synthetic surfactants, a considerable amount of corresponding studies on these rheological behaviours are available in the literature. For instance, Cappelaere et al. [71] studied the linear and non-linear rheological behaviour of CTAB solutions without salt. They found a very unusual power-law exponent of nearly 12 for the zero-shear rate viscosity and 62 for the terminal relaxation time. Kuperkar et al. [72] investigated the steady and dynamic rheological behaviour of CTAB in the presence of sodium nitrate salt using the small-angle neutron scattering (SANS) and cryogenic-transmission electron microscopy (Cryo-TEM). A maximum in the zero-shear viscosity of the surfactant solution was found as the concentration of NaNO_3 increased, and the addition of salt facilitated the formation of micelles, as confirmed by their SANS and Cryo-TEM experiments. In the presence of sodium tosylate salt, the rheological behaviour of CTAB surfactant solutions was studied by Hartmann and Cressely [73]. They found a shear-thickening behaviour at low salt concentrations, whereas a shear-thinning behaviour at high salt concentrations. Not only on steady and dynamic shear rheological measurements but also a significant number of studies on the

extensional rheological measurements were also performed for chemically synthetic surfactants. For instance, Yesilata et al. [74] reported the extensional flow dynamics of erucyl bis(2-hydroxyethyl) methyl ammonium chloride (EHAC) using the capillary breakup extensional rheometer (CaBER). They found a strong extensional thickening behaviour with the Trouton ratio increasing up to two orders of magnitude. Furthermore, they found that the extensional relaxation time was smaller than that obtained from the oscillatory experiments. Garcia and Saraji [75] investigated the extensional rheological behaviour of a surfactant solution composed of N-tetradecyl-N,N-dimethyl-3-ammonio-1-propanesulfonate (TDPS), sodium dodecyl sulfate (SDS), and sodium chloride (NaCl) using the hyperbolic microfluidic geometry. A viscoelastic transition from extensional-thickening to extensional-thinning was observed in their study. Rothstein [76] studied the extensional rheology of a synthetic surfactant of cetyltrimethylammonium bromide and sodium salicylate in de-ionized water using the filament stretching rheometer. They found the existence of a significant strain-hardening and a rupture of filament in their experiments. They proposed that this filament rupture is due to the breakage of long micelles. Recently, Narvaez et al. [77] examined the extensional rheological behaviour of a mixture of surfactant (sodium dodecyl sulfate (SDS)) and polymer (polyethylene oxide (PEO)) using the recently developed dripping-onto-substrate (DoS) technique. They revealed that adding a chemical surfactant to an uncharged polymer solution decreases the critical shear rate for the onset of shear-thinning but hardly influences the extensional relaxation time and viscosity.

Therefore, from the literature cited herein, it is clear that a considerable number of studies have been conducted to examine the shear and extensional rheological behaviours of various chemically synthetic surfactants. In contrast, despite its wide applications in various industrial settings, no corresponding study is available on biosurfactants, particularly rhamnolipid. The present thesis aims to fill this gap of knowledge in the literature. In particular, this thesis aims to present a detailed and systematic investigation of the steady and dynamic shear and extensional rheological behaviours of rhamnolipid biosurfactants at different concentrations. Our study also includes the results of a chemically synthetic surfactant (CTAB) to compare its rheological and physicochemical behaviours with rhamnolipid. We also present results on physicochemical properties such as surface tension, contact angle, particle size distribution, zeta potential, and thermal stability. It

will facilitate an overall comparison between the two surfactants. The primary motivation behind this is that it will help to decide whether the present biosurfactant can replace a chemically synthetic surfactant in any particular application.

2.2 Pressure driven flows of wormlike micellar solutions past a single microcylinder confined in a channel

A model porous system consisting of a microcylinder confined in a channel is often used as a benchmark problem both in experiments and numerical simulations to understand the complex flow dynamics of viscoelastic fluids [78, 79, 80, 81, 82, 83]. This simple geometry can create both shear (in the gap regions between the channel and cylinder walls) and extensional (downstream of the cylinder) flow dominated regions. It has stagnation zones on both the upstream and downstream sides of the cylinder and is free from any geometric singularity. Consequently, several experimental studies have investigated the flow phenomena of wormlike micellar solutions in this model porous system. For instance, Moss and Rothstein [84] employed two WLM solutions, namely, CTAB/NaSal (cetyltrimethyl ammonium bromide / Sodium salicylate) and CPyCl/NaSal (Cetylpyridinium chloride/Sodium salicylate) and for two blockage ratios (ratio of cylinder diameter to that of channel height), namely, 0.2 and 0.1. They found that the normalized pressure drop initially decreased with the Weissenberg number, reaching a plateau at high values. This is due to the dominance of the shear-thinning and extensional properties of the fluid at low and high Weissenberg numbers, respectively. Furthermore, an elastic instability was observed in their CTAB/NaSal solution beyond a critical value of the Weissenberg number. In contrast, it was not seen in the CPyCl/NaSal solution over the range of conditions encompassed in their study. The blockage ratio did not affect the onset of this elastic instability. Subsequently, Moss and Rothstein [85] conducted a similar study for a periodic array of cylinders.

On the other hand, Zhao et al. [86] used CTAB/SHNC (3-hydroxy naphthalene-2-carboxylate) WLM solution in this benchmark flow system over a large range of the Weissenberg number ($O(1)$ to $O(10^5)$) than those encompassed by Moss and Roth-

stein [84]. Over such a wide range of the Weissenberg number, they observed five distinct flow regimes: Newtonian-like flow, bending streamlines, vortex growth upstream, unsteady flow downstream, and finally, three-dimensional and time-dependent flow. Furthermore, their study revealed that all these flow patterns and the onset of the elastic instability strongly depended on the channel blockage ratio. This is in stark contrast to the observation of Moss and Rothstein [84]. Recently, Haward et al. [87] also performed a similar study using CPyCl/NaSal micellar solution with the Weissenberg number up to 3750. They observed a flow transition from a steady and symmetric to a steady and asymmetric one at around the first critical Weissenberg number of 60, characterized as a supercritical pitchfork bifurcation. With a further increase in the value of the Weissenberg number, the flow became time-dependent and exhibited a subcritical Hopf bifurcation at the second critical Weissenberg number of around 130.

Therefore, a reasonable body of experimental information is available on this model porous flow configuration for various wormlike micellar solutions. In contrast, to our knowledge, no corresponding numerical investigation has been reported to date. One of the reasons for this deficiency in numerical studies is that there was no suitable constitutive relation available in the literature for such wormlike micellar solutions until the VCM (Vasquez-Cook-McKinley) model [88] was proposed. This model efficiently captures all the typical rheological characteristics of a WLM solution like the shear-thinning, extensional hardening and subsequent thinning, shear-banding, etc. It models the wormlike micelles as elastic networks composed of Hookean springs, which can continuously break and reform in a flow field. The breakage and reformation dynamics are incorporated based on the discrete and simplified version of Cates’s original reversible breaking theory for wormlike micelles [89]. According to the VCM model, a long wormlike micelle of length L can be broken exactly in the middle to provide two short micelles of length $L/2$ or vice-versa. This is opposed to the Cates theory [89] in which micelles can break into short micelles with equal probability at any point along their length. Also, micelles of any length can join together to form long micelles. However, this simplification allows the VCM model to easily capture the temporal and spatial variations in the number density of the chain species. It should be mentioned here that two types of scission mechanisms are available in the case of a micellar solution: equilibrium reversible and flow-induced scissions. The equilibrium reversible scission transpires when the rates of

micelle formation and dissociation reach a state of equilibrium. Despite continuous scission and recombination, the average micelle length and size remain constant in this type of scission. Comprehending this equilibrium scission phenomenon bears significance, as it enables the fine-tuning of the rheological characteristics of micellar solutions to align with specific applications. On the other hand, in the presence of flow, the breakage of these wormlike micelles is termed as flow-induced scission. Within a flow field, micelles are subjected to both shear and extensional forces, prompting their elongation or stretching. When this elongation surpasses a critical threshold, micelles can experience scission, forming smaller micelles—a phenomenon known as flow-induced scission. The VCM model mainly deals with this flow-induced scission mechanism experienced by micelles. The breakage and reformation dynamics, as well as the variation in the number density of chain species, are not accounted for in the earlier single species bead-spring models for wormlike micelles, for instance, Johnson-Segalman (JS) model [90, 91] or Bautista-Manero-Puig (BMP) model [92]. Therefore, these models do not allow us to relate the stress directly to the micro-structural dynamics of the micelles, as does the VCM model.

For different viscometric flows, a very good agreement has been found between the predictions of the VCM model and the corresponding experimental results [93, 94]. For non-viscometric flows, a good qualitative match has been seen in a recent study [95]. Furthermore, some recent numerical studies showed how the breakage dynamics of the micelles in the VCM model are important to compare with the corresponding experimental observations. For instance, Kalb et al. [96, 97] showed how the chain scission mechanism of the VCM model helps in understanding the formation of lip vortices and the generation of elastic instability in a cross-slot device as seen in the corresponding experiments [98, 99]. Furthermore, a recent study by Sasmal [100] also showed how the breakage dynamics is important to understand the flow characteristics of wormlike micellar solutions through a long micropore with step expansion and contraction as seen in the corresponding experiments [101].

It is thus clear from the aforementioned literature that the breakage and reformation mechanisms are extremely vital to perform an either theoretical or numerical investigation on the flow dynamics of wormlike micellar solutions. Therefore, the aim of this thesis is as follows: we first present a discussion on the flow characteristics of the VCM model in the absence of breakage and reformation dynamics. This limiting case corresponds to

two uncoupled upper convected Maxwell (UCM) models. We then discuss how the flow characteristics, particularly the elastic instability, in a wormlike micellar solution can be influenced in this model system once the breakage and reformation of the micelles become important. In addition, we compare, at least qualitatively, our numerical predictions with some of the available experimental observations [84, 86, 87].

2.3 Pressure driven flows of wormlike micellar solutions past two vertically aligned microcylinders confined in a channel

The flow of micellar solutions through a porous media can exhibit many complex flow behaviours. For instance, in many experiments, it has been found that the micellar solution selects a preferential path or lane during the flow through a porous media. De et al. [22] observed the formation of lanes when a micellar solution comprising of cetyl tri-methyl ammonium bromide (CTAB) and sodium salicylate (NaSal) flows through a model porous media consisting of a microchannel with cylindrical pillars placed in it. Another study [21] of the same authors found a similar formation of lanes and their path-switching phenomena when dealing with a hydrolyzed polyacrylamide (HPAM) polymer solution. Muller et al. [102] also noticed the same phenomena in polyalphaolefine polymer solution flowing in a model porous medium consisting of a glass pipe filled with Duran glass spheres. They further noted spatial and temporal variations of these preferential paths in the porous media. Recently, both Walkama et al. [24], and Eberhard et al. [103] also showed the formation of these lanes in both ordered and disordered model porous structures during the flow of a high molecular weight polyacrylamide (PAA) and xanthan gum polymer solutions, respectively.

To understand such complex flow behaviour of either micellar or polymer solutions in an actual porous media, it is always better to start with a simple system consisting of a single microcylinder placed in a microchannel. As mentioned earlier, this simple benchmark system creates a non-homogeneous flow field in the system, which in turn, facilitates the understanding of the flow behaviour of various complex fluids. This ultimately leads to a better understanding of the flow behaviour in a more complex system. For this reason, a significant amount of studies, comprising of both experiments and numerical simulations, have been carried out on this benchmark system for polymer [81, 80, 104, 105, 106] as well as micellar [84, 86, 87, 107] solutions. Some interesting flow physics have been found from these studies, which were not seen in simple Newtonian fluids under otherwise identical conditions. For instance, the emergence of an elastic instability [106] and flow bifurcation [87] have been found in this model geometry.

Although the geometrical configuration of this model system is simple, the flow dynamics within it can be significantly altered either by changing the blockage ratio (ratio of the cylinder diameter to the channel height) or by placing another microcylinder next or above or bottom to the existing cylinder with various intercylinder spacings. For instance, both Moss and Rothstein [84] and Zhao et al. [86] found that the onset of the elastic instability in CPyCl (cetylpyridinium chloride)/NaSal and CTAB/SHNC (3-hydroxy naphthalene-2-carboxylate) micellar solutions were delayed as the blockage ratio was decreased. Furthermore, Zhao et al. [86] observed a broad spectrum of flow states in this model geometry as the blockage ratio and Weissenberg number were varied, for instance, Newtonian-like, bending streamlines, vortex growth upstream, unsteady downstream, chaotic upstream and three-dimensional time dependent. Recently, Varchanis et al. [108] conducted both experiments using polyethylene oxide (PEO) polymer solution and numerical simulations using the linear Phan-Thien-Tanner (I-PTT) constitutive model over a wide range of the blockage ratio. They found the existence of supercritical and subcritical pitchfork bifurcations in the flow field as the blockage ratio was varied and also observed no bifurcation in the flow for certain ranges of the blockage ratio.

Apart from the influence of the blockage ratio, placing another microcylinder in the channel can also greatly modify the flow field in this model geometry. For example, Haward et al. [109] experimentally found a significant modification in the flow field between the two microcylinders than that seen for the single microcylinder case, particularly at high Weissenberg numbers. Varshney and Steinberg [110] found an increase in the vortex growth between the two microcylinders. This starkly contrasts the findings of suppressing a vortex by the polymer additives into a Newtonian solvent [111, 112]. Both these studies used a polymer solution in their experiments wherein two microcylinders were placed horizontally side-by-side. Recently, Hopkins et al. [113] performed experiments using CPyCl/NaSal micellar solution for the flow past two microcylinders placed vertically side-by-side over a broad range of the intercylinder gaps and Weissenberg numbers. This experimental study, performed for the first time for this geometry, found the existence of three stable flow states in the system depending upon the values of the intercylinder gap and Weissenberg number, namely, diverging (D) state in which all of the fluid preferably passes through the gaps in between the channel walls and cylinder surface, asymmetric-diverging (AD) state in which the fluid prefers to pass through ei-

ther the gap in between the upper channel wall and top cylinder surface or the lower channel wall and bottom cylinder surface, and converging (C) state in which most of the fluid passes through the gap in between the two cylinders. They presented a phase diagram on the existence of all these flow states as a function of the intercylinder gap and Weissenberg number. Also, they found a critical value of the intercylinder gap at which all these three states, namely, D, AD, and C, co-exist together, thereby showing the existence of a tristable state in viscoelastic fluids for the first time.

These studies demonstrate that the flow physics past a microcylinder confined in a channel can become increasingly complex if one changes the blockage ratio or places an additional microcylinder in it. This is primarily due to the variation in the extent of shear and extensional flow fields in the domain and due to the interaction of the elastic stresses generated around the microcylinders. However, it can be seen that most of these investigations are experimental, and compared to this, very few numerical studies have been carried out [108]. Furthermore, these numerical simulations are based on the single-species viscoelastic constitutive equations, thus restricting their applicability to only polymer solutions where breakage and reformation dynamics are absent, unlike wormlike micellar solutions. Therefore, these widely used single-species viscoelastic constitutive equations sometimes cannot predict some typical flow physics happening in wormlike micellar solutions. For instance, many experimental studies have found an existence of unsteady motion of a sphere falling freely in wormlike micellar solutions in the creeping flow regime once the Weissenberg exceeds a critical value [114, 115]. Experimentally, this motion was predicted to be due to the breakage of long and stretched micelles downstream of the sphere, resulting from increased extensional flow strength. Only recently [116], it has been proven that this motion is, indeed, due to the breakage of micelles downstream of the sphere using the two-species Vasquez-Cook-McKinley (VCM) model [88]. Therefore, there is a gap of knowledge present in the literature, particularly for the flow past two vertically aligned microcylinders, which may facilitate the understanding of the formation of preferential paths or lanes during the flow of viscoelastic fluids like micellar solutions in a porous media. Therefore, this thesis aims to numerically investigate how the blockage ratio would tend to influence the flow dynamics of a micellar solution past a single microcylinder placed in a channel using the two-species VCM constitutive model. Secondly, it plans to extend the investigation for two verti-

cally aligned microcylinders placed in a channel for different intercylinder gap ratios and try reproducing some of the flow behaviors observed in recent experiments with WLM solutions [113]. Finally, the present investigation can also facilitate understanding the formation of preferential paths or lanes during the flow of viscoelastic fluids through a porous media based on the analysis of our single and double microcylinder results.

2.4 Electrokinetically driven flows of viscoelastic fluids through a microchannel with step expansion and contraction

Various complex fluids are often transported in many micro and nanofluidic systems with the help of the electrohydrodynamics phenomenon. In this process, fluid flow happens due to the formation and movement of an electrical double layer (EDL) formed along the charged surface of a system under the application of an external electric field [117]. This mode of fluid transport is often preferred over the traditional pressure-driven flows in microfluidic systems. This is because it offers less resistance during the flow because of the formation of a plug-like velocity profile in contrast to a parabolic one in pressure-driven flows. Therefore, over the years, extensive research efforts have been devoted to understanding the electrokinetic transport phenomena of various Newtonian and complex non-Newtonian fluids in many micro-scale systems [118, 119].

In many earlier investigations, however, it has been observed that the electrokinetic transport phenomena in complex non-Newtonian fluids, particularly in viscoelastic fluids, are much more complicated than that seen in simple Newtonian fluids under otherwise identical conditions. For instance, Afonso et al. [120] found the existence of an electro-elastic instability (EEI) in flows through a microfluidic cross-slot geometry once the Weissenberg number (ratio of the viscous to that of the elastic forces) exceeds a critical value. These instabilities in viscoelastic fluids are associated with an unsteady and asymmetric flow field as opposed to that of a steady and symmetric flow field in Newtonian fluids. The presence of such elastic instabilities was also seen in many earlier investigations dealing with pressure-driven viscoelastic flows, and extensive literature is also present on this [20]. In comparison, very few studies are present on the corresponding

electrokinetically driven flows. An interaction between the elastic stresses (originated due to the stretching of viscoelastic microstructure) and the streamline curvature present in a system causes these instabilities. These purely electro-elastic instabilities in a microfluidic cross-slot geometry were later verified experimentally by Pimenta and Alves [121]. They experimented with dilute and semi-dilute polyacrylamide (PAA) polymer solutions. They found a fluctuating flow field with a broad range of excitation frequencies with a power-law decay at large frequencies. The corresponding experiments in a contraction and expansion geometry were performed by Sadek et al. [122]. They also observed the existence of these purely electro-elastic instabilities once the voltage difference between the inlet and outlet of the microchannel exceeded a critical value as seen in the studies of Afonso et al. [120] and Pimenta and Alves [121]. They particularly found two flow regimes as the voltage difference gradually incremented, namely, unsteady symmetric and irregular flows. Similar electro-elastic instabilities were also seen in a more recent numerical study by Ji et al. [123] for a contraction and expansion geometry. Song et al. [124] conducted an experimental study on the electro-elastic instability in flows of viscoelastic fluids through a T-shaped microchannel. It should be mentioned here that these electro-elastic instabilities seen in viscoelastic fluids are not the same as that of electrokinetic instability (EKI) seen in flows of Newtonian fluids. The former instability originated due to the presence of elastic stresses and streamline curvature. In contrast, the latter is caused due to the presence of an electrical conductivity gradient in a system.

Apart from studies on cross-slot and hyperbolic expansion and contraction microgeometries, a reasonable amount of studies are also present on the electrokinetic flows of viscoelastic fluids in a long straight microchannel by considering either the fractional Oldroyd-B or Maxwell viscoelastic fluid model, for instance, see the refs. [125, 126, 127, 126, 128, 129, 130]. Further studies with other more complex viscoelastic constitutive equations, for instance, the Phan-Thien-Tanner (PTT) or FENE-P (finitely extensible non-linear elastic spring with the Peterlin approximation) equations, are also available in the literature. Sarma et al. [131] performed an analytical study using the simplified PTT viscoelastic model and found an enhancement in the volumetric flow rate in a parallel-plate microchannel as the fluid viscoelasticity increases. The electrokinetic flow in a wavy microchannel using the PTT viscoelastic fluid model was studied by Martinez et al. [132], and they also found an increase in the volumetric flow rate compared to that seen

for a Newtonian fluid under the same conditions. Dhinakaran et al. [133] performed an analytical study based on the PTT model and observed a constitutive flow instability once the shear rate and Deborah number exceeded some critical values. Bautista et al. [134] carried out both numerical simulations and asymptotic analysis using the lubrication approximation and found a substantial modification in the velocity and pressure profiles in a slit microchannel due to the presence of fluid viscoelasticity. Ferras et al. [135] studied the effect of solvent viscosity and fluid viscoelasticity. Song et al. [136] performed an experimental study on the electrokinetic instability phenomena in a T microfluidic junction filled with viscoelastic fluids.

Therefore, it can be seen that a sufficient amount of studies on the electroosmotic flows of viscoelastic fluids are present in the literature, and some excellent reviews on the same are also present [137]. However, these studies are restricted to simple geometries like straight microchannel or cross-slot geometry. Compared to this, very few studies are available on more complex geometries like in porous media, and those studies are again constrained to simple Newtonian fluids [138]. In particular, the problem of electrokinetic flow in a porous media has many practical applications, which often deal with various non-Newtonian viscoelastic fluids, such as in electro-chromatography [139, 140], micro-pumping [141, 142, 143], chemical remediation of contaminated soil [144, 145], etc. Therefore, it is imperative to investigate this problem for better equipment design and process operation dealing with various complex fluids.

The flow dynamics of viscoelastic fluids in porous media are much more complex and rich in physics than that seen in simple Newtonian fluids [146]. Many exciting and complicated flow physics have already been observed in viscoelastic fluid's pressure-driven porous media flows. For instance, in many earlier studies, it has been observed that the flow of a viscoelastic fluid inside a porous media becomes chaotic and fluctuating turbulent-like (known as the elastic turbulence [147, 20, 148]) in nature once the flow rate exceeds a critical value [149, 150, 151, 24, 25, 152]. To understand the origin of this complex flow dynamics of viscoelastic fluids in a porous media, one needs to investigate the fluid flow phenomena that are happening at the pore scale. An actual porous media consists of millions of micro-pores interconnected with each other. However, a relatively simple system consisting of a long micropore with step expansion and contraction is also often used as a model porous media to understand the macroscopic flow phenomena seen

in an actual porous media [153]. For the pressure-driven flows, this model porous media is proven to be successful in capturing the flow physics occurring in an actual porous media [154, 155, 156]. For the electrokinetically-driven flows, no corresponding study, either experimental or numerical, is available for such a model porous system filled with viscoelastic fluids. Therefore, this thesis aims to investigate the same in detail. Although the present thesis considers a simple model porous media; however, it will facilitate a better understanding of the complex flow dynamics that can happen in actual porous media. Furthermore, this thesis shows how this model geometry can be used in other practical applications, such as mixing fluids. Due to the laminar flow condition, it is often challenging in micro-scale systems regardless of the external driving agency (pressure or electric field). Therefore, over the years, many designs and techniques based on passive and active modes have been developed to enhance the mixing efficiency in various micro-scale systems; for instance, see some excellent review articles in the literature [157, 158]. This dissertation further aims to show how the mixing process of these complex viscoelastic fluids could be achieved in this model porous system using the phenomenon of electro-elastic instability.

2.5 Electrokinetically driven flows of viscoelastic fluids past a microcylinder confined in a channel

The study of electroosmotic flow in non-Newtonian fluids deserves special attention. This is not only due to their frequent appearance in various practical applications but also to the unusual flow behaviours in these fluids, which are not seen in simple Newtonian fluids under the same conditions. One such flow behaviour often seen during the flow of non-Newtonian viscoelastic fluids is electro-elastic instability (EEI) [120, 122]. This EEI phenomenon in an electroosmotic flow was probably first observed by Bryce and Freeman [159] in their experiments in a long microchannel with many step expansions and contractions present in it. Although they found an unsteady and chaotic flow field inside this flow system because of these instabilities; however, they did not observe any improvement in the mixing process of the two fluids. In contrast, they observed a reduction in the mixing process for viscoelastic fluids than for Newtonian fluids. Some other studies were also performed for this kind of contraction and expansion geometry and found

the existence of this EEI phenomenon once either the applied electric field strength or the Weissenberg number (quantifies the extent of fluid viscoelasticity) exceeded a critical value [122, 123]. Afonso et al. [120] observed this electro-elastic instability in their numerical simulations for a cross-shaped microchannel, which was later verified in an experimental study conducted by the same research group [121]. Song et al. [124] performed the corresponding analysis for a T-shaped microchannel. The EEI phenomenon was even observed in a straight microchannel with non-uniform zeta potentials present on its wall [160]. Park and Lee [161] found that the volumetric flow rates of a viscoelastic fluid were significantly different from that of a Newtonian fluid under the same external electric field during the electroosmotic flow through a rectangular microchannel. Lu et al. [162] experimentally studied the electrophoresis phenomenon in viscoelastic polyethylene oxide (PEO) polymer solutions through a constricted microchannel. They observed unexpected particle oscillating phenomena in the constricted region of the microchannel. Another study [163] found particle aggregates formed in the constricted microchannel region. They proposed that both these phenomena originated due to the non-linear interaction between electrokinetic and viscoelastic forces. Bentor et al. [164] studied the insulator-based dielectrophoretic (iDEP) phenomenon in three non-Newtonian fluids with distinct rheological properties through a constricted microchannel. They reported that the focusing and trapping of particles using the iDEP phenomenon was weakly affected by the moderate fluid viscoelasticity but strongly affected by the highly viscoelastic and shear-thinning properties of polyacrylamide solutions. Recently, they extended this work to an array of microcylinders placed in a microchannel [165] and found relatively weaker iDEP effects in this geometry than seen for a constricted microchannel.

The present thesis focuses on the electroosmotic flows through a microfluidic setup consisting of a straight microchannel with an in-built cylindrical obstacle. This particular geometry is a benchmark setup extensively used to study how a complex fluid would behave in an inhomogeneous pressure-driven flow field [166, 167, 86, 107]. Furthermore, this particular geometry can also serve as a model system to study the flow dynamics in a porous media. In particular, the electroosmotic flow in a porous media has many practical applications, such as electro-chromatography [139], micro-pumping [142, 141], chemical remediation of contaminated soil [144, 145], etc., which often deal with such non-Newtonian viscoelastic fluids. Therefore, it is imperative to study this flow system

to understand and design these processes in a better way. The presence of complex flow phenomena in viscoelastic fluids, such as the EEI phenomenon, provides further motivation to study this particular micro-scale flow geometry. This study particularly plans to investigate how this electro-elastic instability in electroosmotic flows of viscoelastic fluids could generate a flow-switching phenomenon in this geometry, which is absent in simple Newtonian fluids under the same conditions. Therefore, it will show how the electroosmotic flows of viscoelastic fluids in a porous media can become more complex and rich in physics than a simple Newtonian fluid. We also aim to demonstrate how this flow-switching phenomenon could efficiently mix viscoelastic fluids in this simple microfluidic setup. This is particularly important from an application point of view, as mixing fluids in a lab-on-a-chip (LOC) device is still challenging due to the domination of molecular diffusion, demanding a much longer time for the process than that seen in convective mixing. Many passive and active methods have been proposed in the literature to enhance this mixing process in a micro-scale geometry [168, 169, 170, 171], and is still an active area of research in the domain of micro and nanofluidics. Our proposed idea in this study is simple yet efficient for mixing viscoelastic fluids in an easy-to-fabricate microfluidic device consisting of a straight microchannel with a cylindrical obstacle.

Furthermore, this dissertation plans to use the data-driven dynamic mode decomposition (DMD) technique to understand and analyze the coherent flow structures arising from this EEI phenomenon. This technique is one of the reduced order modeling (ROM) techniques widely used in distilling the important spatial features of a flow field in terms of the so-called ‘modes’ [172]. The spatial structures of these modes and their frequency are significant to investigate for a better understanding of various transport phenomena, such as mixing in the present study [173]. To fulfill the present investigation’s objectives, we employ continuum-scale numerical simulations and microfluidic experimental techniques. The numerical simulations involve the solution of mass, momentum, and viscoelastic constitutive equations using an open-source computational fluid dynamics (CFD) code, OpenFOAM [174]. Although full-scale three-dimensional numerical simulations can provide better insights into the present flow phenomena; however, the present study considers two-dimensional numerical simulations, which also offer sufficient information for flow physics with relatively less computational cost. On the other hand, the experimental techniques comprise soft-lithography and fluorescent microscopy for fabri-

cating microfluidic geometry and flow visualization, respectively.

2.5.1 Major objectives of the present thesis

The broad objective of the present thesis is to explore the flow dynamics of complex fluids such as micellar or polymer solutions through a model porous system such as flow past a cylinder confined in a microchannel or flow through a microchannel with step expansion and contraction under both pressure and electrokinetically driven flows. In this regard, the above comprehensive literature survey shows the gap in the current knowledge. The aim of the present thesis to fill this gap of knowledge in the literature is also mentioned at the end of each topic. In particular, the objectives of the present dissertation are as follows:

1. A detailed and systematic study on rheological and physicochemical properties of rhamnolipid biosurfactant solutions and presents a qualitative comparison with chemical surfactant solutions, chapter 4.
2. A comprehensive study on how micelles' chain scission and reformation mechanisms would influence the flow characteristics such as viscoelastic flow instability past a microcylinder confined in a microchannel, chapter 5.
3. An investigation of the effect of the blockage and gap ratios on the flow dynamics of wormlike micellar solutions past single and two vertically aligned microcylinders confined in a microchannel, chapter 6.
4. A detailed study of the electro-elastic instability phenomenon in viscoelastic fluid flows through a microchannel with step expansion and contraction, chapter 7.
5. A thorough study of the flow-switching and mixing phenomena in electroosmotic flows of viscoelastic fluids past a single microcylinder confined in a channel, chapter 8.

Methodology

The present dissertation involves both numerical and experimental methodologies to study the flow dynamics of viscoelastic fluids through a model porous system. The numerical methodology is first presented and discussed here.

3.1 Numerical Methodology

To describe the numerical methodology adopted in the present thesis, the problems that have been solved are broadly divided into two categories, namely, pressure driven flows of viscoelastic wormlike micellar solutions and electrokinetically driven flows of viscoelastic polymer solutions through various model porous geometries.

3.1.1 Governing equations for pressure driven creeping flows of viscoelastic wormlike micellar solutions

The flow field will be governed by the following equations, written in their dimensionless forms

Equation of continuity

$$\nabla \cdot U = 0 \quad (3.1)$$

Cauchy momentum equation

$$-\nabla P + \nabla \cdot \tau = 0 \quad (3.2)$$

In the above equations, U , t , and τ are the velocity vector, time, and total extra stress tensor, respectively. All the spatial dimensions were scaled by a characteristic length L (which was varied depending upon the problem to be solved. For instance, in the case of flow past a microcylinder, the microcylinder radius R was taken as the characteristic length L), velocity was scaled by L/λ_{eff} , stress and pressure were scaled by $\eta_0 U_{in}/L$ and time was scaled by λ_{eff} . Here $\lambda_{eff} = \frac{\lambda_A}{1+c'_{Aeq}\lambda_A}$ is the effective relaxation time for the two-species Vasquez-Cook-McKinley model for micelles in which λ_A and c'_{Aeq} are the dimensional relaxation time and equilibrium breakage rate of the long worm A, respec-

tively, as written in detail below. In the present study, the Weissenberg and Reynolds numbers were defined as $Wi = \frac{\lambda_{eff} U_{in}}{L}$ and $Re = \frac{L U_{in} \rho}{\eta_0}$, respectively. A perfect inertialess (i.e., $Re = 0$) flow condition was simulated for all problems in this thesis by neglecting the convective terms of Cauchy's momentum equation. Here ρ and η_0 are the solution density and zero-shear rate viscosity, respectively. The total extra stress tensor, τ , for a wormlike micellar solution is given as:

$$\tau = \tau_w + \tau_s \quad (3.3)$$

where τ_w is the non-Newtonian contribution from the wormlike micelles, whereas τ_s is the contribution from that of the Newtonian solvent, which is equal to $\beta \dot{\gamma}$. Here the parameter β is the ratio of the solvent viscosity to that of the zero-shear rate viscosity of the wormlike micellar solution and $\dot{\gamma} = \nabla U + \nabla U^T$ is the strain-rate tensor. For the two-species VCM model [88], the total extra stress tensor is given by

$$\tau = \tau_w + \tau_s = (A + 2B) - (n_A + n_B)I + \beta \dot{\gamma} \quad (3.4)$$

Here n_A and A are the number density and conformation tensor of the long worm A, respectively, whereas n_B and B are to that of the short worm B. The temporal and spatial evaluation of the number density and conformation tensor for the short and long worms are written as follows. The VCM constitutive equations provide the species conservation equations for the long (n_A) and short worms (n_B) along with the equations for the evolution of their conformation tensors A and B , respectively. According to this model, the equations for the variations of n_A , n_B , A , and B are given in their non-dimensional forms as follows [88]:

$$\mu \frac{Dn_A}{Dt} - 2\delta_A \nabla^2 n_A = \frac{1}{2} c_B n_B^2 - c_A n_A \quad (3.5)$$

$$\mu \frac{Dn_B}{Dt} - 2\delta_B \nabla^2 n_B = -c_B n_B^2 + 2c_A n_A \quad (3.6)$$

$$\mu A_{(1)} + A - n_A I - \delta_A \nabla^2 A = c_B n_B B - c_A A \quad (3.7)$$

$$\epsilon \mu B_{(1)} + B - \frac{n_B}{2} I - \epsilon \delta_B \nabla^2 B = -2\epsilon c_B n_B B + 2\epsilon c_A A \quad (3.8)$$

Here the subscript $(\cdot)_{(1)}$ denotes the upper-convected derivative defined as $\frac{\partial(\cdot)}{\partial t} + U \cdot \nabla(\cdot) - ((\nabla U)^T \cdot (\cdot) + (\cdot) \cdot \nabla U)$. The non-dimensional parameters μ , ϵ and $\delta_{A,B}$ are defined as

$\frac{\lambda_A}{\lambda_{eff}}$, $\frac{\lambda_B}{\lambda_A}$ and $\frac{\lambda_A D_{A,B}}{R^2}$, respectively, where λ_B is the relaxation time of the short worm B and $D_{A,B}$ are the dimensional diffusivities of the long and short worms. Furthermore, according to the VCM model, the non-dimensional breakage rate (c_A) of the long worm A into two equally sized small worms B depends on the local state of the stress field, given by the expression $c_A = c_{Aeq} + \mu_3^\xi \left(\dot{\gamma} : \frac{\mathbf{A}}{n_A} \right)$. On the other hand, the reforming rate of the long worm A from the two short worms B is assumed to be constant, given by the equilibrium reforming rate, i.e., $c_B = c_{Beq}$. Here the non-linear parameter ξ is the scission energy required to break a long worm into two equal-sized short worms. The significance of this parameter is that as its value decreases, the amount of stress needed to break a micelle increases.

3.1.2 Governing equations for electrokinetically driven creeping flows of viscoelastic polymer solutions

The flow field induced by an electric field will be governed by the following equations written in their dimensional forms, namely,

Continuity equation:

$$\nabla \cdot \mathbf{u} = 0 \quad (3.9)$$

Cauchy momentum equation:

$$0 = -\nabla p + \eta_s \nabla^2 \mathbf{u} + \nabla \cdot \tau_p - \rho_e \mathbf{E} \quad (3.10)$$

In these above equations, t is the time, u is the velocity vector, p is the pressure, η_s is the solvent viscosity, ρ_e is the charge density, \mathbf{E} is the external electric field strength and τ_p is the extra stress due to the presence of viscoelastic microstructure like polymer molecules. Depending upon the rheological responses of a viscoelastic fluid in standard homogeneous flows like simple shear or uniaxial extensional flows, one can select a suitable viscoelastic constitutive relation to evaluate τ_p . In the present study, we have used the Oldroyd-B viscoelastic constitutive equation to evaluate τ_p . This is because of the facts [175] that i) it is a relatively simple viscoelastic model which depends on a single conformation tensor for predicting the state of stress in a liquid and is associated with only two parameters, namely, polymer concentration and polymer relaxation time ii) it has been derived based

on the simplest kinetic theory of polymers in which a polymer molecule is assumed to be a dumbbell with two beads connected by an infinitely stretchable elastic spring iii) it can successfully mimic the rheological behaviour of a constant shear viscosity viscoelastic fluid or the so-called Boger fluid [176]. According to this model, the polymeric stress components are evaluated as follows [2, 175]

$$\tau_p = \frac{\eta_p}{\lambda} (A - I) \quad (3.11)$$

where η_p is the polymer viscosity, λ is the polymer relaxation time, A is the polymeric conformation tensor and I is the identity tensor. The conformation tensor of an Oldroyd-B fluid is evaluated as per the following equation

$$\frac{\partial A}{\partial t} + u \cdot \nabla A = A \cdot \nabla u + (\nabla u)^T \cdot A - \frac{1}{\lambda} (A - I) \quad (3.12)$$

The electric potential (ψ) in the system is computed by solving Gauss's law as follows

$$\nabla \cdot (\epsilon \nabla \psi) = \rho_e \quad (3.13)$$

The charge density is calculated as $\rho_e = F \sum_{i=1}^N z_i c_i$ where F is the Faraday's constant ($96485.33289 \text{ C} \cdot \text{mol}^{-1}$), z_i is the charge valence on species i and c_i is the concentration of species i . The thickness of EDL formed along the channel wall is much smaller than the dimension of the channel, and hence we have used the Poisson-Boltzmann (PB) equation to calculate the ion distribution in the system. Under this assumption, the Gauss's law becomes [117]

$$\nabla \cdot (\epsilon \nabla \psi) = F \sum_{i=1}^N z_i c_{i,0} \exp\left(-\frac{e z_i}{kT} \psi\right) \quad (3.14)$$

where $c_{i,0}$ is the bulk concentration of ion species i in the system, e is the electron charge ($1.6021766341 \times 10^{-19} \text{ C}$), k is the Boltzmann's constant ($1.380649 \times 10^{-23} \text{ J} \cdot \text{K}^{-1}$) and T is the absolute temperature of the fluid. We have used the following values of these parameters in all our electrokinetically driven flows: $c_{i,0} = 9.44 \times 10^{-5} \text{ mol/m}^3$, $T = 298 \text{ K}$, $\epsilon = 7.0922 \times 10^{-10} \text{ F/m}$. The viscoelasticity of the present fluid is quantified in terms of the Weissenberg number, which is defined as $\frac{\lambda U_0}{L}$. Here U_0 is the Helmholtz–Smoluchowski velocity [117] defined as $\frac{\epsilon \zeta_0 E_x}{\eta_0}$, where η_0 is the zero-shear rate viscosity of the present viscoelastic fluid. The polymer viscosity ratio β ($= \frac{\eta_s}{\eta_s + \eta_p}$) is used to study the influence of

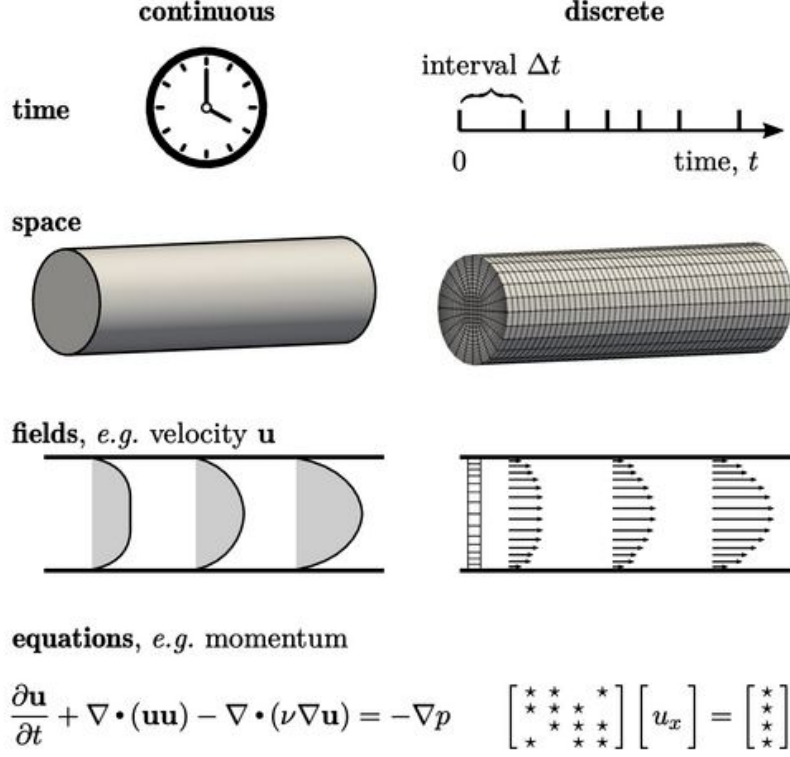


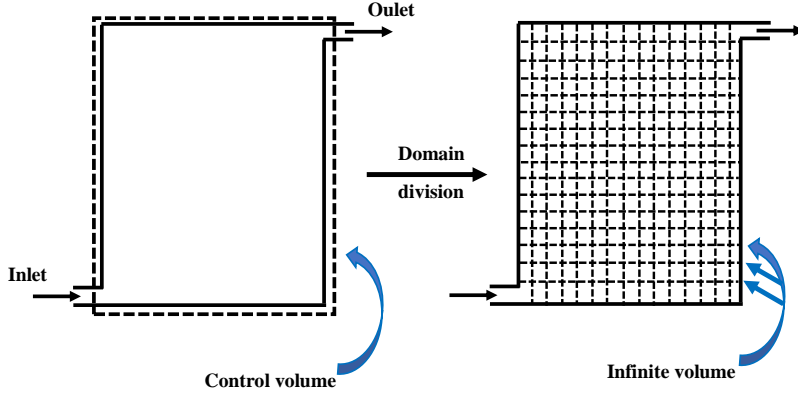
Figure 3.1: An illustration of the transformation of a physical model into discrete forms in numerical simulation methodology [177].

the polymer concentration on the flow dynamics. The present study has simulated a perfect creeping flow condition (i.e., $Re = 0$) by setting the inertial terms of the momentum equation equal to zero.

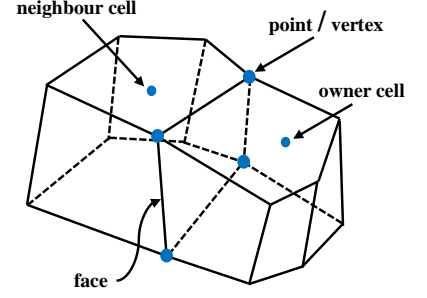
3.1.3 Numerical solution technique

All governing equations used in this thesis have been numerically solved using the finite volume method (FVM) based computational fluid dynamics (CFD) technique. A finite volume method is a numerical approach that converts the partial differential equations constituting conservation laws into discrete algebraic equations over finite volumes. The finite volume method is relatively easy to implement with different boundary conditions and quite suitable for numerical simulations involving fluid flow, heat, and mass transfer. It can handle all kinds of complex flow problems [178]. The different steps in the discretization process are depicted in Fig. 3.1. The numerical simulation technique demonstrates a continuous physical system by equivalent discrete entities, i.e.,

- Time divided into intervals, Δt



(a) Division of representative domain into smaller cells.



(b) Typical contiguous volume elements.

Figure 3.2: Subdivision of domain into finite volume elements or cells, (a), typical interconnected polyhedral cells (b) having a common face. Each face inside the domain is shared by two cells; one is the owner, and the other is the neighboring cell [177].

- Space splits into cells or meshes
- Fields, such as velocity, become discrete values
- The partial differential equations become linear differential equations

Besides the finite volume method, the finite element and finite difference methods are also used for the same purpose. However, the finite volume method has an advantage over the other methods as it discretizes the different terms in the governing equations separately using an efficient and appropriate scheme. Furthermore, the finite volume method directly implements discretization using an integral formulation. On the other hand, the finite element and finite difference methods are used to calculate the field variables. In the finite volume method, the corresponding domain is converted into smaller adjacent volume elements/cells called finite volumes, Fig. 3.2. These elements can be of any irregular polyhedral shape in three dimensional. The constitutive equations are then executed for each cell by balancing the mass and momentum flux across the surfaces between the connected cells and considering the sources or sinks within each cell.

The discretization of the governing equations is carried out in two steps [178]:

1. Integration of the partial differential equations over each element resulting in the conversion of surface and volume integrals (first converted into surface integrals by

utilizing the Gauss theorem) into discrete algebraic relations.

$$\int_s (d\mathbf{S} \cdot \boldsymbol{\Psi}) = \sum_f (\mathbf{S}_f \cdot \boldsymbol{\Psi}_f)$$

Here, $\boldsymbol{\Psi}$ is the general field variable, subscript f represents the face values, $d\mathbf{S} = \mathbf{n}dS$ is the area vector, and \mathbf{S}_f is the face area vector.

2. Transformation of the algebraic relations into algebraic equations of the variables (flux terms). Interpolation schemes are required to relate the surface values to the cell values.

Based on this FVM method, all the governing equations have been solved using OpenFOAM, which is an open-source CFD toolbox. In particular, the recently developed 'rheoFoam' and 'rheoEFOam' solvers available in Rheotool [179] package have been used to solve all the governing equations along with OpenFOAM. All the diffusion terms in the momentum, constitutive, and number density equations were discretized using the second-order accurate Gauss linear orthogonal interpolation scheme. All the diffusion terms in the momentum, constitutive, and number density equations were discretized using the second-order accurate Gauss linear orthogonal interpolation scheme. All the gradient terms were discretized using the Gauss linear interpolation scheme. While the linear systems of the pressure and velocity fields were solved using the preconditioned conjugate solver (PCG) with DIC (Diagonal-based Incomplete Cholesky) preconditioner, the stress fields were solved using the preconditioned bi-conjugate gradient solver (PBiCG) solver with DILU (Diagonal-based Incomplete LU) preconditioner [180, 181]. All the advective terms in the constitutive equations were discretized using the high-resolution CUBISTA (Convergent and Universally Bounded Interpolation Scheme for Treatment of Advection) scheme for its improved iterative convergence properties [182]. All these modifications were done in the 'fvSchemes' and 'fvSolution' subroutines available in the OpenFOAM solvers. For all the problems in the present study, the pressure-velocity coupling was established using the SIMPLE (Semi-Implicit Method for Pressure-Linked Equations) method, and the improved both-side diffusion (iBSD) and log-conformation tensor techniques were used to stabilize the numerical solutions. A typical case file structure in OpenFOAM is shown in Fig. 3.3.

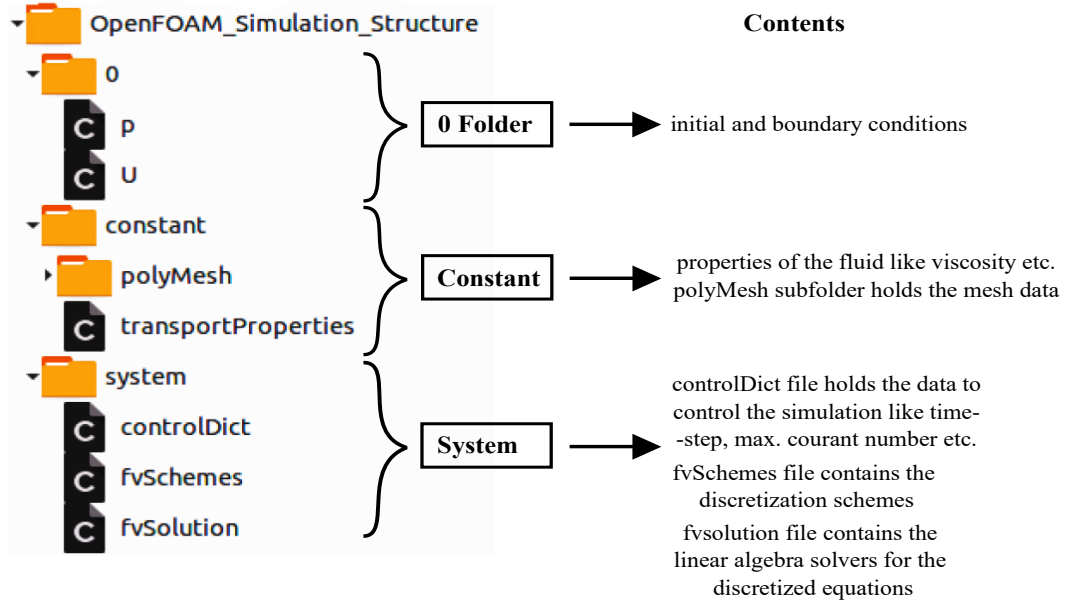


Figure 3.3: A simple case file structure in OpenFOAM [183]. After initiating the terminal, the command is typed to carry out the simulation and the post-processing.

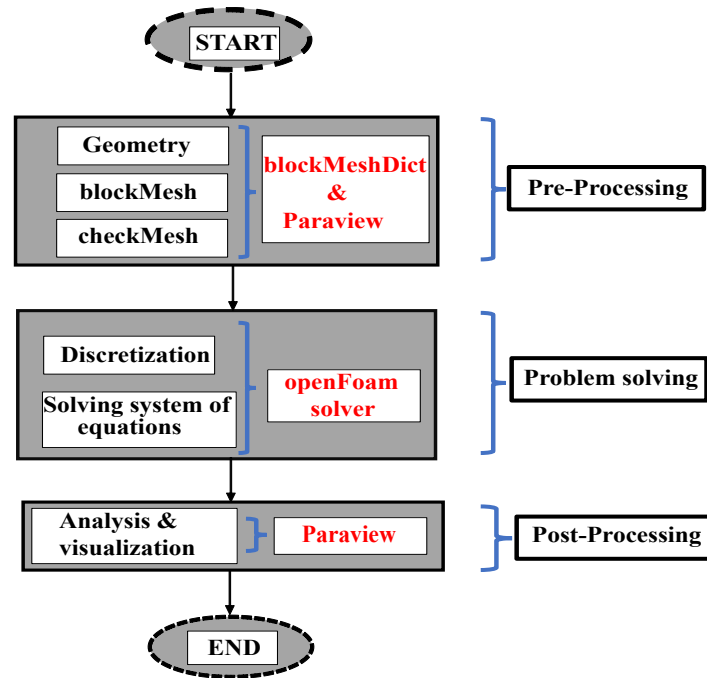


Figure 3.4: Flowchart of the steps followed to solve the present problem using OpenFOAM.

Any CFD simulation consists of three main steps: pre-processing, problem-solving, and post-processing. A schematic of these different steps in OpenFOAM is summarised in Fig. 3.4. The pre-processing step involves the formation of the computational domain

(geometry), followed by mesh generation. The computational domain and its meshing have been done with the help of the blockMeshDict subroutine available in OpenFOAM. During the making of any grid, careful consideration is taken into account. For instance, a very fine mesh is created near a solid wall to capture the steep gradients of velocity, stress, or concentration fields, whereas a relatively coarse mesh is created away from it. The problem-solving step involves the selection of a solver, discretization schemes, and fixing the boundary and initial conditions. For the post-processing step, a third-party ParaView software is used to analyze and visualize the results. Another important factor used in the current study to ensure the simulation's stability is the Courant number. It is defined as the ratio of the time step size Δt to the characteristic convection time scale $\frac{\Delta x}{u}$ (time in which a disturbance convects over a given distance of Δx) and is provided as:

$$Co = \frac{u \Delta t}{\Delta x}$$

To ensure the stability and accuracy of the simulation (explicit numerical schemes), the Courant-Friedrichs-Lewy or CFL condition of $Co \leq 1$ is satisfied for all simulations.

3.2 Experimental Methodology

The experimental methodology involves the rheological and physicochemical characterization and comparison of biosurfactant and chemically derived micellar solutions, which are first presented and discussed here.

3.2.1 Rheological and physicochemical characterization of micellar solutions

Materials

Di-rhamnolipid biosurfactant, $C_{32}H_{58}O_{13}$ (R-90) with 90 % purity (10% mono-rhamnolipid as impurity [184] and mol. wt. 650.79) produced by AGAE technologies (Oregon, USA) was purchased from Sigma Aldrich. It was used as received without any further alteration. The conventionally used cationic surfactant cetyltrimethylammonium bromide, $C_{19}H_{42}BrN$ (mol. wt. 364.4) was purchased from Spectrochem Private Limited (Mumbai, India), and it was also used as received. The molecular structure of both surfactants

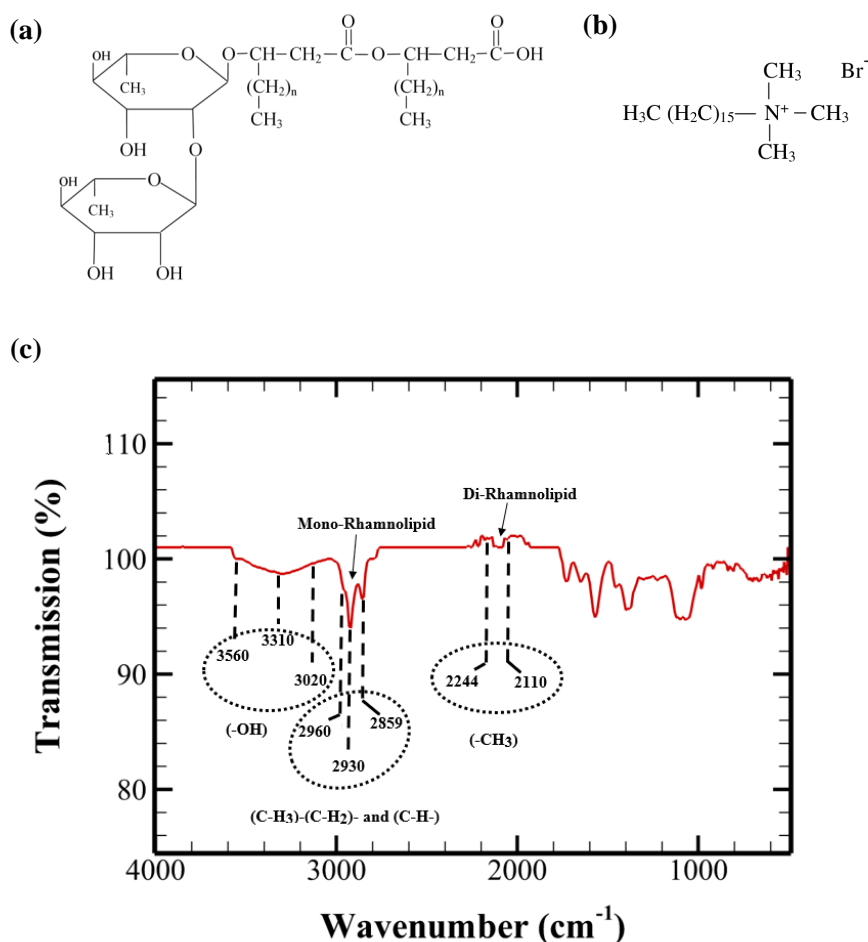


Figure 3.5: Representation of molecular structure of (a) rhamnolipid and (b) CTAB. (c) FTIR results of di-rhamnolipid surfactant, which reveal the presence of mono-rhamnolipid as 10% impurity in it. This observation is in line with that seen by Rahman et al. [185]. The first marked circle from the left side represents -OH stretch due to the hydrogen bonding (3310 cm^{-1}), and the second marked circle represents an aliphatic bond stretching ($2960 - 2859\text{ cm}^{-1}$). Rhamnose rings and hydrocarbon chains are found in these two regions. The third marked circle confirms the presence of di-rhamnolipid.

is shown in Fig. 3.5. The solvent used to prepare the test solutions was double distilled water produced with the help of an in-house facility. All the surfactant solutions at various concentrations were prepared by dissolving a known amount of either rhamnolipid or CTAB surfactant into de-ionized water having a specific conductivity of $1.2\text{ }\mu\text{S cm}^{-1}$. The surfactant solutions were mixed vigorously with a magnetic stirrer at 700 rpm for about 2 hours and left for a whole night to equilibrate before starting any measurement.

Surface tension and contact angle measurements

The surface tension of all the surfactant solutions was measured using the force tensiometer (Sigma 700, purchased from Biolin Scientific) at 25 °C. The tensiometer was first calibrated with distilled water before measuring the surface tension of the present surfactant solutions. For the removal of any contaminant, the glassware used for the measurement was cleaned with ethanol and then rinsed with distilled water. Also, the platinum ring used in this setup was washed with distilled water and heated on a flame before starting any measurement. The ring was hung and dipped into the solution, and then the maximum force required for pulling out the ring from the solution was considered as the surface tension. On the other hand, the surface wetting property of the present surfactant solutions was quantified by measuring the contact angle (CA) using the Wilhelmy plate method. Both the surface tension and contact angle data for each sample were repeated at least three times to achieve the reproducibility of the present results.

Particle size analysis

In the present investigation, a particle size analyzer (Microtrac, Nanotrac wave series, USA) was used to measure the size of the agglomerates formed in the surfactant solutions. It operates based on the concept of the dynamic light scattering technique (DLS) with the detection angle of 186 °. It uses a 4 *mW* He-Ne standard laser, which operates at a wavelength of 633 *nm*. In this technique, a surfactant solution is illuminated by a beam of laser light and then the fluctuation of the scattered light is collected, which is ultimately associated with the distribution of particle size present in a solution. The particle size distribution was measured from the correlation function using the Multiple Narrow Modes algorithm and this algorithm is based upon a non-negative least squares (NNLS) fit [186, 187].

Thermal gravimetric analysis (TGA)

The thermal gravimetric analysis measures a material's mass change as a function of temperature over time when it is heated at a predetermined rate. A surfactant's thermal stability was measured using the SDT 650 apparatus from TA instruments (Finland).

The test was performed at a constant heating ramp rate of 30 °C/min from 20 to 500 °C. The alumina sample pan of 90 μL capacity was used to run the experiment under inert environment condition (nitrogen) at a flow rate of 100 mL/min.

Shear rheological measurement method

For steady and dynamic shear rheological measurements, all surfactant solutions were characterized by using a stress-controlled rheometer (Anton-Paar, MCR 702 twin drive) with cone-plate geometry (60 mm of diameter and cone angle of 1°) with a truncation gap of 100 μm . The experiments were performed at a fixed temperature of 25 °C. The shear rheological characterizations were reported at both fixed shear (10 s^{-1}) and varying shear rates (0.01 to 1000 s^{-1}). After each experiment, the measuring plate was cleaned with distilled water to remove the last sample and then again cleaned with ethanol and dried out before its use. The viscoelastic property of a surfactant solution is essential to understanding the relationship between the change in its microstructure and the complex rheological behaviour. To understand this behaviour, a small amplitude oscillatory shear (SAOS) test was conducted and presented in the results section. The micelles can break and reform simultaneously in a solution with equal tendency and show the Maxwellian behavior when the times for micelles' breaking and reforming processes dominate over the reptation time [29, 74]. In this regime, the storage (G') and loss (G'') moduli of the surfactant solution can be fitted to the Maxwell model as follows [188, 189]:

$$G' = \frac{G_0(\omega\lambda_s)^2}{1 + (\omega\lambda_s)^2} \quad (3.15)$$

$$G'' = \frac{G_0(\omega\lambda_s)}{1 + (\omega\lambda_s)^2} \quad (3.16)$$

where G_0 , ω and λ_s are the plateau modulus, angular frequency, and shear relaxation time, respectively.

Dripping-onto-substrate (DoS) extensional rheometry

The dripping-onto-substrate (DoS) rheometry method is used to measure the extensional viscosity of the present surfactant solutions. The experimental setup used for this method includes a dispensing system and an imaging system, as shown in Fig. 3.6. The dispensing system releases a known amount of sample onto a glass substrate placed under it. An

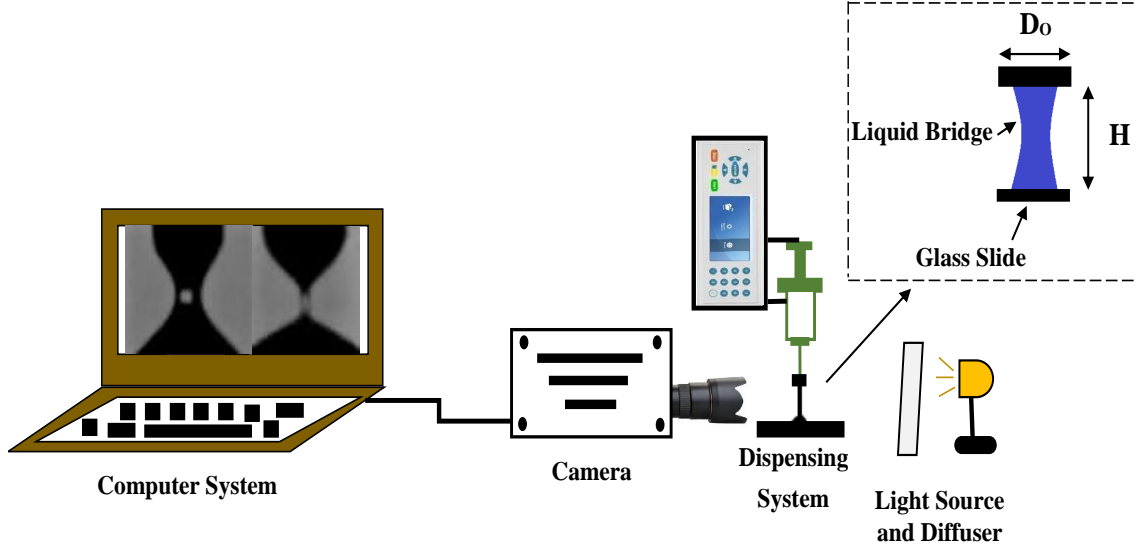


Figure 3.6: Schematic representation of the dripping-onto-substrate (DoS) rheometry setup. It consists of a light source for backlighting the liquid filament, and a high-speed camera connected to a computer system to record the filament thinning and pinch-off dynamics of the liquid bridge formed between the dispensing system and the glass substrate. The dispensing system consists of a syringe pump that releases a known amount of test sample through a nozzle of diameter D_o placed at a height H from the glass substrate.

optimized aspect ratio (H/D_o) of around three was used in the present study [190, 191], where H is the height between the nozzle and the glass substrate and D_o is the outer diameter of the nozzle. A syringe pump dispensed the test sample at a flow rate of 0.02 ml/min, and the flow stopped when the fluid drop touched the glass surface. The slow release of the sample on the glass substrate helps to record the real-time capillary thinning and pinch-off dynamics of a particular sample. This transient phenomenon was captured by a high-speed camera (Photron, Fast Cam SA4) with magnification lenses (A G-type AF-S macro, Nikon) and variable frame rates of up to 12,000 fps. The captured images and videos were processed by using the image processing program ImageJ. Furthermore, an in-house code written in Python was used to analyze the capillary thinning and pinch-off dynamics data.

Chapter 4

Rheological and physicochemical studies of biosurfactant and chemically derived micellar solutions

This chapter aims to present detailed rheological and physicochemical studies of biosurfactant and chemically derived micellar solutions as they are important to investigate the corresponding flow dynamics. In particular, the present thesis has used rhamnolipid and cetyl trimethyl ammonium bromide (CTAB) as bio and chemical surfactants and presented a detailed comparison of their behaviors. The introduction and motivation behind this chapter have already been introduced in section 2.1 of chapter 2. The physicochemical studies include surface tension and contact angle measurement, particle size analysis, and thermal gravimetric analysis, whereas rheological studies include steady shear, small amplitude oscillatory shear (SAOS), and dripping-onto-substrate (DoS) extensional rheometry.

4.1 Results and Discussion

4.1.1 Surface tension and contact angle

The addition of surfactant molecules in a solution greatly influences the surface tension and the surface wetting phenomenon. These are important in various applications that consider fast wetting, such as pesticide spraying, ink-jet printing, etc. [192, 193]. The adsorption of surfactant molecules at the interface decreases the surface tension until the equilibrium value is reached. The results for the surface tension of both surfactant solutions as a function of concentration are plotted in Fig. 4.1. The measurement was carried out for the concentration ranging from 0.01 to 1.0 wt.% at 25 °C. It is seen that the surface tension value of the rhamnolipid surfactant solution is lower than that of the CTAB surfactant solution at the same concentration. The CMC values were observed at around 0.15 wt.% and 0.30 wt.% for rhamnolipid and CTAB surfactants, respectively. This suggests that the rhamnolipid has a stronger ability and efficiency to reduce surface

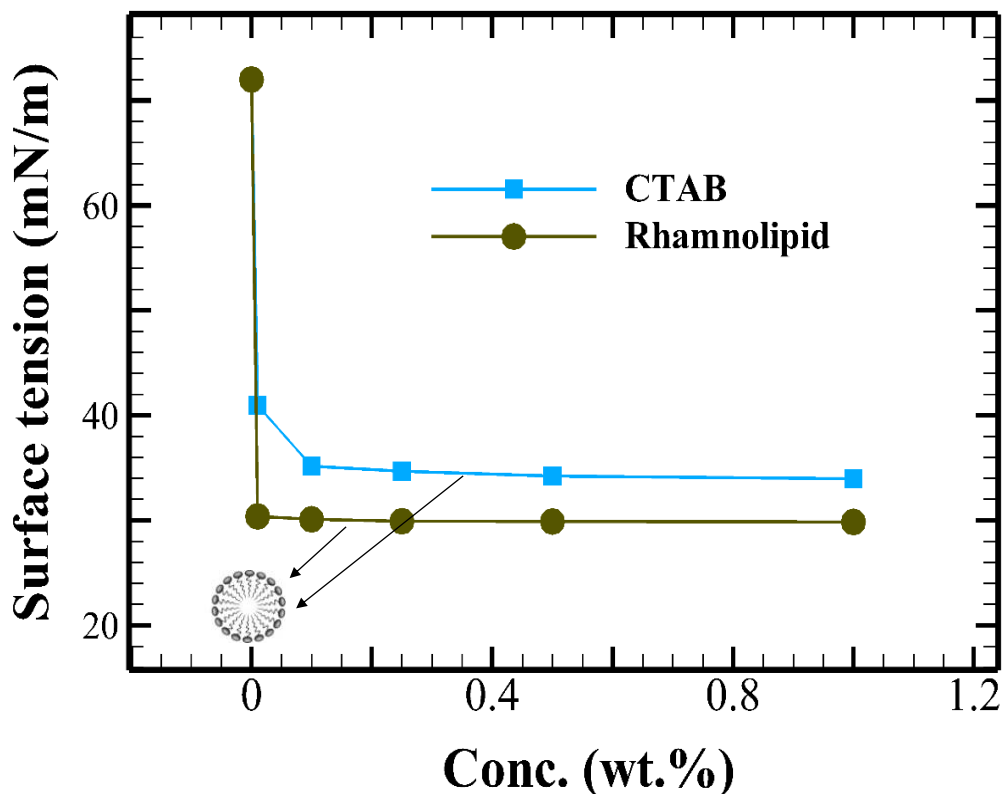


Figure 4.1: Representation of surface tension as a function of surfactant concentration for both rhamnolipid and CTAB surfactant solutions at 25 °C.

tension than the CTAB surfactant. Further increasing the surfactant concentration, it reaches a constant value for both the surfactant solutions. This is because, at high concentrations, the surface is entirely saturated with the micelles, and no vacant site can be further occupied. As a result, no further decrease in the surface tension value is observed [194, 195, 196, 197, 198, 199]. As the critical micelle concentration (CMC) is reached, the change in surface tension with concentration becomes minimal because there is no significant change in the monomer concentration with increasing surfactant concentration. This result indicates that the adsorption of surfactant molecules is greatly affected by the concentration, which concluded that the presence of micelles makes no difference in the adsorption dynamics [200].

For the contact angle measurement, the surfactant equilibrated Wilhemly platinum plate was clamped into the tensiometer balance and immersed into the surfactant solution at a speed of 5 mm/min. The plate was immersed to a depth of 3 mm and then pulled back to get advancing and receding contact angle measurements. Fig 4.2 shows the

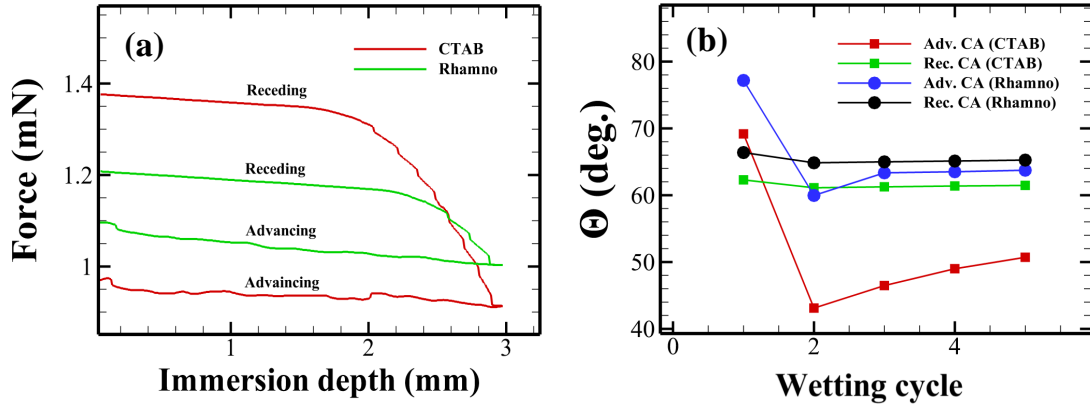


Figure 4.2: (a) Representation of wetting force as a function of immersion depth (b) advancing and receding contact angles (in degree) as a function of wetting cycle number for both CTAB and rhamnolipid surfactant solutions on pre-equilibrated Wilhelmy platinum plate at 1.0 wt.% concentration. The immersion depth and speed were kept at 3 mm and 5 mm/min, respectively.

results for both surfactant solutions. The wetting force decreases with the immersion depth for both surfactants due to buoyancy, as seen from Fig. 4.2(a). In particular, it remains almost constant initially and then starts to decrease with further increment in the depth, and this trend was also observed in earlier experiments [201]. Depending on the nature of the sample (hydrophobic or hydrophilic), the wetting force can be positive or negative. In this case, a positive value of the wetting force is observed due to the downward direction of the force on the surfactant solution. The advancing wetting force is higher, and the receding wetting force is lower for the rhamnolipid surfactant than for the CTAB. Fig. 4.2(b) represents the contact angle (θ) for both surfactants with respect to the number of wetting cycles. In both cases, it is found that the advancing contact angle decreases and then approaches a constant value as the surface becomes wetter in subsequent evaluations. The receding contact angle is almost constant due to the aggregation of the surfactant molecules on the plate surface. As the surfactant concentration gradually increases, the advancing contact angle value shows no significant change irrespective of the surfactant type, see Table 4.1. This is due to the formation of a monolayer of surfactant molecules on the plate surface and then more aggregation of surfactant molecules on the plate surface at high surfactant concentration. Note that here

	CTAB	CTAB	Rhamnolipid	Rhamnolipid
Concentration (wt.%)	Adv. CA	Rec. CA	Adv. CA	Rec. CA
0.01	67.709	57.45	75.685	64.177
0.1	67.901	60.42	75.95	64.874
0.25	68.459	61.266	76.241	65.02
0.5	68.857	61.872	76.951	65.728
1.0	69.162	62.286	77.183	66.38

Table 4.1: Values of the advancing and receding contact angles for both CTAB and rhamnolipid surfactants as a function of concentration.

the advancing and receding contact angles are calculated from the following relation [202]

$$\frac{F}{L} = \gamma_{a/w} \cos \theta - d \Delta \rho g \quad (4.1)$$

where F is the force, L is wetting plate length, $\gamma_{a/w}$ is surface tension at the air/surfactant solution interface, d is the immersing depth, θ is the contact angle, g is the gravity force and $\Delta \rho$ is the water and sample density difference.

4.1.2 Particle size measurement

Particle size analysis is an important characteristic used for quality control in many industrial processes such as pharmaceuticals, paints and coatings, aerosol, food industry, etc. It is one of the important factors that determine the efficiency and performance of the processes. In the present study, this analysis will provide information about the size distribution of micelles in the solution [203, 204]. The particle size or aggregate of the rhamnolipid biosurfactant is smaller than that of the CTAB chemical surfactant as can be seen from see Fig. 4.3. Furthermore, it can be observed that the micelle size distribution of rhamnolipid biosurfactant is better than the distribution of CTAB surfactant in a solution. The particle size distribution curve of the CTAB surfactant is close to that of a skewed distribution function, whereas it is of a mono-modal distribution function for the rhamnolipid surfactant. Furthermore, it has been observed that the rhamnolipid remains well mixed and stable in an aqueous solution than that seen for CTAB, which starts to settle down after some time. The rhamnolipid surfactant consists of a rhamnose group, which is linked together with 3-hydroxyl fatty acids. The carboxyl end of the fatty acid is highly polar; therefore, this biosurfactant is highly water-soluble and stable.

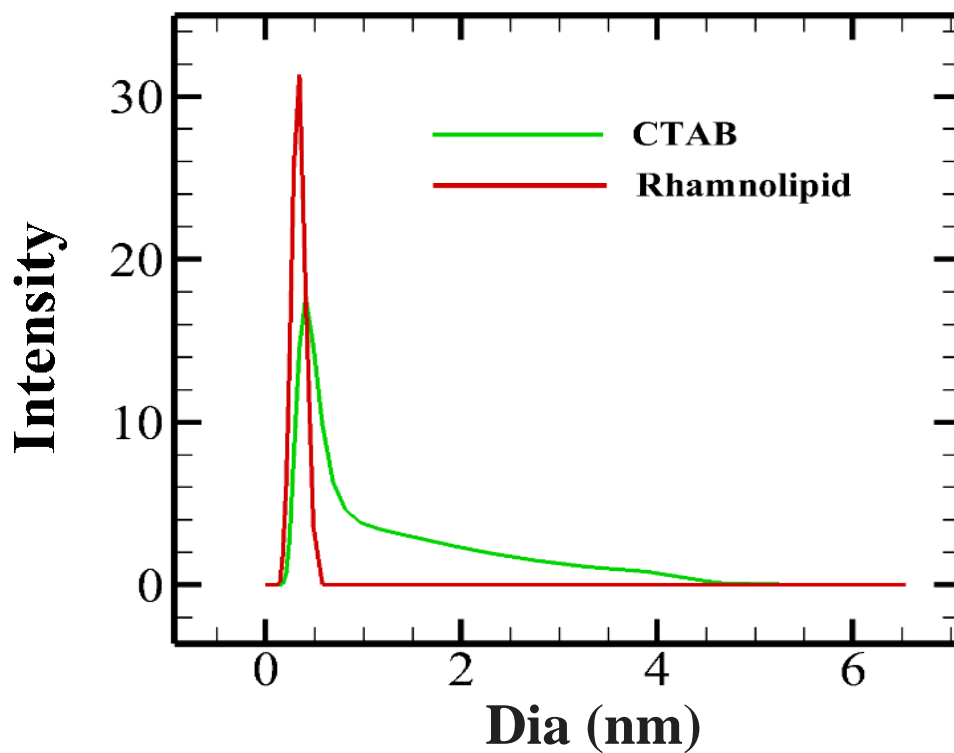


Figure 4.3: Particle size distribution for 1.0 wt.% of (a) CTAB and (b) rhamnolipid surfactant solution at 25 °C.

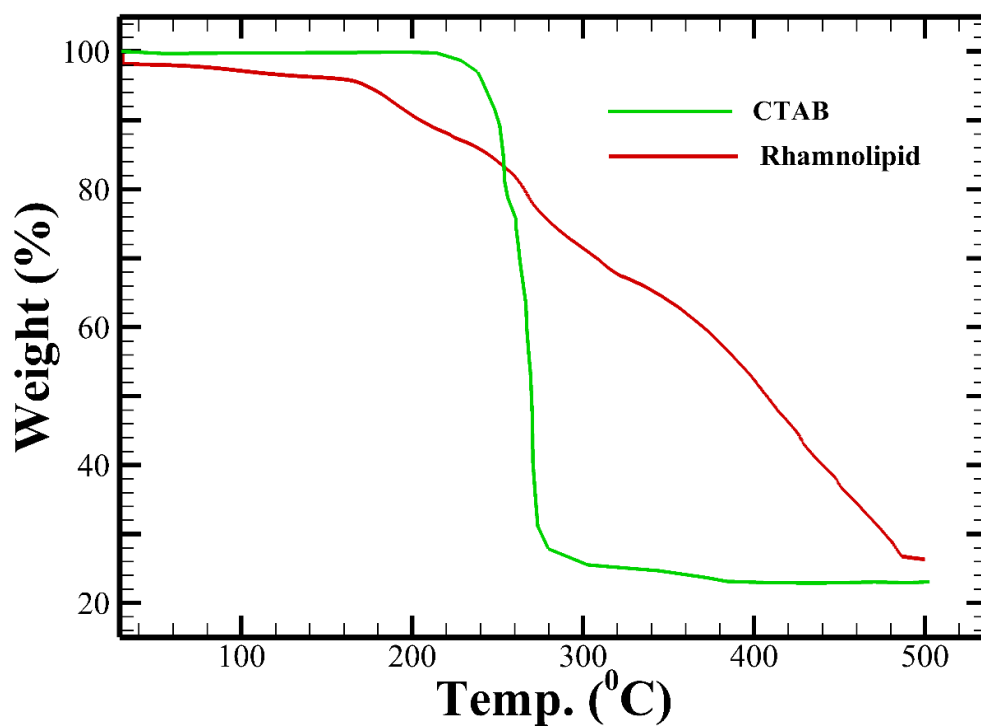


Figure 4.4: Representation of TGA curves in terms of weight loss in % for both surfactants under nitrogen atmosphere conditions and ramp rate 30 °C/min.

4.1.3 Thermal gravimetric analysis

The thermal stability of a surfactant solution is another important property that plays a significant role in many applications, such as in the surfactant flooding-based enhanced oil recovery process. At a relatively high temperature, the performance of a surfactant solution can be affected because of its thermal degradation behaviour. Surfactants get precipitated at high temperatures, decreasing their ability to drastically lower the surface tension. The thermal stability of both surfactants is presented in Fig. 4.4 under a nitrogen atmosphere within a temperature ranging from 20 to 500 °C. It shows no significant weight loss of up to 150 °C of both surfactants. After this temperature, rhamnolipid degrades as the temperature further increases, but CTAB surfactant shows better stability at low temperatures. At around temperature 260-270 °C, severe thermal degradation is observed for the CTAB surfactant, while rhamnolipid performs better at the same temperature. For the CTAB surfactant, around 70 % weight loss is observed at 280 °C, whereas only 26.75 % weight loss is seen for the rhamnolipid surfactant. While rhamnolipid shows an almost linear decreasing trend in the thermal degradation behaviour with the temperature of up to 500 °C, a drastic steep decomposition of the CTAB surfactant occurs at around 260 °C, and then it remains almost constant up to a temperature of 500 °C. These thermal stability tests suggest that the rhamnolipid biosurfactant has better thermal stability at high temperatures (> 300 °C) than the CTAB surfactant. Therefore, it is better suited for high-temperature applications such as in the surfactant flooding-based enhanced oil recovery process.

4.1.4 Steady shear rheological measurements

For the successful formulation of industrial products such as paints, polymers, food, and pharmaceuticals, studying the rheology of surfactant solutions for their better use under various flow conditions is imperative. To do so, first, we examine the variation of the shear viscosity with the shear rate at various surfactant concentrations at 25 °C. Fig. 4.5 depicts the effect of the shear rate on the shear viscosity of both rhamnolipid and CTAB at different concentrations. In all the cases, a shear-thinning behavior is observed between the low and intermediate shear rate regimes irrespective of the surfactant type and concentration. This is because as the shear rate gradually increases, micelles' internal

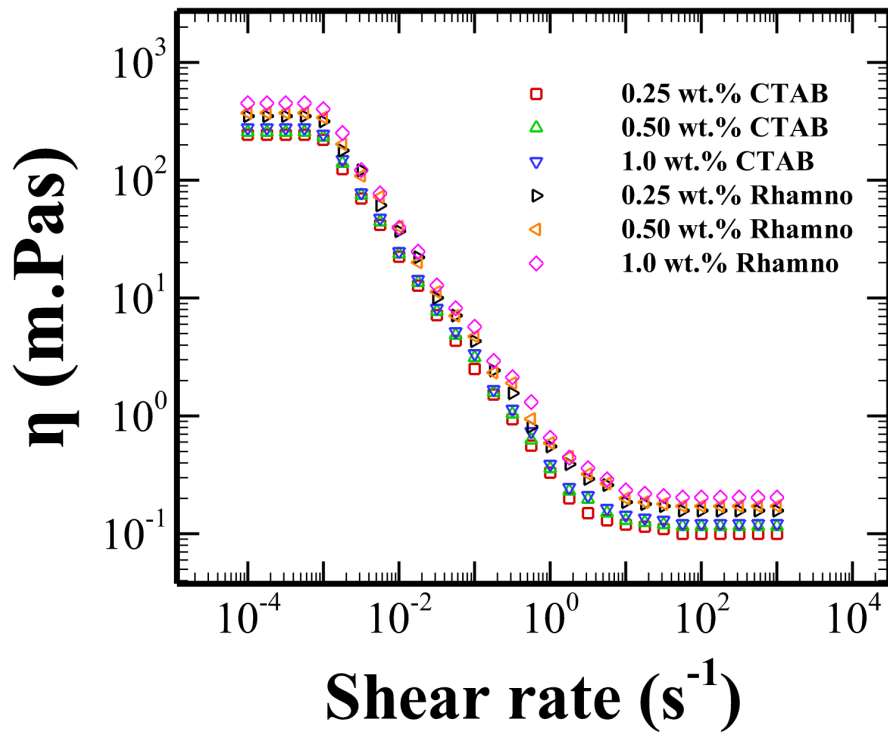


Figure 4.5: Variation of the steady shear viscosity with shear the rates both for CTAB and rhamnolipid solutions at 25 °C.

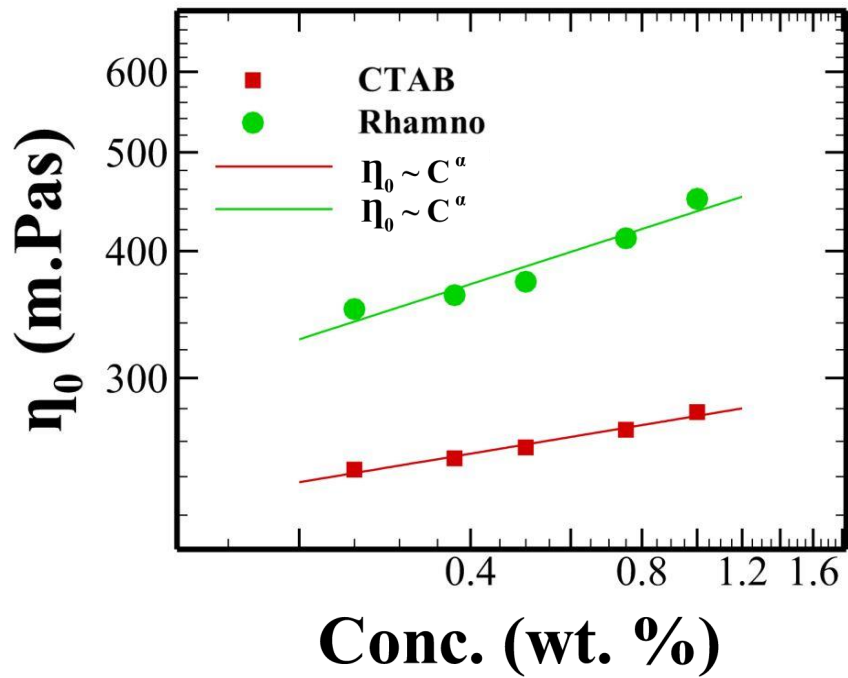


Figure 4.6: Variation of zero-shear viscosity with concentration both for CTAB and rhamnolipid solutions at 25 °C.

entangled network structure is supposed to be disrupted at a higher rate than the rate of structure reformation. They orient themselves parallel to the driving force (known as the shear alignment) [205, 206, 207, 208], ultimately leading to this shear-thinning behavior. Furthermore, a plateau region in the shear viscosity at a low shear rate regime is also observed, followed by a change in its value by order of magnitude at the intermediate shear rate regime [189, 209]. All these suggest that the rheological responses of both bio and chemically-derived surfactant solutions are very sensitive to the change in the shear rate due to the change in their molecular architecture. The shear-thinning behavior of the present surfactant solution is best described by the following power-law model [210]:

$$\eta = k\dot{\gamma}^{n-1} \quad (4.2)$$

Here η is the shear viscosity (mPa.S), $\dot{\gamma}$ is the shear rate (s^{-1}), k is the flow-consistency index (Pa.s^n), and n is the flow behaviour index (dimensionless). For a Newtonian fluid, the flow behaviour index $n = 1$, whereas for shear-thinning (or pseudoplastic) fluids, the flow behaviour index $n < 1$. When $n > 1$, fluid shows a shear-thickening behaviour called a dilatant fluid. Fluid can also exhibit yield stress along with shear-thinning and shear-thickening behaviours, and those fluids can be modeled either with Bingham or Herschel-Bulkley model [211]. The above non-linear power-law model fitted the experimentally measured shear viscosity. For CTAB surfactant solutions, the values of n at 0.25, 0.5, and 1.0 wt.% are 0.861, 0.871, and 0.877, respectively. On the other hand, for rhamnolipid biosurfactant solutions, the corresponding values of n are 0.868, 0.875, and 0.882, respectively. It can be seen that the value of n slightly increases with the surfactant concentration, suggesting that the shear-thinning behaviour of the present surfactant solutions hardly depends on the surfactant concentration. On the other hand, the variation of the zero-shear rate viscosity (η_0) with the surfactant concentration is plotted in Fig. 4.6. It is an important rheological parameter widely used in various practical applications [212, 213]. It is evaluated by extrapolating the shear viscosity data at low shear rate values to its zero value. An increasing trend in its variation with the surfactant concentration can be seen irrespective of the surfactant type due to the increase in the tendency to form an entangled network structure with the surfactant concentration. This trend also aligns with that seen in earlier investigations [214, 215]. At any surfactant concentration, the value of η_0 is higher for rhamnolipid than for CTAB. This is because

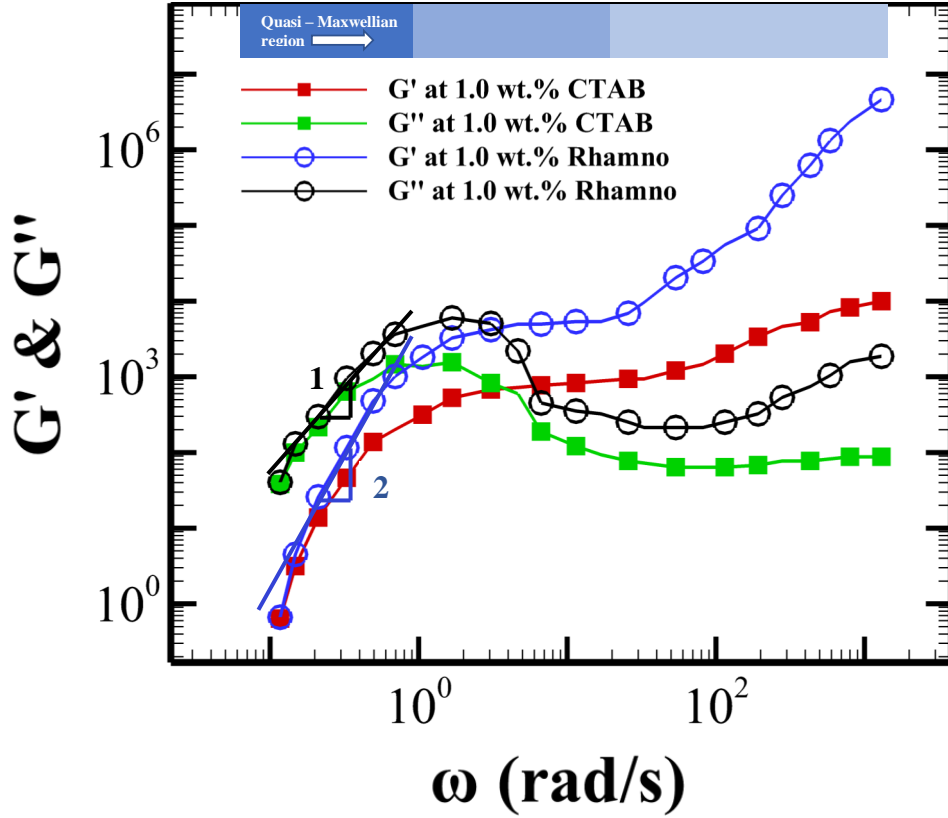


Figure 4.7: Representation of storage (G') and loss (G'') moduli as a function of angular frequency (ω) both for CTAB and rhamnolipid surfactant solutions at 25 °C and shear strain 0.1 %. Slopes 1 and 2 represent the divergence for rhamnolipid biosurfactant.

the latter has a lower molecular weight than the former one, and the zero-shear rate viscosity scales with the molecular weight as $\eta_0 \sim M_w^\alpha$ [216]. We have fitted these results with a form $\eta_0 \sim C^\alpha$ where C is the surfactant concentration. The values of the exponent α are 0.09431 and 0.1876 for CTAB and rhamnolipid, respectively. These values are smaller than that predicted by the scaling theory of Cates and Candau [29]. This may be attributed to the low surfactant concentration and the absence of salt in the present study.

4.1.5 Small amplitude oscillatory shear (SAOS) measurements

Small amplitude oscillatory shear (SAOS) can influence the microstructure of the micelles. Oscillatory shear applies a sinusoidal stress to the material, thereby periodically changing the deformation and stress. This periodic deformation can have a significant effect on the microstructure of the micelles. Due to the oscillatory shear, the micelles experience alternative stretching and relaxation, resulting in a change in the micelles

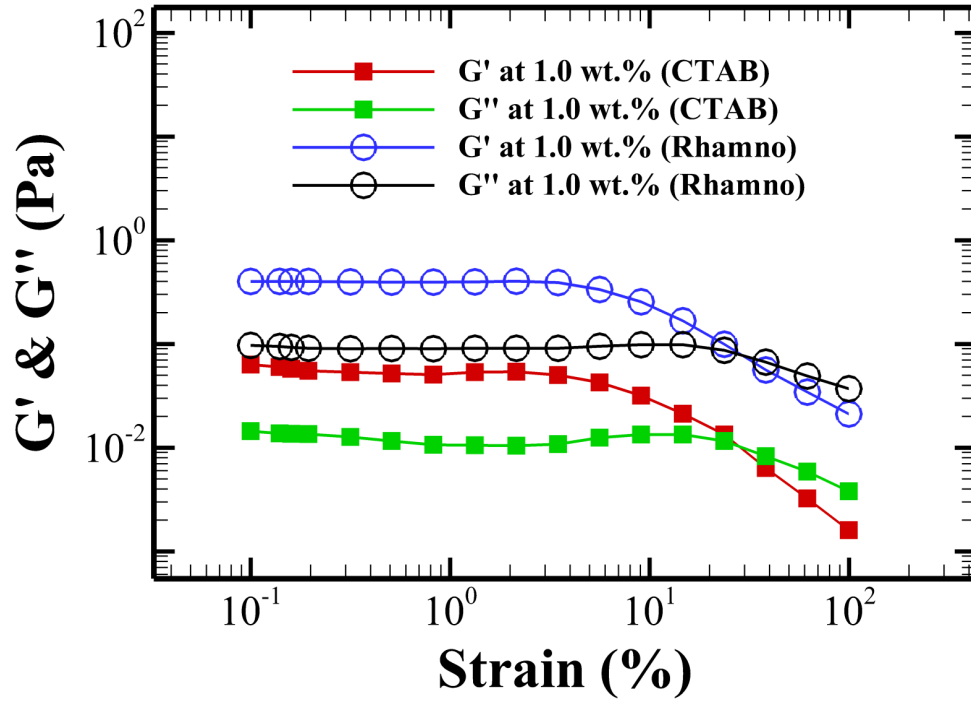


Figure 4.8: Representation of storage (G') and loss (G'') moduli as a function of strain (%) both for CTAB and rhamnolipid surfactant solutions at 25 °C.

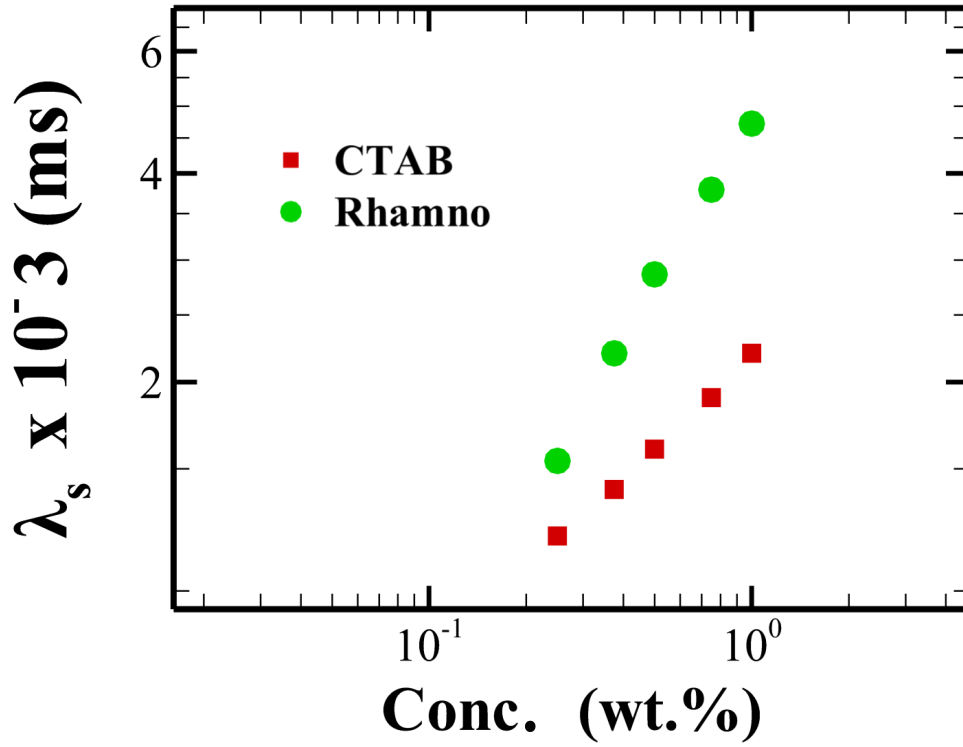


Figure 4.9: Representation of shear relaxation time (λ_s) as a function of surfactant concentration both for CTAB and rhamnolipid surfactant solutions at 25 °C.

microstructure. Small amplitude oscillatory shear measurements are often conducted to measure the viscoelastic property of a complex fluid in the linear regime [217, 218]. In this measurement, the elastic part of the solution is called the storage modulus (G'), which measures the energy stored and recovered. On the other hand, the viscous part is called the loss modulus (G''), which is a measure of the energy dissipated [2, 219]. The storage and loss moduli results against the angular frequency (ω) are shown in Fig. 4.7 at 25 °C. At low angular frequency, the loss modulus (G'') is greater than the storage modulus (G') regardless of the surfactant type, thereby showing a liquid-like behaviour. Further increasing the angular frequency, the storage and loss moduli proceed towards the critical point where $G' = G''$, known as the crossover frequency. Beyond this point, the storage modulus is greater than the loss modulus, showing an elastic solid-like behaviour at high-frequency regions. The storage and loss moduli continue to increase, indicating rod-like micelles in the solution [220, 221]. At low frequencies, the results follow the Maxwellian trend with slopes of 1 and 2 for G' and G'' , respectively. The divergence from viscous to elastic state suggests the formation of micelles in the solution and the transition of the relaxation mode from slower to faster. The results were consistent with Tang et al. [222]. It can be seen that the rhamnolipid biosurfactant shows more elasticity than the CTAB chemical surfactant at all concentrations (results for 0.25 and 0.50 wt.% of surfactant solutions are not shown here as the trends are almost similar as that seen for 1%).

The results for the amplitude sweep experiments of both CTAB and rhamnolipid surfactants are depicted in Fig. 4.8. Irrespective of the surfactant type, the storage modulus (G') as well as loss modulus (G'') remain almost constant up to a strain amplitude of around 10, indicating the existence of a linear viscoelastic regime up to this value of the strain amplitude for both the surfactants. At low strain amplitudes, the storage modulus is always greater than the loss modulus, suggesting the elastic contribution is more dominant than the dissipative contribution. On the other hand, the viscous contribution dominates over the elastic response at high strain amplitudes. Once again, it can be seen that the storage and loss moduli are larger for the rhamnolipid biosurfactant than for the CTAB chemical surfactant over the whole range of the strain amplitude considered in this study. This is again due to the difference in the molecular weight of the two surfactants.

The shear relaxation time λ_s is obtained by fitting the experimental results of G' and G'' using the single-mode Maxwell model [223], and the results are presented in Fig. 4.9

both for rhamnolipid and CTAB. One can see that irrespective of the surfactant type, the shear relaxation time increases with the surfactant concentration. It should be mentioned here that the relaxation time should be independent of the surfactant concentration in the dilute regime [2, 224]. However, we can see almost a linear dependence of the relaxation time on the surfactant concentration. It suggests that the surfactant concentration must be in the semi-dilute or entangled regime, where the relaxation time depends on the concentration. For instance, in the unentangled semi-dilute regime, the relaxation time scales as $\lambda_s \propto \frac{c}{c_*^{\frac{2-3v}{3v-1}}}$ where v is the excluded volume scaling exponent and c_* is the overlap concentration [224, 225]. Furthermore, at any concentration, the relaxation time of the rhamnolipid biosurfactant is larger than that of CTAB due to the higher molecular weight of the former surfactant than the latter one. This trend, i.e., increase in the relaxation time with the molecular weight, can also be seen from the expression of the Zimm relaxation time (although it is valid in the dilute regime) as [2, 226] $\lambda_z = \frac{F[\eta]M_w\eta_s}{RT}$, where F is a parameter which depends on the excluded volume scaling exponent v , $[\eta]$ is the intrinsic viscosity, M_w is the molecular weight, R is the universal gas constant and T is the absolute temperature.

4.1.6 Capillary thinning and pinch-off dynamics by DoS rheometry

The rheological phenomena under an extensional flow field differ from those in the shear flow field. Investigating the extensional property of a material is very important for its use in various applications, such as jetting, coating, spinning, spraying, etc. [227, 228].

In this study, we have used the DoS rheometry protocol to investigate the capillary thinning and pinch-off dynamics of both surfactants at various concentrations. The DoS rheometry setup is shown in Fig. 3.6, and its working principle is already explained in sub-section 2.3. The representative images of different filament shapes during the capillary-thinning process at a time interval of $\Delta t = 0.3$ ms are presented in Fig. 4.10 for both surfactants. This figure shows that both the neck thinning and pinching rates seem to be visually comparable for both surfactants. A slender cylindrical liquid filament is formed, and a small head bead appears at the end in both cases. The corresponding temporal evaluation of the filament radius is displayed in Fig. 4.11. It suggests that both surfactants show qualitatively similar behavior in the temporal evaluation of the

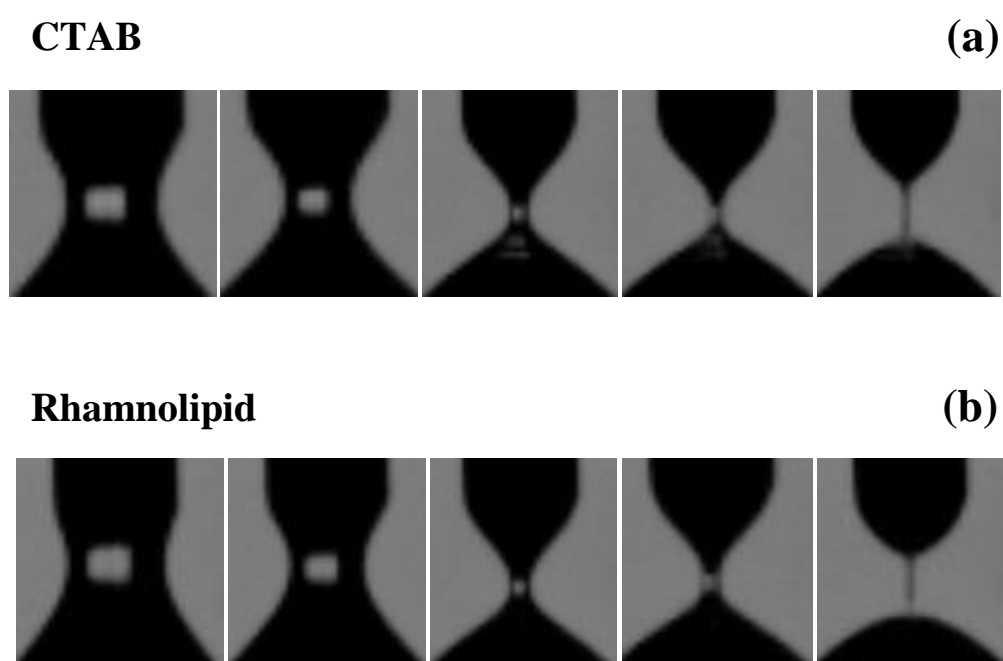


Figure 4.10: Representation of different filament shapes and pinch-off obtained using the dripping-onto-substrate (DoS) method at different times for (a) CTAB and (b) rhamnolipid surfactants at 1 wt.% concentration.

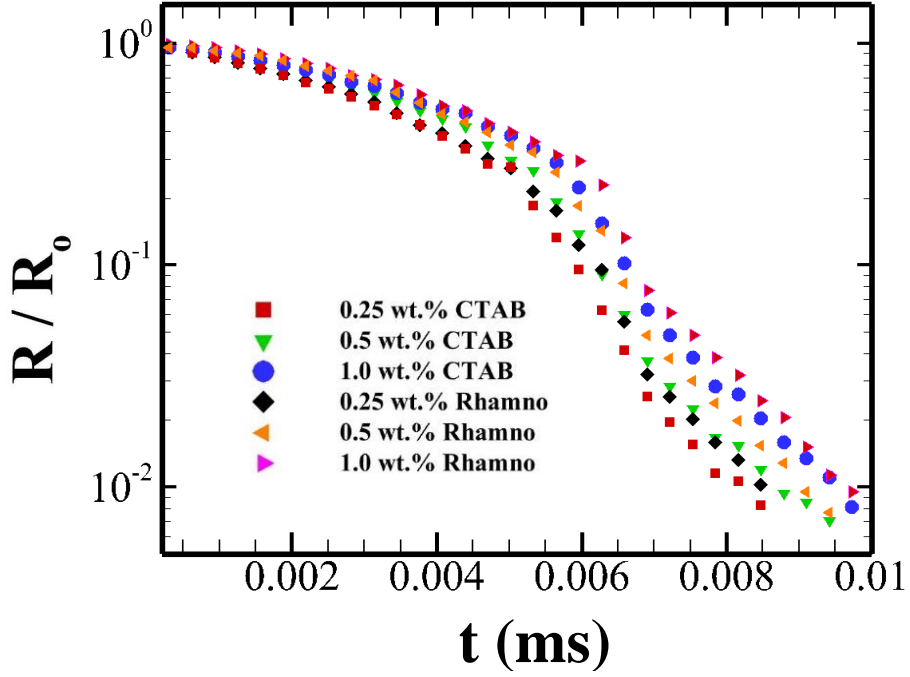


Figure 4.11: Evaluation of radius as a function of time for CTAB and Rhamnolipid surfactant at different concentrations. The plot displayed how the pinch-off time shifted as the surfactant concentration increased.

filament radius. On increasing the surfactant concentration, the pinch-off time is delayed regardless of the surfactant type. This is due to an increase in the formation of viscoelastic network structure with the surfactant concentration, which was also observed in previous studies [190]. Rhamnolipid shows more delay in the pinching off than CTAB due to the former surfactant's higher molecular weight and complex molecular architecture.

In Fig. 4.12, two different regimes are observed in the temporal evaluation of the filament radius: first is the inertia-capillary (IC) regime, where the balance between the inertia governs the thinning dynamics of the liquid filament originated due to the weight of the liquid drop and capillary forces. Second is the elasto-capillary (EC) regime, where the thinning dynamics of the liquid filament are governed by the balance between the fluid elasticity and capillary forces [191]. The transition between these two regimes happens at a time t_c , schematically shown by a dotted line in Fig. 4.12.

The evaluation of the filament radius in the IC regime can be expressed by the following equation [229]

$$\frac{R(t)}{R_0} = 0.8 \frac{(t_{ic} - t)^{2/3}}{t_R} \quad (4.3)$$

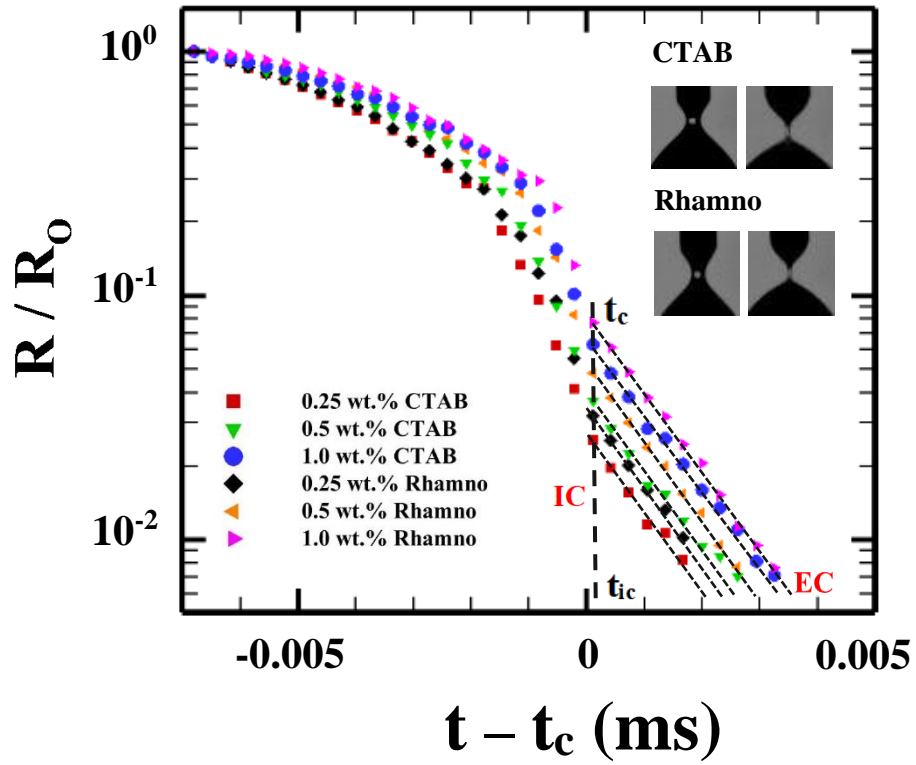


Figure 4.12: Filament radius evaluation plot as a function of time at different concentrations of CTAB and Rhamnolipid. Here the time axis is shifted with time t_c . This figure shows the presence of two regimes: one is the inertia-capillary regime (IC) before t_c and elasto-capillary regime (EC) after t_c .

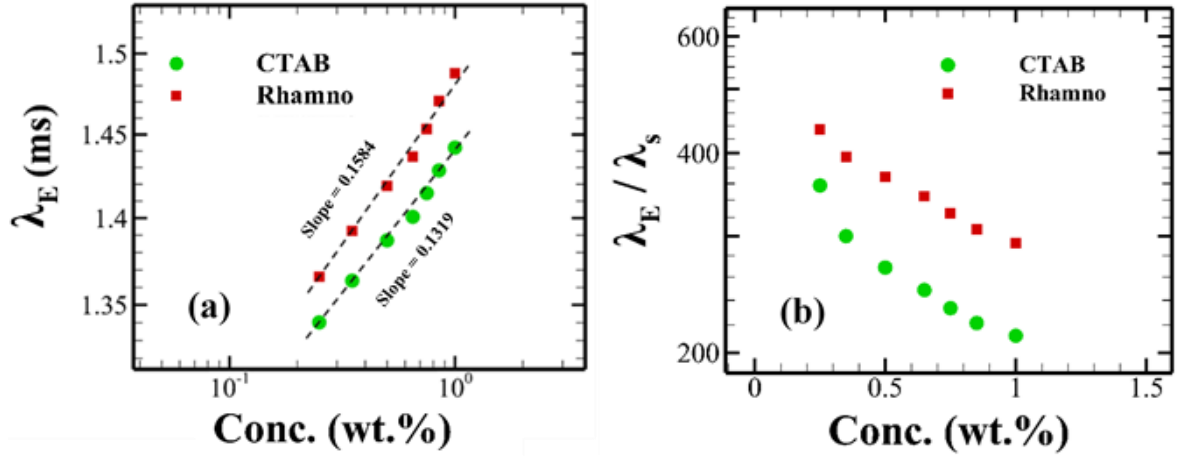


Figure 4.13: (a) Variation of the extensional relaxation time (λ_E) with the surfactant concentration. (b) Variation of the ratio of the extensional and shear relaxation times (λ_S) with the surfactant concentration.

Here R_0 represents the initial radius, t_{ic} is the pinch-off time, and t_R is the Rayleigh time ($t_R = \frac{(\rho R_0^3)^{1/2}}{\sigma}$), which is a characteristic time scale for the inertia-capillary regime. Here ρ and σ are the surfactant density and surface tension, respectively [230, 231]. On the other hand, in the elasto-capillary (EC) regime, the evaluation of the filament radius can be described by the following expression as proposed by Entov and Hinch [232],

$$\frac{R(t)}{R_0} = \frac{(R_0 G_E)^{1/3}}{2\sigma} \exp\left(\frac{-t}{3\lambda_E}\right) \quad (4.4)$$

Here G_E and λ_E are the extensional elastic modulus and extensional relaxation time, respectively. Note that the extensional modulus and extensional relaxation time values are different in magnitude from that of shear modulus and shear relaxation time for both surfactants. Both G_E and λ_E can be computed from the temporal evaluation of the filament radius in the EC regime. One can see that the temporal evaluation of the filament radius in the EC regime shows a linear trend in a semi-log plot. Furthermore, it shows less concentration dependence in the IC regime than in the EC regime. This is because elastic effects become important in the EC regime, and in this regime, different molecular-scale phenomena such as micelles stretching and orientation happen that contribute to the origin of these elastic effects. These again strongly depend on the surfactant concentration. A similar observation was also reported in the experimental works of Dinic et al., and Nodoushan et al. [233, 234, 235, 236].

Figure 4.13(a) shows the variation of the extensional relaxation time λ_E as a function of surfactant concentration. The extensional relaxation time can be obtained by fitting Eq. 6 in the elasto-capillary regime. It can be seen that the extensional relaxation time strongly depends on the surfactant concentration regardless of the surfactant type. As the surfactant concentration increases, the extensional relaxation time also increases due to the formation of strong and long micelles and entanglement among them, which all together make the solution more viscoelastic in nature. Once again, the extensional relaxation time is higher for rhamnolipid than for CTAB because of the larger molecular weight of the former one than the latter one. We have found a linear relationship on a semi-log plot between the variation of the extensional relaxation time with the surfactant concentration. The corresponding slopes of the fitted lines are also mentioned in Fig. 4.13(a).

Figure 4.13(b) depicts the variation of the ratio of extensional (λ_E) to that of shear (λ_S) relaxation times. It can be seen that this ratio of two relaxation times decreases with the surfactant concentration irrespective of the surfactant type. A similar observation was seen in earlier studies by Nodoushan et al. [236], and Sachsenheimer et al. [237] for chemically derived surfactants. The reason behind this is as follows: in extensional flows, micelles align themselves with the flow and form a structure, which is known as the extension-induced structure (EIS) [236, 237]. This alignment of micelles actually increases the extensional relaxation time. However, as the surfactant concentration increases, the tendency to form this alignment of micelles due to this extension-induced structure gradually decreases due to the increase in the entanglement of the micellar network. Therefore, it eventually decreases the ratio of the relaxation times with the surfactant concentration.

The transient extensional viscosity η_E of both surfactant solutions is also reported in this work. It is computed from the elasto-capillary regime data after establishing a homogeneous extensional flow field within the liquid neck. The transient extensional viscosity is calculated using the following equation [191]

$$\eta_E = \frac{\sigma}{\dot{\epsilon}R} = \frac{\sigma}{-2dR(t)/dt} \quad (4.5)$$

where $\dot{\epsilon}$ is the extensional rate measured from the temporal evaluation of the filament radius in the EC regime. Figure 4.14 represents the variation of the transient extensional

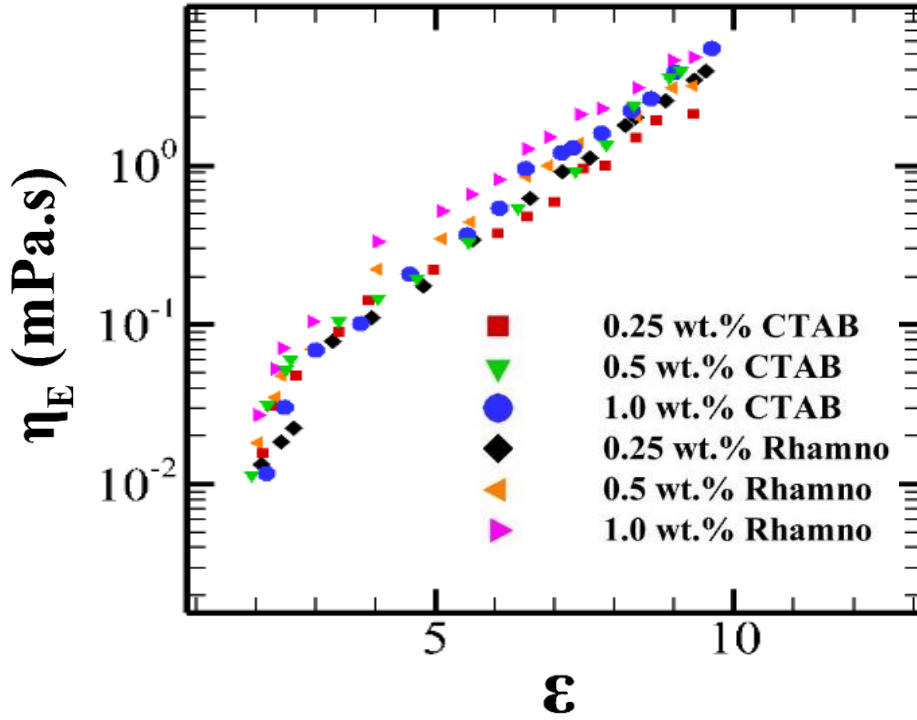


Figure 4.14: Extensional viscosity (η_E) as a function of Hencky strain (ϵ) for both surfactant at different concentrations.

viscosity (η_E) as a function of the Hencky strain ϵ ($= -2\ln \frac{R_0}{R(t)}$) at different surfactant concentrations, which is a standard procedure to represent the transient extensional viscosity. It can be seen that the extensional viscosity increases with the total accumulated strain, irrespective of the surfactant type and concentration. The variation in the transient extensional viscosity for both surfactant solutions appeared to be qualitatively similar. For a Newtonian fluid, the Trouton ratio (ratio of the extensional viscosity to that of the shear viscosity, $T_R = \frac{\eta_E}{\eta_S}$) is 3, whereas, for viscoelastic fluids, T_R value is higher than that seen for Newtonian fluids, often is of the order of $10^1 - 10^5$ [238]. For instance, the Trouton ratios for 0.25 wt.% of CTAB and Rhamnolipid are found to be 33.06 and 43.166, respectively, which are much greater than that seen for Newtonian fluids. These high values of the Trouton ratio indicate the presence of sufficient strain-hardening phenomena in both surfactant solutions. The tendency of this strain-hardening behaviour increases with the surfactant concentration regardless of the surfactant type due to the formation of a strong viscoelastic network structure. As the Trouton ratio is greater than one, the extensional viscosity is naturally always higher than the shear viscosity for all concentrations of surfactant solutions. This increase in the extensional viscosity with the

surfactant concentration also results in a significant delay in the filament breakup, as shown and discussed earlier.

Chapter 5

Pressure driven flows of wormlike micellar solutions past a single microcylinder confined in a channel

The introduction and literature survey on this particular problem is already presented in section 2.2 of chapter 2. This chapter presents and discusses the results in detail for this problem. In particular, this chapter delineates how the chain scission of wormlike micelles will influence the flow dynamics, particularly viscoelastic flow instabilities, during the flow past a single microcylinder confined in a microchannel.

5.1 Problem formulation

The problem considered herein is the study of the flow characteristics of a non-shear banding and incompressible wormlike micellar solution past a circular cylinder of diameter d confined symmetrically in a channel of height H in the creeping flow regime, as shown schematically in Fig. 5.1(a). A fixed value of the blockage ratio (BR) (defined as the ratio of the cylinder diameter to the channel height, i.e., d/H) of 0.67 is considered here. The inlet and outlet lengths of the channel are fixed at $40d$, Fig. 5.1(a). Furthermore, the wormlike micelles are modeled here using the VCM model, as written and discussed in section 3.1.1 of chapter 3. According to this model, the micelles are considered an elastically active network dispersed uniformly in an incompressible Newtonian solvent. Once the flow is initiated, this network strand starts to deform, break, and simultaneously reform, and hence, the resulting motion becomes completely non-linear.

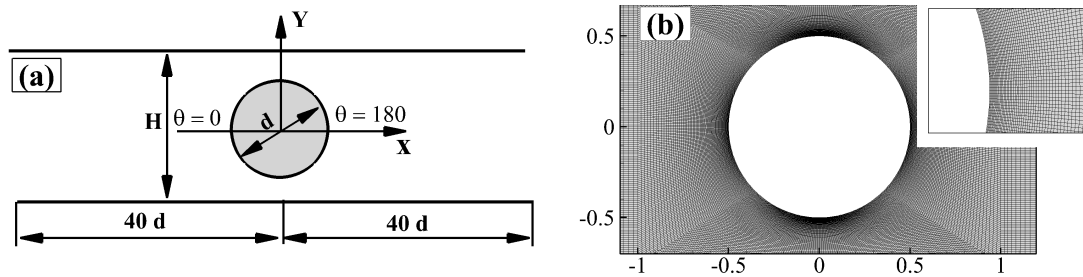


Figure 5.1: (a) Schematic of the present problem (b) A typical mesh used in the present study with a zoomed view near the cylinder surface.

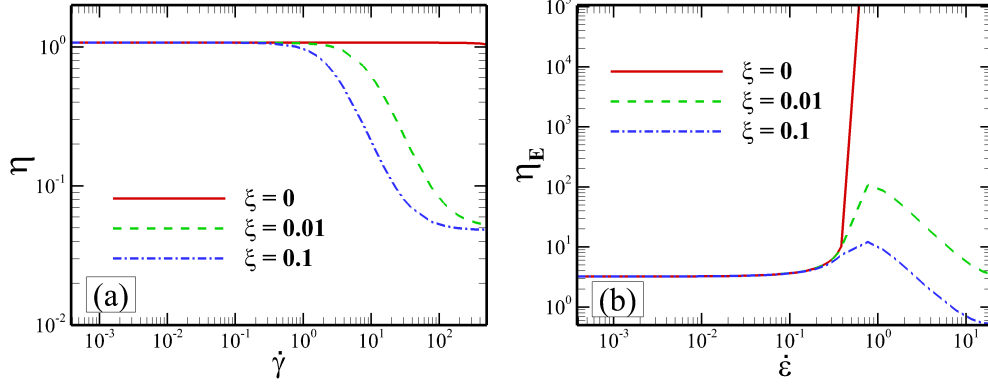


Figure 5.2: (a) Variation of the non-dimensional shear viscosity versus the shear rate in homogeneous shear flow (b) Variation of the non-dimensional extensional viscosity versus the extensional rate in homogeneous planar extensional flow.

Boundary	Velocity	Pressure	Chain number density	Conformation tensor
Inlet	$U_X = 1, U_Y = U_Z = 0$	$\frac{\partial P}{\partial n} = 0$	$n_A = 1, n_B = \sqrt{2C_{Aeq}/C_{Beq}}$	$A = (1 \ 0 \ 0 \ 1 \ 0 \ 1)$ $B = (\phi \ 0 \ 0 \ \phi \ 0 \ \phi)$ where $\phi = n_B/2$
Outlet	$\frac{\partial U}{\partial n} = 0$	$P = 0$	$\frac{\partial n_A}{\partial n} = \frac{\partial n_B}{\partial n} = 0$	$\frac{\partial A}{\partial n} = \frac{\partial B}{\partial n} = 0$
Solid wall	$U_X = U_Y = U_Z = 0$	$\frac{\partial P}{\partial n} = 0$	$\frac{\partial n_A}{\partial n} = \frac{\partial n_B}{\partial n} = 0$	$\frac{\partial A}{\partial n} = \frac{\partial B}{\partial n} = 0$

Table 5.1: Boundary conditions for the present computation domain

5.2 Numerical solution procedure and its validation

The details of the governing and VCM constitutive equations and their numerical solution techniques have already been presented in subsections 3.1.1 and 3.1.3 of chapter 3. The appropriate boundary conditions employed here are presented (in their non-dimensional forms) in Table 5.1. Three different grid densities with a different number of cells on the cylinder surface and in the whole computational domain were created. A grid consisting of 58800 hexahedral cells (with 480 grid points on the cylinder surface and a grid spacing of $\Delta X = 0.00654$) was found to be adequate to capture the flow physics for the whole range of conditions encompassed here. This was confirmed by performing simulations with a higher grid density (almost double) than those selected in the present study, and the results (in terms of the time-averaged drag and lift forces acting on the cylinder as well as the temporal variation of velocity and stress) were almost indistinguishable from each other. A typical mesh used in the present study is shown in Fig. 5.1(b) with a zoomed

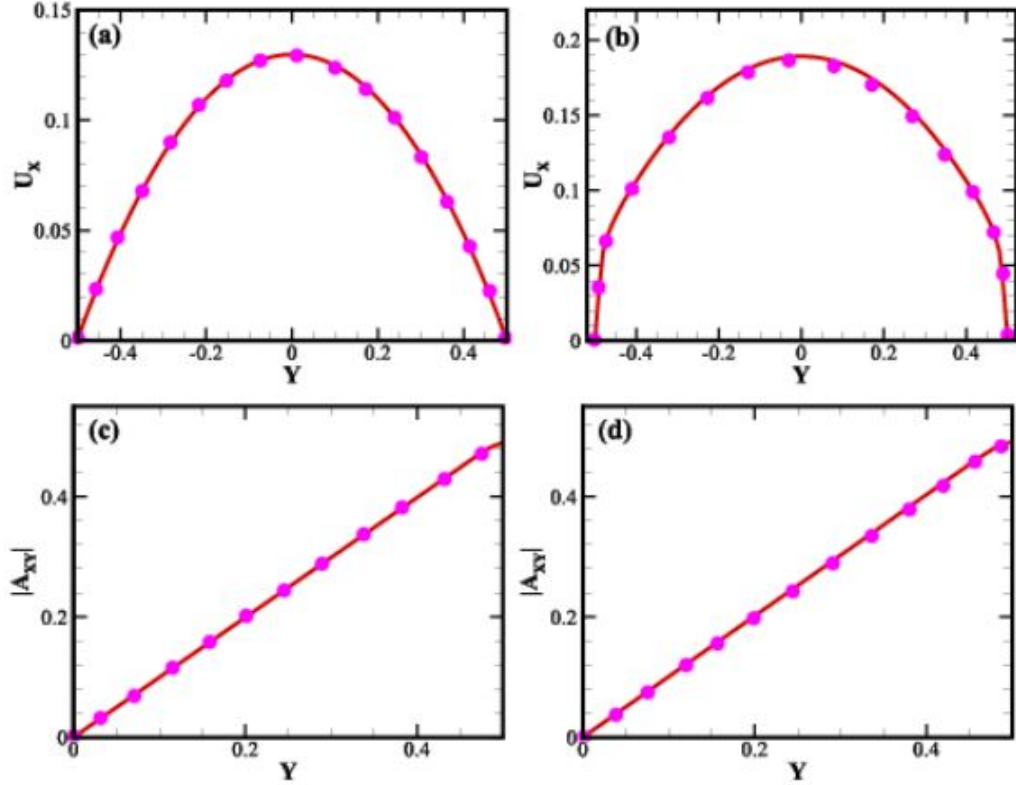


Figure 5.3: Comparison between the present results (lines) and the results of Cromer et al. [239] (symbols) for the flow of a wormlike micellar solution through a straight microchannel at a non-dimensional pressure gradient of $P = 1$. Non-dimensional streamwise velocity at (a) $= 10^{-3}$ and (b) $= 10^{-1}$. The magnitude of the non-dimensional conformational tensor component of the long chain A at two different non-dimensional values of the diffusivity parameter, namely, (c) $D = 10^{-3}$ and (d) $D = 10^{-1}$. Other non-dimensional VCM parameters are: $\beta = 7 \times 10^{-5}$, $\mu = 1.9$, $c_{Aeq} = 0.9$, $c_{Beq} = 1.4$, $\epsilon = 6.27 \times 10^{-4}$, $\xi = 0.3$.

view near the cylinder surface. After fixing the grid density, the present numerical setup was validated against the results of Cromer et al. [239] for the pressure-driven flow of a wormlike micellar solution through a straight microchannel, and an excellent agreement was found between the two results, Fig. 5.3. The normalization scheme for velocity, stress, and time with the definition of Weissenberg number is discussed in subsections 3.1.1 of chapter 3.

5.3 Results and discussion

At the outset, the results for a Newtonian fluid are presented to show how the rheological complexity of a wormlike micellar can influence the flow characteristics in this benchmark system under otherwise identical conditions. As expected, for a Newtonian fluid, the streamlines remain attached to the cylinder surface, and perfect fore-aft symmetry is seen to be present (Fig. 5.4). This aligns with the experimental results of Zhao et al. [86]. We next present the results for a wormlike micellar solution with the non-linear VCM model parameter $\xi = 0$, i.e., without breakage and reformation. In this limit, the VCM constitutive model would tend to behave as two uncoupled upper convective Maxwell (UCM) models [88]. For this limiting case, the simulations were run up to the Weissenberg number of 0.51, and beyond this value, the convergence became difficult, in line with the findings of others [81]. Figure 5.5(a) shows the variation of the stream-wise velocity U_x (non-dimensionalized with the mean inlet velocity U_{in}) along the mid-plane both upstream and downstream of the cylinder and both for Newtonian and VCM fluids for two values of the Weissenberg number, namely, 0.29 and 0.4. Once again, a perfect symmetry in the velocity field is seen for a Newtonian fluid. For the VCM fluid, the symmetry is gradually destroyed as the value of the Weissenberg number progressively increases. Furthermore, a downward velocity shifting with the Weissenberg number is seen upstream and downstream of the cylinder. This observation also aligns with that seen earlier for the UCM fluids [81]. At $Wi = 0.445$, a purely elastic instability appears for the VCM fluid with $\xi = 0$, and due to this, the fore-aft symmetry in the streamline profiles is destroyed, see Fig. 5.4 (b). The emergence of the elastic instability at this Weissenberg number is further confirmed by plotting the temporal variation of the stream-wise velocity at a position near the rear stagnation point of the cylinder at two values of the Weissenberg

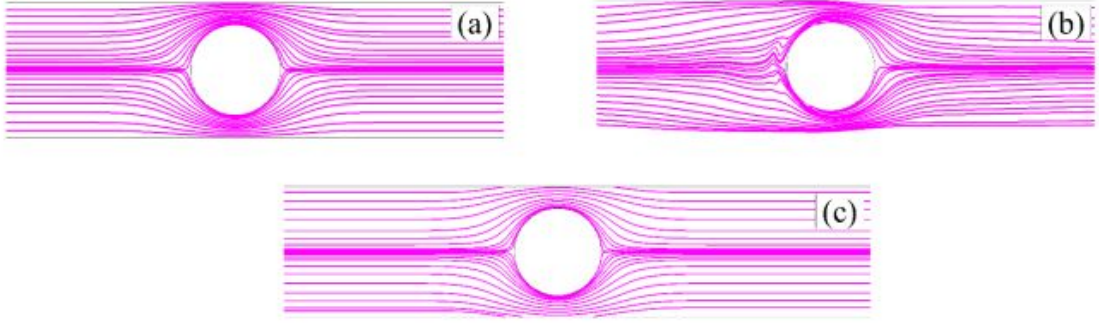


Figure 5.4: Representative of streamline profiles (a) Newtonian fluid (b) WLM solution, $\xi = 0$, $Wi = 0.445$, (c) $\xi = 0.01$, $Wi = 0.001$.

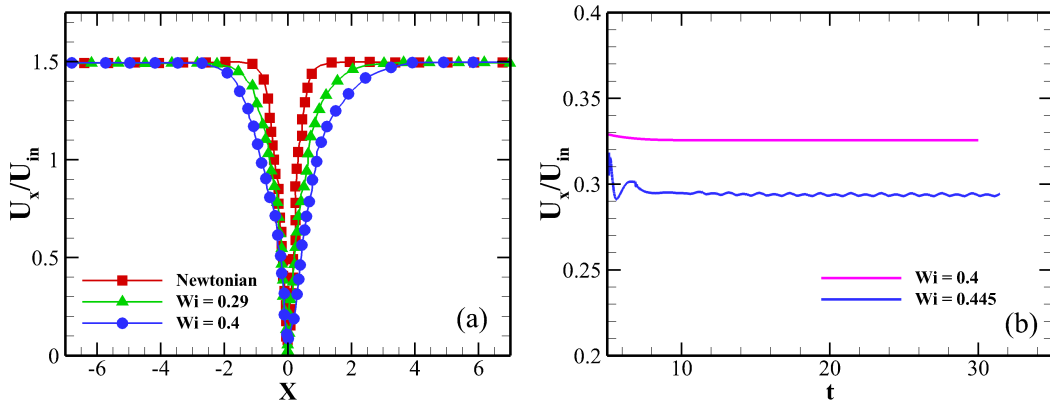


Figure 5.5: (a) Variation of the non-dimensionalized stream-wise velocity both for Newtonian and VCM fluids upstream and downstream mid-plane of the cylinder (b) Temporal variation of the stream-wise velocity at a point downstream of the cylinder for VCM fluids at two different values of the Weissenberg number.

number, namely, 0.4 and 0.445, in sub-Fig. 5.5(b). It is seen that the velocity attains a steady value with time for $Wi = 0.4$, whereas it fluctuates at $Wi = 0.445$. The range of the Weissenberg number at which this instability appears corresponds well with the earlier studies carried out for the UCM fluids [240, 241].

5.3.1 Hydrodynamics

We now focus on analyzing the flow characteristics at finite values of ξ wherein the breakage and reformation dynamics of the micelles are important. To do so, simulations were run for the Weissenberg number ranging from 0.001 to 3 for three values of ξ , namely, 0.01, 0.05, and 0.1. Figure 5.6 shows the streamline profiles at two values of the Weissenberg number, namely, 0.5 and 2.5, and for two values of ξ , namely, 0.01 and 0.1.

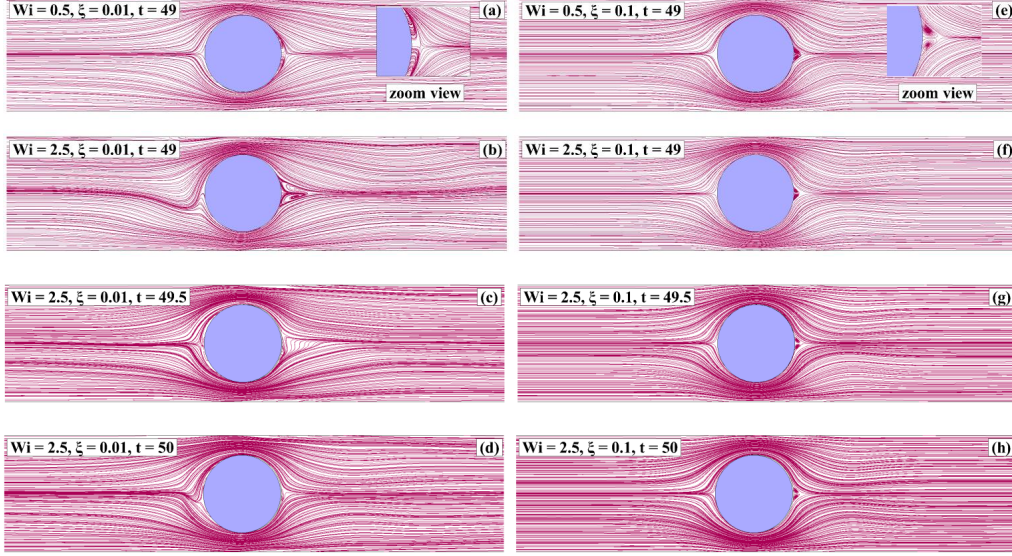


Figure 5.6: Representative streamline patterns at various values of the Weissenberg number and for two values of the non-linear VCM model parameter ξ , namely, 0.01 and 0.1.

A similar trend of streamline profiles was observed at a very low value of the Weissenberg number of 0.0001 as that seen for a Newtonian fluid due to a negligible effect of its non-Newtonian behaviour (Fig. 5.4(c)). However, as the value of Wi increases, say to 0.5, one can clearly see the differences in the streamline profiles for WLM solutions compared to that seen for Newtonian and WLM solutions at low values of the Weissenberg number. At this combination of Wi and ξ , the symmetry along the vertical mid-plane passing through the origin disappears, but the horizontal mid-plane symmetry still exists, see sub-Fig. 5.6(a) for $\xi = 0.01$ and sub-Fig. 5.6(e) for $\xi = 0.1$. Furthermore, two small vortices of equal size and shape are formed downstream of the cylinder, as seen in the zoomed figure. Note that the flow is still steady and laminar up to this value of the Weissenberg number regardless of the value of ξ .

On further increasing the Weissenberg number to 2.5, the horizontal mid-plane symmetry at $Y = 0$ in the streamline profiles still exists for WLM solutions with $\xi = 0.1$; for instance, see sub-Fig. 5.6(f) or (g) or (h). Furthermore, the flow remains steady, as can be seen from the streamline profiles, which are indistinguishable at three different times. However, no symmetry is present in the streamline profiles for wormlike micellar solutions with $\xi = 0.01$. At this value of ξ , the streamlines start to distort, particularly near the

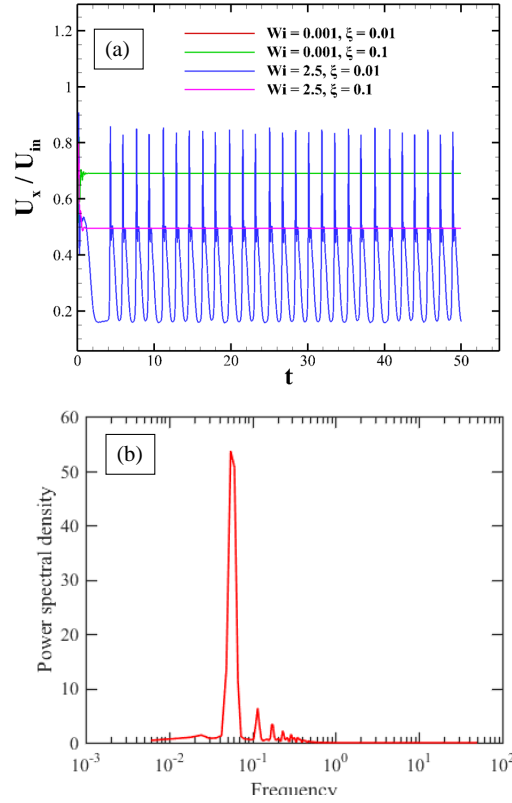


Figure 5.7: (a) Temporal variation of X-component velocity at a position near to the front stagnation point (b) Power spectral density plot of the temporal variation of X-component velocity at $Wi = 2.5$ and $\xi = 0.01$.

cylinder's front and rear stagnation points, sub-Figs. 5.6(b), (c), and (d). Furthermore, the flow becomes unsteady at this value of ξ as the flow pattern becomes time-dependent, which is also evident in the streamline plots. In addition to the distortion of streamlines, small vortex regions are also formed both upstream and downstream of the cylinder near the stagnation points. The size and shape of these stagnant zones vary with time, and sometimes they completely disappear. All these flow characteristics suggest that elastic instability appears in the flow at these values of the Weissenberg number and non-linear VCM model parameter ξ . The instability is seen to be initiated upstream of the cylinder, which is in line with that observed experimentally [86, 87]. However, it should be mentioned here that the range of the Weissenberg number was higher in these experiments than the values used here. The unsteadiness in the flow is further confirmed by plotting the X-component velocity at a point ($X = -0.75d$, $Y = 0$) near the front stagnation point of the cylinder for two values of the Weissenberg number, namely, 0.001 and 2.5, Fig. 5.7(a). In this figure, the velocity reaches a steady state value with time for $Wi = 0.001$ regardless of the value of ξ . On the other hand, at $Wi = 2.5$, the velocity

again reaches a steady state value with time for $\xi = 0.1$, but it fluctuates and becomes time-dependent for $\xi = 0.01$. The nature of this unsteadiness is further examined by plotting the power spectral density of the temporal variation of the X-velocity component in Fig. 5.7(b). It is seen that a single fundamental dominant frequency governs the velocity fluctuation in the power spectrum plot. This suggests that the flow seems to reach a quasi-periodic state at these values of the Weissenberg number and non-linear VCM model parameter ξ .

Next, we explored the reasons for this elastic instability and why the onset of this instability is facilitated by the decreasing value of ξ for a wormlike micellar solution. This can be explained, at least, qualitatively as follows: as pointed out earlier, the physical significance of ξ is that the higher the value of this parameter, the lower the stress or stretch (or scission energy) needed to break the micelles. As the micelles reach the front stagnation point of the cylinder ($\theta = 0$), they gradually stretch as they travel along the cylinder surface towards the rear stagnation point ($\theta = 180$) due to a strong shearing motion in this region. At higher values of ξ , for instance, at $\xi = 0.1$ used in this study, the long micelles tend to easily break into smaller micelles during their movement, even at a very low flow strength, as they are easier to break. For this reason, the energy stored during the stretching of the micelles is released during the breakdown of the micelles, and it happens before the stretching of the micelles could trigger the onset of elastic instability. With the decreasing values of ξ , the maximum extent up to which the micelles can be stretched gradually increases, and it also becomes progressively difficult to break the micelles. This results in an increase in both the stream-wise and span-wise normal stresses in both the upstream and downstream regions of the cylinder. This eventually leads to elastic instability. This is further confirmed in Fig. 5.8 wherein the temporal variation of the span-wise normal stress component $\tau_{w,YY}$ at a point near the front stagnation point of the cylinder is plotted for two values of ξ , namely, 0.1 and 0.01 at a fixed value of $Wi = 2.5$. In this figure, the normal stress component becomes time-dependent and also higher in magnitude for the WLM solution with $\xi = 0.01$ compared to that of a steady value seen with $\xi = 0.1$.

To add further weight to the preceding explanation, we analyze the extension rate ($\dot{\epsilon}_{XX}$) along the mid-plane downstream of the cylinder at $Wi = 2.0$ and $\xi = 0.01$ (sub-Fig. 5.9(a)). This is similar to the calculation by Moss and Rothstein [84]. The extension

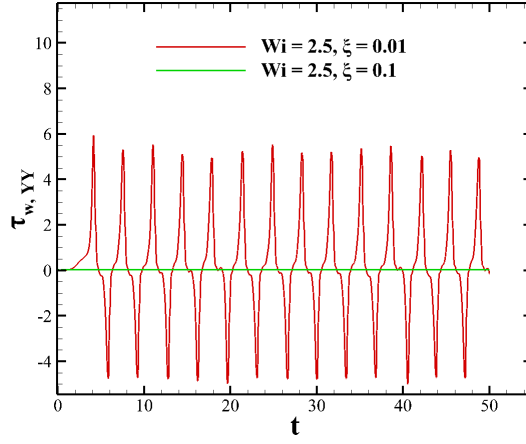


Figure 5.8: Temporal variation of the normal stress component $\tau_{w,YY}$.

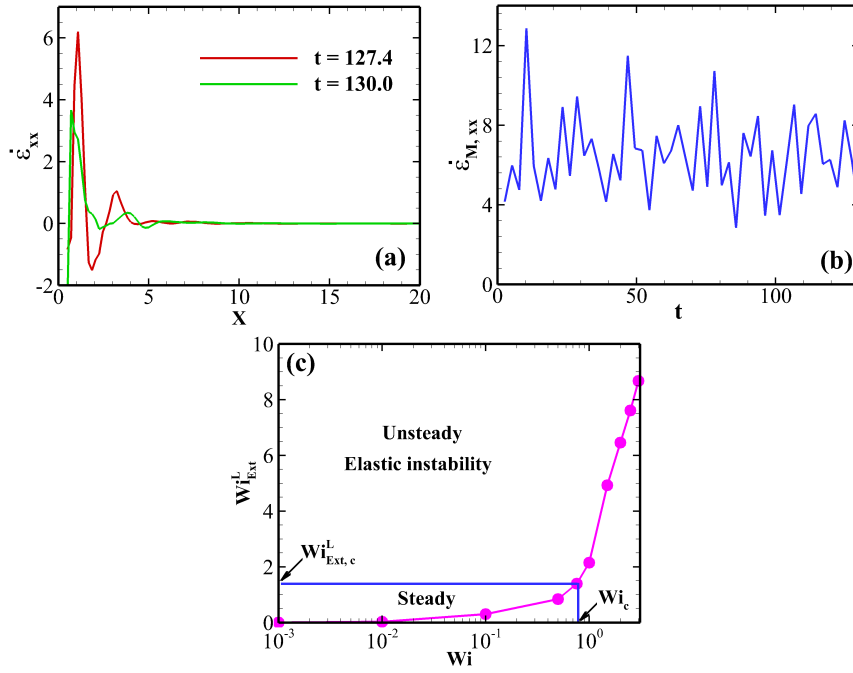


Figure 5.9: (a) Variation of extension rate ($\dot{\epsilon}_{XX}$) along the mid-plane downstream of the cylinder at $Wi = 2.0$ at two different times (b) Temporal variation of the maximum extension rate ($\dot{\epsilon}_M$) downstream of the cylinder at $Wi = 2.0$ (c) Variation of the local extensional Weissenberg number (Wi_{Ext}^L) with the Weissenberg number

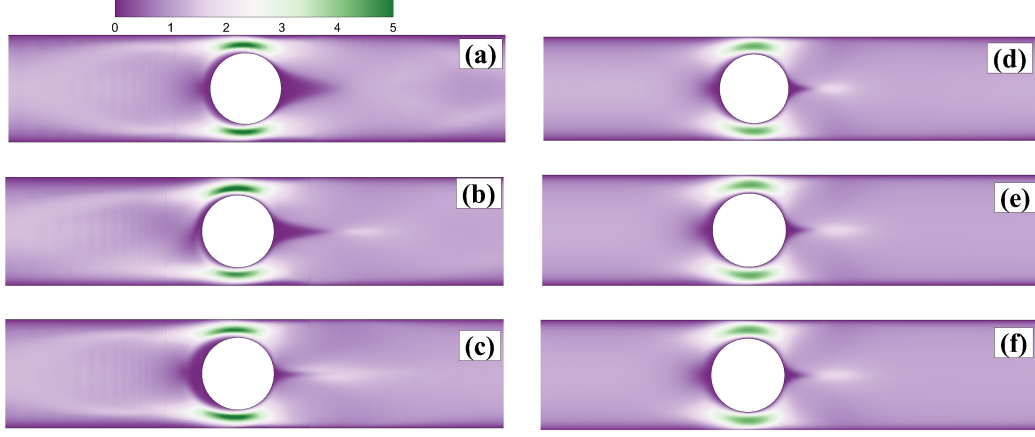


Figure 5.10: Velocity magnitude plot (a) $Wi = 1.5, \xi = 0.01, t = 49$ (b) $Wi = 2.5, \xi = 0.01, t = 49.1$ (c) $Wi = 2.5, \xi = 0.01, t = 50$ (d) $Wi = 1.5, \xi = 0.1, t = 49$ (e) $Wi = 2.5, \xi = 0.1, t = 49.1$ (f) $Wi = 2.5, \xi = 0.1, t = 50$.

rate is seen to be maximum near the rear stagnation point of the cylinder and time-dependent, which gradually becomes zero far away from the cylinder. The temporal variation of this local maximum extension rate ($\dot{\epsilon}_{M,XX}$) is plotted in sub-Fig. 5.9(b). We now define a local extensional Weissenberg number based on the time-averaged value of this local maximum extension rate, i.e., $Wi_{Ext}^L = \lambda_{eff} \dot{\epsilon}_{M,XX}$ and its variation with the global Weissenberg number is shown in sub-Fig. 5.9(c). One can see that the value of such a local extensional Weissenberg number gradually increases with the global Weissenberg number due to the increase in the extension rate. The flow becomes unsteady when the value of Wi_{Ext}^L (or the value of the global Weissenberg number is nearly equal to 0.76) becomes at around 1.41, which is indicated in sub-Fig. 5.9(c). Calculating the local extensional Weissenberg number has also been used in the experiments of a falling sphere in wormlike micellar solutions [114, 242] to explain the onset of the elastic instability.

Fig. 5.10 shows the velocity magnitude (non-dimensionalized with the inlet velocity, U_{in}) plot at various values of the Weissenberg number and two values of ξ , namely, 0.01 and 0.1. Similar to the streamline profiles, there is a fore-aft symmetry present in the velocity magnitude plot both for Newtonian fluids and wormlike micellar solution at a low Weissenberg number of $Wi = 0.001$ (Figs. 5.11 (a) and (b)). In line with the overall mass balance, the magnitude of the velocity is always higher in the narrow gap between the cylinder and channel walls, irrespective of the fluid type.

At higher Wi , say to 1.5, the symmetry in the velocity magnitude plot along the vertical mid-plane passing through the origin is destroyed. However, the horizontal symmetry

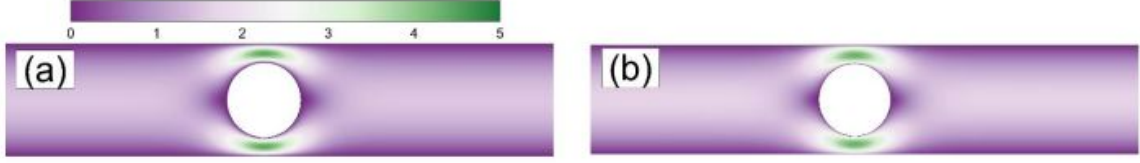


Figure 5.11: Velocity magnitude plots (a) Newtonian fluid (b) WLM solution, $\xi = 0.01$, $Wi = 0.001$.

still persists both for $\xi = 0.01$ (sub-Fig. 5.10(a)) and 0.1 (sub-Fig. 5.10(d)). Furthermore, as discussed above, a conical-shaped region of almost zero velocity magnitude is formed due to the formation of vortices for the WLM solution. On further increasing the Weissenberg number to 2.5, the vertical symmetry at $Y = 0$ in the velocity magnitude plot still exists for the micellar solution with $\xi = 0.1$. However, the horizontal and vertical symmetries disappear for the WLM solution with $\xi = 0.01$. Moreover, at these values of the Weissenberg number and non-linear VCM model parameter ξ , the magnitude of the velocity is seen to be higher in the upper gap region between the cylinder and upper channel walls, sub-Fig. 5.10(b) at time $t = 49.1$, whereas at a later time of $t = 50$, it is seen to be higher in the lower gap region between the cylinder and lower channel walls, sub-Fig. 5.10(c). This suggests that the highest velocity magnitude zone region changes its position with time between these two gap regions. This temporal shifting of the higher velocity magnitude zone has also recently been observed in the experiments of Haward et al. [87] and in the numerical simulations of Varchanis et al. [108] dealing with polymer solutions. Therefore, one would expect the cross-correlation function (CCF) of either the stream-wise or cross-stream velocity component at these two locations to be highly anti-correlated. Indeed, the cross-correlation function of the stream-wise velocity component at two locations, namely, one at $X = 0$, $Y = 0.626$ (upper gap region) and another at $X = 0$, $Y = -0.625$ (lower gap region), are shown in Fig. 5.12. The stream-wise velocity components at these two locations are highly anti-correlated.

This behaviour is explained as follows: when the flow becomes quasi-periodic, the stresses generated due to wormlike micelles in the solution also oscillate and become periodic, as shown in Fig. 5.8. At any instant of time, when the normal stress is higher in the upward direction, it then exerts a force normal to the flow in the upward direction, which in turn, forces the fluid to pass through the lower gap region with a higher velocity

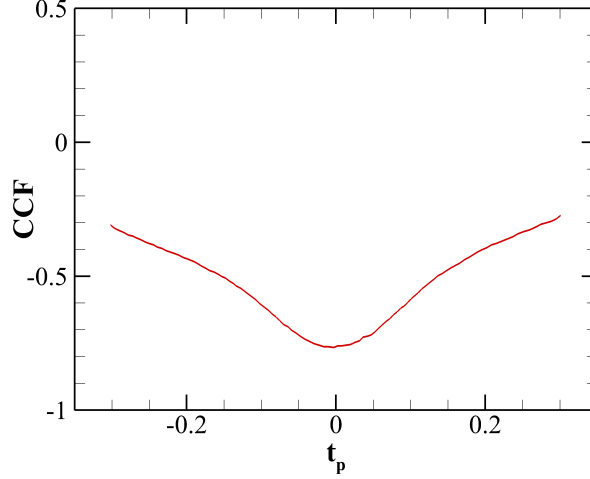


Figure 5.12: Cross-correlation function plot for the X-component velocity at two locations, one at the upper gap region and another at the lower gap region of the channel.

magnitude to satisfy the mass conservation principle. This higher velocity region drags and stretches the micelles more in the downward direction, resulting in the stress component being higher in the downward direction at the next moment. This stress component again produces a force normal to the flow in the downward direction (negative Y direction). As a result, the higher velocity magnitude zone will be shifted to the upper gap region.

This continuous shifting of the higher velocity magnitude zone between the upper and lower gap regions generates a wave in the flow structure downstream of the cylinder. This is known as the 'elastic wave', which has been recently observed in experiments dealing with polymer solutions [106, 243, 244]. We calculated the speed of this elastic wave propagation downstream of the cylinder by calculating the cross-correlation function of the stream-wise velocity at two different locations in the flow domain. If the two observation points are separated by a distance Δx , there is a peak shift (or lag) time t_p in the cross-correlation function between the two points. The elastic wave speed can be calculated as $e_v = e'_v \lambda_{eff} / d = \lambda_{eff} / d \left(U_{in} + \frac{\Delta x}{t_p} \right)$. The variation of the non-dimensional values of the elastic wave speed with the Weissenberg number is shown in Fig. 5.13 as symbols, whereas a power-law fit of the data in the form of $e_v = C_1 Wi^{C_2}$ with $C_1 = 2.51$ and $C_2 = 0.92$ is also shown as a line. This figure shows that the elastic wave speed increases non-linearly with the Weissenberg number as seen in polymer solutions [106, 243].

To visualize the wavy nature of the flow field due to the propagation of this elastic

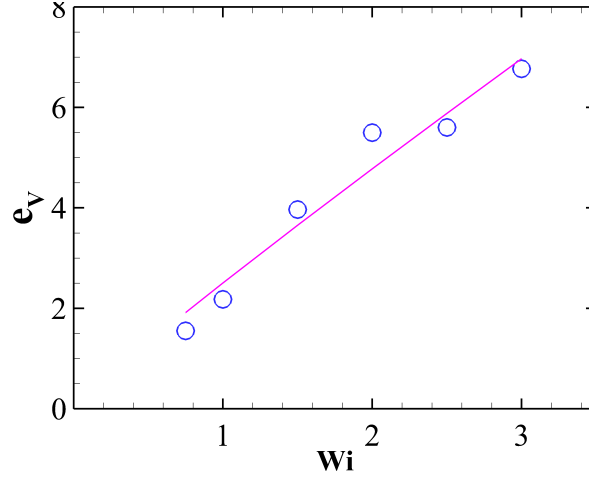


Figure 5.13: Variation of the elastic wave speed with the Weissenberg number. Here the results are presented for the non-linear VCM model parameter $\xi = 0.01$.

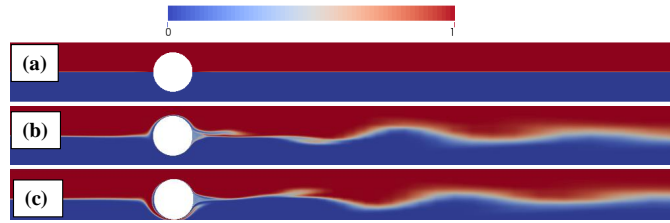


Figure 5.14: Variation of dye concentration at (a) $t = 0$ (b) $t = 35.0$ and (c) $t = 35.7$.

wave downstream of the cylinder, a dye with a finite concentration in the upper horizontal half of the channel and a zero concentration in the lower half of the channel is introduced as shown in Fig. 5.14(a) at $t = 0$. After that, a convective-diffusive mass transfer equation was solved for the variation of the dye concentration along with the continuity, momentum, and constitutive equations. A wavy flow field can be clearly seen in sub-Figs. 5.14(b) and (c) at two different times for the wormlike micellar solution with $\xi = 0.01$. In addition to the emergence of this elastic wave, the shifting of the fluid from the mid-horizontal plane in the upward (sub-Fig. 5.14(b)) and downward directions (sub-Fig. 5.14(c)) is also evident in the front stagnation region of the cylinder in the same figure. This study, for the first time, provides evidence of the existence of such an elastic wave in a wormlike micellar solution which has recently been seen in polymer solutions in the creeping flow regime [106, 243].

5.3.2 Variation of micellar concentration and principal stress difference

One of the main features of a WLM solution is the breakage and reformation of the micelles. The distribution of micelle concentration within a flow system will help our understanding of the flow physics like the elastic instability discussed in the preceding section and the variation of the principal stress differences, which will be defined and discussed later in this section, Figure 5.15.

At very low Weissenberg numbers, such as 0.001, the distribution of the long chain density is almost uniform throughout the whole system regardless of the value of ξ due to a very low flow strength. As the value of Wi increases says to 0.5, the distribution becomes non-uniform within the system (sub-Figs. 5.16 (c) and (d)). However, the non-homogeneity in the distribution of long chains is more pronounced in the case of the WLM solution with $\xi = 0.1$ than that seen with $\xi = 0.01$ as the former is easier to break than in the latter case. Irrespective of the values of Wi and ξ , the long chain number density is always lower in the vicinity of the cylinder and the gap regions between the cylinder and channel walls. This is due to the high shearing fluid motion in these regions, which causes the breakage of many long micelles. Furthermore, with the increasing Weissenberg number, the non-uniformity in the distribution of the long chain number density extends more downstream of the cylinder along the mid-plane of the channel and near the channel walls, see sub-Fig. 5.15(c) or (d). This is so simply because of the strong extensional flow field in this region, whose strength increases with the increasing Weissenberg number.

The principal stress difference (PSD) is defined as $\sqrt{(\tau_{w,XX} - \tau_{w,YY})^2 + 4\tau_{w,XY}^2}$ where $\tau_{w,XX}$ and $\tau_{w,YY}$ are the normal stress components in X and Y directions respectively and $\tau_{w,XY}$ is the shearing component. It provides useful information on the alignment and stretching of micelles, and it is directly related to the flow-induced birefringence (Δn) pattern, which can be measured experimentally. In particular, for a material that follows the stress-optical rule, the principal stress difference is directly proportional to the flow-induced birefringence (FIB) through the relation $\Delta\sigma = \Delta n/C$ where C is the stress-optical coefficient. At very low Weissenberg numbers, for instance, at $Wi = 0.001$, the principal stress difference is maximum near the cylinder and channel walls in the gap regions. In contrast, it is almost zero at the front and rear stagnation regions; for

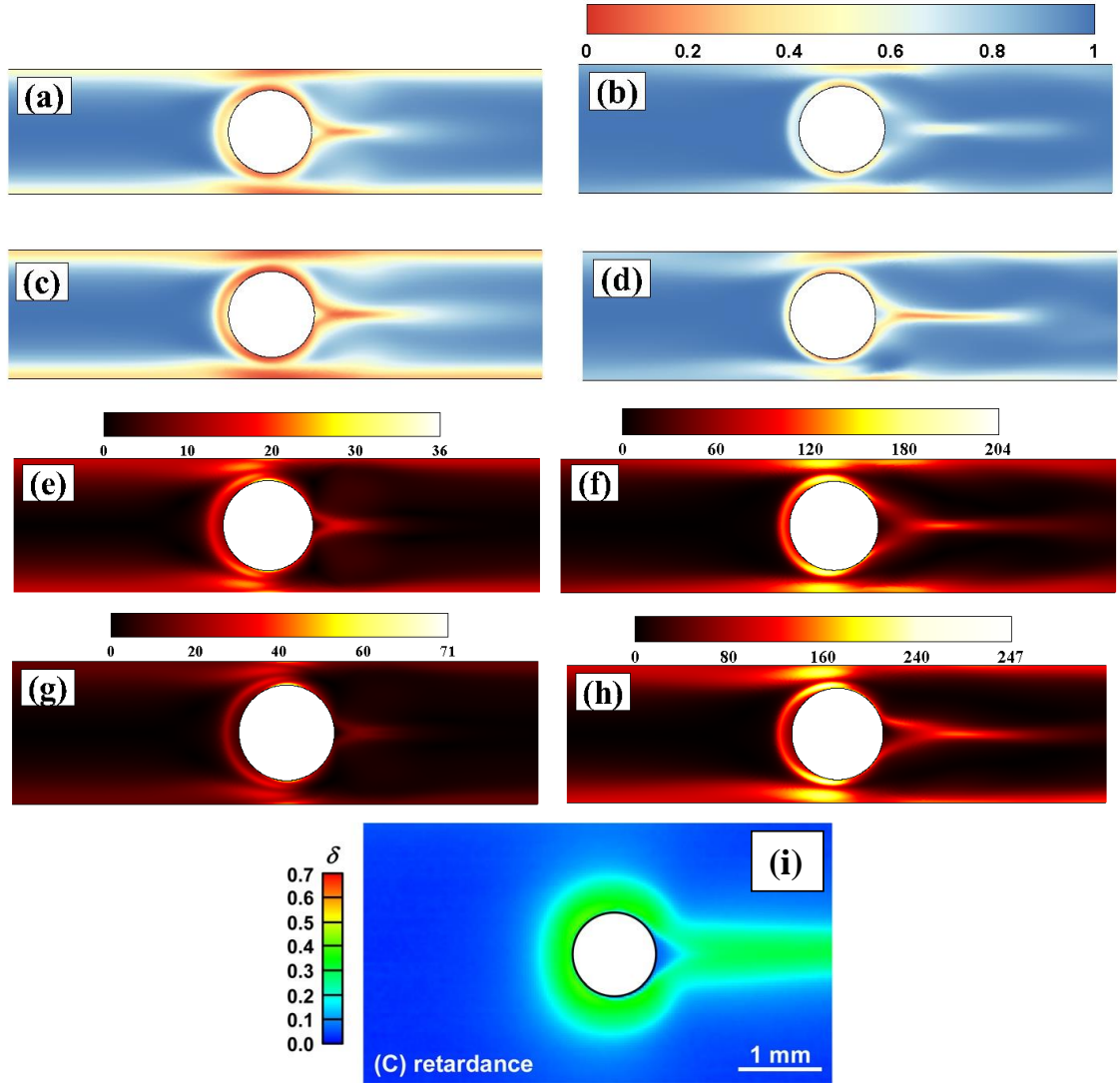


Figure 5.15: Distribution of the long chain number density (a-d) and principal stress difference (e-h). (a,e) $Wi = 1.5, \xi = 0.1$ (b,f) $Wi = 1.5, \xi = 0.01$ (c,g) $Wi = 2.5, \xi = 0.1$ (d,h) $Wi = 2.5, \xi = 0.01$. (i) Flow-induced birefringence image taken in the experiments of Sun and Huang [245] at $Wi = 1.48$.

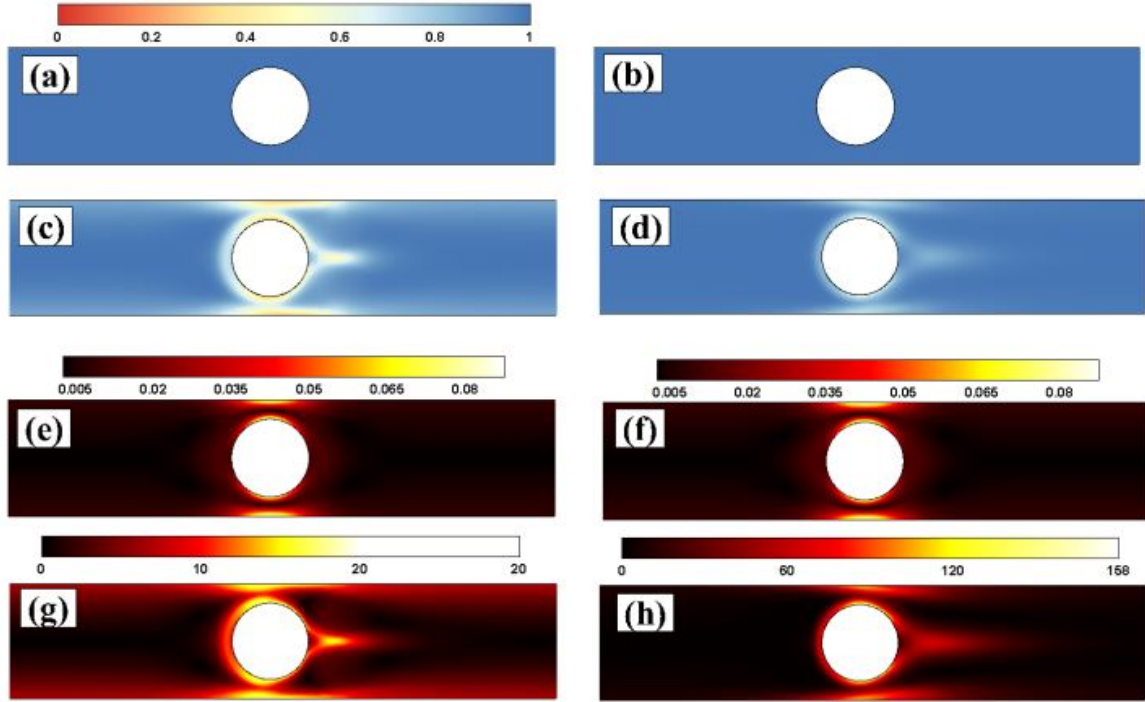


Figure 5.16: Distribution of the long chain number density (a-d) and principal stress difference (e-h). (a,e) $Wi = 0.001, \xi = 0.1$ (b,f) $Wi = 0.001, \xi = 0.01$ (c,g) $Wi = 0.5, \xi = 0.1$ (d,h) $Wi = 0.5, \xi = 0.01$.

instance, see sub-Fig. 5.16 (e) or (f). Furthermore, at such low Weissenberg numbers, a fore-aft symmetry is present in the PSD contour, as seen in the streamline and velocity magnitude plots. However, once the Weissenberg number increases to a higher value of 1.5, the fore-aft symmetry in the PSD contour is destroyed, sub-Figs. 5.15 (e) and (f). Also, the value of the principal stress difference increases at the front stagnation point regardless of the value of ξ . However, a triangular zone with an almost zero PSD value appears at the rear stagnation region, which was also observed in the corresponding experimental investigations [245], sub-Fig. 5.15 (i). In addition, a long and thin region of the PSD contour with a very high value appears along the mid-plane of the channel downstream of the cylinder. This is due to the presence of a highly extensional flow field in this region, which leads to a high stretching and/or breakage of the micelles. This strand of high principal stress difference was also observed in the corresponding experiments dealing with WLM solutions [245, 84] and polymer solutions [246, 109]. As expected, the value of the principal stress difference increases with the increasing Weissenberg number due to the increase in the flow strength and decreasing values of the non-linear VCM

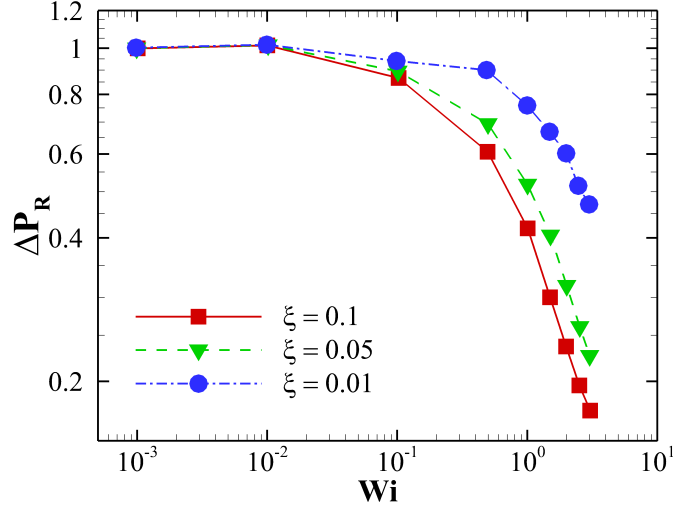


Figure 5.17: Variation of the pressure drop with the Weissenberg number and non-linear VCM model parameter ξ .

model parameter ξ due to a high stretching of the micelles.

5.3.3 Variation of pressure drop

Figure 5.17 shows the pressure drop variation across the cylinder with the Weissenberg number and non-linear VCM model parameter ξ . The pressure drop is non-dimensionalized by the corresponding Newtonian value, which is obtained by running simulations with the same zero-shear rate viscosity and mean inlet velocity as that used for the wormlike micellar solution, i.e., $\Delta P_R = \frac{\Delta P_{WLM}}{\Delta P_{New}}$. Furthermore, the pressure drop ratio is normalized with the corresponding value at the lowest value of the Weissenberg number for each value of ξ to clearly show the shear-thinning or thickening property. This figure shows that at very low Weissenberg numbers ($Wi \ll 1$), the pressure drop is independent of the Weissenberg number regardless of the value of ξ . This is so simply because at this low value of Wi , the flow strength is so low that it is insufficient to deform the micelles, and hence, the resulting solution behaves almost like a Newtonian fluid. However, as the value of the Weissenberg number gradually increases, the flow-induced stresses start to deform the micelles due to the increase in their strength, thereby changing the solution's rheological behavior. The pressure drop decreases with the increasing values of the Weissenberg number irrespective of the value of ξ . The reason behind this trend is due to the dominance of the shear-thinning as well as extensional thinning properties of the WLM solution within this range of the Weissenberg number considered in this study. This ob-

ervation aligns well with that seen experimentally for WLM solutions [84] and polymer solutions both experimentally and numerically [247, 248]. However, it is seen that the extent of thinning in the variation of the pressure drop is seen to be more pronounced as the value of ξ increases. This is because the shear-thinning property of the WLM solution increases with the increasing value of ξ as shown in Fig. 5.2.

Chapter 6

Pressure driven flows of wormlike micellar solutions past two vertically aligned microcylinders confined in a channel

The main aim of this chapter is to delineate the effects of the blockage and gap ratios on the flow dynamics of wormlike micellar solutions past single and two microcylinders, respectively, confined in a microchannel. In particular, this chapter aims to investigate how these blockage and gap ratios would influence the elastic instability and flow bifurcation phenomena during the flow of wormlike micellar solutions. The introduction and motivation behind this chapter have already been discussed in the subsection 2.3 of chapter 2.

6.1 Problem formulation

The present chapter aims to investigate the flow behavior of wormlike micellar solutions past a single and two vertically aligned microcylinders of diameter d (or of radius R) placed in a rectangular microchannel with different blockage (BR) and gap (G) ratios, as shown schematically in sub-Fig. 6.1(a) and (c), respectively. The WLM solution enters the channel with a uniform velocity of U_{in} . In the case of a single cylinder, the blockage ratio is defined as the ratio of the cylinder diameter to that of the channel height, i.e., $BR = \frac{d}{H}$. Whereas, in the case of double cylinders, the gap ratio is defined as $G = \frac{S_1}{S_1 + S_2}$, where S_1 is the distance between the two cylinders and S_2 is the distance between the channel wall and the surface of the cylinder. A value of $G = 0$ implies that the surfaces of the top and bottom cylinders touch each other, while $G = 1$ indicates that the cylinder surface touches the channel wall. In the case of double cylinders, a fixed blockage ratio of $BR = 0.2$ is used in the present study, whereas for the single cylinder case, a range of values of the blockage ratio ($0.167 < BR < 0.67$) is used. Furthermore, in both the cases of single and double cylinders, the upstream (L_u) and downstream (L_d) length of the channel are kept as $100d$. This length is found to be sufficiently high so that it does

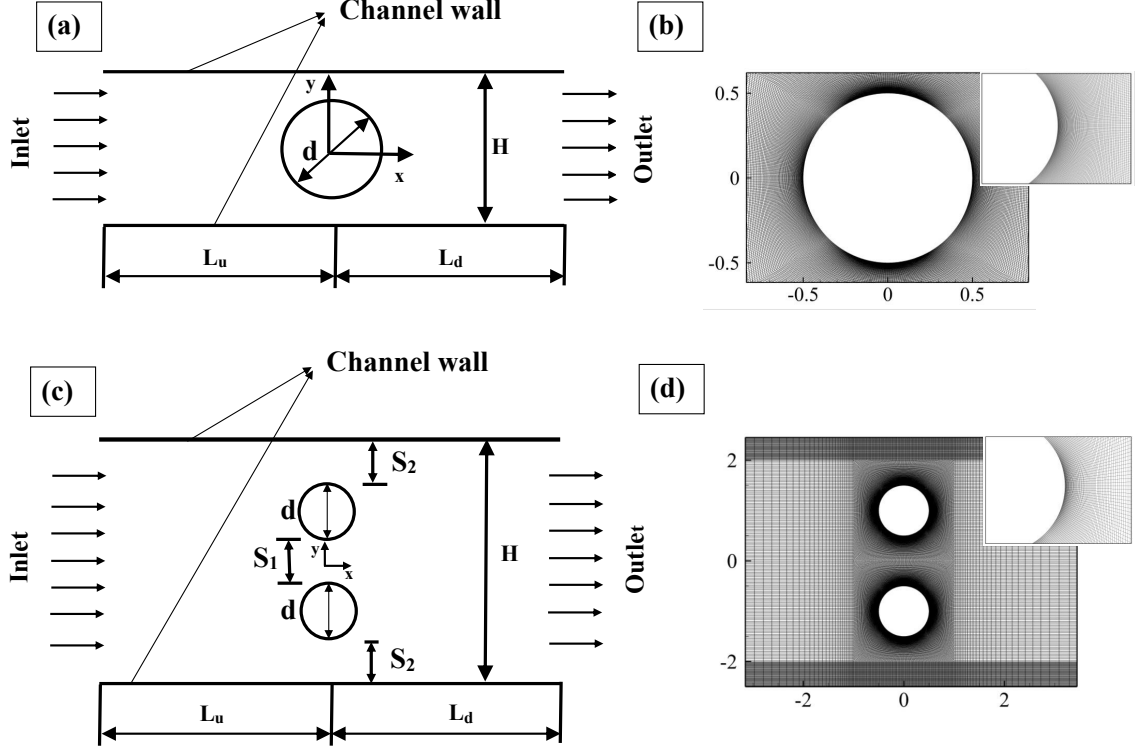


Figure 6.1: Schematic of the present problem for (a) single microcylinder and (c) side-by-side vertically aligned two microcylinders. A typical mesh density was used in the present study for single (b) and two (d) microcylinders. Here the flow direction is shown by arrows in the schematic.

not influence the flow dynamics around the microcylinders.

6.2 Numerical details

The details of the governing and VCM constitutive equations and their numerical solution techniques have already been presented in subsections 3.1.1 and 3.1.3 of chapter 3. The values of the VCM model parameters chosen for the present investigation are as follows [107, 96]: $\beta_{VCM} = 10^{-4}$, $\mu = 2.6$, $C_{Aeq} = 1.6$, $C_{Beq} = 0.8607$, $\epsilon = 0.005$, $\delta_A = \delta_B$ and $\xi = 0.00001, 0.01, 0.1$. The response of the present micellar solution with these VCM model parameters in standard viscometric flows is shown in Fig. 6.2. One can see that the solution exhibits the shear-thinning property in shear flows and extensional hardening and subsequent thinning in uniaxial extensional flows, which are very often seen to occur for a wormlike micellar solution. Furthermore, as the value of ξ increases, the shear-thinning tendency of the micellar solution increases, whereas extensional hardening and subsequent thinning tendencies decrease. The standard grid independence study selects

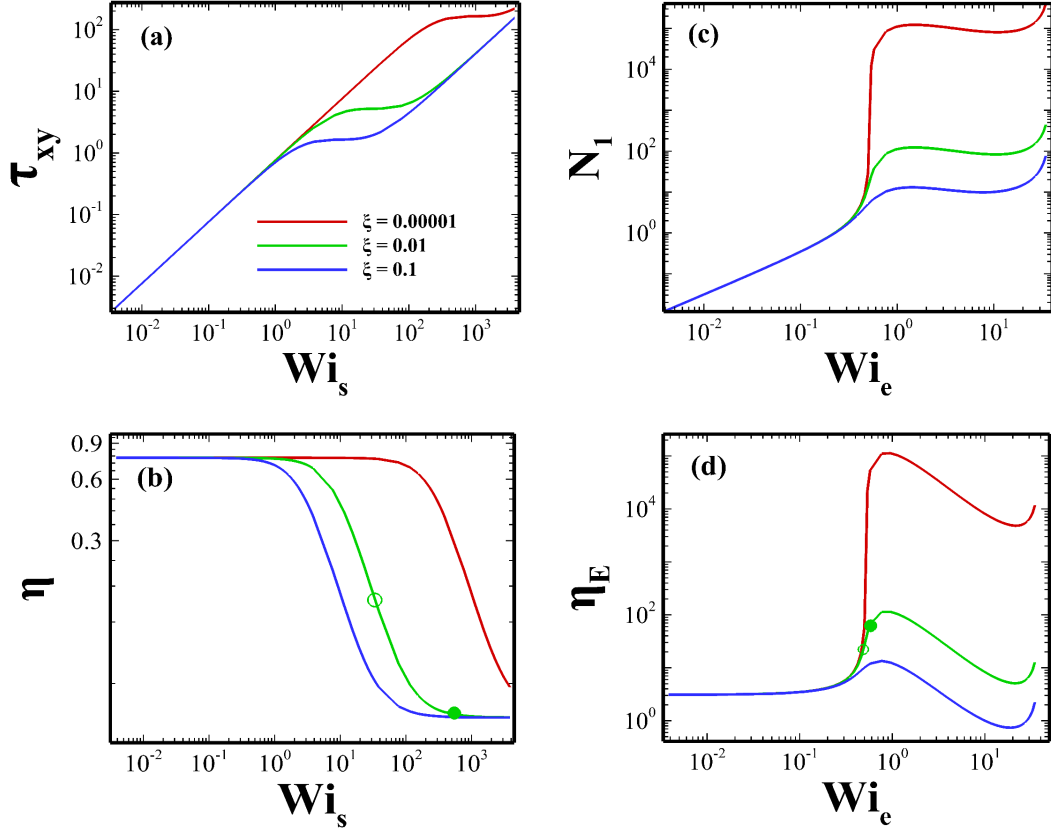


Figure 6.2: Variations of the non-dimensional shear stress (a) and shear viscosity (b) with the non-dimensional shear rate (or the shear Weissenberg number) and first normal stress difference (c) and extensional viscosity (d) with the non-dimensional extension rate (or the extensional Weissenberg number) in homogeneous shear and uniaxial extensional flows, respectively. Here, the symbols (both filled and open) are used to discuss some results presented in section 6.3.

a suitable grid density for both cases. In doing so, three different grid densities for each blockage (in the case of a single microcylinder) and gap (in the case of two microcylinders) ratio, namely, G1, G2, and G3, consisting of a different number of grid points on the cylinder surface as well as in the whole computational domain were created. The simulations were run at the highest value of the Weissenberg number considered in the present study. After inspecting the results (in terms of the variation of the velocity, stress, and number densities of micelles at different probe locations in the computation domain) obtained for different grid densities, the grid G2 with a range of 59280-82900 (depending upon the blockage ratio) hexahedral cells for the single microcylinder and 83200-88200 (depending upon the gap ratio) hexahedral cells for the two microcylinders cases were found to be adequate for the present study. During the making of any grid, careful consideration is taken into account. For instance, a very fine mesh is created near the solid cylinder wall to capture the steep gradients of velocity, stress, or concentration fields. In contrast, a relatively coarse mesh is made away from the solid wall, sub-Figs. 6.1(b) and (d). Likewise, the grid independence study, a systematic time independence study, was also carried out to choose an optimum time step size. A non-dimensional time step size of 0.00001 was selected for both cases. The normalization scheme for velocity, stress, and time with the definition of Weissenberg number is discussed in subsections 3.1.1 of chapter 3.

6.3 Results and discussion

6.3.1 Single microcylinder case: Effect of blockage ratio

Before studying the complex flow dynamics of a wormlike micellar solution, first, we present the results of the flow behavior of a simple Newtonian fluid around a single microcylinder confined between two parallel channel walls at different blockage ratios. Figure 6.3 shows the streamlines and velocity magnitude plots of a Newtonian fluid at a particular value of $BR = 0.34$. It can be seen that both the streamline and velocity magnitude plots show a perfect fore-aft symmetry along the horizontal and vertical mid planes passing through the origin, as expected for a simple Newtonian fluid flowing under the creeping flow condition. The streamlines follow a smooth order and steady path without crossing each other. Furthermore, the streamlines are seen to be attached to the

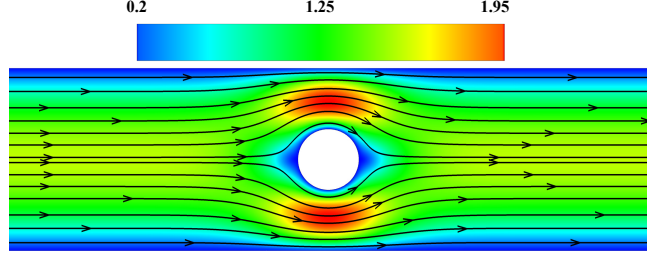


Figure 6.3: Representative streamline and velocity magnitude plots for Newtonian fluid with blockage ratio of $BR = 0.34$.

cylinder surface; hence, no flow separation happens. This result aligns with that observed experimentally by Zhao et al. [86]. The velocity magnitude is maximum in the narrow gap between the channel wall and the cylinder surface. A similar flow pattern is observed for the Newtonian fluid for other blockage ratios. The only difference seen is that the maximum velocity magnitude in the gaps between the channel wall and cylinder surface decreases as the blockage ratio decreases. This is simply due to an increase in the flow area with the decreasing value of the blockage ratio.

Unlike the Newtonian fluid, the flow of WLM solutions is expected to be strongly dependent on the blockage ratio due to its complex rheological behaviour. Additionally, one can expect a strong dependency on the values of the non-dimensional parameters like the Weissenberg number and non-linear VCM model parameter ξ . Simulations are carried out for a range of the Weissenberg number ($0.01 - 3$) and at three values of ξ , namely, 0.00001 , 0.01 , and 0.1 . Due to the high Weissenberg number problem (HWNP) associated with viscoelastic fluid simulations, it was not possible to carry out the simulations beyond Weissenberg number 3 . At very low values of the Weissenberg number, for instance, at $Wi = 0.01$, the flow behaviour of WLM solutions at different blockage ratios is similar to that observed for the Newtonian fluid (results are not shown here). This is due to the presence of a weak viscoelastic effect. However, as the Weissenberg number gradually increases to higher values, the flow dynamics become strongly dependent on the values of the blockage ratio, Weissenberg number, and non-linear VCM model parameter ξ . For example, at $Wi = 1$, although the flow remains steady, and the streamlines follow a nice order path as that seen for Newtonian fluid and WLM solutions at $Wi = 0.01$, the symmetry in the flow profiles along the vertical mid-plane passing through the origin starts to break, see Fig. 6.4. As the blockage ratio increases, the tendency to destroy this vertical symmetry increases; for instance, see the results in sub-Figs 6.4(b) and (d)

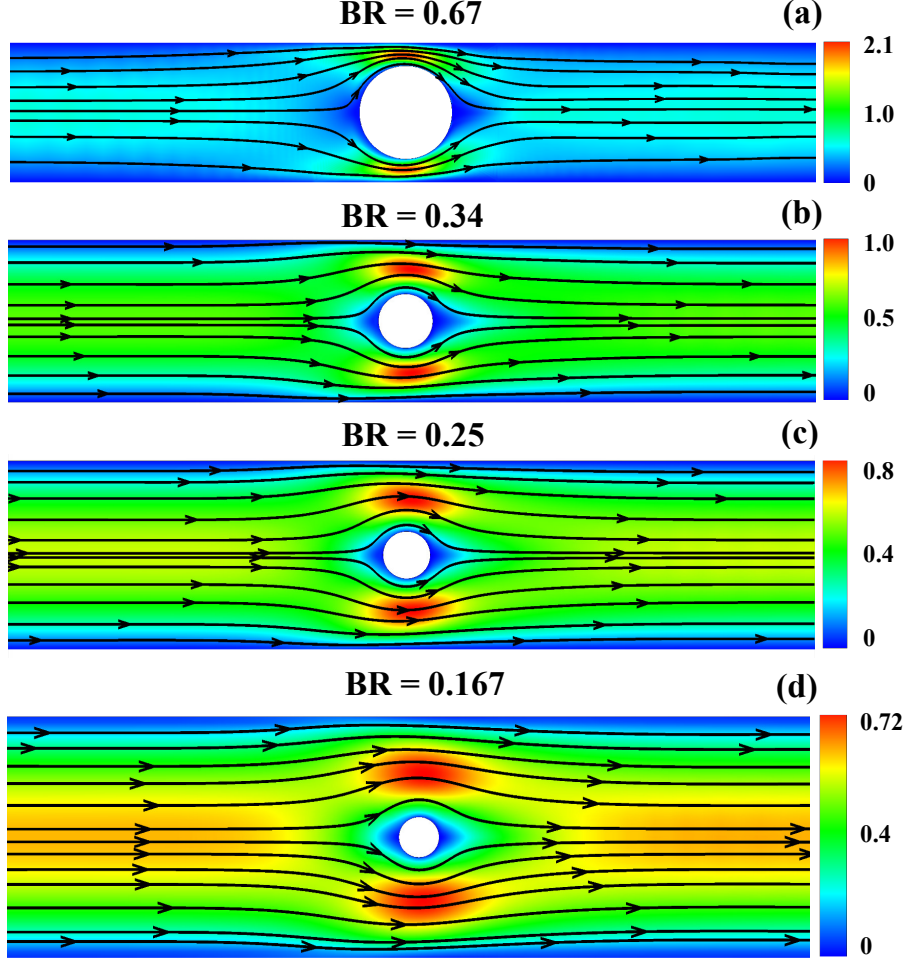


Figure 6.4: Representative streamline and velocity magnitude plots of a WLM solution at $Wi = 1.0$ and $\xi = 0.01$ for different blockage ratios, (a) $BR = 0.67$, (b) $BR = 0.34$, (c) $BR = 0.25$, (d) $BR = 0.167$.

at the values of $BR = 0.34$ and 0.167 , respectively. However, the horizontal symmetry still exists at this value of the Weissenberg number irrespective of the value of BR . The corresponding surface plot of the non-dimensional principal stress difference, defined as $PSD = \sqrt{(\tau_{xx} - \tau_{yy})^2 + (2\tau_{xy})^2}$, is presented in Fig. 6.5 at different blockage ratios. Regardless of the blockage ratio, the PSD value is high near the cylinder surface due to a high shearing zone. Apart from this, a strand of high PSD value, also known as the birefringent strand, is formed along the mid-horizontal plane downstream of the cylinder. This is due to the formation of a highly extensional flow field in this region, thereby aligning more long micelles in the flow field and breaking them into smaller ones. Both these facts tend to increase the PSD value in this region. As the blockage ratio increases, the thickness and value of this birefringent strand increase due to an increase in both the shear and extensional flow strengths.

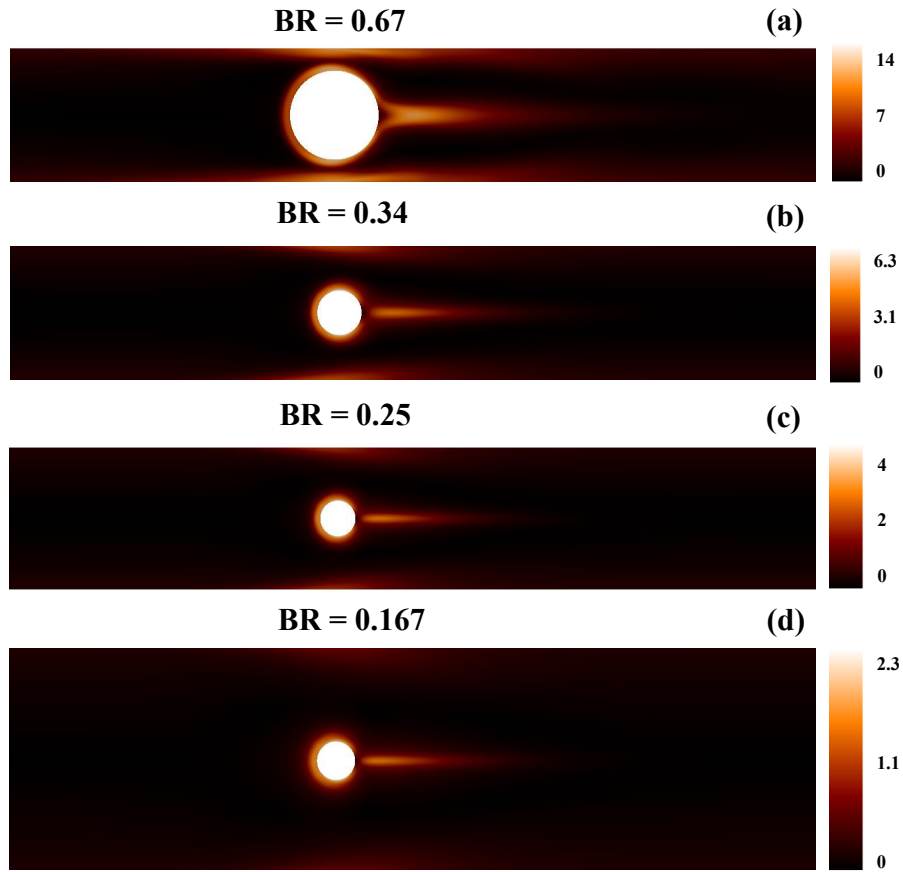


Figure 6.5: Surface plot of principle stress difference of a WLM solution at $Wi = 1.0$ and $\xi = 0.01$ for different blockage ratios, (a) $BR = 0.67$, (b) $BR = 0.34$, (c) $BR = 0.25$, (d) $BR = 0.167$.

As the value of the Weissenberg number is further incremented, say to 2.5, the flow remains steady and horizontally symmetric in the case of the least blockage ratio of $BR = 0.167$, sub-Fig. 6.6(e). On the other hand, at the maximum blockage ratio of $BR = 0.67$ considered in this study, the flow becomes unsteady and quasi-periodic at the same Weissenberg number. At this blockage ratio, a distortion in the streamline profiles is observed, particularly at the rear side of the cylinder. Furthermore, the region of the maximum velocity magnitude changes its position between the lower (sub-Fig. 6.6(a)) and upper narrow gap (sub-Fig. 6.6(b)) regions situated in between the channel wall and cylinder surface. This suggests the emergence of an elastic instability in the flow field and an elastic wave downstream of the cylinder due to the shifting in the maximum velocity magnitude zone between the two gap regions, as discussed and explained in detail in the previous chapter. Moreover, a small vortex is seen to form downstream of the cylinder at this blockage ratio and Weissenberg number. The nature of the flow field at these two extreme blockage ratios, namely, at $BR = 0.167$ and 0.67 , is further confirmed in Fig. 6.7(a) wherein the temporal variation of the non-dimensional stream-wise velocity is plotted at a probe location placed at the mid-point in between the cylinder surface and channel wall for different blockage ratios. At $BR = 0.167$, it reaches a steady value with time, suggesting the presence of a steady-state flow field. Whereas, at $BR = 0.67$, it fluctuates with time, showing instability in the flow field. The power spectrum of these velocity fluctuations is presented in sub-Fig. 6.7(d), and from this figure, it can be seen that a single dominant frequency governs the flow along with a broad spectrum of small frequencies. This indicates the quasi-periodic nature of the flow field at these values of Wi and BR .

In between these two extreme blockage ratios considered in this study, there is a range of blockage ratios present wherein the fluid prefers to flow through one side of the cylinder, for instance, see sub-Figs. 6.6(c) and (d) for the results at $BR = 0.34$ and 0.25 , respectively. This results in an almost stagnant region on the opposite side of the cylinder. Here the preferential side occurs at $Y < 0$ for $BR = 0.34$ (sub-Fig. 6.6(c)), whereas for $BR = 0.25$, it occurs at $Y > 0$ (sub-Fig. 6.6(d)). However, the selection of this preferential side for the flow is completely random; hence, there is an equal opportunity when the fluid can go through the other side of the cylinder. This flow asymmetry indicates the origin of a pitchfork bifurcation in the flow field. This kind of bifurcation in the flow field

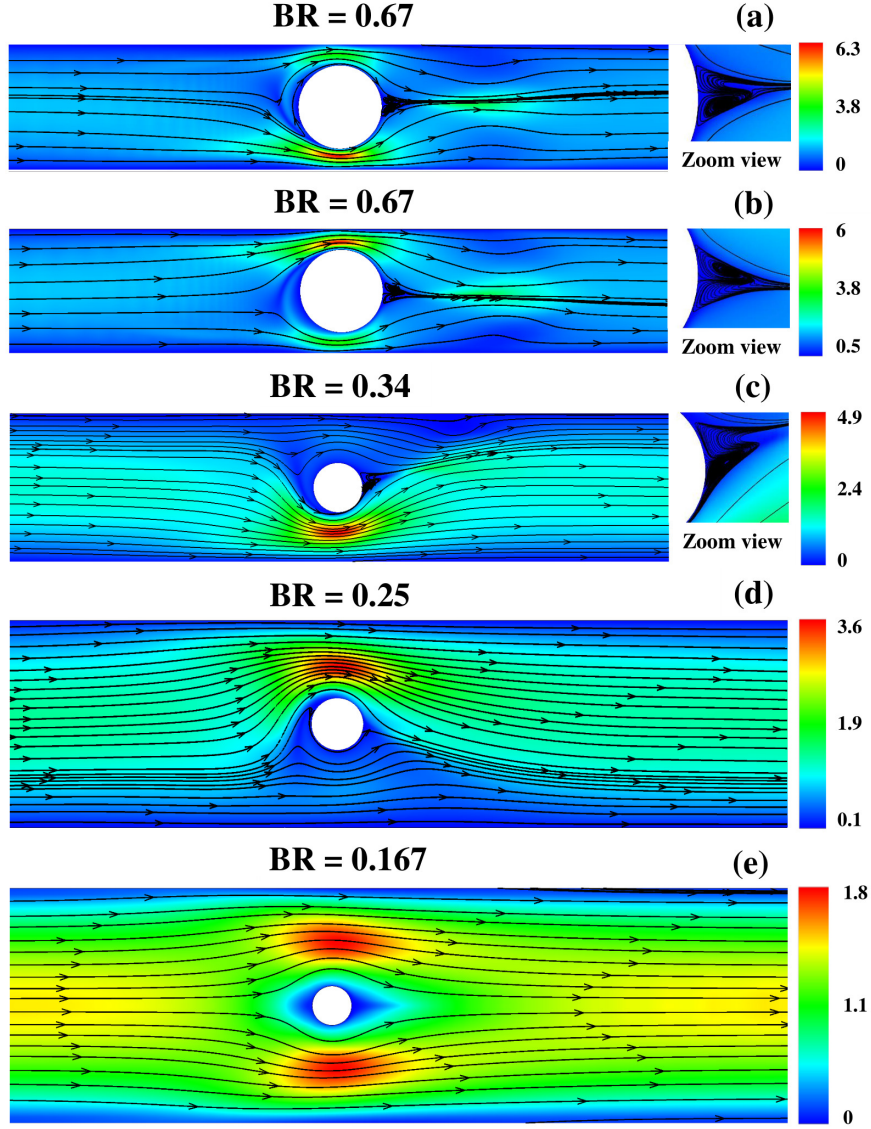


Figure 6.6: Representative streamline and velocity magnitude plots of a WLM solution at $Wi = 2.5$ and $\xi = 0.01$ for different blockage ratios, (a) $BR = 0.67$, $t = 30$ (b) $BR = 0.67$, $t = 30.2$, (c) $BR = 0.34$, (d) $BR = 0.25$, (e) $BR = 0.167$.

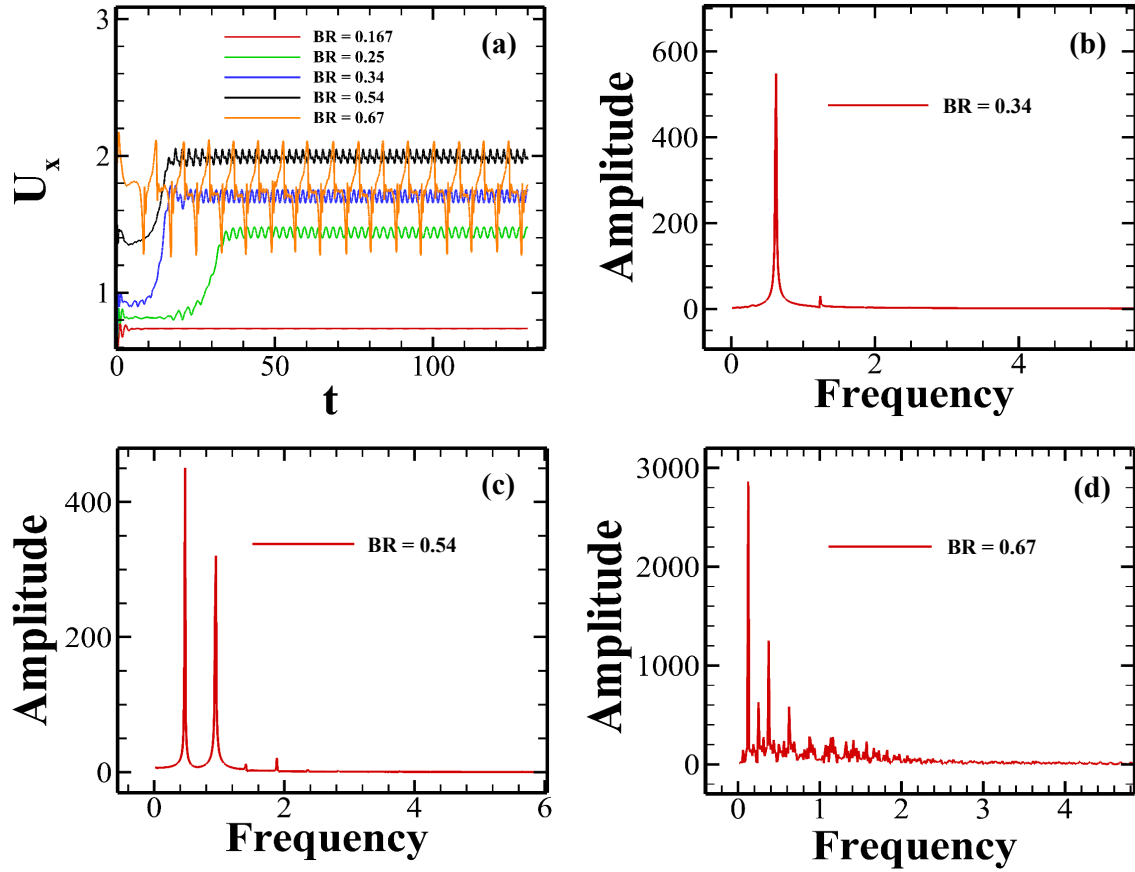


Figure 6.7: (a) Temporal variation of the stream-wise velocity component at a probe location placed in the middle in between the cylinder surface and upper channel wall and (b-d) power spectral density plot of the velocity fluctuations at different blockage ratios at $Wi = 2.5$ and $\xi = 0.01$.

has also been observed in earlier experimental investigations dealing with polymer [249] and WLM solutions [87], as well as in numerical investigations performed with a single-species viscoelastic constitutive model [108]. The flow field seems unsteady at $BR = 0.34$, whereas it is steady at $BR = 0.167$, which can be seen from the temporal variation of the non-dimensional stream-wise velocity presented in sub-Fig. 6.7(a). The corresponding power spectrum plot for velocity fluctuations at $BR = 0.34$ is depicted in sub-Figs. 6.7(b). From this figure, one can see that the flow is governed by a single dominant frequency, thereby suggesting the occurrence of a regular periodic unsteadiness in the flow field. At $BR = 0.54$, an asymmetry in the flow field is also seen (results not shown here), and the flow field is again found to be unsteady, which is quasi-periodic, as can be evident from the power spectrum plot of velocity fluctuations presented in sub-Fig. 6.7(c). The corresponding variation of the PSD value at $Wi = 2.5$ and different blockage ratios is depicted in Fig. 6.8. Once again, at this Weissenberg number, a long birefringent strand of high PSD value is seen to form downstream of the cylinder; likewise, it is seen at $Wi = 1$ (Fig. 6.5). However, the PSD value is higher at $Wi = 2.5$ than that seen at $Wi = 1$ due to increased flow strength. Furthermore, the strand is seen to be bending in nature downstream of the cylinder at blockage ratios 0.34 (sub-Fig. 6.8(b)) and 0.25 (sub-Fig. 6.8(c)) due to the presence of an asymmetric flow at these blockage ratios.

To characterize the asymmetric nature of the flow more quantitatively, we define a dimensionless flow asymmetry parameter I_s as follows [108, 87]

$$I_s = \frac{U_{X,1} - U_{X,2}}{U_{X,1} + U_{X,2}} \quad (6.1)$$

Here $U_{X,1}$ and $U_{X,2}$ are the stream-wise velocities at the midpoints between the cylinder surface and upper and lower channel walls, respectively. A value of $|I_s| = 0$ denotes a perfect symmetric flow, whereas $|I_s| = \pm 1$ implies a perfect asymmetric flow when the whole fluid passes through one side of the cylinder. Note that in the case of an unsteady flow, a time-averaged value of U_X is considered in the calculation of I_s . The variation of the absolute value of I_s with the Weissenberg number and blockage ratio is presented in Fig. 6.9. It can be seen that the value of I_s is essentially zero for the blockage ratios of 0.17 and 0.67. This is due to the existence of the steady symmetric and unsteady symmetric quasi-periodic flows at these two blockage ratios, respectively. On the other hand, at blockage ratios 0.25 and 0.34, a critical value of the Weissenberg number is seen

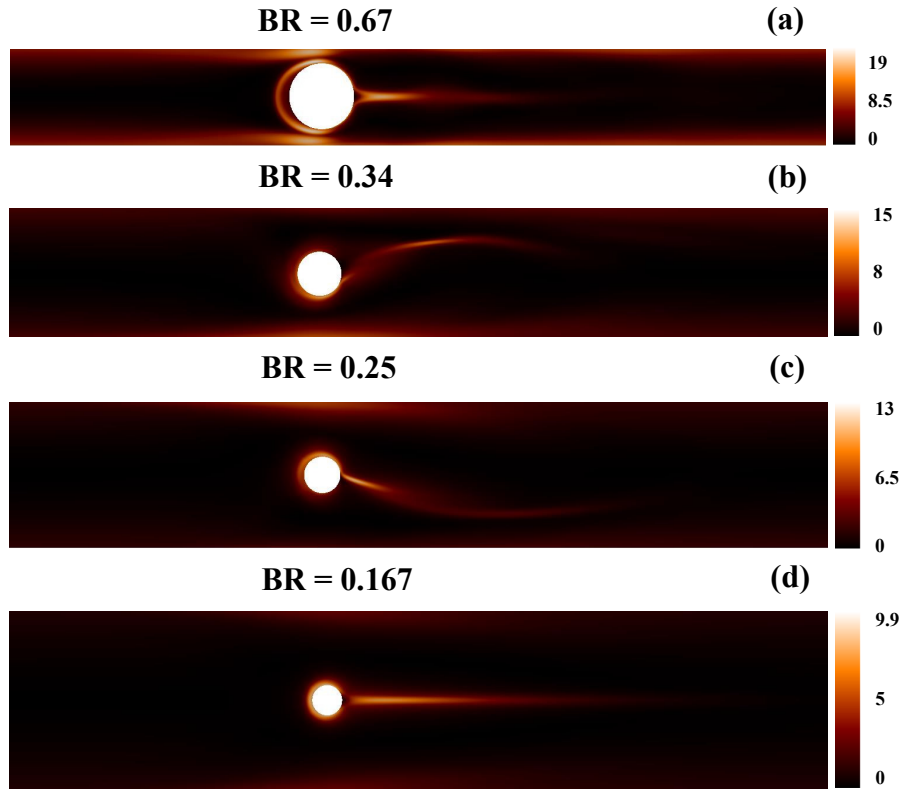


Figure 6.8: Surface plot of principle stress difference of a WLM solution at $Wi = 2.5$ and $\xi = 0.01$ for different blockage ratios, (a) $BR = 0.67$, (b) $BR = 0.34$, (c) $BR = 0.25$, (d) $BR = 0.167$.

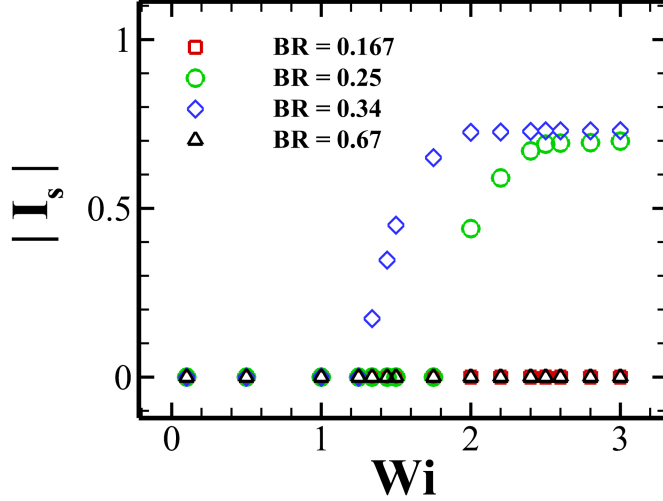


Figure 6.9: Variation of the flow asymmetry parameter (I_s) with the Weissenberg number and blockage ratio at $\xi = 0.01$.

to present up to which the asymmetry parameter is zero. Beyond that, it suddenly starts to increase and finally reaches almost a constant value at high Weissenberg numbers. The critical value of the Weissenberg number at which the transition from symmetric to an asymmetric flow occurs (i.e., the onset of the pitchfork bifurcation) increases as the blockage ratio decreases. For instance, at $BR = 0.34$, it is around 1.25, while it is around 1.75 at $BR = 0.25$.

Furthermore, one can see that the value of the flow asymmetry parameter I_s increases with the blockage ratio, which is in line with that observed by Varchanis et al. [108] in their simulations. Based on the value of the flow asymmetry parameter, a phase diagram is presented in Fig. 6.10 wherein different flow states observed in the present study with the blockage ratio, are summarized at a Weissenberg number of 2.5 and non-linear VCM model parameter $\xi = 0.01$. The flow is steady and symmetric at a blockage ratio lower than 0.167. Beyond that and up to $BR = 0.27$, a steady and asymmetric flow transition occurs. After that, the flow transits to an unsteady periodic state and then to a quasi-periodic state as the blockage ratio gradually increases. On further increasing the blockage ratio of more than around 0.55, the flow transits to a quasi-periodic and symmetric state where a resymmetrization in the flow occurs.

Next, we aim to explain the origin of this asymmetric flow resulting from the flow bifurcation and elastic instabilities in WLM solutions. It is well known that the onset of elastic instabilities either in polymer or micellar solutions is the result of the presence of curved streamlines in the vicinity of the microcylinder and the accumulation of the elastic

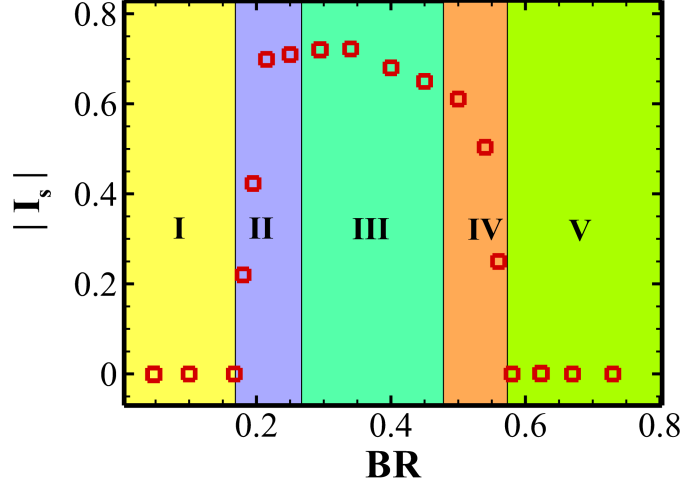


Figure 6.10: Variation of the flow asymmetry parameter (I_s) with the blockage ratio at $Wi = 2.5$ and $\xi = 0.01$. In this figure (I) steady and symmetric (II) steady and asymmetric (III) unsteady, periodic, and asymmetric (IV) unsteady, quasi-periodic and asymmetric, and (V) unsteady, quasi-periodic, and symmetric.

stresses downstream of the microcylinder [250, 18, 251, 86], which can be seen from the streamlines plot (Fig. 6.6) and the PSD contours (Fig. 6.5) presented here as well. Very often, the criteria developed by McKinley and co-workers are used to figure out the onset of these purely elastic instabilities, written as [18]

$$\left(\frac{\lambda U}{R} \frac{\tau_{xx}}{\eta_0 \dot{\gamma}} \right) \geq M_{crit}^2 \quad (6.2)$$

Where R is the characteristic radius of streamline curvature and τ_{xx} is the tensile or normal stress along the flow direction. If the dimensionless value of the left-hand side of Eq. 6.2 becomes greater than or equal to the critical M_{crit}^2 value at any position in the flow field, an instability will then originate in the system. For the flow of a constant viscosity viscoelastic polymer (Boger fluid) solution past a cylinder confined in a channel, a value of $M_{crit} = 6.08$ was found from the linear stability analysis [18]. However, for the present case of a wormlike micellar solution, this value should not be obviously the same due to the presence of shear-thinning viscous properties and breakage and reformation dynamics of the micelles. Once this instability is triggered in the flow field, then a small and random lateral fluctuation of the birefringent strand (as shown in Fig. 6.8) of high elastic stresses downstream of the cylinder either in the $-Y$ or $+Y$ direction creates a resistance to the flow of fluid in that direction. This forces the fluid to pass through the other side of the cylinder. This will eventually create an imbalance in the shear rate at

the two sides of the cylinder. If the fluid shows shear-thinning properties, this imbalance in the shear rate and hence the viscosity gets accentuated, thereby resulting in the fluid passing through one side (at which the shear rate is high or the viscosity is low) of the cylinder. This explanation aligns with that provided earlier for the flow of either WLM solution [87] or polymer solution [249] past a cylinder. Therefore, to show the asymmetric flow, the fluid should have shear-thinning properties and a sufficient amount of elastic stresses should be accumulated downstream of the cylinder [249].

To explicitly explain this, we calculate the local shear (Wi_s^l) and extensional (Wi_e^l) Weissenberg numbers based on the local shear rate in the gap region and local extension rate downstream of the cylinder respectively for $BR = 0.34$, $Wi = 2.5$ and $\xi = 0.01$ at which an asymmetric flow was observed (sub-Fig. 6.6(c)). We find that these values (presented as open symbols in Fig. 6.2) lay in the shear-thinning region (in case of the shear Weissenberg number) and extensional hardening region (in case of the extensional Weissenberg number) in the plots presented in Fig. 6.2. As the blockage ratio increases to 0.67, the values (presented as filled symbols in Fig. 6.2) of both (Wi_s^l) and (Wi_e^l) increase due to the increase in the flow velocity resulting from the decrease in the flow area. Once again, these values are shown in the same figure as symbols. One can see that although the value of (Wi_e^l) lies in the extensional hardening region, the value of (Wi_s^l) lies in the plateau region in shear viscosity plot. This causes a resymmetrization in the flow field at this blockage ratio, as shown in sub-Figs. 6.6 (a) and (b).

This is further confirmed by changing the value of ξ , which indicates the scission energy needed to break a micelle. As the value of ξ increases to 0.1 or the micelles become progressively easier to break, a symmetric flow (with $|I_s| = 0$) is seen to present (sub-Fig. 6.11(c)) at the same $BR = 0.34$ and $Wi = 2.5$ as opposed to a symmetric flow seen at $\xi = 0.01$. This is simply due to the fact that although the shear-thinning property increases with an increase in ξ due to the easy breakage of micelles, the magnitude of the elastic stresses downstream of the cylinder becomes insufficient to create instability in the system. It is further noticed that at this value of $\xi = 0.1$, the streamlines are first converged and then diverged downstream of the cylinder. This can be explained as follows: the breakage of micelles just downstream of the cylinder results in the decrease of the viscosity of the micellar solution at this region, which in turn, allows the streamlines to be converged at this region. As we move away from this region, the breakage of

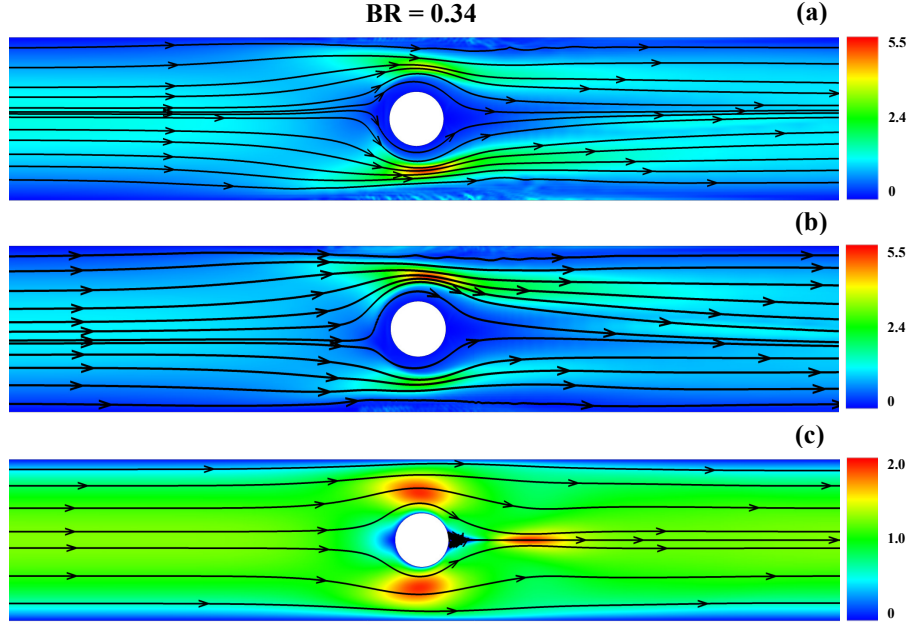


Figure 6.11: Representative streamline and velocity magnitude plots at $BR = 0.34$ and $Wi = 2.5$. (a) and (b) $\xi = 0.00001$, (c) $\xi = 0.1$.

micelles will progressively decrease due to the decrease in the extensional flow strength. Therefore, the viscosity will increase in the region away from the cylinder. This will diverge the streamlines in the region far away downstream of the cylinder. On the other hand, further simulations were also run to a lower value of $\xi = 0.0001$ at which the micelles become harder to break. It can be again seen a resymmetrization in the flow field, sub-Figs. 6.11(a) and (b) shown at two different times. At this value of ξ , although the value of Wi_e^l increases, the value of Wi_s^l lies in the plateau region shown in Fig. 6.2.

6.3.2 Two vertically aligned microcylinders case: Effect of gap ratio

After discussing the results for the case of a single microcylinder, we now turn our attention to the case of two vertically side-by-side placed microcylinders in a channel, as schematically shown in Fig. 6.1(c). The streamlines and velocity magnitude plots for this configuration are depicted in Fig. 6.12 at two gap ratios, namely, 0.28 (a-d) and 0.50 (e-f) for a range of values of the Weissenberg number. Likewise, in the single cylinder case, for a Newtonian fluid, a perfect symmetry along the horizontal and vertical mid-planes passing through the origin is present in the flow profiles irrespective of the value of the gap ratio G , see sub-Fig 6.12(a) and (e). Although the fluid passes through all the three

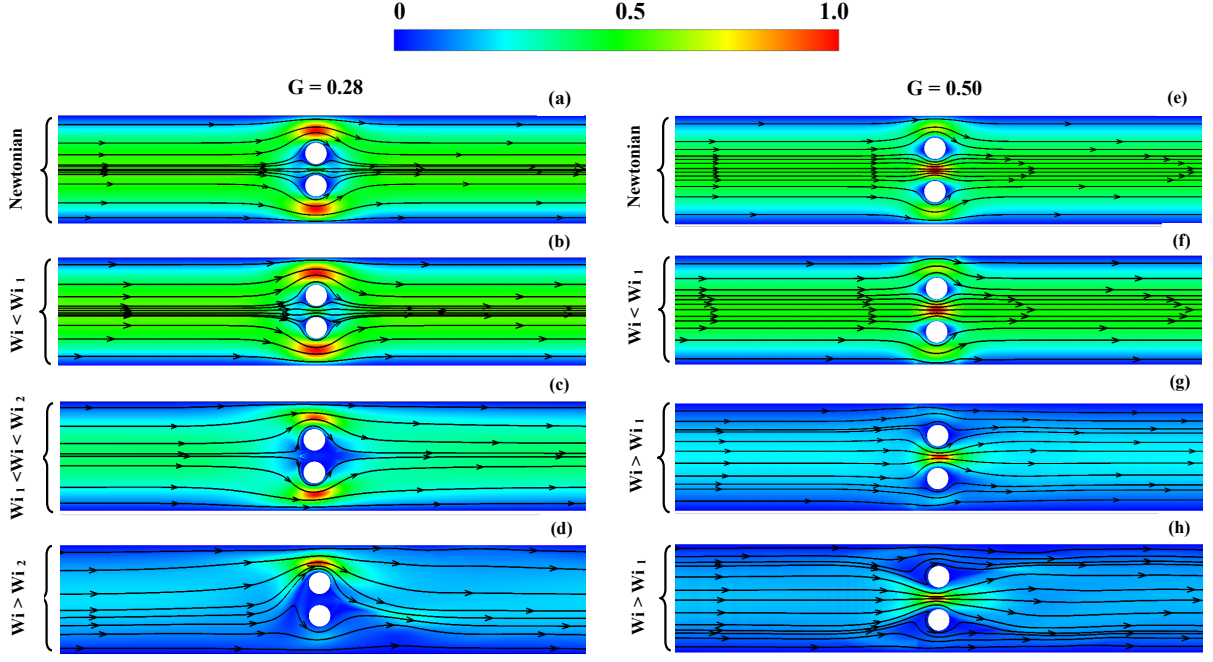


Figure 6.12: Representative streamline and velocity magnitude plots for vertically side-by-side two microcylinders case at $\xi = 0.01$, (a) $G = 0.28$, Newtonian (b) $G = 0.28$, $Wi = 0.3$ (c) $G = 0.28$, $Wi = 1.0$ (d) $G = 0.28$, $Wi = 2.5$ (e) $G = 0.5$, Newtonian (f) $G = 0.5$, $Wi = 0.3$ (g) $G = 0.5$, $Wi = 1.0$ (h) $G = 0.5$, $Wi = 2.5$.

gaps available in the system; however, at $G = 0.28$, the magnitude of the velocity is larger at the gap regions in between either the top or bottom cylinder and the channel wall than that seen at the gap region in between the two cylinders. In contrast to this, a reverse trend is seen for the gap ratio of $G = 0.50$. This is simply due to the fact that for a Newtonian fluid and in the creeping flow regime, the volumetric flow rate of the fluid is linearly proportional to the available flow area. At $G = 0.28$, the flow area is larger at the gap in between either the top or bottom cylinder and the channel wall than that seen in between the two cylinders, whereas, at $G = 0.50$, the other way around happens. Below a critical low value of the Weissenberg number $Wi < Wi_1 \approx 0.3$, the flow characteristics of a WLM solution look similar to that of a Newtonian fluid regardless of the gap ratio, as it was also seen for the single cylinder case. For instance, see the results that are presented in sub-Figs. 6.12(b) and (f) for gap ratios of 0.28 and 0.50, respectively. This is solely due to the fact that at this low Weissenberg and Reynolds number flows, the elastic effects, as well as the breakage and reformation dynamics of micelles are very weak, and hence, it behaves like a Newtonian fluid.

However, as the Weissenberg number gradually increases to higher values and exceeds the first critical Weissenberg number (Wi_1), the system then undergoes the first transition

due to the increase in the elastic forces. For instance, at $G = 0.28$, a transition from the low-Weissenberg number symmetric state to a diverging (D) state occurs, in which the fluid passes through the gaps in between the cylinder and channel wall, and it completely avoids the region in between the two cylinders, sub-Fig. 6.12(c). The flow still remains steady and symmetric along the horizontal mid-plane passing through the origin, as can be observed in sub-Fig. 6.13(a), wherein the temporal variation of the non-dimensional stream-wise velocity is plotted at a probe location placed at the origin. On further increasing the Weissenberg number beyond a second critical value of the Weissenberg number $Wi > Wi_2$, a second transition in the flow state is observed, in which the micellar solution mostly prefers to flow through only the gap in between the top cylinder and the channel wall ($Y > 0$), as shown in sub-Fig. 6.12(d). However, there is an equal opportunity present in which most of the fluid can also pass through the gap between the bottom cylinder and the channel wall ($Y < 0$) (not shown here). This state is known as the asymmetric-diverging state (AD). In this state, the flow becomes unsteady, as can be evident in sub-Fig. 6.13(a) wherein the non-dimensional stream-wise velocity is seen to be fluctuating with time. The nature of this unsteadiness is quasi-periodic as the power spectrum of the velocity fluctuations is governed by more than one dominant frequency, sub-Fig. 6.13(b). This state is analogous to the state observed in sub-Fig. 6.6(d) for the case of a single cylinder. On the other hand, at $G = 0.5$, only one transition in the flow state happens when the Weissenberg number exceeds its first critical value $Wi > Wi_1$. In this state, the whole micellar solution preferentially passes through the gap region between the two cylinders, avoiding the gap between the cylinder and the channel wall. This state is known as the converging state (C). However, a transition from a steady flow field to an unsteady one occurs within this state as the Weissenberg number gradually increases. For instance, one can see that the non-dimensional stream-wise velocity reaches a steady value at $Wi = 1.5$; whereas, it becomes fluctuating in nature as the Weissenberg number is further increased to 2.5, sub-Fig. 6.13(c). These velocity fluctuations are governed by two dominant frequencies (sub-Fig. 6.13(d)) as opposed to a range of frequency spectrum seen at $G = 0.28$ (sub-Fig. 6.13(b)) under otherwise identical conditions. Furthermore, the amplitude of these velocity fluctuations is seen to be very large in the latter case as compared to that seen in the former one.

Likewise, Hopkins et al. [113], we also calculate two asymmetrical parameters, namely,

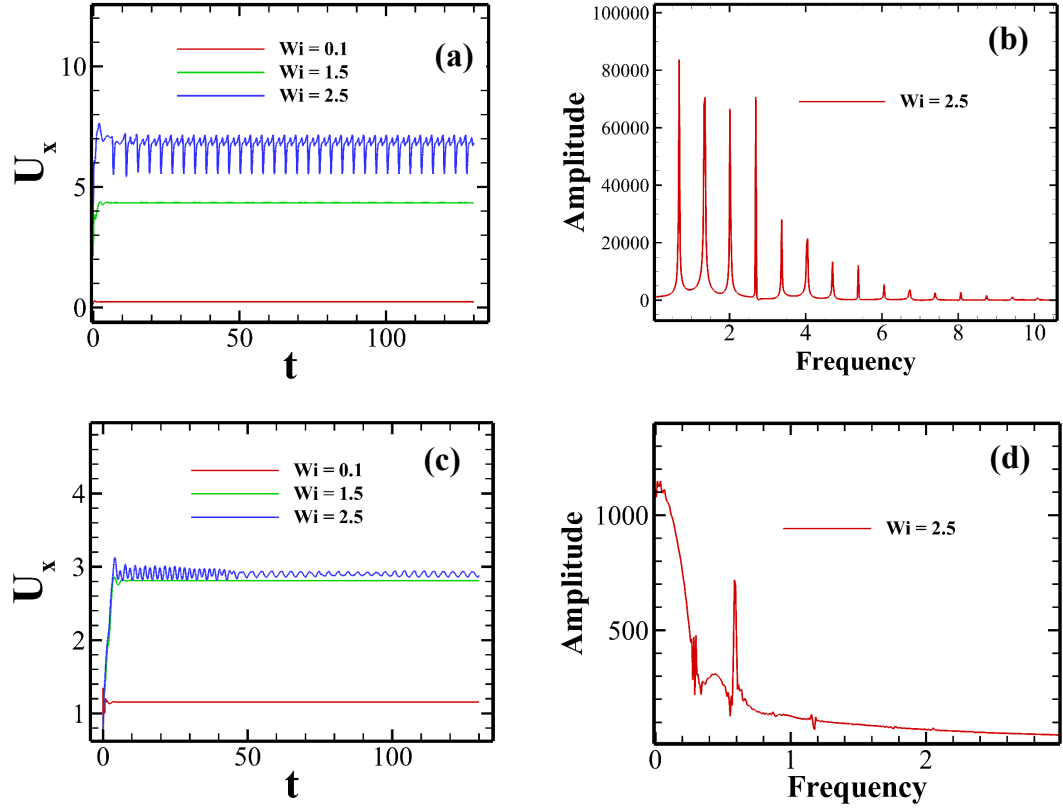


Figure 6.13: Temporal variation of the stream-wise velocity component at a probe location $X = 0$ and $Y = 0$ for two gap ratios, namely, 0.28 (a) and 0.5 (b). The corresponding power spectral density plot of the velocity fluctuations at $G = 0.28$ (b) and at $G = 0.5$. Here all the results are presented for non-linear VCM model parameter $\xi = 0.01$.

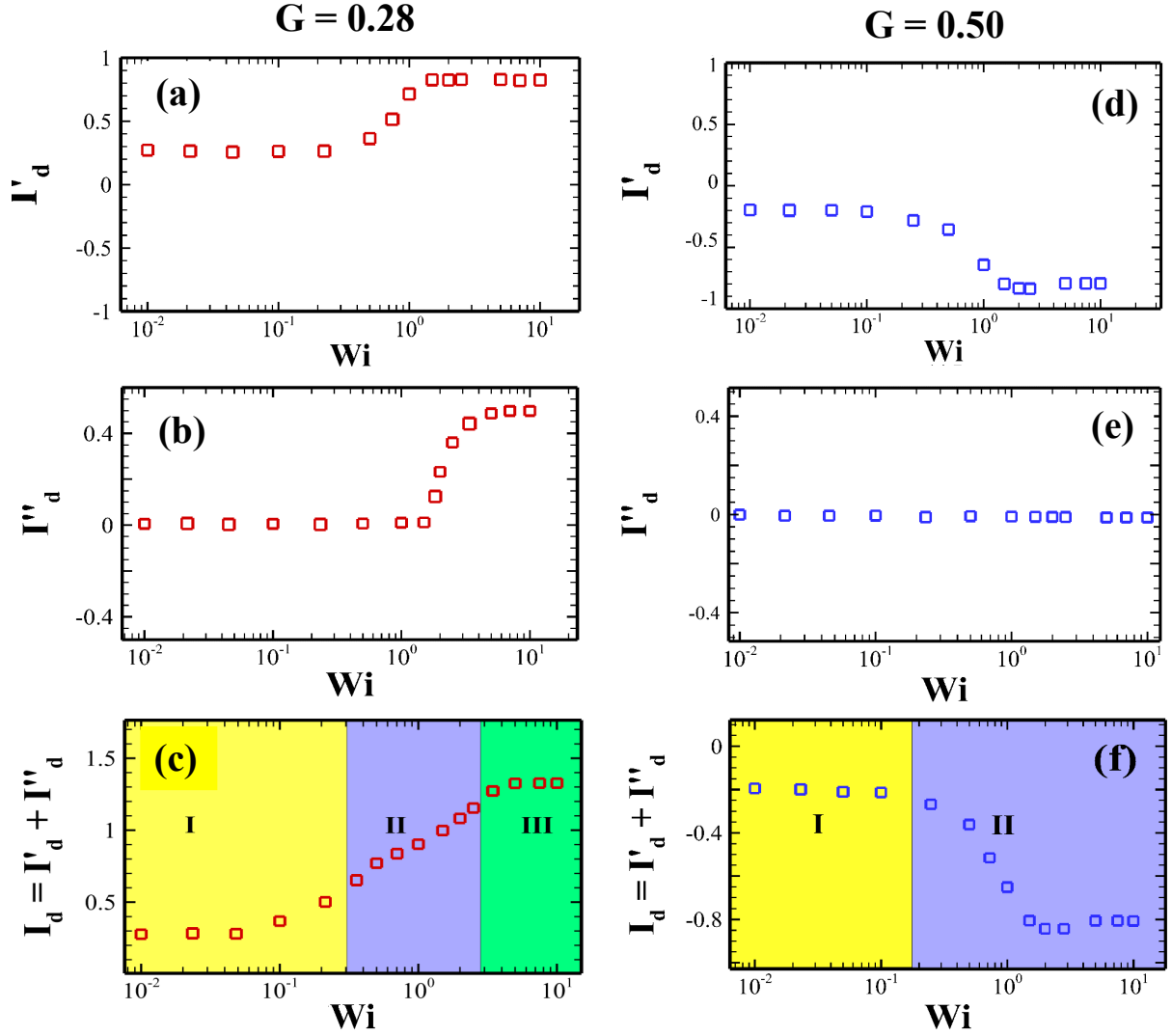


Figure 6.14: Variation of the flow asymmetry parameter for the two microcylinders case at $G = 0.28$ (a-c) and at $G = 0.5$ (d-f). In subfigure (c), (I) Newtonian-like state (II) Diverging or 'D' state and (III) Asymmetric-diverging or 'AD' state, whereas in subfigure (f), (I) Newtonian-like state and (II) converging or 'C' state.

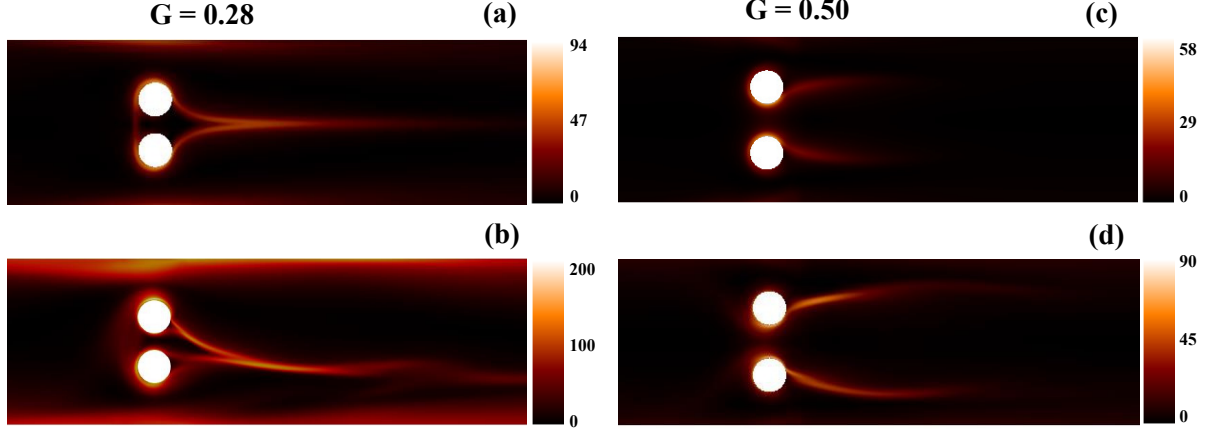


Figure 6.15: Variation of the principle stress difference for the two microcylinders case (a) $G = 0.28$, $Wi = 1.0$ (b) $G = 0.28$, $Wi = 5.0$ (c) $G = 0.5$, $Wi = 1.0$ (d) $G = 0.5$, $Wi = 5.0$.

I'_d and I''_d to distinguish the flow states more quantitatively for the two microcylinders case. These are defined as follows:

$$I'_d = \frac{\frac{1}{2}(U_{X,u} + U_{X,l}) - U_{X,m}}{\frac{1}{2}(U_{X,u} + U_{X,l}) + U_{X,m}} \quad (6.3)$$

$$I''_d = \frac{U_{X,u} - U_{X,l}}{U_{X,u} + U_{X,l} + U_{X,m}} \quad (6.4)$$

In the above equations, $U_{X,u}$, $U_{X,l}$ and $U_{X,m}$ are the time-averaged stream-wise velocities obtained at the mid-points placed in the upper gap (between the top cylinder and channel wall), lower gap (between the bottom cylinder and lower channel wall) and in the gap in between the two cylinders, respectively. The variations of I'_d and I''_d with the Weissenberg number are shown in sub-Figs. 6.14 (a-b) and (d-f) for the gap ratios of 0.28 and 0.5, respectively. The total asymmetry parameter $I_d = I'_d + I''_d$, showing the complete bifurcation diagram, is presented in sub-Figs.(c) and (f) at $G = 0.28$ and 0.50, respectively. The first transition in the value of I'_d occurs at $Wi \approx 0.3$ when the flow transits from symmetric to diverging state (D). After this transition, as the Weissenberg number gradually increases, one can see that the value of I'_d also gradually increases, ultimately leveling off to a value of 1, see sub-Fig. 6.14(a). This trend in I'_d thereby suggests that almost no fluid passes in between the two cylinders as the Weissenberg number increases. The second transition in the flow state from the diverging (D) to asymmetric-diverging (AD) state occurs when the transition in the value of I''_d occurs at

$Wi \approx 2.5$, sub-Fig. 6.14(b). The complete bifurcation diagram at $G = 0.28$ is shown in sub-Fig. 6.14(c) in terms of the variation of the total asymmetry parameter I_d with Wi . It can be seen that the first bifurcation leads to $I_d \rightarrow 1$, whereas the second bifurcation results in $I_d \rightarrow 1.5$. On the other hand, at $G = 0.50$, the first bifurcation occurs when the flow transits from symmetric to converging state (C) at $Wi \approx 0.15$, which can be marked by the transition of the value of I_d' in sub-Fig. 6.14(d). As the Weissenberg number increases, the value of I_d' tends to -1, thereby suggesting that all of the fluid prefers to flow through the gap region in between the two cylinders. The value of I_d'' almost remains zero over the whole range of the Weissenberg number considered (sub-Fig. 6.14(e)), and hence, a second bifurcation is not observed at $G = 0.50$ as it was seen at $G = 0.28$. The complete bifurcation diagram for this gap ratio is depicted in sub-Fig. 6.14(f).

To explain the formation of these different flow states in the case of flow past two microcylinders, the corresponding PSD plots at these two gap ratios are presented in Fig. 6.15. At $G = 0.28$ and $Wi = 1.0$ at which 'D' states occur, it can be observed that the gap between the two cylinders is closed by a region of high PSD value (sub-Fig. 6.15 (a)), thereby blocking the fluid to pass through this region. Furthermore, at this Weissenberg number, a long birefringent strand of high PSD value is also formed in the mid-horizontal plane downstream of the cylinders. As the Weissenberg number further increases to higher values, both the length and magnitude of this strand increase. A little and random lateral fluctuation in this strand in either $+Y$ or $-Y$ direction downstream of the cylinder blocks the flow of fluid in that direction, resulting in the formation of 'AD' state (sub-Fig. 6.15(b)). This is reminiscent of that seen in the case of a single microcylinder. On the other hand, at $G = 0.5$, the velocity magnitude in between the two cylinders progressively increases as the Weissenberg number increases due to the shear-thinning property of the micellar solution, and hence more fluid prefers to pass through this area due to the formation of a low-viscosity region. As a result, the birefringent strands formed downstream of both the cylinders shift towards the channel walls (see sub-Figs. 6.15 (c) and (d)), thereby blocking the fluid from passing through the gap regions in between the cylinder surface and channel wall. This facilitates more fluid to pass through the gap region between the two cylinders. This effect gets accumulated as the Weissenberg number further increases, resulting in the formation of the 'C' state. At this gap ratio, the space in between the two cylinders is not closed by a region of high

PSD value (sub-Fig. 6.15 (c)) as that seen at $G = 0.28$ which can block the flow, and therefore, the fluid can easily pass through this space. Likewise the single microcylinder case, we have again found that the flow bifurcation can be completely suppressed if the non-linear VCM model parameter ξ increases to 0.1. In other words, if the micelles become progressively easier to break, this bifurcation in the two cylinders case can also be completely avoided due to the increase in the shear-thinning and decrease in the elastic effects, Fig. 6.2. On the other hand, with a decreasing value of $\xi = 0.0001$ when the micelles become progressively harder to break, we have again observed the disappearance of these bifurcations in the flow irrespective of the gap ratio, due to an increase in the elastic and decrease in the shear-thinning effects; likewise, we have seen for the single microcylinder case in the preceding subsection. The explanation presented herein for the occurrence of different flow states in the case of double microcylinders based on the variation of the PSD value is, somehow, missing in the studies of Hopkins et al. [113]. Therefore, this study provides a complete understanding of the flow phenomena occurring for the double microcylinders case. Due to the existence of an excellent qualitative agreement between the present results and that of Hopkins et al. [113], this study further shows the ability of the VCM model to predict the complex flow dynamics of a micellar solution.

All these results presented and discussed here for single and two microcylinders cases now may facilitate the understanding of the selection of a preferential path or lane of a viscoelastic fluid during its flow through either an ordered or disordered porous matrix observed in many prior experiments [21, 22, 24, 103, 102]. The onset of this phenomenon may happen due to the flow bifurcation (either 'A' or 'AD' or 'C' state) resulting from the interaction between the shear-thinning properties of the micellar solution and elastic stresses generated in the system, as explained above. Once the fluid prefers to flow through a particular gap region in the porous media due to the flow bifurcation, it forms a lane or path as it moves forward.

Chapter 7

Electrokinetically driven flows of viscoelastic fluids through a microchannel with step expansion and contraction

This chapter aims to demonstrate how the electrokinetically driven flows of viscoelastic polymer solutions generate elastic instability during the flow through a model porous media consisting of a microchannel with step expansion and contraction. The introduction and motivation behind this chapter have already been discussed in section 2.4 of chapter 2.

7.1 Problem illustration

This chapter investigates the problem of electroosmotic transport of viscoelastic fluids in a model porous system consisting of a long micropore with many step expansions and contractions, as schematically shown in Fig. 7.1(a). As the present geometry has a repeating geometrical structure, we have considered a unit cell of this system in our simulations to reduce the computational burden, as schematically depicted in Fig. 7.1(b). The height of both the inlet and outlet sections is H ($= 10\mu m$), whereas the total height of the micropore is $4H$. Here EL and CL are the expansion and contraction lengths of the micropore, respectively, which are varied to investigate their influence on the flow dynamics and other governing parameters. All the solid walls of the micropore possess a constant negative wall zeta potential of ζ_0 . We have placed two electrodes, anode, and cathode, at the micropore inlet and outlet, respectively, and an external potential bias and/or voltage V_0 is applied between them. This, in turn, generates an electric field strength $E_x = \frac{V_0}{L}$ between the two electrodes, where L is the total distance between the inlet and outlet of the microchannel. The electroosmotic flow will happen from the anode towards the cathode due to the interaction between the external applied electric field and the net charges accumulated within the EDL formed in the micropore wall's proximity. The viscoelastic fluid is mixed with a binary monovalent electrolyte, KCl or NaCl, to facilitate this electroosmotic flow. The viscoelastic electrolyte fluid is assumed

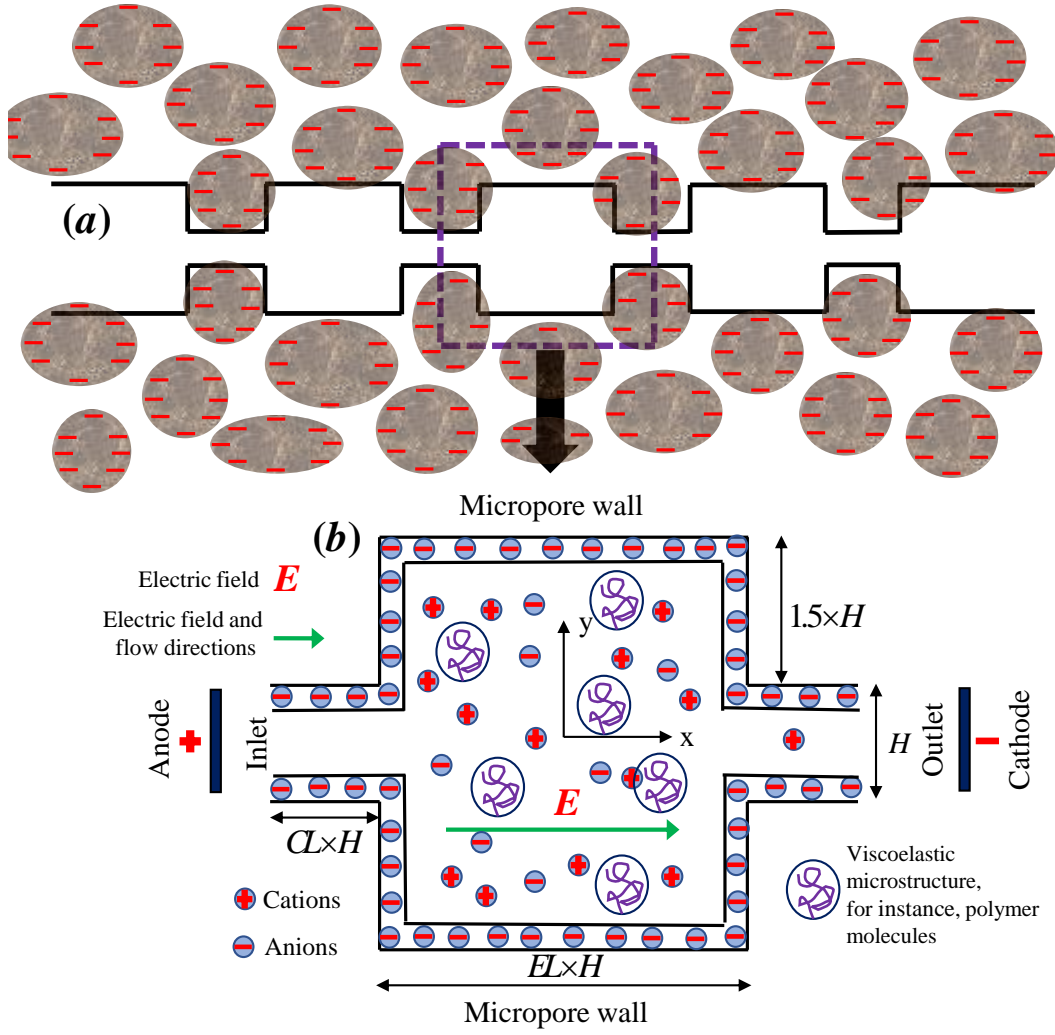


Figure 7.1: (a) Schematic of the present problem (b) Computational domain

to be incompressible. The present study has simulated a perfect creeping flow condition (i.e., $Re = 0$) by setting the inertial terms of the momentum equation equal to zero.

7.2 Numerical details

The governing equations for the electrokinetically driven flows of viscoelastic polymer solutions have already been presented in section 3.1.2 of chapter 3. The following boundary conditions have been employed in this study to tackle the present problem numerically: at all solid walls of the micropore, the standard no-slip and no-penetration conditions ($\mathbf{u} = 0$) for the velocity; a zero gradient ($\nabla p = 0$) for the pressure; a fixed negative value ($\psi = -\zeta_0$) for the electric potential; values are linearly extrapolated for the viscoelas-

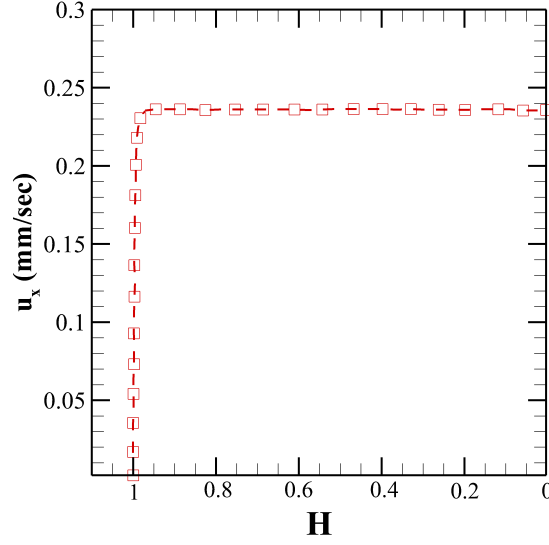


Figure 7.2: Comparison of the stream-wise velocity in a microfluidic channel between the present numerical and analytical results of Afonso et al. [252] at a constant wall zeta potential of $\xi_0 = -110$ mV. Note that the results are presented here for the half non-dimensional height of the microchannel.

tic stress at the micropore wall. At the inlet and outlet sections, a zero gradient for the velocity and viscoelastic stress and a zero value for the pressure are imposed. Furthermore, the computational domain was created using the blockMeshDict subroutine available in OpenFOAM, and a regular hexahedral mesh was used to discretize it. To capture the steep gradients of the velocity, stress, and potential fields in the vicinity of the micropore solid wall, a concentrated mesh was used in this region. For each value of the contraction and expansion length of the micropore, a grid independence test was conducted at the highest value of the Weissenberg number considered in this study. Around 30000 to 45000 hexahedral cells (depending upon the values of EL and CL) in the whole computational domain were adequate to capture the flow physics inside the micropore. This was confirmed by comparing the time-averaged velocity and stress fields at different probe locations and planes passing through the origin of the micropore obtained with at least three different grid densities. Finally, we have presented some validation studies comparing the stream-wise electroosmotic velocity in a microfluidic channel between the present numerical and analytical study of Afonso et al. [252] in Fig. 7.2 for an Oldroyd-B viscoelastic fluid. An excellent agreement can be seen between the two results.

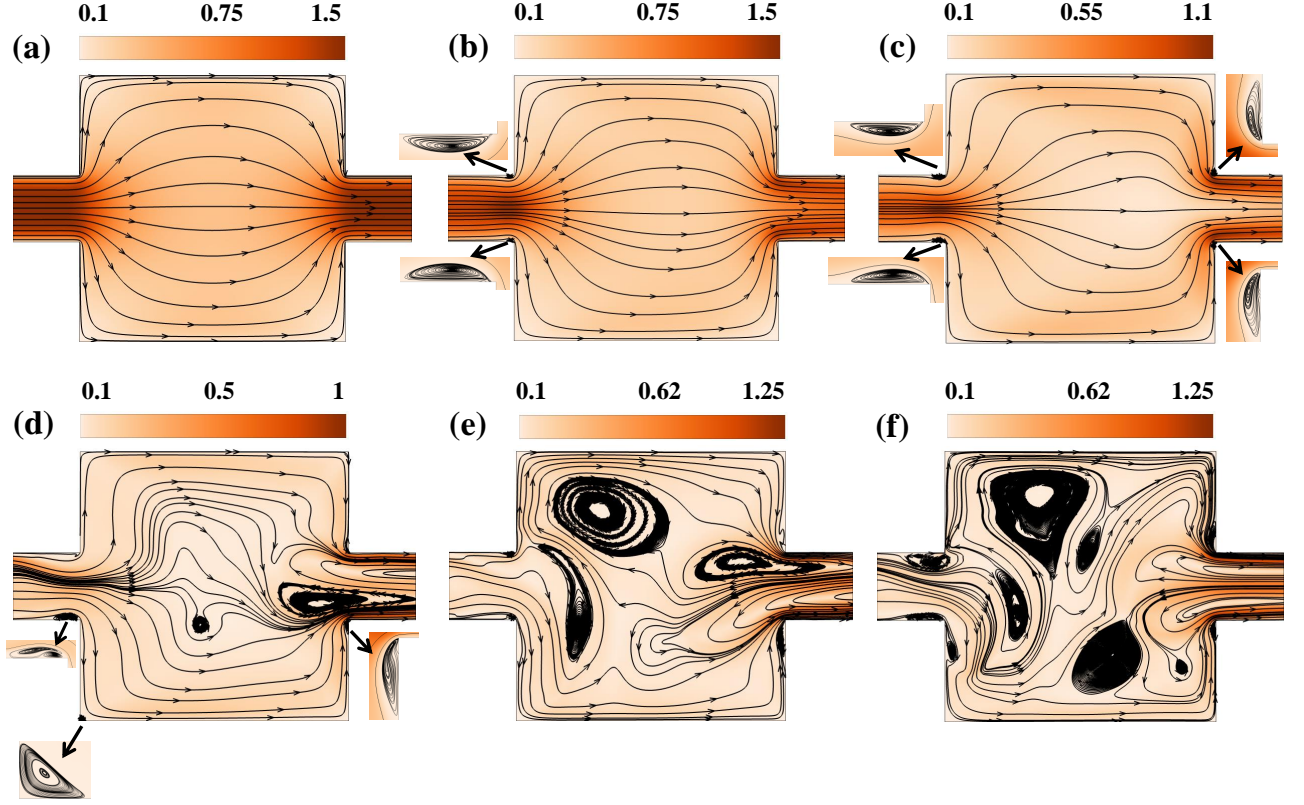


Figure 7.3: Streamlines and velocity magnitude plots for (a) Newtonian and viscoelastic fluids with different Weissenberg numbers, namely, (b) $Wi = 0.5$, (c) $Wi = 2$, (d) $Wi = 7$, (e) and (f) $Wi = 15$ at two different times.

7.3 Results and discussion

7.3.1 Effect of Weissenberg number

The effect of the Weissenberg number on the flow dynamics inside the micropore is studied for the following values of the parameters, namely, $E_x = 5000$ V/m, $EL = 4$, $CL = 1$ and $\beta = 0.4$. The Weissenberg number is varied between 0 and 15. Results for a Newtonian fluid (for which the Weissenberg number is essentially zero, i.e., $Wi = 0$) are also included in the discussion to show the direct effect of elastic properties of the fluid on the flow dynamics inside the micropore. At the outset of our discussion, we present the streamlines and velocity magnitude plots in Fig. 7.3 both for Newtonian and viscoelastic fluids with different Weissenberg numbers to visualize the velocity field inside the micropore. For Newtonian fluids, a steady and symmetric flow field is observed inside the micropore, Fig. 7.3. The symmetry is seen both along the horizontal and vertical mid-planes passing

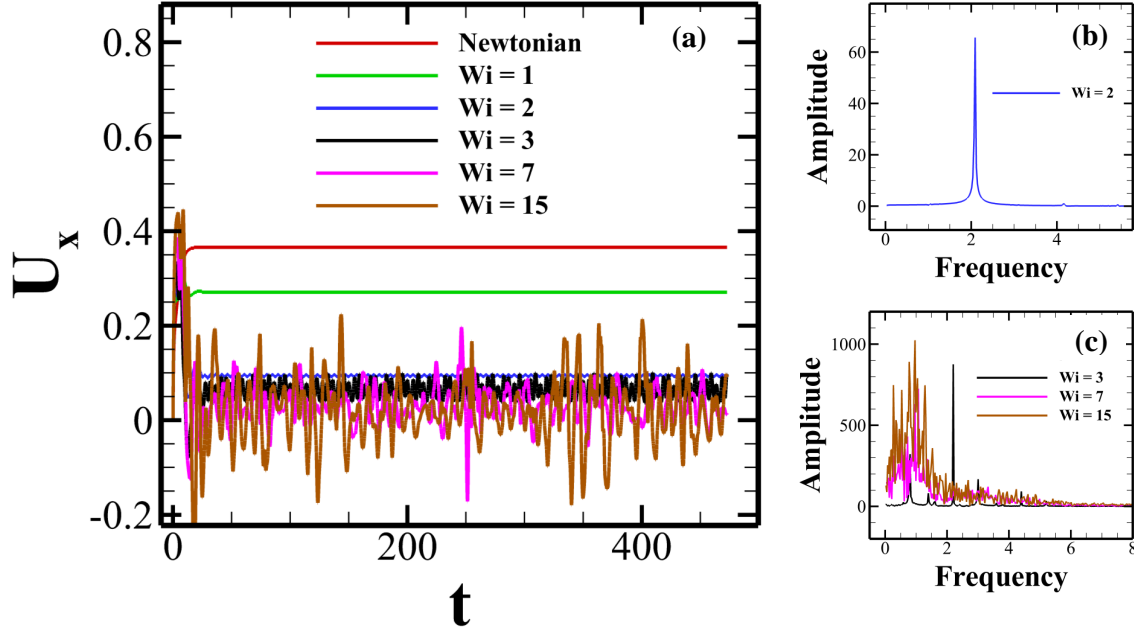


Figure 7.4: (a) Temporal variation of the non-dimensional stream-wise (U_x) velocity component at the origin of the micropore at different Weissenberg numbers. (b) and (c) Power spectral density plots of velocity fluctuations.

through the origin of the micropore. The streamlines are concentrated in the contraction regions (inlet and outlet of the micropore), whereas they are dispersed in the expansion region of the micropore. The velocity magnitude is high in the contraction region and low in the expansion region, as expected from the conservation of mass principle. This kind of flow behaviour is expected for a Newtonian fluid flowing in a symmetric geometry in the creeping flow regime.

On the other hand, the flow phenomena for viscoelastic fluids inside the micropore become increasingly complex as the Weissenberg number gradually increases. At very low values of the Weissenberg number (< 0.1), the flow dynamics inside the micropore resemble the Newtonian fluid behaviour (the results are not seen here). This is because, at these very low values of the Weissenberg number, the elastic forces are so small that they can not overcome the effect of the viscous forces. Hence, the viscoelastic fluid behaves like a Newtonian fluid. However, as the Weissenberg number gradually further increases, the elastic forces also progressively increase. As a result, the flow dynamics inside the micropore also change significantly. For instance, at a relatively higher value of $Wi = 0.5$, one can see that the vertical symmetry seen in the flow profile is destroyed; however, the horizontal flow symmetry still exists, as seen from sub-Fig. 7.3(b). Furthermore, at this

Weissenberg number, lip vortices are formed at the entrant corners of the micropore. As the Weissenberg number further increases to 2 (sub-Fig. 7.3(c)), lip vortices are also seen to form near the re-entrant corners of the micropore. As we have simulated a perfect creeping flow condition in the present study, the effect of the inertial forces on the flow dynamics is absent. Therefore, the formation of such a lip vortex is purely driven by the elastic forces present in the viscoelastic fluid. The appearance of such lip vortex around the corners has also been seen in the pressure-driven flows of polymer and micellar solutions in geometries like sharp bend, cross-slot, micropore with step and contraction, etc. [253, 254, 255, 97, 100]. The size of these lip vortices increases with the Weissenberg number, as was also observed in the pressure-driven flows.

With the further increment in the Weissenberg number, say to $Wi = 7$ (sub-Fig. 7.3(d)), the streamlines become distorted. Also, vortices are formed inside the micropore, indicating the presence of a chaotic flow field inside the micropore. These tendencies become more pronounced as the Weissenberg number further increases; for instance, see the results presented at $Wi = 15$ in sub-Figs. 7.3(e) and (f) at two different times. The size and location of these vortices become time-dependent, as can be seen from the results presented at two different times for $Wi = 15$. As the Weissenberg number gradually increases, the following trend in the vortex dynamics inside the micropore occurs: lip vortices at the entrant corners \rightarrow lip vortices both at entrant and re-entrant corners \rightarrow vortices inside the micropore.

Therefore, a transition in the flow field from steady to unsteady happens in the micropore as the Weissenberg number gradually increases. It is further clear from Fig. 7.4 wherein the temporal variation of the non-dimensional stream-wise velocity U_x at a probe location placed at the origin of the micropore is presented at different Weissenberg numbers. As expected, the velocity reaches a constant value with time for a Newtonian fluid. Similarly, it happens for viscoelastic fluids with a Weissenberg number of up to 1, indicating the presence of a steady flow field inside the micropore. However, at $Wi = 2$, the velocity is seen to fluctuate with time, which is a signature of the presence of unsteadiness in the flow field. The corresponding power spectral density plot (calculated by applying the Fast Fourier Transform (FFT) on the time-series of velocity signal at a probe location) of the velocity fluctuations is shown in sub-Fig. 7.4(b) to know the nature of this unsteadiness in the flow field. The velocity fluctuations are governed by

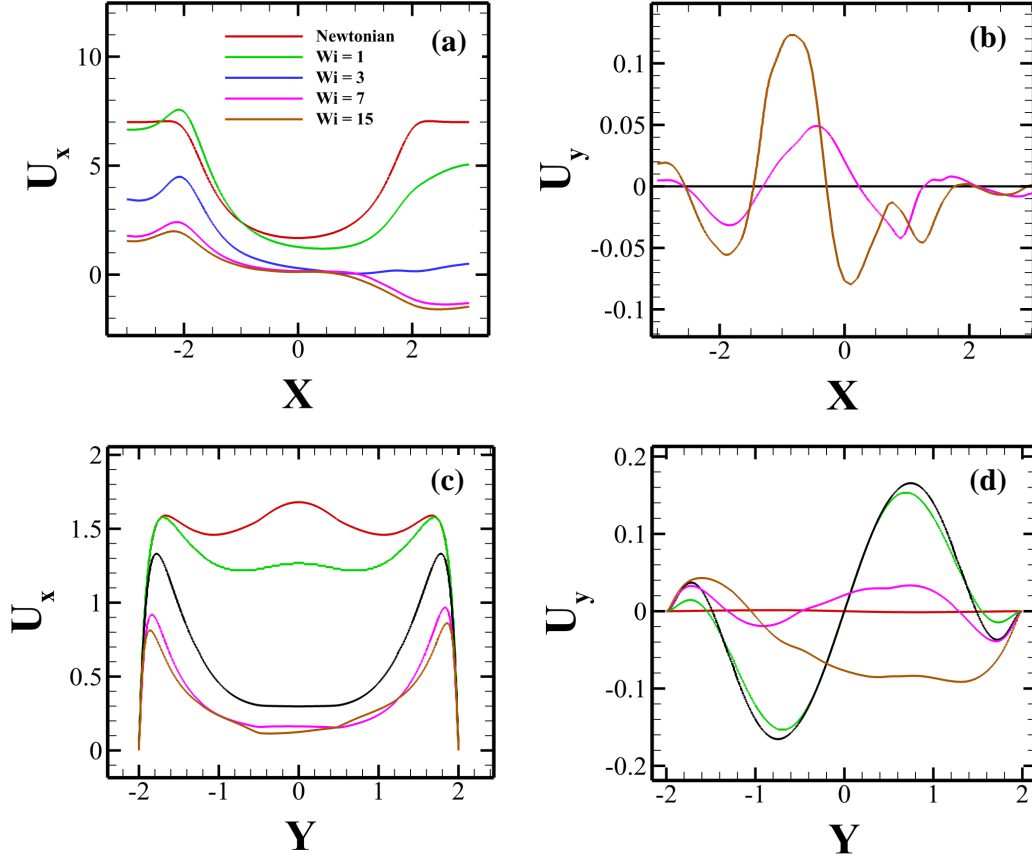


Figure 7.5: Variation of the non-dimensional stream-wise (U_x) and span-wise (U_y) velocity components along horizontal (a and b) and vertical (c and d) mid-planes passing through the origin of the micropore.

a single dominant frequency at $Wi = 2$, suggesting the presence of a periodic unsteady flow field inside the micropore. As the Weissenberg number further increases, say to 7, an aperiodic fluctuation in the velocity field can be seen. This tendency increases further as the Weissenberg number further increases to 15. A dominant primary frequency now governs the velocity fluctuations and several secondary frequencies instead of a single frequency at $Wi = 2$. Such secondary frequencies suggest that the excitation of the fluid motion now occurs over a broad spectrum of time and length scales. This indicates the presence of a quasi-periodic flow state in the micropore at these values of the Weissenberg number. At this state, the flow inside the micropore also becomes highly asymmetric. Therefore, in summary, as the Weissenberg number gradually increases, the transition in the flow field inside the micropore occurs as: steady and symmetric \rightarrow unsteady, periodic and symmetric \rightarrow unsteady, quasi-periodic and asymmetric.

To get more insights into the flow physics, both the time-averaged stream-wise and span-wise velocities are plotted along the horizontal and vertical mid-planes passing

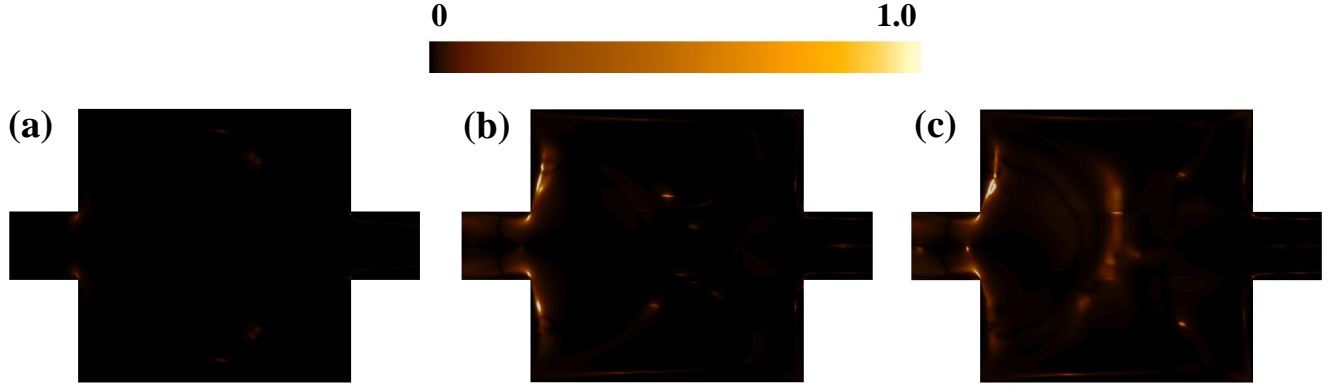


Figure 7.6: Variation of the Pakdel-McKinley M parameter at different Weissenberg numbers, namely, (a) $Wi = 0.5$, (b) $Wi = 6$, and (c) $Wi = 15$.

through the origin of the micropore in Fig. 7.5. For Newtonian fluids, as expected, the stream-wise velocity shows a perfect symmetry both along the horizontal and vertical mid-planes of the micropore. In contrast, the span-wise velocity remains almost zero, indicating the presence of a one-dimensional flow field inside the micropore. However, for viscoelastic fluids, the stream-wise velocity shows an overshoot in its value at the entrant region of the micropore, sub-Fig. 7.5(a). This is due to the formation of the lip vortex, which squeezes the flow in the middle of the entrant region. The stream-wise velocity profile along the horizontal mid-plane also progressively becomes asymmetric in its distribution with the Weissenberg number, which suggests an increase in the tendency to form an asymmetric flow field within the micropore. Furthermore, the span-wise velocity now acquires a finite value, particularly at high Weissenberg numbers, sub-Fig. 7.5(b). Therefore, it indicates a two-dimensional flow field inside the micropore at high Weissenberg numbers. The stream-wise velocity along the vertical mid-plane of the micropore shows maximum values in the middle of the micropore for Newtonian fluids. In contrast, the maximum values for viscoelastic fluids occur near the top and bottom horizontal walls, as seen from sub-Fig. 7.5(c). Furthermore, these velocity overshoots near the top and bottom horizontal walls decrease with the Weissenberg number. Once again, the span-wise velocity along the vertical mid-plane is zero for Newtonian fluids. In contrast, it gains an increasing value with the Weissenberg number for viscoelastic fluids, sub-Fig. 7.5(d).

Therefore, from the results presented here, it is clear that the flow field inside the micropore transits from steady to an unsteady and fluctuating one as the Weissenberg number gradually increases in the case of viscoelastic fluids. The reason behind the

origin of such an unstable flow field is due to the increase in the elastic stresses with the Weissenberg number, which ultimately leads to an electro-elastic instability in the system. As mentioned earlier in the introduction section, these instabilities originated due to the interaction between the normal tensile stresses and streamline curvature present in the system. It has already been observed in many prior electrokinetically driven microflows [120, 121, 122]. To understand these instabilities in more detail, the following M parameter criterion developed by McKinley and co-workers [18, 250] is often used

$$M = \sqrt{\frac{\tau_{11}}{\eta_0 \dot{\gamma}} \frac{\lambda U}{\mathcal{R}}} \geq M_{crit} \quad (7.1)$$

In the above equation, τ_{11} is the normal elastic stress in the flow direction along a curved streamline, $\dot{\gamma}$ is the characteristic value of the local deformation rate, \mathcal{R} is the characteristic radius of the streamline curvature. For a two-dimensional flow field, these can be determined as follows [256]. The streamline curvature can be calculated as

$$\frac{1}{\mathcal{R}(x,y)} = \frac{\left(\frac{\partial \psi}{\partial x}\right)^2 \frac{\partial^2 \psi}{\partial y^2} + \left(\frac{\partial \psi}{\partial y}\right)^2 \frac{\partial^2 \psi}{\partial x^2} - 2 \frac{\partial \psi}{\partial y} \frac{\partial \psi}{\partial x} \frac{\partial^2 \psi}{\partial x \partial y}}{\left[\left(\frac{\partial \psi}{\partial x}\right)^2 + \left(\frac{\partial \psi}{\partial y}\right)^2\right]^{3/2}} \quad \text{where } \psi \text{ is the stream function and } u_x = -\frac{\partial \psi}{\partial y}$$

and $u_y = \frac{\partial \psi}{\partial x}$. The normal elastic stress along a curved streamline can be calculated as $\tau_{11} = \mathbf{t} \cdot \boldsymbol{\tau} \cdot \mathbf{t} = \tau_{xx} t_x^2 + \tau_{yy} t_y^2 + 2\tau_{xy} t_x t_y$ where $\mathbf{t} = t_x \mathbf{e}_x + t_y \mathbf{e}_y$ is the tangent vector along a streamline whose components are calculated as $t_x = -\frac{\frac{\partial \psi}{\partial y}}{|\nabla \psi|}$ and $t_y = \frac{\frac{\partial \psi}{\partial x}}{|\nabla \psi|}$. Here \mathbf{e}_x and \mathbf{e}_y are the unit vectors in the x and y directions, respectively. According to this criterion, elastic instability will emerge in a flow field when this non-dimensional parameter M exceeds a critical value M_{crit} . We have also calculated this M parameter and plotted it in Fig. 7.6 at three different values of the Weissenberg number, namely, 0.5, 6, and 15. We have used the time-averaged velocity field to calculate this parameter, whose values are adjusted on a scale between 0 and 1. At a very low value of the Weissenberg number, for instance, at $Wi = 0.5$ (sub-Fig. 7.6(a)), the value of the M parameter is so small that the plot becomes almost black. However, its value increases as the Weissenberg number increases due to an increase in the elastic stresses within the system; for instance, see the results presented at $Wi = 6$ and 15 in sub-Figs. 7.6(b) and (c), respectively. In particular, one can see that the value of the M parameter is high around the entrant corners of the micropore due to the presence of high streamline curvature and high elastic stresses in these regions. Therefore, these regions are prone to the origin of these purely elastic in-

stabilities in the system. For the electrokinetically driven flows in microfluidic cross-slot and flow-focusing devices, a similar finding was also seen [121].

7.3.2 Effect of expansion and contraction lengths

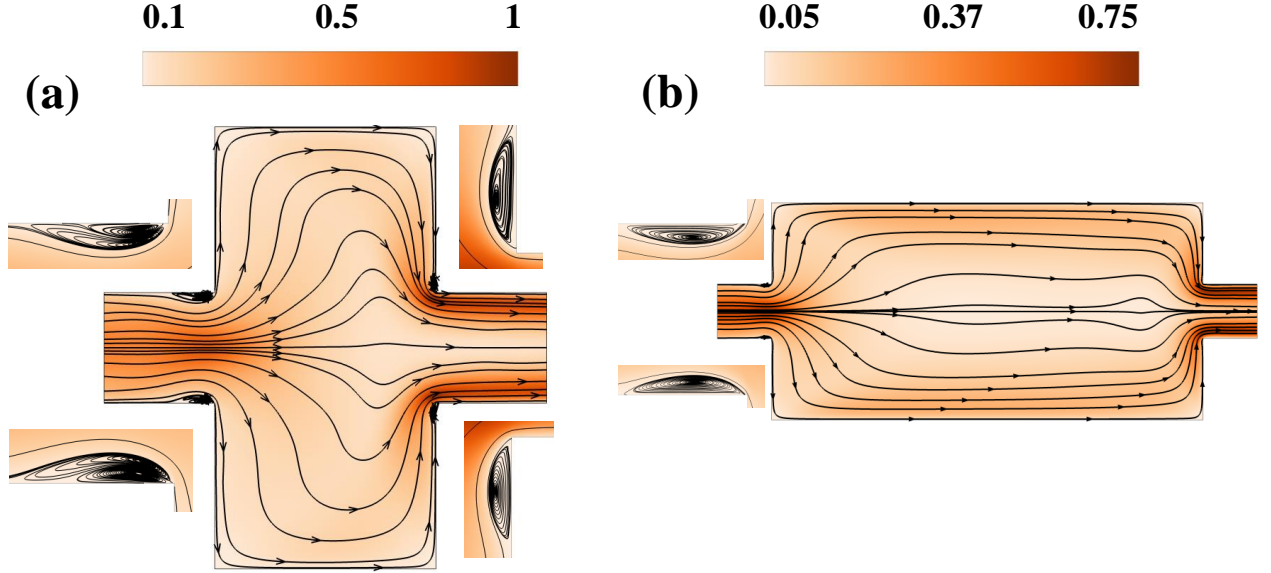


Figure 7.7: Streamlines and velocity magnitude plots inside the micropore at two different values of EL , namely, 2 (a) and 8 (b) at $Wi = 3$. Note that here the x-axis label values in the zoomed-in figures are non-dimensional.

This subsection shows how the expansion (EL) and contraction (CL) lengths of the micropore tend to influence the onset of the electro-elastic instability and the associated flow dynamics inside the micropore. While the electric field strength and polymer viscosity ratio are kept constant at 5000 V/m and 0.5 for this study, the non-dimensional values of EL and CL are varied as 2, 4, 8, and 1, 3, 5, respectively. For each value of either EL or CL , the Weissenberg number is varied between 0 and 15. Figure 7.7 shows the streamlines and velocity magnitude plots inside the micropore at two different values of the expansion length, namely, 2 and 8 at $Wi = 3$. First, irrespective of the value of EL , lip vortices are formed near entrant corners of the micropore. This can be seen from the zoomed-in sub-figures in Fig. 7.7. The length of this lip vortex is larger for $EL = 2$ than that for $EL = 8$. The streamlines are more distorted, particularly in the middle of the micropore for $EL = 2$ than $EL = 8$. This is simply due to the availability of more span-wise space than stream-wise space for the fluid to flow in the former micropore than in the latter one. The velocity magnitude is seen to be high in the entrant and re-entrant

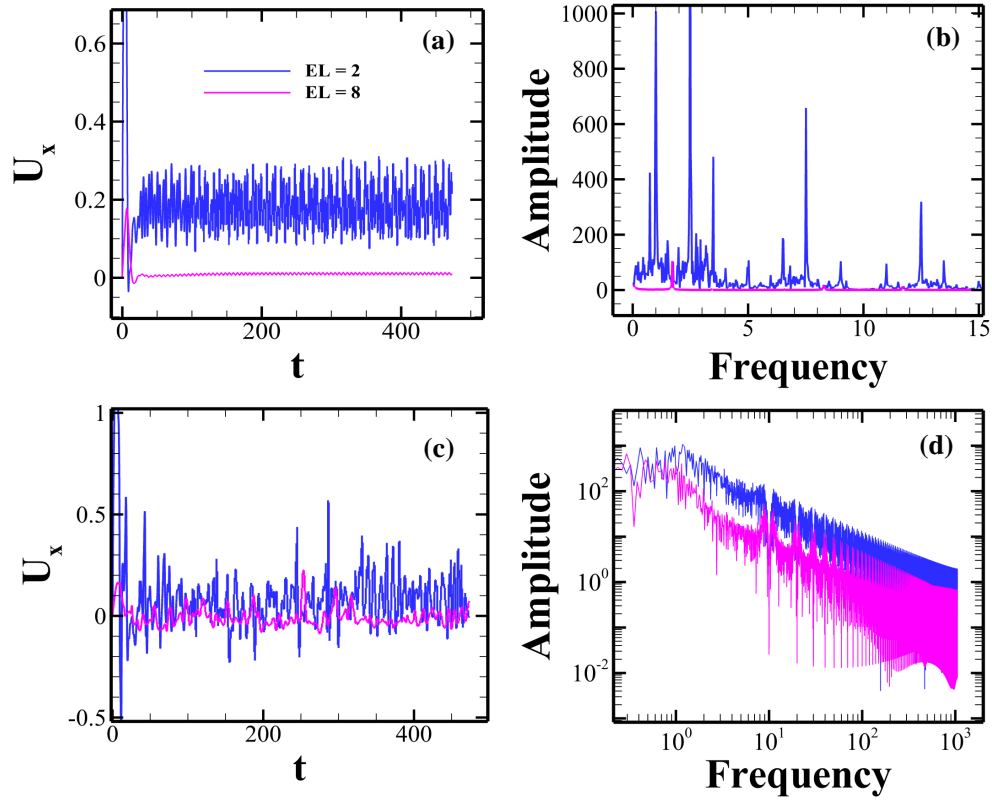


Figure 7.8: Temporal variation of the stream-wise velocity at a probe location placed at the origin of the micropore at $Wi = 3$ (a) and 15 (c) at two different values of the expansion length, namely, 2 and 8. The corresponding power spectrum plot of the velocity fluctuations is presented in (b) and (d), respectively.

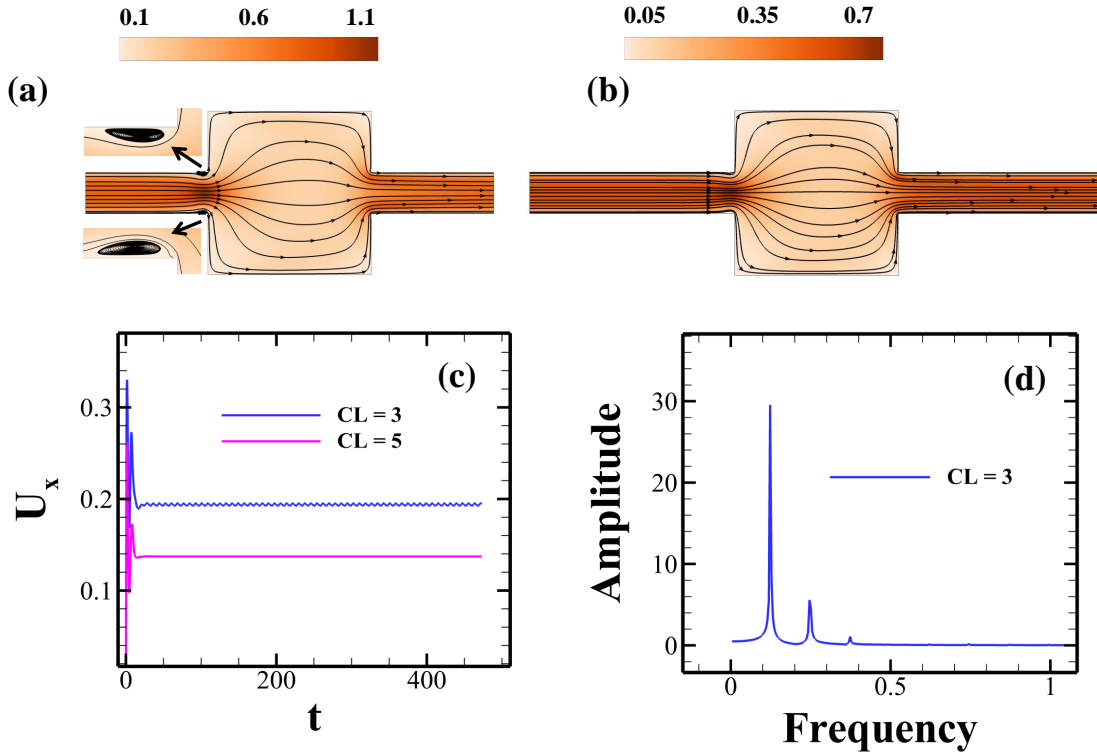


Figure 7.9: Streamlines and velocity magnitude plots inside the micropore with $CL = 3$ (a) and 5 (b). The temporal variation of the stream-wise velocity and power spectrum of velocity fluctuations are shown in sub-Figures (c) and (d). Here all the results are presented at $Wi = 3$. Note that the x-axis label values in the zoomed-in figures are non-dimensional.

regions of both the micropores; however, its maximum value is found to be larger for $El = 2$ than that seen for $El = 8$ due to the availability of less area for the former micropore than the latter one. Furthermore, lip vortices appear near re-entrant corners for $EL = 2$, whereas they are absent for $EL = 8$ under the same conditions. This is because the effect of elastic forces (which ultimately leads to the formation of these lip vortices) on the flow dynamics around the re-entrant corners is expected to be more for micropore with $EL = 2$ than that with $EL = 8$ due to the smaller stream-wise length of the former micropore. Therefore, this trend in the flow behaviour suggests that the influence of the fluid elasticity on the flow dynamics inside the micropore gradually diminishes as its expansion length progressively increases, keeping everything else the same.

To gain more insights into the flow behaviour at different values of the expansion length, we have plotted the temporal variation and power spectrum of fluctuations of the non-dimensional stream-wise velocity component in Fig. 7.8. At $Wi = 3$, the velocity shows a regular and periodic fluctuation for $EL = 8$, whereas an irregular and aperiodic

fluctuation is observed for $EL = 2$. This suggests that the onset of the electro-elastic instability is delayed to higher values of the Weissenberg number as the expansion length of the micropore increases. The reason behind this can be explained as follows: to study the effect of the fluid elasticity on the local flow dynamics, we can define a local Deborah number based on the time required for a fluid parcel to travel from the entrant region to the re-entrant region of the micropore. This time is directly proportional to the expansion length of the micropore, resulting in a decrease in the local Deborah number with the expansion length. Therefore, the effect of the fluid elasticity on the flow field inside the micropore also decreases with the expansion length. This ultimately delays the onset of the electro-elastic instability inside the micropore.

Furthermore, the intensity of the velocity fluctuations increases with the decreasing value of the expansion length, as evident from the PSD plot presented in sub-Fig. 7.4(b). This is because of the increase in the local Deborah number with the decreasing value of the expansion length. On the other hand, at $Wi = 15$, the stream-wise velocity (at the same probe location as that presented at $Wi = 3$) shows an irregular and aperiodic variation with time for both the values of the expansion length, suggesting the presence of a more chaotic flow state inside the micropore, sub-Fig. 7.8(c). It is more obvious from the power spectrum plot of the velocity fluctuations presented in sub-Fig. 7.8(d) wherein the excitation of the fluid motion over a wide range of continuum frequencies can be seen.

The influence of the contraction length (CL) on the flow dynamics inside the micropore is shown in Fig. 7.9 at $Wi = 3$. The formation of entrant lip vortices can be seen both for $CL = 3$ and 5. However, the lip vortex size is larger for $CL = 3$ than for $CL = 5$; see the zoomed-in subfigures. The temporal variation of the non-dimensional stream-wise velocity and its power spectrum at a probe location placed at the origin of the micropore is shown in sub-Fig. 7.9 for two values of the contraction length. The velocity shows regular periodic fluctuations for $CL = 3$, whereas it reaches a steady value for $CL = 5$ at the same Weissenberg number of 3. Therefore, it suggests that the transition in the flow field from periodic to quasi-periodic (as well as the onset of electro-elastic instability) happens at lower values of the Weissenberg number as the contraction length of the micropore decreases. Furthermore, the flow field inside the micropore also becomes more chaotic as its contraction length gradually decreases.

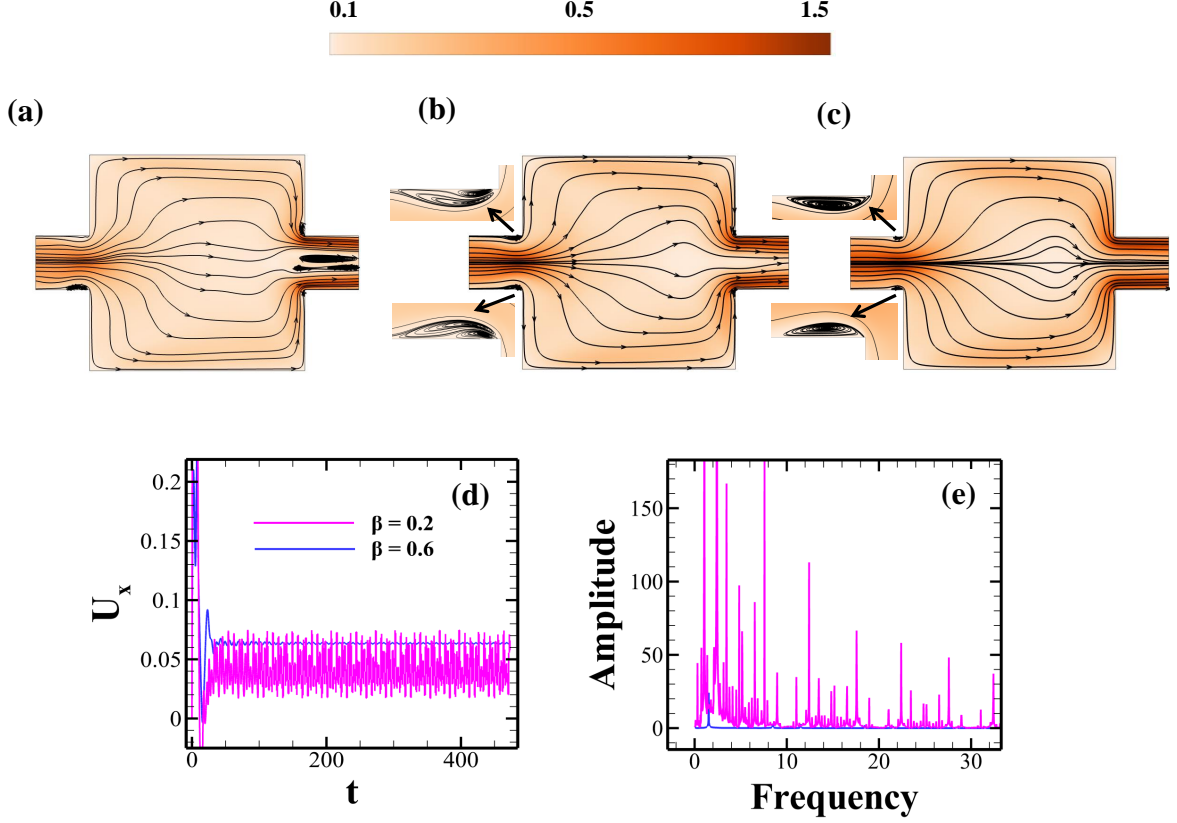


Figure 7.10: Streamlines and velocity magnitude plots at different values of the polymer viscosity ratio, (a) $\beta = 0.2$, (b) $\beta = 0.4$, and (c) $\beta = 0.6$. (d) Temporal variation of the stream-wise velocity at a probe location placed at the origin of the micropore at two different values of the polymer viscosity ratio. (e) The corresponding power spectrum plot of velocity fluctuations at $\beta = 0.2$. Here all the results are presented at $Wi = 3$.

7.3.3 Effect of polymer viscosity ratio

In this subsection, we have studied the influence of the polymer viscosity ratio β on the flow dynamics inside the micropore. It is related to the polymer concentration by the formula $\beta = \frac{1}{1+c}$, where c is the polymer concentration in the solution [257]. To perform so, we have carried out simulations for three different values of the polymer viscosity ratio, namely, 0.2, 0.4, and 0.6. The electric field strength is kept constant at $E_x = 5000$ V/m, whereas the Weissenberg number is varied between 0 and 15 for each value of β . Note that as the value of β increases, the polymer concentration in the solution decreases, and it ultimately reaches to zero when $\beta = 1$, which represents the Newtonian solvent only. The streamlines and velocity magnitude inside the micropore at three different values of the polymer viscosity ratio are shown in Fig. 7.10 at $Wi = 3$. First, the maximum value of the velocity magnitude increases with the decreasing value of the

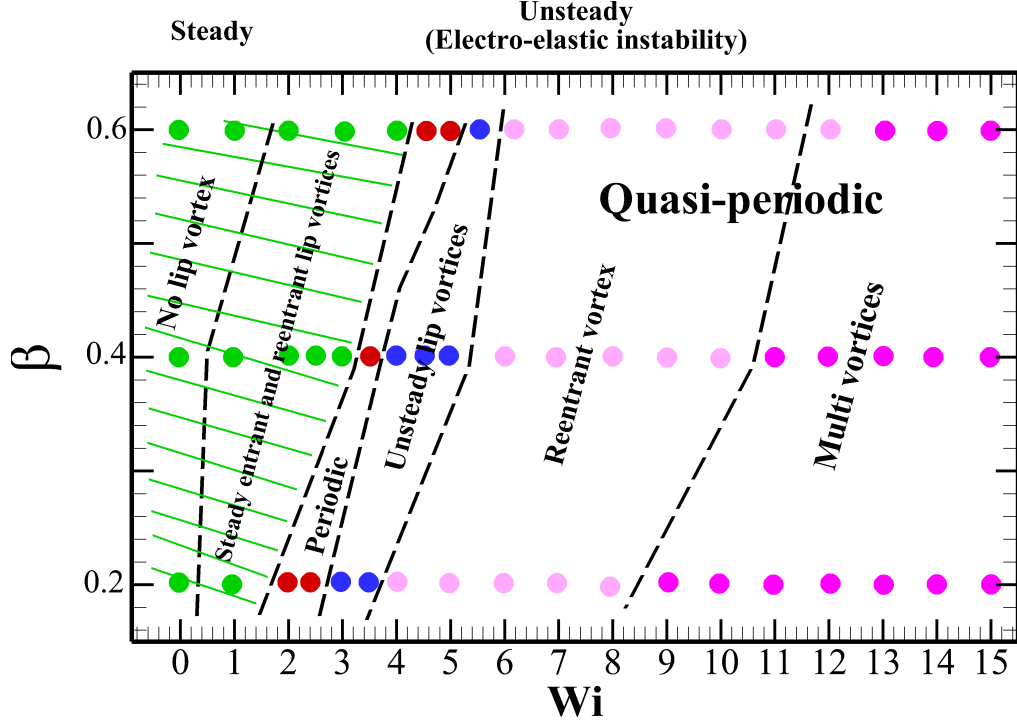


Figure 7.11: Phase diagram showing the existence of different flow states in $\beta - Wi$ space.

polymer viscosity ratio. Secondly, at this value of the Weissenberg number, both the entrant and re-entrant lip vortices are formed for $\beta = 0.2$, sub-Fig. 7.10(a). In contrast, only the entrant lip vortex appears for $\beta = 0.4$ (sub-Fig. 7.10(b), whereas no lip vortex appears for $\beta = 0.6$ (sub-Fig. 7.10(c)). Furthermore, the entrant lip vortex size is larger for $\beta = 0.2$ than that seen for $\beta = 0.4$. Therefore, it suggests that the tendency in appearing lip vortices inside the micropore increases as the polymer viscosity ratio decreases and/or the polymer concentration in the solution increases. This trend is further accentuated as the Weissenberg number further increases.

The type of flow field inside the micropore also strongly depends on the polymer viscosity ratio. In sub-Fig. 7.10(d), the temporal variation of the non-dimensional stream-wise velocity at a probe location placed at the micropore origin is plotted at two values of the polymer viscosity ratio, namely, 0.2 and 0.6. It shows that the flow dynamics become fluctuating inside the micropore at $\beta = 0.2$ and 0.6. However, from the PSD plot presented in sub-Fig. 7.10(e), it is seen that the fluctuations of the flow field are quasi-periodic at $\beta = 0.2$, whereas they are periodic at $\beta = 0.6$. This flow behaviour indicates that the transition from a steady to unsteady flow regime (where the electro-elastic instability starts to appear) delays to higher values of the Weissenberg number as

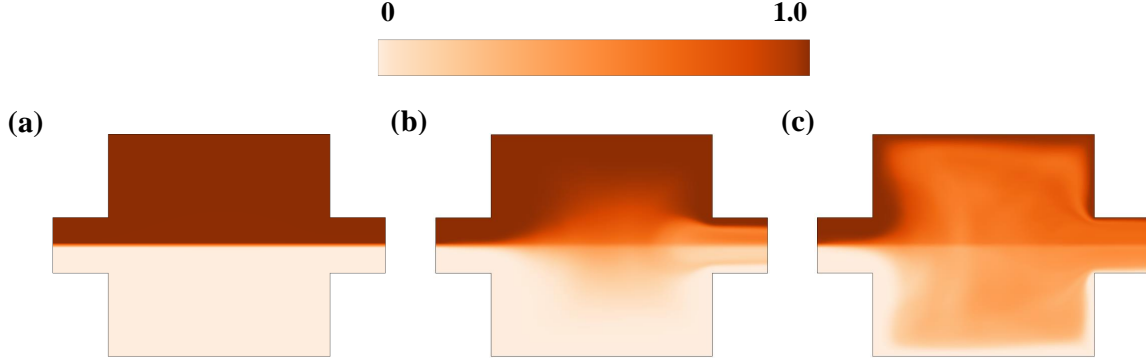


Figure 7.12: Instantaneous dye concentration profile inside the micropore. (a) $Wi = 0.1$ (b) $Wi = 6$ and (c) $Wi = 15$. Here the profile at different values of the Weissenberg number is shown at the same non-dimensional time of $t = 100$. Other simulation parameters are kept constant as $E_x = 5000$ and $\beta = 0.4$.

the polymer viscosity ratio gradually increases.

A phase diagram plot demarcating different flow states in $\beta - Wi$ space is presented in Fig. 7.11. It demonstrates that the critical value of the Weissenberg number increases (at which the transition from steady to unsteady flow field or the onset of the electro-elastic instability occurs) as the polymer viscosity ratio increases. For instance, at $\beta = 0.2$, this critical value is around 2, whereas it is around 3.8 at $\beta = 0.6$. Below this critical value of the Weissenberg number, a steady flow field exists, which can be further classified into the following categories with the gradual increment of the Weissenberg number at any value of β , namely, steady and symmetric or Newtonian-like, steady and asymmetric, the appearance of the steady entrant and re-entrant lip vortices. On the other hand, beyond this critical value of the Weissenberg number, an unsteady flow field exists, broadly classified into two flow states, namely, periodic and quasi-periodic. Other flow states can also be seen within the latter category, such as unsteady lip vortex, re-entrant vortex, multi vortices, etc. This phase diagram clearly shows that the transition from any flow state to another is delayed to higher values of the Weissenberg number as the polymer viscosity ratio increases.

7.3.4 Further applications

Not only the present model system would be helpful to understand the transport of complex viscoelastic fluids under the influence of an electric field in porous media, but it

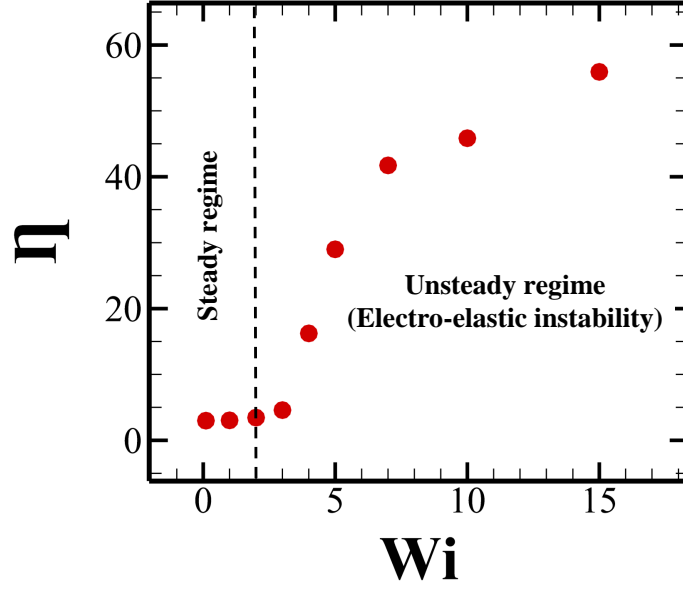


Figure 7.13: Variation of the mixing efficiency parameter η with the Weissenberg number.

can also be used in other practical applications such as mixing fluids. This process is often needed for chemical and biochemical analyses in lab-on-chip microfluidic devices [258, 170]. However, due to the presence of laminar flow conditions, mixing fluids is often challenging in these small-scale systems. Therefore, over the years, many designs and techniques based on passive and active modes have been developed to enhance the mixing efficiency in various micro-scale systems; for instance, see some excellent review articles on electrokinetic mixing in the literature [157, 158]. In this study, we show that if the working fluids to be mixed are viscoelastic (or one can add a minute amount of solid polymers into the working fluid to make it viscoelastic). One can use this model system of a long micropore with step expansion and contraction to mix such fluids. To show the potential of the proposed approach, we have taken the same fluids which are needed to be mixed. We have added a dye with a finite concentration into the fluid entering into the upper half of the micropore. In contrast, a zero dye concentration is taken in the fluid entering the micropore's lower half, as schematically shown in sub-Fig. 7.12(a). The following convective-diffusive equation has been solved to track the dye concentration inside the microchannel to evaluate the mixing efficiency.

$$\frac{\partial c}{\partial t} + u \cdot \nabla c = D \nabla^2 c \quad (7.2)$$

In the above equation, c is the dye concentration, and D is the diffusivity of the dye. Here, the value of the diffusivity D is kept constant at a very lower value of $4 \times 10^{-14} \text{ m}^2/\text{s}$. Therefore, the Peclet number ($Pe = \frac{HU_0}{D}$) becomes much larger than one so that the mixing phenomenon of the dye becomes dominated due to the advection, not due to the diffusion. Figure 7.12 shows the instantaneous dye concentration profile inside the microchannel at different Weissenberg numbers at the same time. It is seen that at a low Weissenberg number, for instance, at $Wi = 0.1$ (sub-Fig. 7.12(a)), no mixing of the fluids happens. However, as the Weissenberg number increases to 6, the mixing of the two fluids can be seen mainly in the middle of the micropore, sub-Fig. 7.12(b). This is because of the presence of the electro-elastic instability at this Weissenberg number, resulting in an increase in the chaotic advection and hence the mixing phenomenon. As the Weissenberg number further increases to 15, the strength of this chaotic advection inside the micropore due to this EEI further increases, and hence the mixing phenomenon between the two fluids also further increases, sub-Fig. 7.12(c).

To quantitatively show the mixing efficiency between the two fluids, we have also calculated the mixing index η defined as [157, 158]

$$\eta = 1 - \frac{\sqrt{\frac{1}{N} \sum_1^N (\bar{C}_s - \bar{C}_s^*)^2}}{\sqrt{\frac{1}{N} \sum_1^N (\bar{C}_s^0 - \bar{C}_s^*)^2}} \quad (7.3)$$

Here \bar{C}_s , \bar{C}_s^* and \bar{C}_s^0 are the dye concentration at a point within the micropore, dye concentration for a perfectly mixed fluid and dye concentration for an unmixed fluid, respectively. The value of \bar{C}_s^0 can be either 0 or 1, and hence the value of \bar{C}_s^* would be 0.5. Therefore, the denominator of equation 7.3 has a constant value of 0.5. The theoretical range of η lies between 0 and 1, representing perfectly unmixed and mixed fluids, respectively. Note that the calculation of this parameter is performed at the outlet of the micropore. Figure 7.13 depicts the variation of the mixing efficiency parameter with the Weissenberg number. The mixing efficiency is seen to be almost zero in the steady flow regime. However, it attains a finite value in the unsteady flow regime once the electro-elastic instability develops in the system after a critical value of the Weissenberg number. Then it gradually increases with the Weissenberg number due to the progressive increase in the chaotic advection inside the micropore. All these results confirm that the present simple system of a long micropore with step expansion and contraction could also be

successfully used to mix two viscoelastic fluids under the influence of an electric field. It should be mentioned here that the enhancement of mixing due to this elastic instability was also observed in earlier investigations dealing with pressure-driven flows in geometries such as Couette cell [147, 259]. This study further shows that this enhancement in mixing even could be achieved in electrokinetically driven flows through a relatively simpler geometry consisting of a microchannel with step expansion and contraction with no moving parts.

Chapter 8

Electrokinetically driven flows of viscoelastic fluids past a microcylinder confined in a channel

This chapter aims to demonstrate how the electro-elastic instability (EEI) phenomenon in viscoelastic fluid flows past a cylindrical obstacle confined in a microchannel originating the flow-switching phenomenon and, subsequently, facilitating the mixing of these fluids in this simple microdevice. To achieve this, both numerical simulations and experimental investigations have been conducted. Furthermore, the data-driven dynamic mode decomposition (DMD) technique has been employed to better understand the chaotic flow dynamics arising in this flow system. The introduction and motivation behind this chapter have already been discussed in section 2.5 of chapter 2.

8.1 Microfluidic setup

The schematic of the present microfluidic setup considered in this study is depicted in sub-Fig. 8.1(a). It consists of a single microcylinder of diameter $d = 0.5 \text{ mm}$ placed in the middle of a long microchannel of width $w = 0.6 \text{ mm}$, and of a total length of $L = L_u + L_d = 14 \text{ mm}$. Here L_u and L_d are the upstream and downstream lengths of the channel, as schematically shown in Fig. 8.1(a). The depth of the microchannel is $100 \mu\text{m}$. The present study considers a fixed blockage ratio of $BR = \frac{d}{w} = 0.83$ both in the simulations and experiments. Two electrodes have been placed at the channel inlet and outlet, and a voltage bias of V_0 is applied between them so that an external electric field strength of $E_x = \frac{V_0}{L}$ is created. This, in turn, creates an electric potential in the domain to induce the flow. All the solid walls of the geometry possess a constant negative wall zeta potential of ζ_0 . The electroosmotic flow occurs from the anode to the cathode due to the interaction between the external electric field and the net charge accumulated within the electrical double layer (EDL). To facilitate this electroosmotic flow, the viscoelastic fluid is mixed with a binary monovalent electrolyte, and the resulting viscoelastic electrolyte fluid is assumed to be incompressible.

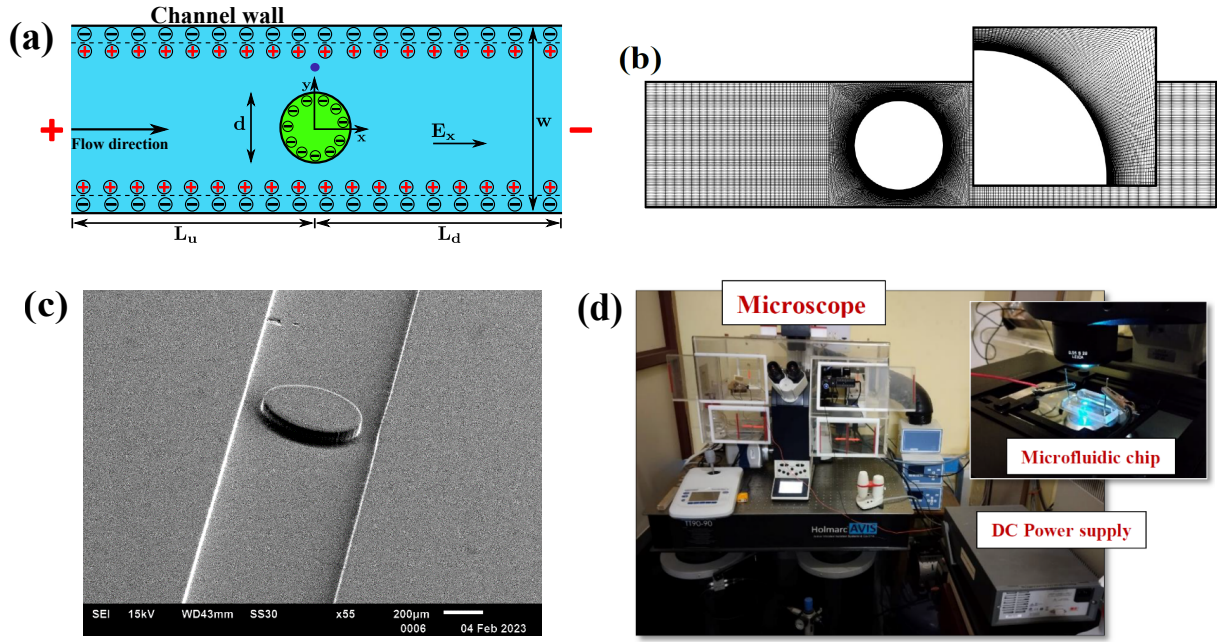


Figure 8.1: (a) Schematic of the present problem and (b) grid structure (grid G3) used in the present numerical simulation. (c) SEM image of PDMS microfluidic setup, and (d) experimental setup with the platinum electrode and connected DC power supply. Here, the blue dot in the schematic of the problem setup is the probe location where the velocity is measured and analyzed.

8.2 Methodology

8.2.1 Numerical details

The governing equations and numerical solution technique details have already been presented in subsection 3.1 of chapter 3. The following boundary conditions have been employed to solve the present problem numerically: at all solid walls of the microchannel and cylinder, the standard no-slip and no-penetration conditions ($\mathbf{u} = 0$) for the velocity; a zero gradient ($\nabla p = 0$) for the pressure; a fixed negative value ($\psi = -\zeta_0$) for the electric potential; values are linearly extrapolated for the viscoelastic stress at the channel wall. At the inlet and outlet sections, a zero gradient for the velocity and viscoelastic stress and a zero value for the pressure are imposed. A regular hexahedral mesh was used to discretize the whole computational domain. A very fine mesh was used near the cylinder to capture the steep gradients of velocity, stress, and potential fields, as schematically shown in Fig. 8.1(b). An optimum grid number was chosen by performing the standard grid-independent test conducted at the highest voltage and Weissenberg number values considered in this study. Around 60000 hexahedral cells (grid G3) in the whole compu-

Grid	Total number of cells	$u_{x,avg}$
G1	38400	5.45e-4
G2	48600	6.18e-4
G3	60000	6.35e-4
G4	72600	6.35e-4
G5	86200	6.35e-4

Table 8.1: Details of the grid independence study carried out at $E_x = 4285.71 \text{ V/m}$ and $Wi = 1.05 \times 10^{-3}$. Here $u_{x,avg}$ is the time-averaged stream-wise velocity evaluated at a probe location placed at the upper cylinder gap region (blue dot in sub-Fig.1(a)).

tational domain were found to be adequate to capture the flow physics inside the present micro-scale geometry. It was confirmed by comparing the time-averaged x-component velocity at a probe location in the gap between the upper channel wall and the cylinder surface, see Table 8.1. Furthermore, the polymeric stress fields were also compared for different grid densities, and once again, grid G3 was found to be sufficient for the present study.

8.2.2 Dynamic mode decomposition (DMD) analysis

Like the global stability analyses, the DMD technique extracts structures related to flow disturbances that better explain the underlying cause of instability. To perform this analysis, we utilize the algorithm developed by Schmid [172] and also employed in our recent studies [260, 261]. First, a sequence of $M = 2000$ snapshots of the concentration field is sampled at an equispaced time interval of 0.005 s . These snapshots are then arranged in a matrix by converting each snapshot into a vector form $X_1^M = \{x_j\}_{j=1}^M$. A linear mapping approximation is made between the two consecutive snapshots of this matrix, which remains constant over the whole sequence. Therefore, the system can be represented as $X_2^M = \mathbf{A}X_1^{M-1} \approx X_1^{M-1}\mathbf{S}$. This is followed by the singular value decomposition (SVD) of the \mathbf{S} matrix to compute its eigenvalues (Ritz values) and eigenvectors (Ritz vectors). These Ritz vectors quantify the spatial flow features in the form of "modes" (denoted by ϕ_j), and the associated Ritz values (denoted by λ_j) capture their temporal dynamics. The mode frequency (ω_j) and growth rate (σ_j) are calculated from the Ritz values as $\omega_j = \text{Im}(\log(\lambda_j)/\Delta t)$ and $\sigma_j = \text{Re}(\log(\lambda_j)/\Delta t)$, respectively. The energy contribution of each mode is determined by calculating its norm, given by $\|\phi_j\|$. In most of the DMD studies, this quantity is used to select and rank a subset of modes to provide an efficient

and better representation of the physical quantity of interest, which is the concentration field in the present study. A higher norm value corresponds to higher mode energy and greater information about the original flow field represented by a particular mode.

8.3 Microfluidic experiments

The microfluidic device used in this study was fabricated from polydimethylsiloxane (PDMS, Sylgard 184 elastomer kit obtained from Sigma-Aldrich) using the soft-lithography technique [262, 263]. The fabrication of the device started with the transfer of the design from the photomask to the negative SU-8 (Kayaku Advanced Material, USA) coated mold by exposing it to ultraviolet (UV) light. After the UV exposure, we obtained a mold after developing it into a 1-methoxy-2-propanol acetate solvent (PGMEA, Kayaku Advanced Material, USA). A mixture of PDMS and cross-linking curing agent in the ratio of 6:1 was then poured into the mold and heated in an oven at 80°C for 2 hours. Once the PDMS became hard, it was peeled off from the mold, and a mold replica was obtained on the PDMS block. Finally, the PDMS microchannel block and the glass substrate (on which the block was placed) were treated in the oxygen plasma for two minutes. The SEM image of the PDMS microchannel is presented in sub-Fig. 8.1(c). As the PDMS is non-conductive, the coating of gold was done before the SEM imaging to make the channel surface conductive. It was performed only for taking the SEM image, whereas all the microfluidic experiments were performed using a PDMS channel without this gold coating. The dimensions of the fabricated microchannel are the same as those used in the numerical simulations of the present work.

The working fluid in this study is a constant viscosity Boger fluid, comprised of 37.5 *wt. %* (4.69×10^{-2} mol/liter) polyethylene glycol (mol wt. 8000 g/mol) and 0.2 *wt. %* (2.22×10^{-6} mol/liter) polyethylene oxide (mol wt. 900000 g/mol) dissolved in de-ionized water [264], both obtained from Sigma-Aldrich and used without further alteration. The solution was stirred continuously for 24 hours at room temperature and left for one day for complete hydrolysis. The shear rheology of the prepared solution was then measured at 30°C using a stress-controlled rheometer (Anton-Paar, MCR 702 twin drive) with cone-plate geometry (60 mm of diameter and cone angle of 1°) with a truncation gap of 100 μm . After rheological confirmation of the Boger fluid (Fig. 8.2), 1.0 *wt. %* of

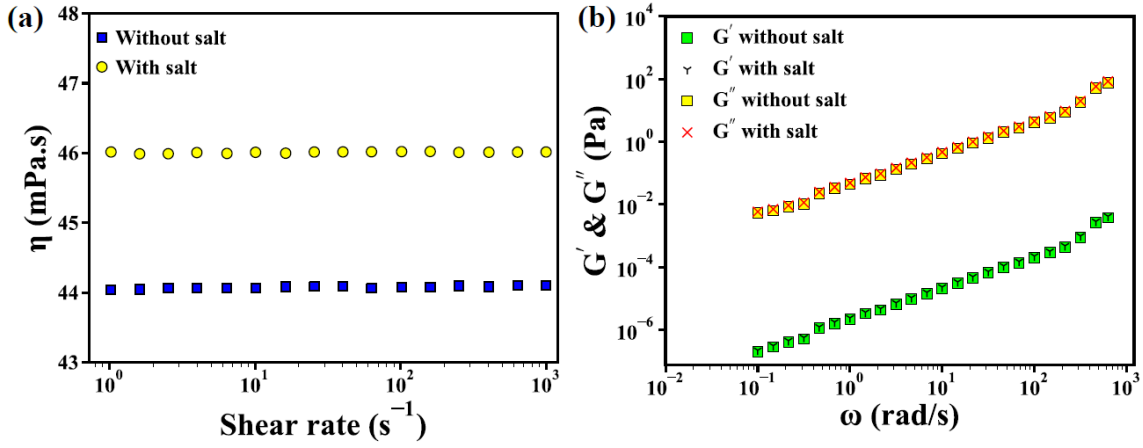


Figure 8.2: (a) Variation of the shear viscosity with the shear rate. (b) Variation of the storage (G') and loss (G'') modulus with the angular frequency for viscoelastic Boger fluids at 30 °C both in the presence of salt and without salt.

NaCl was added to the solution. The Boger fluid, both with and without salt, exhibits a constant viscosity over the entire range of shear rate considered in the measurement, sub-Fig. 8.2(a). The small amplitude oscillatory shear (SAOS) experiments with 1.0 % strain rate were also conducted to measure the storage (G') and loss (G'') modulus, and the results are presented in sub-Fig. 8.2(b). It can be seen the addition of salt to a Boger fluid increases the zero-shear viscosity but hardly influences the values of G' and G'' .

Before the experiments, a zeta potential was created on the PDMS wall to facilitate the electro-osmotic flow in the microchannel. In doing so, the procedure described in the work of Song et al. [265] was used in this study. As per their procedure, 5 wt.% (0.133 mol/liter) of polybrene (Sigma-Aldrich, mol wt. 374.2 g/mol) solution was pumped into the PDMS channel for 4 minutes and then left for 15 minutes to create a negative wall zeta potential on the microchannel wall. The wall zeta potential value of $\zeta_0 = 60.1$ mV was obtained from the literature at this polybrene concentration [265, 266, 267] and also used in the present simulations. Furthermore, the present study used the current monitoring method (as proposed by Song et al. [265]) to calculate the value of ζ_0 and found a value of 58.58 mV, which is very close to that obtained from the literature. The working Boger fluid with fluorescent particles (Rhodamine B of 1 μ m size obtained from Sigma-Aldrich) was first injected into the microchannel at a desired amount. The platinum electrodes were then inserted into the inlet and outlet reservoirs of the microchannel, which were connected to a DC power supply (Keithley 2231-A triple channel). The whole experimental setup was placed under an inverted microscope (Leica DM16000B)

to capture the flow dynamics with a 4X objective, Fig. 8.1(d). The obtained images were finally post-processed using the open-source particle image velocimetry PIVlab software from MATLAB [268].

8.4 Results and discussion

At the onset, the results of the flow dynamics inside the present microfluidic setup are presented and discussed, obtained with both CFD simulations and experiments. The numerical simulations have been carried out for a range of values of the applied electric field strength and Weissenberg number and at a fixed value of the blockage ratio of $BR = 0.83$. The results for a Newtonian fluid are also included in the present study so that a direct comparison of the flow dynamics with the viscoelastic fluids can be made under the same conditions. The experiments have also been carried out for the same range of the electric field strength as that used in numerical simulations. The flow dynamics results are discussed with the help of velocity vector and velocity magnitude plots and presented for a region near the obstacle. Furthermore, a statistical analysis of the point-wise velocity fluctuations is also provided to get further insights into flow physics.

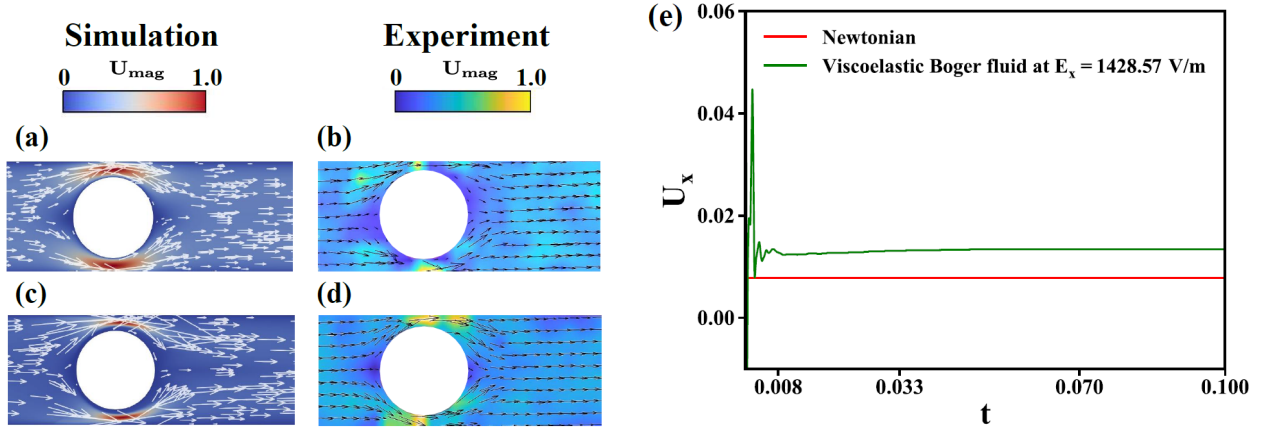


Figure 8.3: Velocity vector and magnitude plots both for Newtonian ((a) and (b)) and viscoelastic fluids ((c) and (d)) at an applied electric field strength of $E_x = 1428.57$ V/m and $Wi = 3.53 \times 10^{-4}$. (e) Temporal variation of the non-dimensional stream-wise (U_x) velocity at a probe location placed at the upper cylinder gap region for both fluids at the same conditions.

Figure 8.3 shows the velocity vector and magnitude plots near the obstacle at an electric field strength of $E_x = 1428.57$ V/m both for viscoelastic ($Wi = 3.53 \times 10^{-4}$) and

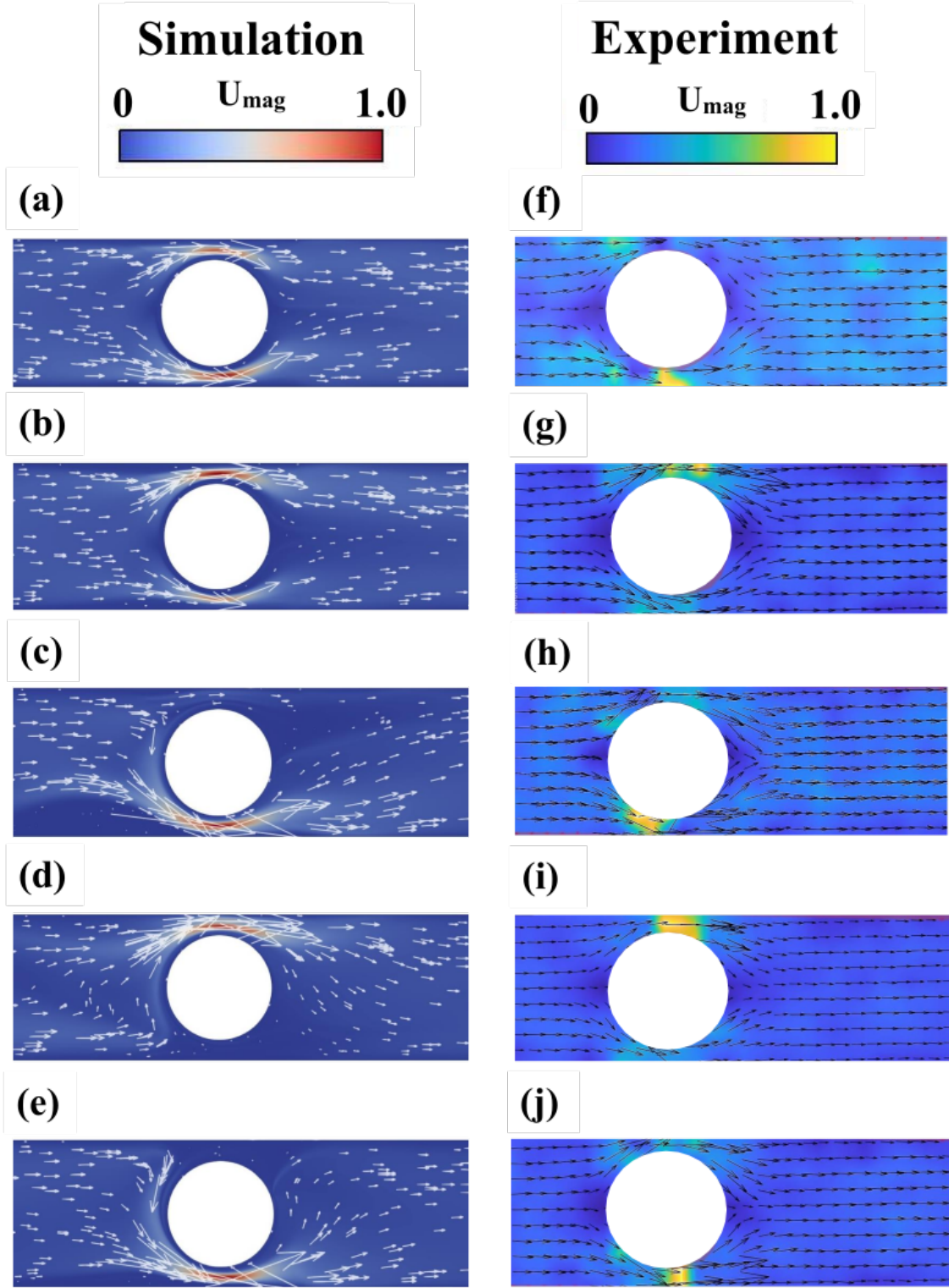


Figure 8.4: Velocity vector and magnitude plots for viscoelastic fluids at $E_x = 2857.14$ V/m and $Wi = 7.06 \times 10^{-4}$ for two different times both in simulations ((a) $t = 0.077$, (b) $t = 0.08$) and experiments ((f) $t = 0.087$ (g) $t = 0.092$). The same at $E_x = 4285.71$ V/m and $Wi = 1.05 \times 10^{-3}$ for three different times both in simulations ((c) $t = 0.09$, (d) $t = 0.093$, (e) $t = 0.098$) and experiments ((h) $t = 0.095$, (i) $t = 0.1$, (j) $t = 0.103$)

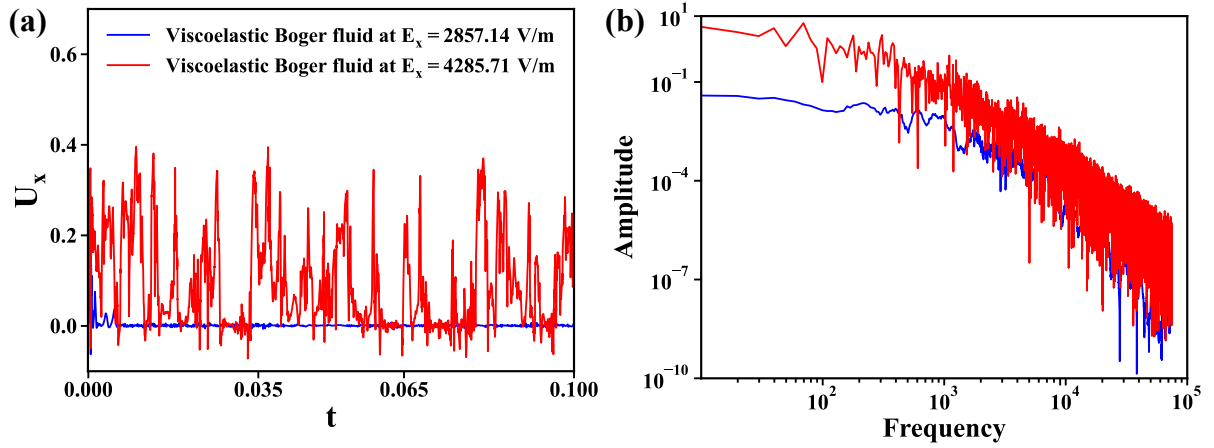


Figure 8.5: Temporal variation of the non-dimensional stream-wise (U_x) velocity component (a) and power spectral density plot of velocity fluctuations for viscoelastic fluids (b) at two values of the electric field strength, namely, 2857.14 V/m ($Wi = 7.06 \times 10^{-4}$) and 4285.71 V/m ($Wi = 1.05 \times 10^{-3}$).

Newtonian fluids. The flow exhibits almost a symmetric profile at this electric field strength in both simulations and experiments. The velocity magnitude (normalized with its maximum value) zone with the highest value is seen to be present at the upper and lower gaps between the channel wall and cylinder surface. This is simply because the flow area is less in this region due to the obstruction by the cylindrical obstacle. Hence, the velocity magnitude increases in this region to obey the mass conservation principle. The flow field also remains steady at this condition for both fluids. This is evident in sub-Fig 8.3(e), wherein the temporal variation of the non-dimensionalized stream-wise velocity at a probe location placed in the gap between the upper channel wall and cylinder surface (blue dot in sub-Fig 8.1(a)) is plotted. It clearly shows that this velocity component reaches a steady value with time.

The applied electric field strength is now increased to $E_x = 2857.14$ V/m, and the corresponding flow dynamics inside the microfluidic setup is shown in Fig 8.4 for viscoelastic fluids with $Wi = 7.06 \times 10^{-4}$. First, the flow symmetry is destroyed at this electric field strength. The maximum velocity magnitude zone now switches positions with time between the upper and lower gap regions between the cylinder surface and the channel wall. This suggests that at a particular time, most of the fluid passes through the lower gap region (sub-Fig 8.4(a)), whereas at the next time, it traverses through the upper gap region (sub-Fig 8.4(b)). The same flow pattern is also observed in the corresponding experiments at the same electric field strength; for instance, see sub-Figs 8.4(f) and (g).

This suggests the presence of a flow-switching phenomenon in the microfluidic setup at this condition. As the electric field strength further increases to $E_x = 4285.71 \text{ V/m}$ (and the corresponding Weissenberg number increases to 1.05×10^{-3}), this tendency in the flow behaviour of viscoelastic fluids further increases. This is noticeable both in numerical simulations (sub-Figs. 8.4(c)-(e)) and experiments (sub-Figs. 8.4(h)-(j)) presented at three different times.

Therefore, these results suggest that the flow field becomes unsteady or time-dependent for viscoelastic fluids with the increased value of the applied electric field strength. This is further explained in sub-Fig. 8.5(a), wherein the temporal variation of the stream-wise velocity (at the same probe location depicted as the blue dot in sub-Fig. 8.1(a)) is plotted, showing aperiodic fluctuations with time. This plot shows that the intensity of velocity fluctuations increases with the electric field strength. The corresponding power spectral density plot of velocity fluctuations is presented in sub-Fig. 8.5(b) at two different values of E_x , namely, 2857.14 and 4285.71 V/m to get further insights into this unsteady flow dynamics. It can be seen that the excitation of fluid motion occurs over a wide range of continuum frequencies for both the applied electric field strengths. Furthermore, a plateau in the power spectrum is seen in the low-frequency range, and at high frequencies, a power-law decay (ω^α) is seen, which covers almost a decade of the frequency range. The fitted values of the power-law exponent α are 1.54 and 1.929 for $E_x = 2857.14$ and 4285.71 V/m, respectively. This range of α values has also been seen in the electroosmotic flows of viscoelastic fluids through cross-slot and flow-focusing devices [121]. All these suggest that an electro-elastic instability with fluctuating hydrodynamics is established inside the system for viscoelastic fluids once the electric field strength exceeds a critical value. Note that such a chaotic flow field is not observed for Newtonian fluids, even at this study's highest applied electric field strength.

Several previous studies have explained the reason behind this purely elastic instability both for pressure driven [250, 18] and electrokinetically driven flows [120, 160]. It is due to the interaction between the applied electric field, which acts on the free ions within the EDL, and non-linear elastic stresses in a viscoelastic fluid. In this electrokinetically driven flow, the wall zeta potential is influenced by the EDL distribution, and the electric potential is expected to be a Gaussian distribution. Therefore, the applied electric field on the EDL (near the channel wall) and fluid viscoelasticity instigated the chaotic motion of

the fluid, resulting in instability in the channel. The curved streamlines around the flow past the microcylinder facilitate the onset of this instability inside the system. The flow-switching phenomenon happens once this EEI phenomenon is triggered in the system. Also, viscoelastic fluid flow generates a long strand of elastic stresses downstream of the microcylinder. This is due to the presence of a highly extensional flow field in this region, which causes the alignment and stretching of polymer molecules in this region. It eventually increases the elastic stresses in this region and forms a strand. This can be visualized in Fig. 8.6, where the xx -component of the elastic stresses, τ_{xx} is plotted at two different values of the electric field strength, namely, 1428.57 and 2857.14 V/m. As expected, the length and value of this elastic stress strand increase with E_x due to the increase in the electroosmotic velocity strength. Once the EEI phenomenon originates in the system, this strand also fluctuates with time. At any instance, when this strand moves upward, it acts as a barrier to the flow through the upper gap region between the channel wall and cylinder surface. Therefore, most fluid passes through the lower gap between the lower channel wall and the cylinder surface. In contrast, a reverse trend is seen when the strand moves downward, i.e., most fluid goes through the upper gap region. This ultimately results in the generation of this flow-switching phenomenon inside the system. Therefore, the electroosmotic flows of viscoelastic fluids through an actual porous media may become unsteady and chaotic once the electric field strength exceeds a critical value due to this EEI phenomenon. This is because a real porous media consists of many curved and interconnected flow paths of micron sizes, which may easily trigger this instability inside a system during the flow of a viscoelastic fluid. This has been seen in many recent studies dealing with pressure-driven flows [24, 269].

Next, we demonstrate how this flow-switching phenomenon could efficiently mix two viscoelastic fluids in this microfluidic setup with the help of numerical simulations. To show this potential, we have placed a viscoelastic fluid with a finite dye concentration in the upper half of the geometry and the same viscoelastic fluid with a zero dye concentration in the lower half of the geometry, as schematically shown in Fig 8.7. At low values of the electric field strength (sub-Fig. 8.7(a)), the fluids present in the upper and lower halves of the geometry move side by side without mixing due to the presence of a laminar flow condition. However, as the electric field strength increases to higher values, say to 1428.57 V/m, the interface between the dyed and non-dyed fluids starts to dis-

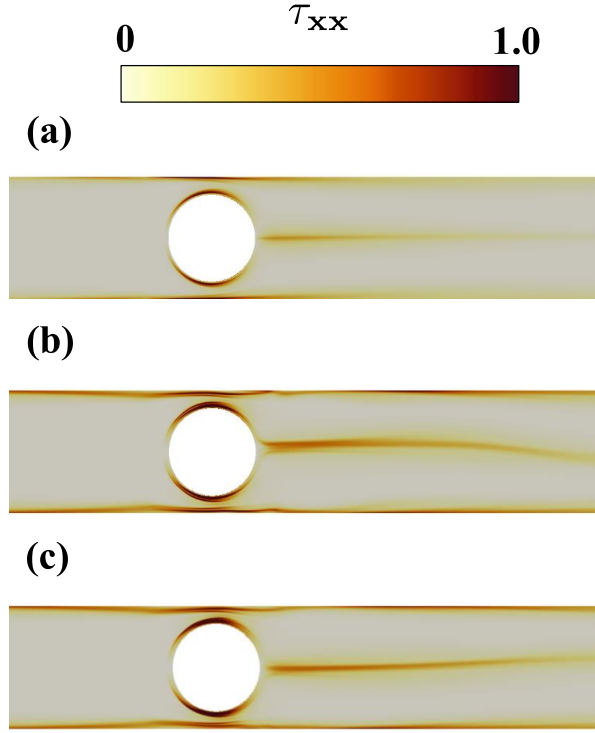


Figure 8.6: Surface plot of the non-dimensional elastic stress component τ_{xx} for $E_x = 1428.57 \text{ V/m}$ ($Wi = 3.53 \times 10^{-4}$) at $t = 0.071$ and $E_x = 2857.14 \text{ V/m}$ ($Wi = 7.06 \times 10^{-4}$) at two different times, namely, (b) $t = 0.077$ and (c) $t = 0.08$.

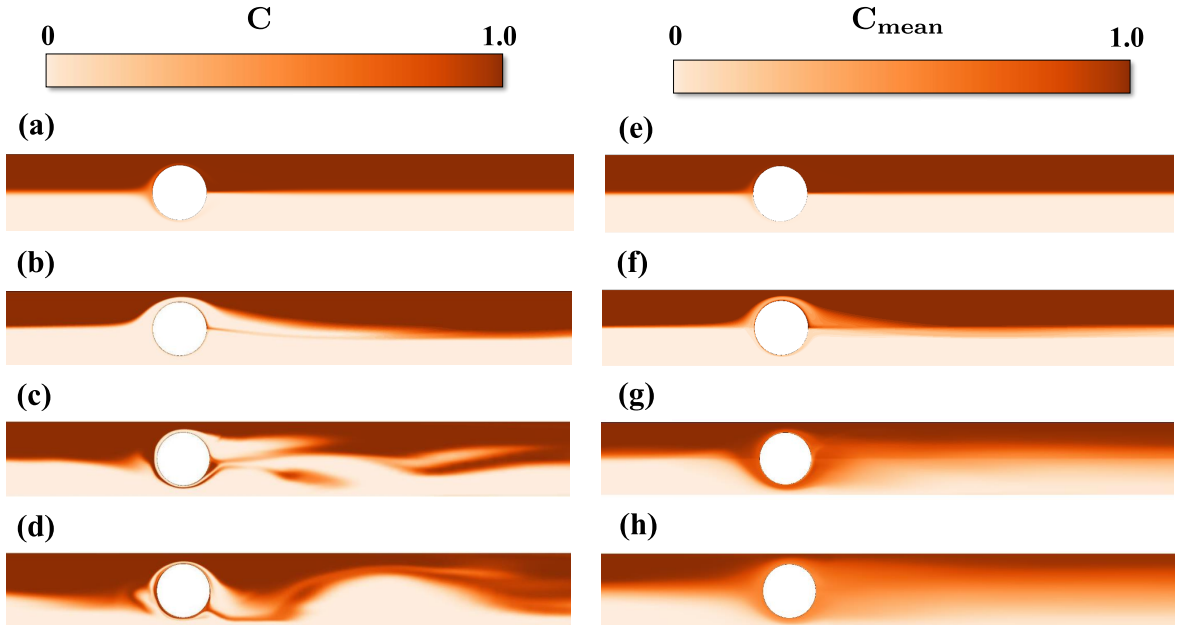


Figure 8.7: Instantaneous dye concentration profiles (at a time $t = 5 \text{ s}$) inside the microchannel at (a) 71.42 V/m , (b) 1428.57 V/m , (c) 2857.14 V/m , and (d) 4285.71 V/m . The corresponding time-averaged mean dye concentration profiles ((e)-(h)) at the same applied electric field strengths.

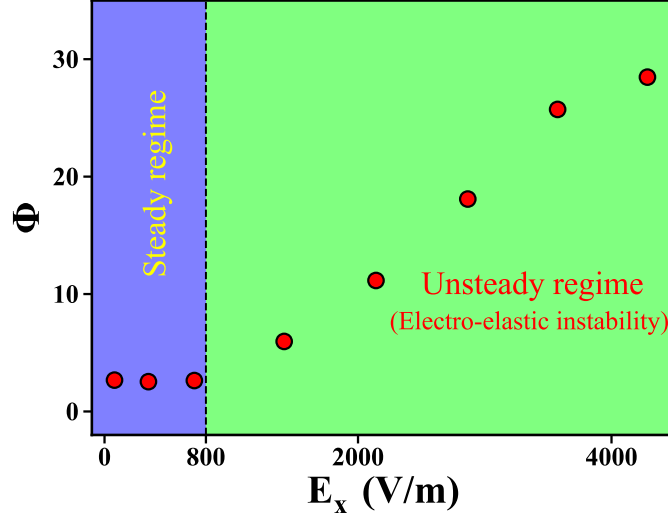


Figure 8.8: Variation of the mixing efficiency parameter Φ with the applied electric field strength E_x . Here the calculation is performed for a time of 5 μ s.

tort due to the onset of the EEI phenomenon inside the system, sub-Fig. 8.7(b). As the electric field strength further increases, the interface becomes more distorted due to the increased instability intensity, sub-Fig. 8.7(c-d). In particular, the flow-switching phenomenon, originating from the elastic instability, drives the dyed fluid from the upper half of the channel to its lower half and dye-free fluid in the opposite direction, upstream of the microcylinder. This ultimately leads to efficiently mixing the two fluids downstream of the microcylinder. This can be seen from the plot of the time-averaged mean dye concentration in the flow domain presented in sub-Figs. 8.7(e)-(h) at different applied electric field strength values.

To present this mixing process more quantitatively, we have calculated the mixing efficiency parameter Φ defined as

$$\Phi = 1 - \frac{\sqrt{\frac{1}{N} \sum_1^N (\bar{C}_s - \bar{C}_s^*)^2}}{\sqrt{\frac{1}{N} \sum_1^N (\bar{C}_s^0 - \bar{C}_s^*)^2}} \quad (8.1)$$

Here \bar{C}_s , \bar{C}_s^* and \bar{C}_s^0 are the mean dye concentration at a point within the geometry, dye concentration for perfectly mixed viscoelastic fluids and dye concentration for an unmixed viscoelastic fluid, respectively. Here, N is the number of grid points along the vertical line at the channel outlet where the mixing efficiency is calculated. The value of \bar{C}_s^0 is either 0 or 1, and the value of \bar{C}_s^* is 0.5. Therefore, the denominator of equation 8.1 has a constant value of 0.5. The theoretical range of Φ lies between 0 and 1, representing

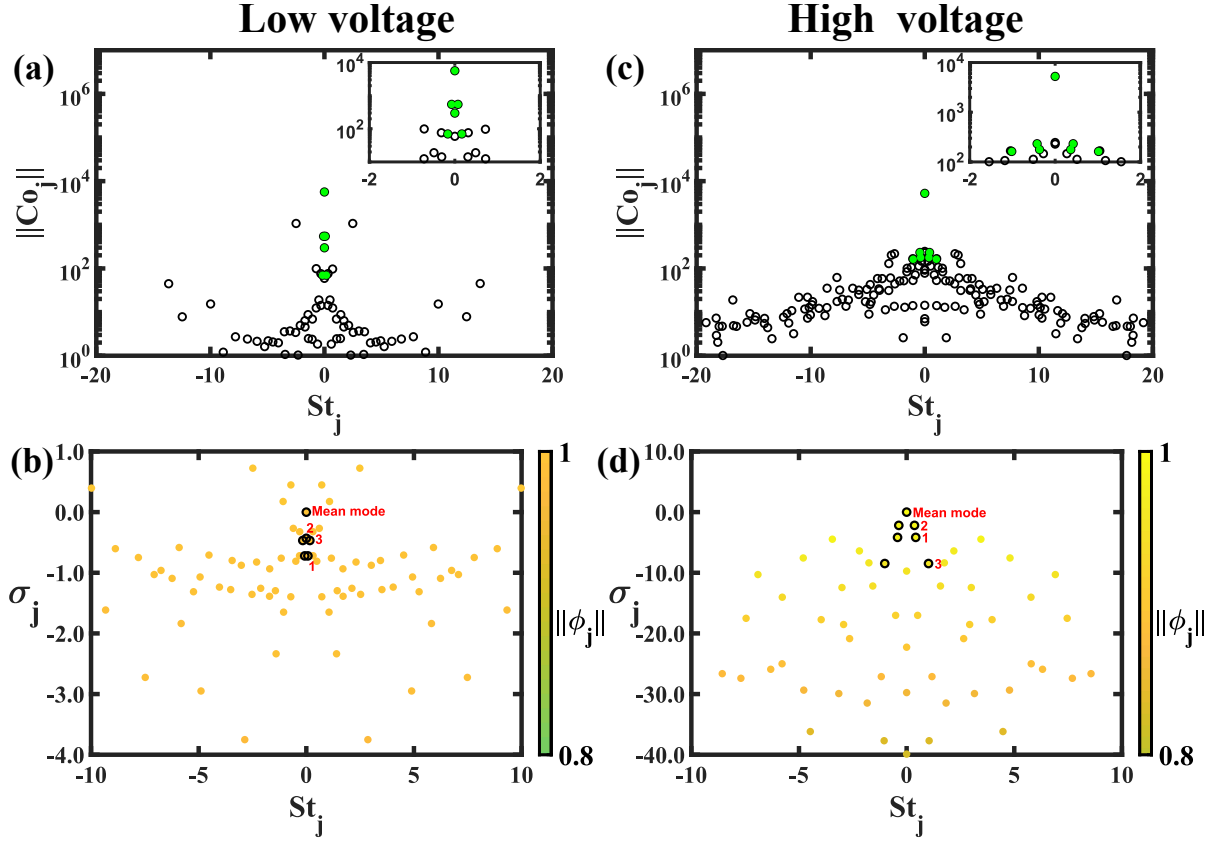


Figure 8.9: Time coefficient norm ($\|Co_j\|$) and growth rate (σ_j) against the frequency (St_j) at $E_a = 357.14V/m$ ((a) and (b), Low voltage case) and $E_a = 4285.71V/m$ ((c) and (d), High voltage case). The color bar in σ_j vs St_j represents the mode norm ($\|\phi_j\|$). Also, in the same plot, the encircled modes are the modes sorted based on the time coefficient norm $\|Co_j\|$, where unlabeled modes are complex conjugates of the labeled ones.

perfectly unmixed and mixed viscoelastic fluids. Figure 8.8 depicts the variation of Φ with E_x . It can be seen that the mixing efficiency increases drastically after a critical value of the electric field strength for viscoelastic fluids due to the presence of the EEI phenomenon inside the system.

Finally, we conduct the DMD analysis of the dye evaluation pattern inside the flow system. Note that we conducted the DMD analysis based on our numerical simulation results, not our experimental results. In doing so, we aim to provide an insight into the underlying flow features originating from this elastic instability and the resulting mixing phenomena. The results are presented for two cases, namely, $E_x = 357.14V/m$ (Low voltage) and $E_x = 4285.71V/m$ (High voltage), to describe the effect of varying electric field strengths on the coherent structures. In both cases, DMD extracts a large number of modes with slight differences in their norms ($\|\phi_j\|$); see the plots of the growth rate

(σ_j) with respect to the frequency ($St_j = \frac{\omega_j}{2\pi}$) in Fig. 8.9. Here, the value of the norm ($||\phi_j||$) for most of the modes varies between 0.8 and 1 only. This is due to the highly chaotic nature of the flow, which results in the evolution of multiple flow structures (and associated frequencies) with nearly the same energy content. The existence of multiple frequencies in the flow field is also evident from the PSD plots presented in Fig. 8.5. Thus, the selection of modes based solely on the energy content might not be perfect here. Moreover, in the same plot, very few modes are neutrally stable (i.e., non-damping), and most of them have a negative growth rate, implying that these structures decay with time. This is intuitive as mixing is a transient phenomenon. Adding to this, there is no imposed frequency in the flow field (e.g., a rotating impeller), which could be used to sort the relevant modes. Therefore, the ranking of the modes becomes complicated. To circumvent this complexity, we resort to another parameter known as the time coefficient norm ($||Co_j||$), which considers not only a mode's initial energy contribution but also its temporal dynamics, thereby sorting the modes in the most effective way possible. In simple terms, the mode having a high amplitude (initial energy contribution to the flow field) and a low growth rate (least damping) will have the highest value of the time coefficient norm. This criterion was also employed in our earlier study [261], where the expression to compute this quantity is presented. Based on this norm ($||Co_j||$), for the sake of brevity, we explain the coherent structures in the first four modes only, highlighted in Fig. 8.9 (where the time coefficient norm is plotted against the frequency). These chosen modes are also encircled in the growth rate (σ_j) versus frequency plots.

We first present the dominant modes in Fig. 8.10. At the top, instantaneous concentration fields at the final snapshot of the sequence are shown. It is clear from these plots that the mixing phenomenon occurs downstream of the cylinder and is more intense at the higher electric field strength than at the lower one. On decomposition, the mode with the highest value of the time coefficient norm is the mean mode. This mode has zero frequency and zero growth rate (see sub-Figs. 8.9(b) and (d)) and corresponds to the time-averaged concentration field. Comparing the mean structures of the two cases shows that mixing is higher when the flow is driven under the influence of high electric field strength. All other modes have negative growth rates, indicating the flow's dissipative nature. Moreover, their frequencies (St_j) are symmetric about the zero value as the DMD of real-valued data yields complex-conjugate pairs of eigenvalues. Moving

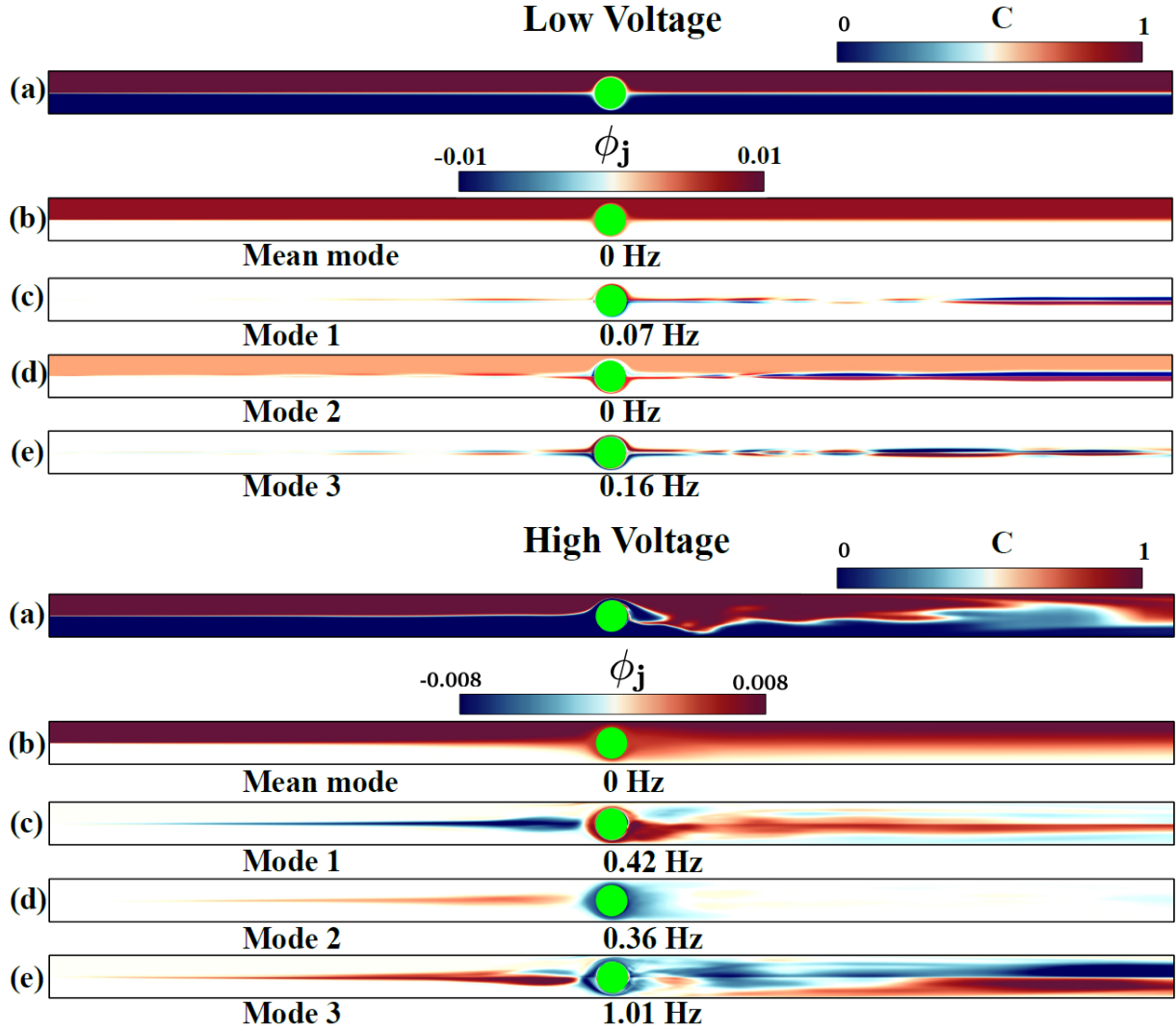


Figure 8.10: Instantaneous concentration field (a) and representative DMD modes (b)-(e) at $E_a = 357.14V/m$ (Low voltage case) and $E_a = 4285.71V/m$ (High voltage case), respectively. Here, (b) is the mean mode, and (c), (d), and (e) correspond to mode 1, mode 2, and mode 3, along with associated frequencies for each electric field strength.

on to mode 1, narrow structures appear on the cylinder surface and at the interface for low voltage cases, extending throughout the downstream distance. These structures signify the existence of disturbance at the interface between the high and low-concentration streams. Less concentrated structures are also visible in the upstream direction of the cylinder, which suggests that instability also exists in this region. This observation was only possible after the DMD analysis of the flow field, as it was not apparent from the concentration fields (even at the highest electric field strength used in this study). Upon careful observation, it can be seen that these structures exist in an anti-symmetric fashion. This arrangement occurs due to the wavy nature of the instability in space, and the associated frequency of this wave is 0.07 Hz. On the other hand, these structures in mode 1 of the high electric field strength case are more concentrated and broader in the spanwise direction. Furthermore, the anti-symmetric arrangement is lost, and the structures convect at a higher frequency of 0.42 Hz. All these features point out that at higher electric field strengths, the instability and subsequent mixing process become highly chaotic in nature, resulting in more mixing. For the low electric field strength case, higher modes (mode 2 and mode 3) have qualitative similarities in their coherent features and only differ in their frequencies. These modes are markedly different for the high electric field strength case. In mode 2, negative structures surround the region near the cylinder, unlike mode 1, where positive structures occupy this space. The same trend is also observed in other modes, where positive and negative structures move at different frequencies and surround the cylinder alternatively. This arises as the fluids in the top and bottom half of the geometry engulf the cylinder during the flow-switching phenomenon. Therefore, the DMD captures this phenomenon in different modes along with their respective frequencies. Finally, mode 3 again captures intense mixing downstream of the cylinder with significant positive and negative structures encompassing the whole space in this part of the microfluidic channel. Moreover, the intensity of these structures increases as we move toward the end of the channel due to the enhancement of the mixing phenomenon. It should be noted that the modes with higher frequencies are less dominant, thereby dissipating at a faster rate.

Chapter 9

Conclusions and future scope

In conclusion, the present thesis has attempted to investigate both the pressure-driven and electrokinetically-driven flow dynamics of viscoelastic fluids, such as wormlike micellar solutions or polymer solutions, through various model porous systems in the creeping flow regime using numerical simulations and microfluidic experiments. An investigation of the rheological and physicochemical properties of these fluids has also been performed in the present thesis. The numerical simulations were conducted using the computational fluid dynamics (CFD) technique. In particular, the mass, momentum, and viscoelastic constitutive equations have been solved numerically with the help of the open-source CFD code OpenFOAM and the RheoTool package, which was recently developed for simulating viscoelastic fluids. The Vasquez-Cook-McKinley (VCM) and Oldroyd-B constitutive models have been utilized to realize the rheological behaviors of wormlike micellar solutions and constant viscosity polymer solutions (Boger fluids), respectively, in the present numerical simulations. On the other hand, the experimental methods adopted in this study were the soft lithography technique for making a model microfluidic porous chip and the flow visualization technique using an inverted fluorescent microscope. Furthermore, various rheological studies, such as steady shear, small-amplitude oscillatory shear (SAOS), and dripping-onto-substrate (DoS) extensional rheometry, have also been performed in the present thesis. The investigations carried out in the present dissertation have found some significant conclusions. These are summarized as follows:

Both rhamnolipid biosurfactant-derived and chemically cetyltrimethylammonium bromide (CTAB) surfactant-derived micellar solutions exhibited shear-thinning behaviour in steady shear flow, which was hardly dependent on the surfactant concentration. The zero-shear rate viscosity and shear relaxation time increased with the surfactant concentration regardless of the surfactant type. On the other hand, the extensional viscosity (and hence the strain-hardening behaviour) and extensional relaxation time also increased with the surfactant concentration, irrespective of the surfactant type. However, the values were found to be higher for rhamnolipid than those for CTAB. Furthermore, the rhamnolipid

biosurfactant showed less surface tension, more contact angle (both advancing and pre-
ceding), and higher thermal stability than CTAB. Therefore, rhamnolipid biosurfactant
may become a better choice than CTAB for high-temperature applications such as oilfield
applications (Chapter 4).

In the case of pressure-driven flows of wormlike micellar solutions through a model
porous system consisting of a long microchannel with a cylindrical obstacle, an elastic in-
stability with unsteady and fluctuating hydrodynamics originated once the flow strength
(quantified in terms of the Weissenberg number) exceeded a critical value. This elastic
stress-induced instability was further found to be strongly dependent on how it was easy
or hard to break a micelle (Chapter 5).

Chapter 6 investigated the pressure-driven flow dynamics of wormlike micellar solu-
tions through a microfluidic system comprised of a long microchannel with either a single
or two microcylinders. A flow bifurcation was found in this model porous geometry once
the flow strength (quantified in terms of the Weissenberg number) exceeded a critical
value. This phenomenon was found to be significantly dependent on the blockage ratio
(in the case of flow past a single microcylinder) and gap ratio (in the case of flow past
two microcylinders) along with how it was easy or hard to break a micelle. An excel-
lent qualitative agreement was found between the present numerical results and prior
experimental results.

The electrokinetically driven flows of constant viscosity viscoelastic fluids (Boger fluid)
through a model porous system consisting of a long microchannel with step expansion
and contraction was studied in Chapter 7, and an electro-elastic instability was found
in the flow field once either the applied electric field strength or the fluid viscoelasticity
(quantified in terms of the Weissenberg number) exceeded a critical value. This instabil-
ity was further found to be dependent on the polymer concentration, constriction, and
expansion lengths of the micropore. It was further demonstrated that this model porous
system could also be successfully utilized for mixing two fluids if they are viscoelastic in
nature.

Both numerical simulations and experiments on the electrokinetically driven flows of
viscoelastic Boger fluids through a long microchannel with a cylindrical obstacle were
carried out in Chapter 8. A flow-switching phenomenon resulting from electro-elastic

instability was observed in the flow field once the applied electric field strength exceeded a critical value. This flow phenomenon was further shown to facilitate mixing two viscoelastic fluids in this simple microfluidic setup. A data-driven reduced order model, the dynamic mode decomposition (DMD) technique, was also employed in this study to further analyze the unsteady flow dynamics and the mixing phenomenon in this model system.

All in all, the investigations carried out in the present dissertation have shown that the flow dynamics of viscoelastic fluids, such as wormlike micellar solutions or polymer solutions, through a model porous system could become very complex and rich in physics, such as the generation of elastic instability and flow bifurcation, than that seen in simple Newtonian fluids under the same conditions. This is mainly due to non-linear elastic stresses in these viscoelastic fluids and breakage and reformation phenomena in the case of micellar solutions. Therefore, the studies in the present thesis would help to better understand and control the flow of these complex fluids through a real porous system, which has many practical applications, such as in enhanced oil recovery, soil remediation, and electro-chromatography.

A further significant scope is present for future studies in this area of flow dynamics of complex fluids through a porous media. Some of those are mentioned here.

1. The present dissertation deals with two-dimensional flows; however, the flow could transit to three-dimensional, particularly during the onset and development of elastic instability regime. Therefore, full-scale three-dimensional studies both in numerical simulations and experiments, would be helpful to get more insights into flow physics.
2. The present thesis considers very simple model porous systems. Therefore, the corresponding flow dynamics study could be extended to more complex geometries akin to a real porous system used in practical applications.
3. The number of studies on the pressure-driven flows of viscoelastic fluids is much larger than the corresponding electrokinetically driven flows. Therefore, further studies on this particular fluid transport mechanism should be carried out due to its wide applications in microfluidics and nanofluidics.
4. So far in the literature, no study is present on electrokinetic flows of wormlike

micellar solutions, particularly using the VCM model. Therefore, further studies should be carried out to fill this knowledge gap in the literature.

5. The present thesis deals with the viscoelastic fluids that exhibit shear-thinning and elastic behaviors. However, some polymer and micellar solutions can also display shear-thickening and elastic properties simultaneously. Therefore, it would be interesting to investigate how the latter properties could influence different flow phenomena seen for shear-thinning and elastic fluids, such as elastic instability and flow asymmetry phenomena.

Bibliography

- [1] R. P. Chhabra and J. F. Richardson. *Non-Newtonian Flow and Applied Rheology: Engineering Applications*. Butterworth-Heinemann, 2011.
- [2] R. B. Bird, R. C. Armstrong, and O. Hassager. Dynamics of Polymeric Liquids, Volume 1: Fluid Mechanics. 1987.
- [3] S. Gupta, W. S. Wang, and S. A. Vanapalli. Microfluidic viscometers for shear rheology of complex fluids and biofluids. *Biomicrofluidics*, 10(4):043402, 2016.
- [4] A. N. Beris, J. S. Horner, S. Jariwala, M. J. Armstrong, and N. J. Wagner. Recent advances in blood rheology: A review. *Soft Matter*, 17(47):10591–10613, 2021.
- [5] C. A. Dreiss. Wormlike Micelles: An Introduction. 2017.
- [6] G. H. McKinley. A hitchhikers guide to complex fluids. *Rheology Bulletin*, 84:14, 2015.
- [7] J. Bear. *Dynamics of Fluids in Porous Media*. Courier Corporation, 1988.
- [8] J. Bear and Y. Bachmat. *Introduction to Modeling of Transport Phenomena in Porous Media*, volume 4. Springer Science & Business Media, 2012.
- [9] A. E. Scheidegger. The physics of flow through porous media. In *The Physics of Flow Through Porous Media (3rd Edition)*. University of Toronto Press, 2020.
- [10] A. Anbari, H. Chien, S. S. Datta, W. Deng, D. A. Weitz, and J. Fan. Microfluidic model porous media: Fabrication and applications. *Small*, 14(18):1703575, 2018.
- [11] P. R. de Souza Mendes. Dimensionless non-newtonian fluid mechanics. *Journal of Non-Newtonian Fluid Mechanics*, 147(1-2):109–116, 2007.
- [12] W. Ostwald and R. Auerbach. Ueber die viskosität kolloider lösungen im struktur, laminarund turbulenzgebiet: Ueber die geschwindigkeitsfunktion der viskosität disperser systeme. *Kolloid-Zeitschrift*, 38:261–280, 1926.

- [13] H. Giesekus. Nicht-lineare effekte beim strömen viskoelastischer flüssigkeiten durch schlitz-und lochdüsen. *Rheologica Acta*, 7:127–138, 1968.
- [14] J. R. A. Pearson. Instability in non-newtonian flow. *Annual Review of Fluid Mechanics*, 8(1):163–181, 1976.
- [15] G. V. Vinogradov and A. Y. Malkin. *Rheology of Polymers: Viscoelasticity and Flow of Polymers*. Springer, 1980.
- [16] S. J. Muller, R. G. Larson, and E. S. G. Shaqfeh. A purely elastic transition in taylor-couette flow. *Rheologica Acta*, 28:499–503, 1989.
- [17] E. S. G. Shaqfeh. Purely elastic instabilities in viscometric flows. *Annual Review of Fluid Mechanics*, 28(1):129–185, 1996.
- [18] G. H. McKinley, P. Pakdel, and A. Öztekin. Rheological and geometric scaling of purely elastic flow instabilities. *Journal of Non-Newtonian Fluid Mechanics*, 67:19–47, 1996.
- [19] R. J. Poole. Three-dimensional viscoelastic instabilities in microchannels. *Journal of Fluid Mechanics*, 870:1–4, 2019.
- [20] S. S. Datta, A. M. Ardekani, P. E. Arratia, A. N. Beris, I. Bischofberger, J. G. Eggers, J. E. López-Aguilar, S. M. Fielding, A. Frishman, and M. D. Graham. Perspectives on viscoelastic flow instabilities and elastic turbulence. *Physical Review Fluids*, 7(8):1–80, 2021.
- [21] S. De, J. Van Der Schaaf, N. G. Deen, J. A. M. Kuipers, E. A. J. F. Peters, and J. T. Padding. Lane change in flows through pillared microchannels. *Physics of Fluids*, 29(11):113102, 2017.
- [22] S. De, S. P. Koesen, R. V. Maitri, M. Golombok, J. T. Padding, and J. F. M. van Santvoort. Flow of viscoelastic surfactants through porous media. *AIChE Journal*, 64(2):773–781, 2018.
- [23] S. De, J. A. M. Kuipers, E. A. J. F. Peters, and J. T. Padding. Viscoelastic flow simulations in random porous media. *Journal of Non-Newtonian Fluid Mechanics*, 248:50–61, 2017.

- [24] D. M. Walkama, N. Waisbord, and J. S. Guasto. Disorder suppresses chaos in viscoelastic flows. *Physical Review Letters*, 124(16):164501, 2020.
- [25] S. J. Haward, C. C. Hopkins, and A. Q. Shen. Stagnation points control chaotic fluctuations in viscoelastic porous media flow. *Proceedings of the National Academy of Sciences*, 118(38):e2111651118, 2021.
- [26] A. Chauhan, S. Gupta, and C. Sasmal. Effect of geometric disorder on chaotic viscoelastic porous media flows. *Physics of Fluids*, 2021.
- [27] J. Yang. Viscoelastic wormlike micelles and their applications. *Current Opinion in Colloid & Interface Science*, 7(5-6):276–281, 2002.
- [28] L. Maibaum, A. R. Dinner, and D. Chandler. Micelle formation and the hydrophobic effect. *The Journal of Physical Chemistry B*, 108(21):6778–6781, 2004.
- [29] M. E. Cates and S. J. Candau. Statics and dynamics of worm-like surfactant micelles. *Journal of Physics: Condensed Matter*, 2(33):6869, 1990.
- [30] J. N. Israelachvili, D. J. Mitchell, and B. W. Ninham. Theory of self-assembly of hydrocarbon amphiphiles into micelles and bilayers. *Journal of the Chemical Society, Faraday Transactions 2: Molecular and Chemical Physics*, 72:1525–1568, 1976.
- [31] Z. Chu, C. A. Dreiss, and Y. Feng. Smart wormlike micelles. *Chemical Society Reviews*, 42(17):7174–7203, 2013.
- [32] D. P. Acharya and H. Kunieda. Wormlike micelles in mixed surfactant solutions. *Advances in Colloid and Interface Science*, 123:401–413, 2006.
- [33] J. N. Israelachvili. *Intermolecular and Surface Forces*. Academic Press, 2011.
- [34] H. H. G. W. H. Hoffmann, H. Rehage, G. Platz, W. Schorr, H. Thurn, and W. Ulbricht. Investigations on a detergent system with rodlike micelles. *Colloid and Polymer Science*, 260(11):1042–1056, 1982.
- [35] I. Wunderlich, H. Hoffmann, and H. Rehage. Flow birefringence and rheological measurements on shear induced micellar structures. *Rheologica Acta*, 26(6):532–542, 1987.

- [36] S. R. Raghavan and E. W. Kaler. Highly viscoelastic wormlike micellar solutions formed by cationic surfactants with long unsaturated tails. *Langmuir*, 17(2):300–306, 2001.
- [37] C. Moitzi, N. Freiburger, and O. Glatter. Viscoelastic wormlike micellar solutions made from nonionic surfactants: structural investigations by sans and dls. *The Journal of Physical Chemistry B*, 109(33):16161–16168, 2005.
- [38] S. Huang. Viscoelastic characterization and prediction of a wormlike micellar solution. *Acta Mechanica Sinica*, 37:1–11, 2021.
- [39] D. R. Perinelli, M. Cespi, N. Lorusso, G. F. Palmieri, G. Bonacucina, and P. Blasi. Surfactant self-assembling and critical micelle concentration: One approach fits all? *Langmuir*, 36(21):5745–5753, 2020.
- [40] S. Wu, F. Liang, D. Hu, H. Li, W. Yang, and Q. Zhu. Determining the critical micelle concentration of surfactants by a simple and fast titration method. *Analytical Chemistry*, 92(6):4259–4265, 2019.
- [41] T. Tadros. *Critical Micelle Concentration*, pages 209–210. Springer Berlin Heidelberg, Berlin, Heidelberg, 2013.
- [42] M. Szwarc. Living polymers and mechanisms of anionic polymerization. *Advances in Polymer Science*, 49:1–177, 1983.
- [43] M. Szwarc. Living polymers. their discovery, characterization, and properties. *Journal of Polymer Science Part A: Polymer Chemistry*, 36(1):IX–XV, 1998.
- [44] J. P. Rothstein and H. Mohammadigoushki. Complex flows of viscoelastic wormlike micelle solutions. *Journal of Non-Newtonian Fluid Mechanics*, 285:104382, 2020.
- [45] M. Aguirre-Ramírez, H. Silva-Jiménez, I. M. Banat, and M. A. D. De Rienzo. Surfactants: physicochemical interactions with biological macromolecules. *Biotechnology Letters*, pages 1–13, 2021.
- [46] J. Velikonja and N. Kosaric. *Biosurfactant in Food Applications*. Marcel Dekker Inc., New York, 1993.

- [47] Q. Xu, M. Nakajima, Z. Liu, and T. Shiina. Biosurfactants for microbubble preparation and application. *International Journal of Molecular Sciences*, 12(1):462–475, 2011.
- [48] P. Eslami, H. Hajfarajollah, and S. Bazsefidpar. Recent advancements in the production of rhamnolipid biosurfactants by *Pseudomonas aeruginosa*. *RSC Advances*, 10(56):34014–34032, 2020.
- [49] A. M. Abdel-Mawgoud, F. Lépine, and E. Déziel. Rhamnolipids: diversity of structures, microbial origins and roles. *Applied Microbiology and Biotechnology*, 86(5):1323–1336, 2010.
- [50] S. Lang and D. Wullbrandt. Rhamnose lipids—biosynthesis, microbial production and application potential. *Applied Microbiology and Biotechnology*, 51(1):22–32, 1999.
- [51] V. U. Irorere, L. Tripathi, R. Marchant, S. McClean, and I. M. Banat. Microbial rhamnolipid production: a critical re-evaluation of published data and suggested future publication criteria. *Applied Microbiology and Biotechnology*, 101(10):3941, 2017.
- [52] Y. Zhang, W. J. Maier, and R. M. Miller. Effect of rhamnolipids on the dissolution, bioavailability, and biodegradation of phenanthrene. *Environmental Science & Technology*, 31(8):2211–2217, 1997.
- [53] S. Itoh and T. Suzuki. Effect of rhamnolipids on growth of *Pseudomonas aeruginosa* mutant deficient in n-paraffin-utilizing ability. *Agricultural and Biological Chemistry*, 36(12):2233–2235, 1972.
- [54] A. Lebrón-Paler, J. E. Pemberton, B. A. Becker, W. H. Otto, C. K. Larive, and R. M. Maier. Determination of the acid dissociation constant of the biosurfactant monorhamnolipid in aqueous solution by potentiometric and spectroscopic methods. *Analytical Chemistry*, 78(22):7649–7658, 2006.
- [55] S. A. Adu, P. J. Naughton, R. Marchant, and I. M. Banat. Microbial biosurfactants in cosmetic and personal skincare pharmaceutical formulations. *Pharmaceutics*, 12(11):1099, 2020.

- [56] M. Ramesh and K. Sakthishobana. Significance of biosurfactants in oil recovery and bioremediation of crude oil. In *Green Sustainable Process for Chemical and Environmental Engineering and Science*, pages 211–226. Elsevier, 2021.
- [57] A. P. Karlapudi, T. C. Venkateswarulu, J. Tammineedi, L. Kanumuri, B. K. Ravuru, V. R. Dirisala, and V. P. Kodali. Role of biosurfactants in bioremediation of oil pollution-a review. *Petroleum*, 4(3):241–249, 2018.
- [58] L. Rodrigues, I. M. Banat, J. Teixeira, and R. Oliveira. Biosurfactants: potential applications in medicine. *Journal of Antimicrobial Chemotherapy*, 57(4):609–618, 2006.
- [59] R. Marchant and I. M. Banat. Biosurfactants: a sustainable replacement for chemical surfactants? *Biotechnology Letters*, 34(9):1597–1605, 2012.
- [60] P. K. S. M. Rahman and E. Gakpe. Production, characterisation and applications of biosurfactants-review. *Biotechnology*, 7(2):360–370, 2008.
- [61] A. M. Shete, G. Wadhawa, I. M. Banat, and B. A. Chopade. Mapping of patents on bioemulsifier and biosurfactant: a review. *Journal of Scientific and Industrial Research*, 65(2):91–115.
- [62] J. D. Desai and I. M. Banat. Microbial production of surfactants and their commercial potential. *Microbiology and Molecular Biology Reviews*, 61(1):47–64, 1997.
- [63] E. Z. Ron and E. Rosenberg. Biosurfactants and oil bioremediation. *Current Opinion in Biotechnology*, 13(3):249–252, 2002.
- [64] A. Perfumo, I. M. Banat, and R. Marchant. Going green and cold: biosurfactants from low-temperature environments to biotechnology applications. *Trends in Biotechnology*, 36(3):277–289, 2018.
- [65] A. N. Mendes, L. A. Filgueiras, J. C. Pinto, and M. Nele. Physicochemical properties of rhamnolipid biosurfactant from pseudomonas aeruginosa pa1 to applications in microemulsions. *Journal of Biomaterials and Nanobiotechnology*, 6(01):64, 2015.

- [66] M. O. Ilori, C. J. Amobi, and A. C. Odocha. Factors affecting biosurfactant production by oil degrading aeromonas spp. isolated from a tropical environment. *Chemosphere*, 61(7):985–992, 2005.
- [67] R. B. Lovaglio, F. J. dos Santos, M. J. Junior, and J. Contiero. Rhamnolipid emulsifying activity and emulsion stability: ph rules. *Colloids and Surfaces B: Biointerfaces*, 85(2):301–305, 2011.
- [68] J. M. D. A. Câmara, M. A. S. B. Sousa, E. L. B. Neto, and M. C. A. Oliveira. Application of rhamnolipid biosurfactant produced by pseudomonas aeruginosa in microbial-enhanced oil recovery (meor). *Journal of Petroleum Exploration and Production Technology*, 9(3):2333–2341, 2019.
- [69] D. Bais, A. Trevisan, R. Lapasin, P. Partal, and C. Gallegos. Rheological characterization of polysaccharide–surfactant matrices for cosmetic o/w emulsions. *Journal of Colloid and Interface Science*, 290(2):546–556, 2005.
- [70] I. Kralova and J. Sjöblom. Surfactants used in food industry: a review. *Journal of Dispersion Science and Technology*, 30(9):1363–1383, 2009.
- [71] E. Cappelaere, R. Cressely, and J. P. Decruppe. Linear and non-linear rheological behaviour of salt-free aqueous ctab solutions. *Colloids and Surfaces A: Physicochemical and Engineering Aspects*, 104(2-3):353–374, 1995.
- [72] K. Kuperkar, L. Abezgauz, D. Danino, G. Verma, P. A. Hassan, V. K. Aswal, D. Varade, and P. Bahadur. Viscoelastic micellar water/ctab/nano3 solutions: rheology, sans and cryo-tem analysis. *Journal of Colloid and Interface Science*, 323(2):403–409, 2008.
- [73] V. Hartmann and R. Cressely. Linear and non linear rheology of a wormlike micellar system in presence of sodium tosylate. *Rheologica Acta*, 37(2):115–121, 1998.
- [74] B. Yesilata, C. Clasen, and G. H. McKinley. Nonlinear shear and extensional flow dynamics of wormlike surfactant solutions. *Journal of Non-Newtonian Fluid Mechanics*, 133(2-3):73–90, 2006.

- [75] B. F. García and S. Saraji. Mixed in-situ rheology of viscoelastic surfactant solutions using a hyperbolic geometry. *Journal of Non-Newtonian Fluid Mechanics*, 270:56–65, 2019.
- [76] J. P. Rothstein. Transient extensional rheology of wormlike micelle solutions. *Journal of Rheology*, 47(5):1227–1247, 2003.
- [77] C. D. V. M. Narváez, T. Mazur, and V. Sharma. Dynamics and extensional rheology of polymer-surfactant association complexes. *Soft Matter*, 17:6116–6126, 2021.
- [78] N. Kanaris, D. Grigoriadis, and S. Kassinos. Three dimensional flow around a circular cylinder confined in a plane channel. *Physics of Fluids*, 23(6):064106, 2011.
- [79] F. Rehim, F. Aloui, S. B. Nasrallah, L. Doubiez, and J. Legrand. Experimental investigation of a confined flow downstream of a circular cylinder centred between two parallel walls. *The Journal of Fluids and Structures*, 24(6):855–882, 2008.
- [80] G. H. McKinley, R. C. Armstrong, and R. Brown. The wake instability in viscoelastic flow past confined circular cylinders. *Transactions of the Royal Society of London Society A: Mechanical, Physical and Engineering Sciences*, 344(1671):265–304, 1993.
- [81] M. A. Alves, F. T. Pinho, and P. J. Oliveira. The flow of viscoelastic fluids past a cylinder: finite-volume high-resolution methods. *Journal of Non-Newtonian Fluid Mechanics*, 97(2-3):207–232, 2001.
- [82] P. Y. Huang and J. Feng. Wall effects on the flow of viscoelastic fluids around a circular cylinder. *Journal of Non-Newtonian Fluid Mechanics*, 60(2-3):179–198, 1995.
- [83] H. P. W. Baaijens, G. W. M. Peters, F. P. T. Baaijens, and H. E. H. Meijer. Viscoelastic flow past a confined cylinder of a polyisobutylene solution. *Journal of Rheology*, 39(6):1243–1277, 1995.
- [84] G. R. Moss and J. P. Rothstein. Flow of wormlike micelle solutions past a confined circular cylinder. *Journal of Non-Newtonian Fluid Mechanics*, 165(21-22):1505–1515, 2010.

- [85] G. R. Moss and J. P. Rothstein. Flow of wormlike micelle solutions through a periodic array of cylinders. *Journal of Non-Newtonian Fluid Mechanics*, 165(1-2):1–13, 2010.
- [86] Y. A. Zhao, A. Q. Shen, and S. J. Haward. Flow of wormlike micellar solutions around confined microfluidic cylinders. *Soft Matter*, 12(42):8666–8681, 2016.
- [87] S. J. Haward, N. Kitajima, K. Toda-Peters, T. Takahashi, and A. Q. Shen. Flow of wormlike micellar solutions around microfluidic cylinders with high aspect ratio and low blockage ratio. *Soft Matter*, 15(9):1927–1941, 2019.
- [88] P. A. Vasquez, G. H. McKinley, and P. L. Cook. A network scission model for wormlike micellar solutions: I. Model formulation and viscometric flow predictions. *Journal of Non-Newtonian Fluid Mechanics*, 144(2-3):122–139, 2007.
- [89] M. E. Cates. Reptation of living polymers: dynamics of entangled polymers in the presence of reversible chain-scission reactions. *Macromolecules*, 20(9):2289–2296, 1987.
- [90] P. D. Olmsted, O. Radulescu, and C. Y. D. Lu. Johnson–segalman model with a diffusion term in cylindrical couette flow. *Journal of Rheology*, 44(2):257–275, 2000.
- [91] C. Y. D. Lu, P. D. Olmsted, and R. C. Ball. Effects of nonlocal stress on the determination of shear banding flow. *Physical Review Letters*, 84(4):642, 2000.
- [92] F. Bautista, J. M. De Santos, J. E. Puig, and O. Manero. Understanding thixotropic and antithixotropic behavior of viscoelastic micellar solutions and liquid crystalline dispersions. I. The model. *Journal of Non-Newtonian Fluid Mechanics*, 80(2-3):93–113, 1999.
- [93] C. J. Pipe, N. J. Kim, P. A. Vasquez, L. P. Cook, and G. H. McKinley. Wormlike micellar solutions: II. Comparison between experimental data and scission model predictions. *Journal of Rheology*, 54(4):881–913, 2010.
- [94] L. Zhou, G. H. McKinley, and L. P. Cook. Wormlike micellar solutions: III. VCM model predictions in steady and transient shearing flows. *Journal of Non-Newtonian Fluid Mechanics*, 211:70–83, 2014.

- [95] H. Mohammadigoushki, A. Dalili, L. Zhou, and P. Cook. Transient evolution of flow profiles in a shear banding wormlike micellar solution: Experimental results and a comparison with the vcm model. *Soft Matter*, 15:5483–5494, 2019.
- [96] A. Kalb, L. A. Villasmil-Urdaneta, and M. Cromer. Elastic instability and secondary flow in cross-slot flow of wormlike micellar solutions. *Journal of Non-Newtonian Fluid Mechanics*, 262:79–91, 2018.
- [97] A. Kalb, L. A. Villasmil-Urdaneta, and M. Cromer. Role of chain scission in cross-slot flow of wormlike micellar solutions. *Physical Review Fluids*, 2(7):071301, 2017.
- [98] S. J. Haward and G. H. McKinley. Stagnation point flow of wormlike micellar solutions in a microfluidic cross-slot device: Effects of surfactant concentration and ionic environment. *Physical Review E*, 85(3):031502, 2012.
- [99] N. Dubash, P. Cheung, and A. Q. Shen. Elastic instabilities in a microfluidic cross-slot flow of wormlike micellar solutions. *Soft Matter*, 8(21):5847–5856, 2012.
- [100] C. Sasmal. Flow of wormlike micellar solutions through a long micropore with step expansion and contraction. *Physics of Fluids*, 32(1):013103, 2020.
- [101] E. S. Boek, J. T. Padding, V. J. Anderson, W. J. Briels, and J. P. Crawshaw. Flow of entangled wormlike micellar fluids: Mesoscopic simulations, rheology and μ -piv experiments. *Journal of Non-Newtonian Fluid Mechanics*, 146(1-3):11–21, 2007.
- [102] M. Müller, J. Vorwerk, and P. O. Brunn. Optical studies of local flow behaviour of a non-newtonian fluid inside a porous medium. *Rheologica Acta*, 37(2):189–194, 1998.
- [103] U. Eberhard, H. J. Seybold, E. Secchi, J. Jiménez-Martínez, P. A. Rühs, A. Ofner, J. S. Andrade, and M. Holzner. Mapping the local viscosity of non-Newtonian fluids flowing through disordered porous structures. *Scientific Reports*, 10(1):1–12, 2020.
- [104] H. H. Hu and D. D. Joseph. Numerical simulation of viscoelastic flow past a cylinder. *Journal of Non-Newtonian Fluid Mechanics*, 37(2-3):347–377, 1990.

- [105] A. H. Shiang, J. C. Lin, A. Öztekin, and D. Rockwell. Viscoelastic flow around a confined circular cylinder: measurements using high-image-density particle image velocimetry. *Journal of Non-Newtonian Fluid Mechanics*, 73(1-2):29–49, 1997.
- [106] B. Qin, P. F. Salipante, S. D. Hudson, and P. E. Arratia. Upstream vortex and elastic wave in the viscoelastic flow around a confined cylinder. *Journal of Fluid Mechanics*, 864:1–11, 2019.
- [107] M. B. Khan and C. Sasmal. Effect of chain scission on flow characteristics of worm-like micellar solutions past a confined microfluidic cylinder: A numerical analysis. *Soft Matter*, 16:5261–5272, 2020.
- [108] S. Varchanis, C. C. Hopkins, A. Q. Shen, J. Tsamopoulos, and S. J. Haward. Asymmetric flows of complex fluids past confined cylinders: A comprehensive numerical study with experimental validation. *Physics of Fluids*, 32(5):053103, 2020.
- [109] S. J. Haward, K. Toda-Peters, and A. Q. Shen. Steady viscoelastic flow around high-aspect-ratio, low-blockage-ratio microfluidic cylinders. *Journal of Non-Newtonian Fluid Mechanics*, 254:23–35, 2018.
- [110] A. Varshney and V. Steinberg. Elastic wake instabilities in a creeping flow between two obstacles. *Physical Review Fluids*, 2(5):051301, 2017.
- [111] J. R. Cressman, Q. Bailey, and W. I. Goldburg. Modification of a vortex street by a polymer additive. *Physics of Fluids*, 13(4):867–871, 2001.
- [112] L. Zhu and L. Xi. Vortex dynamics in low-and high-extent polymer drag reduction regimes revealed by vortex tracking and conformation analysis. *Physics of Fluids*, 31(9):095103, 2019.
- [113] C. C. Hopkins, S. J. Haward, and A. Q. Shen. Tristability in viscoelastic flow past side-by-side microcylinders. *Physical Review Letters*, 126(5):054501, 2021.
- [114] H. Mohammadigoushki and S. J. Muller. Sedimentation of a sphere in wormlike micellar fluids. *Journal of Rheology*, 60(4):587–601, 2016.
- [115] S. Chen and J. P. Rothstein. Flow of a wormlike micelle solution past a falling sphere. *Journal of Non-Newtonian Fluid Mechanics*, 116(2-3):205–234, 2004.

- [116] C. Sasmal. Unsteady motion past a sphere translating steadily in wormlike micellar solutions: A numerical analysis. *Journal of Fluid Mechanics*, In press, 2021.
- [117] J. H. Masliyah and S. Bhattacharjee. *Electrokinetic and Colloid Transport Phenomena*. John Wiley & Sons, 2006.
- [118] A. Alizadeh, W. Hsu, M. Wang, and H. Daiguji. Electroosmotic flow: From microfluidics to nanofluidics. *Electrophoresis*, 42(7-8):834–868, 2021.
- [119] C. H. Ko, D. Li, A. Malekanfard, Y. N. Wang, L. M. Fu, and X. Xuan. Electroosmotic flow of non-newtonian fluids in a constriction microchannel. *Electrophoresis*, 40(10):1387–1394, 2019.
- [120] A. M. Afonso, F. T. Pinho, and M. A. Alves. Electro-osmosis of viscoelastic fluids and prediction of electro-elastic flow instabilities in a cross slot using a finite-volume method. *Journal of Non-Newtonian Fluid Mechanics*, 179:55–68, 2012.
- [121] F. Pimenta and M. A. Alves. Electro-elastic instabilities in cross-shaped microchannels. *Journal of Non-Newtonian Fluid Mechanics*, 259:61–77, 2018.
- [122] S. H. Sadek, F. T. Pinho, and M. A. Alves. Electro-elastic flow instabilities of viscoelastic fluids in contraction/expansion micro-geometries. *Journal of Non-Newtonian Fluid Mechanics*, 283:104293, 2020.
- [123] J. Ji, S. Qian, and Z. Liu. Electroosmotic flow of viscoelastic fluid through a constriction microchannel. *Micromachines*, 12(4):417, 2021.
- [124] L. Song, L. Yu, D. Li, P. P. Jagdale, and X. Xuan. Elastic instabilities in the electroosmotic flow of non-newtonian fluids through t-shaped microchannels. *Electrophoresis*, 41(7-8):588–597, 2020.
- [125] C. Zhao and C. Yang. Exact solutions for electro-osmotic flow of viscoelastic fluids in rectangular micro-channels. *Applied Mathematics and Computation*, 211(2):502–509, 2009.
- [126] X. Wang, Y. Jiang, Y. Qiao, H. Xu, and H. Qi. Numerical study of electroosmotic slip flow of fractional Oldroyd-B fluids at high zeta potentials. *Electrophoresis*, 41(10-11):769–777, 2020.

- [127] X. Yang, H. Qi, and X. Jiang. Numerical analysis for electroosmotic flow of fractional Maxwell fluids. *Applied Mathematics Letters*, 78:1–8, 2018.
- [128] S. Wang and M. Zhao. Analytical solution of the transient electro-osmotic flow of a generalized fractional Maxwell fluid in a straight pipe with a circular cross-section. *European Journal of Mechanics-B/Fluids*, 54:82–86, 2015.
- [129] X. Chen, Y. Jian, and Z. Xie. Slippery electrokinetic flow of viscoelastic fluids with pressure-dependent viscosity and relaxation time. *Colloids and Surfaces A: Physicochemical and Engineering Aspects*, page 128354, 2022.
- [130] J. Escandón, E. Jiménez, C. Hernández, O. Bautista, and F. Méndez. Transient electroosmotic flow of maxwell fluids in a slit microchannel with asymmetric zeta potentials. *European Journal of Mechanics-B/Fluids*, 53:180–189, 2015.
- [131] R. Sarma, N. Deka, K. Sarma, and P. K. Mondal. Electroosmotic flow of phan-thien–tanner fluids at high zeta potentials: An exact analytical solution. *Physics of Fluids*, 30(6):062001, 2018.
- [132] L. Martínez, O. Bautista, J. Escandón, and F. Méndez. Electroosmotic flow of a Phan-Thien-Tanner fluid in a wavy-wall microchannel. *Colloids and Surfaces A: Physicochemical and Engineering Aspects*, 498:7–19, 2016.
- [133] S. Dhinakaran, A. M. Afonso, M. A. Alves, and F. T. Pinho. Steady viscoelastic fluid flow between parallel plates under electro-osmotic forces: Phan-thien–tanner model. *Journal of Colloid and Interface Science*, 344(2):513–520, 2010.
- [134] O. Bautista, S. Sánchez, J. C. Arcos, and F. Méndez. Lubrication theory for electro-osmotic flow in a slit microchannel with the Phan-Thien and Tanner model. *Journal of Fluid Mechanics*, 722:496–532, 2013.
- [135] L. L. Ferrás, A. S. Cavadas, P. R. Resende, A. M. Afonso, and F. T. Pinho. Effect of the solvent viscosity on pure electro-osmotic flow of viscoelastic fluids. *Journal of Non-Newtonian Fluid Mechanics*, 259:125–129, 2018.
- [136] L. Song, P. Jagdale, L. Yu, Z. Liu, D. Li, C. Zhang, and X. Xuan. Electrokinetic instability in microchannel viscoelastic fluid flows with conductivity gradients. *Physics of Fluids*, 31(8):082001, 2019.

- [137] C. Zhao and C. Yang. Electrokinetics of non-newtonian fluids: a review. *Advances in Colloid and Interface Science*, 201:94–108, 2013.
- [138] S. D. Fraia, N. Massarotti, and P. Nithiarasu. Modelling electro-osmotic flow in porous media: a review. *International Journal of Numerical Methods for Heat & Fluid Flow*, 2018.
- [139] A. S. Rathore and C. S Horváth. Capillary electrochromatography: theories on electroosmotic flow in porous media.
- [140] Q. H. Wan. Capillary electrochromatography: effect of electrolyte concentration on electroosmotic flow and column efficiency. *Journal of Chromatography A*, 782(2):181–189, 1997.
- [141] S. Zeng, C. H. Chen, J. C. Mikkelsen Jr, and J. G. Santiago. Fabrication and characterization of electroosmotic micropumps. *Sensors and Actuators B: Chemical*, 79(2-3):107–114, 2001.
- [142] S. Yao and J. G. Santiago. Porous glass electroosmotic pumps: theory. *Journal of Colloid and Interface Science*, 268(1):133–142, 2003.
- [143] M. Wang, J. Wang, S. Chen, and N. Pan. Electrokinetic pumping effects of charged porous media in microchannels using the lattice poisson–boltzmann method. *Journal of Colloid and Interface Science*, 304(1):246–253, 2006.
- [144] A. P. Shapiro and R. F. Probstein. Removal of contaminants from saturated clay by electroosmosis. *Environmental Science & Technology*, 27(2):283–291, 1993.
- [145] C. Cameselle. Enhancement of electro-osmotic flow during the electrokinetic treatment of a contaminated soil. *Electrochimica Acta*, 181:31–38, 2015.
- [146] T. Sochi. Non-newtonian flow in porous media. *Polymer*, 51(22):5007–5023, 2010.
- [147] A. Groisman and V. Steinberg. Elastic turbulence in a polymer solution flow. *Nature*, 405(6782):53–55, 2000.
- [148] V. Steinberg. Elastic turbulence: an experimental view on inertialess random flow. *Annual Review of Fluid Mechanics*, 53:27–58, 2021.

- [149] C. A. Browne and S. S. Datta. Elastic turbulence generates anomalous flow resistance in porous media. *Science Advances*, 7(45):1–10, 2021.
- [150] J. Mitchell, K. Lyons, A. M. Howe, and A. Clarke. Viscoelastic polymer flows and elastic turbulence in three-dimensional porous structures. *Soft Matter*, 12(2):460–468, 2016.
- [151] A. Clarke, A. M. Howe, J. Mitchell, J. Staniland, L. Hawkes, and K. Leeper. Mechanism of anomalously increased oil displacement with aqueous viscoelastic polymer solutions. *Soft Matter*, 11(18):3536–3541, 2015.
- [152] A. M. Howe, A. Clarke, and D. Giernalczyk. Flow of concentrated viscoelastic polymer solutions in porous media: effect of mw and concentration on elastic turbulence onset in various geometries. *Soft Matter*, 11(32):6419–6431, 2015.
- [153] C. A. Browne, A. Shih, and S. S. Datta. Pore-scale flow characterization of polymer solutions in microfluidic porous media. *Small*, 16(9):1903944, 2020.
- [154] F. J. Galindo-Rosales, L. Campo-Deano, F. T. Pinho, E. Van Bokhorst, P. J. Hamersma, M. S. N. Oliveira, and M. A. Alves. Microfluidic systems for the analysis of viscoelastic fluid flow phenomena in porous media. *Microfluidics and Nanofluidics*, 12(1-4):485–498, 2012.
- [155] C. A. Browne, A. Shih, and S. S. Datta. Bistability in the unstable flow of polymer solutions through pore constriction arrays. *Journal of Fluid Mechanics*, 890, 2020.
- [156] M. Kumar, S. Aramideh, C. A. Browne, S. S. Datta, and A. M. Ardekani. Numerical investigation of multistability in the unstable flow of a polymer solution through porous media. *Physical Review Fluids*, 6(3):033304, 2021.
- [157] C. Chang and R. Yang. Electrokinetic mixing in microfluidic systems. *Microfluidics and Nanofluidics*, 3(5):501–525, 2007.
- [158] S. Rashidi, H. Bafekr, M. S. Valipour, and J. A. Esfahani. A review on the application, simulation, and experiment of the electrokinetic mixers. *Chemical Engineering and Processing-Process Intensification*, 126:108–122, 2018.

- [159] R. M. Bryce and M. R. Freeman. Abatement of mixing in shear-free elongationally unstable viscoelastic microflows. *Lab on a Chip*, 10(11):1436–1441, 2010.
- [160] C. Sasmal. A simple yet efficient approach for electrokinetic mixing of viscoelastic fluids in a straight microchannel. *Scientific Reports*, 12(1):1–13, 2022.
- [161] H. M. Park and W. M. Lee. Effect of viscoelasticity on the flow pattern and the volumetric flow rate in electroosmotic flows through a microchannel. *Lab on a Chip*, 8(7):1163–1170, 2008.
- [162] X. Lu, S. Patel, M. Zhang, S. W. Joo, S. Qian, A. Ogale, and X. Xuan. An unexpected particle oscillation for electrophoresis in viscoelastic fluids through a microchannel constriction. *Biomicrofluidics*, 8(2):021802, 2014.
- [163] X. Lu, J. DuBose, S. W. Joo, S. Qian, and X. Xuan. Viscoelastic effects on electrokinetic particle focusing in a constricted microchannel. *Biomicrofluidics*, 9(1):014108, 2015.
- [164] J. Bantor, A. Malekanfard, M. K. Raihan, S. Wu, X. Pan, Y. Song, and X. Xuan. Insulator-based dielectrophoretic focusing and trapping of particles in non-newtonian fluids. *Electrophoresis*, 42(21-22):2154–2161, 2021.
- [165] J. Bantor, M. K. Raihan, C. McNeely, Z. Liu, Y. Song, and X. Xuan. Fluid rheological effects on streaming dielectrophoresis in a post-array microchannel. *Electrophoresis*, 43(5-6):717–723, 2022.
- [166] C. C. Hopkins, S. J. Haward, and A. Q. Shen. Upstream wall vortices in viscoelastic flow past a cylinder. *Soft Matter*, 18(26):4868–4880, 2022.
- [167] C. C. Hopkins, A. Q. Shen, and S. J. Haward. Effect of blockage ratio on flow of a viscoelastic wormlike micellar solution past a cylinder in a microchannel. *Soft Matter*, 18(46):8856–8866, 2022.
- [168] I. Glasgow, J. Batton, and N. Aubry. Electroosmotic mixing in microchannels. *Lab on a Chip*, 4(6):558–562, 2004.
- [169] I. Glasgow and N. Aubry. Enhancement of microfluidic mixing using time pulsing. *Lab on a Chip*, 3(2):114–120, 2003.

- [170] C. Lee, C. Chang, and L. Wang, Y.and Fu. Microfluidic mixing: a review. *International Journal of Molecular Sciences*, 12(5):3263–3287, 2011.
- [171] C. Lee, W. Wang, C. Liu, and L. Fu. Passive mixers in microfluidic systems: A review. *Chemical Engineering Journal*, 288:146–160, 2016.
- [172] P. J. Schmid. Dynamic mode decomposition of numerical and experimental data. *Journal of Fluid Mechanics*, 656:5–28, 2010.
- [173] Q. Zhang, Y. Liu, and S. Wang. The identification of coherent structures using proper orthogonal decomposition and dynamic mode decomposition. *Journal of Fluids and Structures*, 49:53–72, 2014.
- [174] H. G. Weller, G. Tabor, H. Jasak, and C. Fureby. A tensorial approach to computational continuum mechanics using object-oriented techniques. *Computers in Physics*, 12(6):620–631, 1998.
- [175] E. S. G. Shaqfeh and B. Khomami. The oldroyd-b fluid in elastic instabilities, turbulence and particle suspensions. *Journal of Non-Newtonian Fluid Mechanics*, 298:104672, 2021.
- [176] D. F. James. Boger fluids. *Annual Review of Fluid Mechanics*, 41:129–142, 2009.
- [177] C. Greenshields and H. Weller. Notes on computational fluid dynamics: General principles. *CFD Direct Ltd.: Reading, UK*, 2022.
- [178] *The finite volume method in computational fluid dynamics: an advanced introduction with OpenFOAM and Matlab®, author=Darwish, M. and Moukalled, F., year=2021, publisher=Springer.*
- [179] F. Pimenta and M.A. Alves. rheoTool. <https://github.com/fppimenta/rheoTool>, 2016.
- [180] M. A. Ajiz and A. Jennings. A robust incomplete choleski-conjugate gradient algorithm. *International Journal for Numerical Methods in Engineering*, 20(5):949–966, 1984.

- [181] J. Lee, J. Zhang, and C. C. Lu. Incomplete LU preconditioning for large scale dense complex linear systems from electromagnetic wave scattering problems. *Journal of Computational Physics*, 185(1):158–175, 2003.
- [182] M. A. Alves, P. J. Oliveira, and F. T. Pinho. A convergent and universally bounded interpolation scheme for the treatment of advection. *International Journal for Numerical Methods in Fluids*, 41(1):47–75, 2003.
- [183] H. Medina, A. Beecham, J. Saul, S. Porter, S. Aleksandrova, and S. Benjamin. Open source computational fluid dynamics using openfoam. In *Royal Aeronautical Society, General Aviation Conference, London*, 2015.
- [184] J. Zhou, R. Xue, S. Liu, N. Xu, F. Xin, W. Zhang, M. Jiang, and W. Dong. High di-rhamnolipid production using pseudomonas aeruginosa kt1115, separation of mono/di-rhamnolipids, and evaluation of their properties. *Frontiers in Bioengineering and Biotechnology*, 7:245, 2019.
- [185] P. K. S. M. Rahman, G. Pasirayi, V. Auger, and Z. Ali. Production of rhamnolipid biosurfactants by pseudomonas aeruginosa ds10-129 in a microfluidic bioreactor. *Biotechnology and Applied Biochemistry*, 55(1):45–52, 2010.
- [186] S. Twomey. *Introduction to the Mathematics of Inversion in Remote Sensing and Indirect Measurements*. Elsevier, 2013.
- [187] C. L. Lawson and R. J. Hanson. *Solving Least Squares Problems*. SIAM, 1995.
- [188] K. Aramaki, M. Fujii, and Y. Sakanishi. Rheological properties of silicone-surfactant-based wormlike micellar solution. *Colloids and Surfaces A: Physicochemical and Engineering Aspects*, 581:123841, 2019.
- [189] M. Kamada, S. Shimizu, and K. Aramaki. Manipulation of the viscosity behavior of wormlike micellar gels by changing the molecular structure of added perfumes. *Colloids and Surfaces A: Physicochemical and Engineering Aspects*, 458:110–116, 2014.
- [190] J. Dinic, M. Biagioli, and V. Sharma. Pinch-off dynamics and extensional relaxation times of intrinsically semi-dilute polymer solutions characterized by dripping-

- onto-substrate rheometry. *Journal of Polymer Science Part B: Polymer Physics*, 55(22):1692–1704, 2017.
- [191] J. Dinic, Y. Zhang, L. N. Jimenez, and V. Sharma. Extensional relaxation times of dilute, aqueous polymer solutions. *ACS Macro Letters*, 4(7):804–808, 2015.
- [192] J. Eastoe and J. S. Dalton. Dynamic surface tension and adsorption mechanisms of surfactants at the air–water interface. *Advances in Colloid and Interface Science*, 85(2-3):103–144, 2000.
- [193] H. Yunfei, S. Yazhuo, L. Honglai, L. Dominique, and S. Anniina. Surfactant adsorption onto interfaces: Measuring the surface excess in time. *Langmuir*, 28(6):3146–3151, 2012.
- [194] S. Ghosh, D. Khatua, and J. Dey. Interaction between zwitterionic and anionic surfactants: spontaneous formation of zwitanionic vesicles. *Langmuir*, 27(9):5184–5192, 2011.
- [195] R. Wang, Y. Li, and Y. Li. Interaction between cationic and anionic surfactants: detergency and foaming properties of mixed systems. *Journal of Surfactants and Detergents*, 17(5):881–888, 2014.
- [196] M. B. Khan and S. Anwar. Optimization technique for the evaluation of physicochemical properties of cationic surfactant in presence of alkali/metal halide salt and their effects on acidic crude oil. *Journal of Chemical and Petroleum Engineering*, 55(1):11–32, 2021.
- [197] M. B. Khan and S. Anwar. Surface tension and wettability analysis during the interaction of alkali-nano silica and its effect on acidic crude oil. *Safety in Extreme Environments*, 3(1):51–61, 2021.
- [198] G. C. D. Silva, C. G. F. T. Rossi, A. A. D. Neto, T. N. C. Dantas, and J.L. C. Fonseca. Characterization of wormlike micellar systems using dls, rheometry and tensiometry. *Colloids and Surfaces A: Physicochemical and Engineering Aspects*, 377(1-3):35–43, 2011.

- [199] C. Oelschlaeger and N. Willenbacher. Mixed wormlike micelles of cationic surfactants: Effect of the cosurfactant chain length on the bending elasticity and rheological properties. *Colloids and Surfaces A: Physicochemical and Engineering Aspects*, 406:31–37, 2012.
- [200] M. J. Qazi, S. J. Schlegel, E. H. G. Backus, M. Bonn, D. Bonn, and N. Shahidzadeh. Dynamic surface tension of surfactants in the presence of high salt concentrations. *Langmuir*, 36(27):7956–7964, 2020.
- [201] J. Park, U. Pasaogullari, and L. Bonville. Wettability measurements of irregular shapes with wilhelmy plate method. *Applied Surface Science*, 427:273–280, 2018.
- [202] D. Tiab and E. C. Donaldson. Applications of darcy’s law. *Petrophysics (Third Edition)*. Boston: Gulf Professional Publishing, 2012.
- [203] E. Buhler, C. Oelschlaeger, G. Waton, and S. J. Candau. Viscoelastic properties of hydrocarbon/fluorocarbon mixed wormlike micelles at high ionic strength. *The Journal of Physical Chemistry B*, 108(30):11236–11243, 2004.
- [204] G. Garg, P. A. Hassan, and S. K. Kulshreshtha. Dynamic light scattering studies of rod-like micelles in dilute and semi-dilute regime. *Colloids and Surfaces A: Physicochemical and Engineering Aspects*, 275(1-3):161–167, 2006.
- [205] J. F. Berret. Rheology of wormlike micelles: Equilibrium properties and shear banding transitions. In *Molecular Gels*, pages 667–720. Springer, 2006.
- [206] M. R. Rojas, A. J. Müller, and A. E. Sáez. Shear rheology and porous media flow of wormlike micelle solutions formed by mixtures of surfactants of opposite charge. *Journal of Colloid and Interface Science*, 326(1):221–226, 2008.
- [207] F. Lequeux. Structure and rheology of wormlike micelles. *Current Opinion in Colloid & Interface Science*, 1(3):341–344, 1996.
- [208] K. Aramaki, S. Hoshida, and S. Arima. Effect of carbon chain length of cosurfactant on the rheological properties of nonionic wormlike micellar solutions formed by a sugar surfactant and monohydroxy alcohols. *Colloids and Surfaces A: Physicochemical and Engineering Aspects*, 366(1-3):58–62, 2010.

- [209] M. Kamada, C. Pierlot, V. Molinier, J. M. Aubry, and K. Aramaki. Rheological properties of wormlike micellar gels formed by novel bio-based isosorbide surfactants. *Colloids and Surfaces A: Physicochemical and Engineering Aspects*, 536:82–87, 2018.
- [210] M. B. Khan. Rheological behavior of polyacrylamide solution in the presence of cationic gemini surfactants/conventional surfactants. *Asia-Pacific Journal of Chemical Engineering*, 12(4):671–678, 2017.
- [211] L. Gentile and S. Amin. Rheology primer for nanoparticle scientists. In *Colloidal Foundations of Nanoscience*, pages 289–306. Elsevier, 2022.
- [212] R. Oda, P. Panizza, M. Schmutz, and F. Lequeux. Direct evidence of the shear-induced structure of wormlike micelles: Gemini surfactant 12- 2- 12. *Langmuir*, 13(24):6407–6412, 1997.
- [213] S. A. Rogers, M. A. Calabrese, and N. J. Wagner. Rheology of branched wormlike micelles. *Current Opinion in Colloid & Interface Science*, 19(6):530–535, 2014.
- [214] S. J. Candau, A. Khatory, F. Lequeux, and F. Kern. Rheological behaviour of wormlike micelles: effect of salt content. *Le Journal de Physique IV*, 3(C1):C1–197, 1993.
- [215] V. Hartmann and R. Cressely. Influence of sodium salicylate on the rheological behaviour of an aqueous ctab solution. *Colloids and Surfaces A: Physicochemical and Engineering Aspects*, 121(2-3):151–162, 1997.
- [216] F. J. Stadler, C. Piel, J. Kaschta, S. Rulhoff, W. Kaminsky, and H. Münstedt. Dependence of the zero shear-rate viscosity and the viscosity function of linear high-density polyethylenes on the mass-average molar mass and polydispersity. *Rheologica Acta*, 45(5):755–764, 2006.
- [217] P. E. Boukany and S. Q. Wang. Nature of steady flow in entangled fluids revealed by superimposed small amplitude oscillatory shear. *Journal of Rheology*, 53(6):1425–1435, 2009.

- [218] Q. Yuan, X. Lu, K. H. Khayat, D. Feys, and C. Shi. Small amplitude oscillatory shear technique to evaluate structural build-up of cement paste. *Materials and Structures*, 50(2):1–12, 2017.
- [219] M. B. Khan, M. F. Khoker, M. Husain, M. Ahmed, and S. Anwer. Effects of nanoparticles on rheological behavior of polyacrylamide related to enhance oil recovery. *Academic Journal of Polymer Science*, 1:1–2, 2018.
- [220] Y. Bai, S. Liu, G. Liang, Y. Liu, Y. Chen, Y. and Bao, and Y. Shen. Wormlike micelles properties and oil displacement efficiency of a salt-tolerant c22-tailed amidosulfobetaine surfactant. *Energy Exploration & Exploitation*, 39(4):1057–1075, 2021.
- [221] H. Rehage and H. Hoffmann. Rheological properties of viscoelastic surfactant systems. *The Journal of Physical Chemistry*, 92(16):4712–4719, 1988.
- [222] H. Tang, J. Song, M. Zhao, Z. Zhang, W. Liu, and Z. Yan. Performance evaluation and mechanism study of seawater-based circulatory fracturing fluid based on ph-regulated wormlike micelles. *Frontiers in Chemistry*, 10:364, 2022.
- [223] M. Doi and S. F. Edwards. The theory of polymer dynamics clarendon, 1986.
- [224] P. G. De Gennes. *Scaling concepts in polymer physics*. Cornell University Press, 1979.
- [225] Y. Liu, Y. Jun, and V. Steinberg. Concentration dependence of the longest relaxation times of dilute and semi-dilute polymer solutions. *Journal of Rheology*, 53(5):1069–1085, 2009.
- [226] F. D. Giudice, S. J. Haward, and A. Q. Shen. Relaxation time of dilute polymer solutions: A microfluidic approach. *Journal of Rheology*, 61(2):327–337, 2017.
- [227] E. Guzmán, S. Llamas, A. Maestro, L. Fernández-Peña, A. Akanno, R. Miller, F. Ortega, and R. Rubio. Polymer–surfactant systems in bulk and at fluid interfaces. *Advances in Colloid and Interface Science*, 233:38–64, 2016.
- [228] T. L. Carlson, J. Y. Lock, and R. L. Carrier. Engineering the mucus barrier. *Annual Review of Biomedical Engineering*, 20:197–220, 2018.

- [229] R. F. Day, E. J. Hinch, and J. R. Lister. Self-similar capillary pinchoff of an inviscid fluid. *Physical Review Letters*, 80(4):704, 1998.
- [230] S. Middleman. *Modeling axisymmetric flows: dynamics of films, jets, and drops*. Academic Press, 1995.
- [231] C. Bonnoit, T. Bertrand, E. Clément, and A. Lindner. Accelerated drop detachment in granular suspensions. *Physics of Fluids*, 24(4):043304, 2012.
- [232] V. M. Entov and E. J. Hinch. Effect of a spectrum of relaxation times on the capillary thinning of a filament of elastic liquid. *Journal of Non-Newtonian Fluid Mechanics*, 72(1):31–53, 1997.
- [233] J. Dinic and V. Sharma. Power laws dominate shear and extensional rheology response and capillarity-driven pinching dynamics of entangled hydroxyethyl cellulose (hec) solutions. *Macromolecules*, 53(9):3424–3437, 2020.
- [234] J. Dinic and V. Sharma. Macromolecular relaxation, strain, and extensibility determine elastocapillary thinning and extensional viscosity of polymer solutions. *Proceedings of the National Academy of Sciences*, 116(18):8766–8774, 2019.
- [235] J. Dinic and V. Sharma. Computational analysis of self-similar capillary-driven thinning and pinch-off dynamics during dripping using the volume-of-fluid method. *Physics of Fluids*, 31(2):021211, 2019.
- [236] E. J. Nodoushan, Y. J. Lee, G. H. Lee, and N. Kim. Quasi-static secondary flow regions formed by microfluidic contraction flows of wormlike micellar solutions. *Physics of Fluids*, 33(9):093112, 2021.
- [237] D. Sachsenheimer, C. Oelschlaeger, S. Müller, J. Küstner, S. Bindgen, and N. Willenbacher. Elongational deformation of wormlike micellar solutions. *Journal of Rheology*, 58(6):2017–2042, 2014.
- [238] S. J. Haward, V. Sharma, and J. A. Odell. Extensional opto-rheometry with biofluids and ultra-dilute polymer solutions. *Soft Matter*, 7(21):9908–9921, 2011.

- [239] M. Cromer, L. P. Cook, and G. H. McKinley. Pressure-driven flow of wormlike micellar solutions in rectilinear microchannels. *Journal of Non-Newtonian Fluid Mechanics*, 166(3-4):180–193, 2011.
- [240] H. Dou and N. Phan-Thien. Viscoelastic flow past a confined cylinder: Instability and velocity inflection. *Chemical Engineering Science*, 62(15):3909–3929, 2007.
- [241] H. S. Dou and N. Phan-Thien. An instability criterion for viscoelastic flow past a confined cylinder. *Korea-Australia Rheology Journal*, 20(1):15–26, 2008.
- [242] Y. Zhang and S. J. Muller. Unsteady sedimentation of a sphere in wormlike micellar fluids. *Physical Review Fluids*, 3(4):043301, 2018.
- [243] A. Varshney and V. Steinberg. Elastic alfvén waves in elastic turbulence. *Nature Communications*, 10(1):652, 2019.
- [244] C. C. Hopkins, S. J. Haward, and A. Q. Shen. Purely elastic fluid–structure interactions in microfluidics: Implications for mucociliary flows. *Small*, 16(9):1903872, 2019.
- [245] C. Sun and H. Y. Huang. Measurements of flow-induced birefringence in microfluidics. *Biomicrofluidics*, 10(1):011903, 2016.
- [246] R. Cressely and R. Hocquart. Biréfringence d’écoulement localisée induite à l’arrière d’obstacles. *Optica Acta: International Journal of Optics*, 27(5):699–711, 1980.
- [247] J. M. Verhelst and F. I. M. Nieuwstadt. Visco-elastic flow past circular cylinders mounted in a channel: experimental measurements of velocity and drag. *Journal of Non-Newtonian Fluid Mechanics*, 116(2-3):301–328, 2004.
- [248] F. P. T. Baaijens, S. H. A. Selen, H. P. W. Baaijens, G. W. M. Peters, and H. E. H. Meijer. Viscoelastic flow past a confined cylinder of a low density polyethylene melt. *Journal of Non-Newtonian Fluid Mechanics*, 68(2-3):173–203, 1997.
- [249] S. J. Haward, C. C. Hopkins, and A. Q. Shen. Asymmetric flow of polymer solutions around microfluidic cylinders: Interaction between shear-thinning and viscoelasticity. *Journal of Non-Newtonian Fluid Mechanics*, 278:104250, 2020.

- [250] Peyman Pakdel and Gareth H McKinley. Elastic instability and curved streamlines. *Physical Review Letters*, 77(12):2459, 1996.
- [251] M. A. Fardin and S. Lerouge. Instabilities in wormlike micelle systems. *The European Physical Journal E*, 35(9):1–29, 2012.
- [252] A. M. Afonso, M. A. Alves, and F. T. Pinho. Analytical solution of mixed electro-osmotic/pressure driven flows of viscoelastic fluids in microchannels. *Journal of Non-Newtonian Fluid Mechanics*, 159(1-3):50–63, 2009.
- [253] B. Wojcik, J. LaRuez, M. Cromer, and L. A. V. Urdaneta. The role of elasticity in the vortex formation in polymeric flow around a sharp bend. *Applied Sciences*, 11(14):6588, 2021.
- [254] M. Y. Hwang, H. Mohammadigoushki, and S. J. Muller. Flow of viscoelastic fluids around a sharp microfluidic bend: Role of wormlike micellar structure. *Physical Review Fluids*, 2(4):043303, 2017.
- [255] P. C. Sousa, F. T. Pinho, M. S. N. Oliveira, and M. A. Alves. Purely elastic flow instabilities in microscale cross-slot devices. *Soft matter*, 11(45):8856–8862, 2015.
- [256] A. Öztekin, B. Alakus, and G. H. McKinley. Stability of planar stagnation flow of a highly viscoelastic fluid. *Journal of Non-Newtonian Fluid Mechanics*, 72(1):1–29, 1997.
- [257] P. J. Oliveira. Method for time-dependent simulations of viscoelastic flows: vortex shedding behind cylinder. *Journal of Non-Newtonian Fluid Mechanics*, 101(1-3):113–137, 2001.
- [258] Y. K. Suh and S. Kang. A review on mixing in microfluidics. *Micromachines*, 1(3):82–111, 2010.
- [259] A. Groisman and V. Steinberg. Efficient mixing at low reynolds numbers using polymer additives. *Nature*, 410(6831):905–908, 2001.
- [260] F. Hamid, C. Sasmal, and R. P. Chhabra. Dynamic mode decomposition analysis and fluid-mechanical aspects of viscoelastic fluid flows past a cylinder in laminar vortex shedding regime. *Physics of Fluids*, 34(10):103114, 2022.

- [261] F. Hamid and C. Sasmal. Strong effect of fluid rheology on electrokinetic instability and subsequent mixing phenomena in a microfluidic t-junction. *Physics of Fluids*, 35(1):013107, 2023.
- [262] S. K. Tiwari, S. Bhat, and K. K. Mahato. Design and fabrication of low-cost microfluidic channel for biomedical application. *Scientific Reports*, 10(1):1–14, 2020.
- [263] G. V. Casquillas, T. Houssin, and L. Durieux. Microfluidics and microfluidic devices: A review. *Elveflow Microfluidic Instruments RSS*, 2018.
- [264] P. Dontula, C. W. Macosko, and L. E. Scriven. Model elastic liquids with water-soluble polymers. *AIChE journal*, 44(6):1247–1255, 1998.
- [265] Y. Song, J. Li, and D. Li. Zeta potentials of polydimethylsiloxane surfaces modified by polybrene of different concentrations. *Electrophoresis*, 37(4):567–572, 2016.
- [266] B. J. Kirby and E. F. Hasselbrink Jr. Zeta potential of microfluidic substrates: 2. data for polymers. *Electrophoresis*, 25(2):203–213, 2004.
- [267] Y. Liu, J. C. Fanguy, J. M. Bledsoe, and C. S. Henry. Dynamic coating using polyelectrolyte multilayers for chemical control of electroosmotic flow in capillary electrophoresis microchips. *Analytical Chemistry*, 72(24):5939–5944, 2000.
- [268] W. Thielicke and R. Sonntag. Particle Image Velocimetry for MATLAB: Accuracy and enhanced algorithms in PIVlab. *Journal of Open Research Software*, 9(1), 2021.
- [269] A. Chauhan, S. Gupta, and C. Sasmal. Effect of geometric disorder on chaotic viscoelastic porous media flows. *Physics of Fluids*, 34(9):093105, 2022.